Thesis

Novel Pixel Sensors in HV-CMOS Technology and Test Beam Infrastructure for Upgrades of the ATLAS Inner Tracking System

RISTIC, Branislav

Abstract

In the search for new physics, the Large Hadron Collider at CERN will be upgraded around year 2025, increasing its integrated luminosity by an order of magnitude. For the Inner Tracker (ITk) of the ATLAS experiment, the elevated levels of radiation, pile-up and data rate will require a complete replacement. Active pixel sensors built in sub-micron High Voltage CMOS (HV-CMOS) processes are candidates for the ITk outer pixel detector layers. Being high voltage tolerant, thus supporting drift-based charge collection, they allow to build radiation hard detectors in industry standard technology. On-sensor signal processing permits replacing complex and cost-intensive hybridisation techniques by simpler ones, ultimately leading to fully monolithic devices. In this thesis, sensors built in the ams H18 180nm process were investigated as hybrid detectors. Several design versions were characterised in laboratory and in-beam measurements. The FE-I4 Telescope, a particle tracker for beam based detector characterisation was built to facilitate measurements on HV-CMOS sensors. Its construction and performance as well as the findings on [...]

Reference

RISTIC, Branislav. *Novel Pixel Sensors in HV-CMOS Technology and Test Beam Infrastructure for Upgrades of the ATLAS Inner Tracking System*. Thèse de doctorat : Univ. Genève, 2018, no. Sc. 5238

DOI : 10.13097/archive-ouverte/unige:138543
URN : urn:nbn:ch:unige-1385436

UNIVERSITÉ DE GENÈVE
Section de Physique
Département de Physique Nucléaire et Corpusculaire

FACULTÉ DES SCIENCES
Prof. Giuseppe Iacobucci

Novel Pixel Sensors in HV-CMOS Technology and Test Beam Infrastructure for Upgrades of the ATLAS Inner Tracking System

THÈSE

présentée à la Faculté des Sciences de l'Université de Genève
pour obtenir le grade de docteur ès Sciences, mention Physique

par

Branislav Ristić
de
Dortmund (Allemagne)

Thèse N° 5238
Genève - 2018

UNIVERSITÉ
DE GENÈVE
FACULTÉ DES SCIENCES

DOCTORAT ÈS SCIENCES, MENTION PHYSIQUE

Thèse de Monsieur Branislav RISTIC

intitulée :

«Novel Pixel Sensors in HV-CMOS Technology and Test Beam Infrastructure for Upgrades of the ATLAS Inner Tracking System»

La Faculté des sciences, sur le préavis de Monsieur G. IACOBUCCI, professeur ordinaire et directeur de thèse (Département de physique nucléaire et corpusculaire), Monsieur M. NESSI, professeur titulaire (Département de physique nucléaire et corpusculaire), Monsieur M. WEBER, professeur (Laboratorium für Hochenergiephysik (LHEP) Physikalisches Institut, Universität Bern, Schweiz), autorise l'impression de la présente thèse, sans exprimer d'opinion sur les propositions qui y sont énoncées.

Genève, le 23 juillet 2018

Thèse - 5238 -

Le Décanat

N.B. - La thèse doit porter la déclaration précédente et remplir les conditions énumérées dans les "Informations relatives aux thèses de doctorat à l'Université de Genève".

Abstract

Since 2008 the Large Hadron Collider (LHC) has been delivering proton collisions at unprecedented energies that lead to high precision measurements of the Standard Model and the discovery of new particles and states of matter. In the search of physics beyond the Standard Model, the LHC will be upgraded in 2024 – 2026, increasing its integrated luminosity by an order of magnitude. For the Inner Tracker (ITk) of the ATLAS experiment, the elevated levels of radiation, number of concurrent events per collision (pile-up) and data rate will require a complete replacement. Active pixel sensors built in deep submicron High Voltage CMOS (HV-CMOS) processes are candidates for the outer pixel detector layers of the upgraded tracker. Being high voltage tolerant, thus allowing drift-based charge collection, they offer an opportunity to build radiation hard detectors in industry standard technology. On-sensor signal processing electronics permits replacing complex and cost-intensive hybridisation techniques by simpler ones, holding a prospect of eventually constructing fully monolithic devices. In this thesis, sensors built in the ams H18 180 nm process have been investigated as a hybrid detector solution for the ATLAS ITk. Several sensor design versions have been characterised in laboratory and in-beam measurements for which new test benches and techniques have been developed. The FE-I4 Telescope, a particle tracker device for beam based detector characterisation was built in order to facilitate measurements on HV-CMOS sensors. The construction and performance of the telescope setup as well as the resulting findings on detection performance of the HV-CMOS prototypes, especially after irradiation, are presented.

Resumé

Depuis 2008, le grand collisionneur de hadrons (The Large Hadron Collider, LHC) produit des collisions de protons à des énergies sans précédent qui ont permis des mesures de haute précision du modèle standard et à la découverte de nouvelles particules et des états de la matière. En ce qui concerne la recherche en physique des particules au-delà du modèle standard, le LHC sera amélioré en 2024 – 2026, augmentant sa luminosité intégrée d'un ordre de grandeur. Du fait des niveaux élevés de radiations, du nombre d'événements simultanés par collision (pile-up), de l'augmentation du débit de données et que le détecteur interne actuel sera en fin de vie il sera nécessaire construire un trajectographe interne (ITK) pour ATLAS. Des détecteurs avec des pixels actifs construits avec de l'électronique intégrée submicronique, HV-CMOS, sont candidats pour les couches externes du détecteur de pixels. Ils sont tolérants aux hautes tensions et permettent une collecte rapide du signal grâce à la dérive de charges. Cela permet de construire avec une technologie standard industrilles des détecteurs avec une grande capacité à tolérer les radiations. L'électronique directement intégrée sur la partie capteur permet de remplacer des techniques d'hybridation complexes et coûteuses par des techniques plus simples et ouvre éventuellement la perspective de construire des dispositifs entièrement monolithiques. Dans cette thèse, les capteurs construits dans le processus ams H18 180 nm ont été étudiés en tant que solution de détection hybride pour l'ATLAS ITk. Plusieurs versions de conception de capteurs ont été caractérisées dans les mesures en laboratoire et dans le faisceau pour lesquelles de nouveaux bancs d'essai et techniques ont été développés. Le télescope FE-I4, un trajectographe de particules pour la caractérisation des détecteurs dans un faisceau de particules, a été construit afin de faciliter les mesures sur les capteurs HV-CMOS. La construction et la performance du télescope ainsi que les résultats obtenus sur la performance de détection des prototypes HV-CMOS, en particulier après irradiation, sont présentés.

Contents

Introduction

Curiosity is an aspect, so deeply rooted in human kind, it can be traced back to the days of early human evolution. Questions about the origin of life, the composition of everything visible and invisible, its place and function in nature and its future are already present in ancient historical tradition. By explaining nature starting from first principles, physics approaches these questions at the most fundamental level. In this manner, it explores all scales from the quantum to the astronomical ones in an interplay of theoretical formulation and experimental observations. The need for precise and sophisticated measurements has been constantly forcing the limits of what is possible, leading to technological advancements and innovation that shaped the world.

High Energy Physics is working on the quantum scale, striving to explain the origin and nature of matter and its behaviour at the level of elementary particles. Over the last half a century, it saw major advancements by establishing the Standard Model of Particle Physics. Observations thanks to innovative accelerators and detectors allowed the successful verification of the theory. With the discovery of amongst others, neutral currents and the W and Z bosons, CERN became a driving force in this effort (Chapter 1). Measurements at CERN's Large Hadron Collider, the currently most powerful particle accelerator, allowed to extend the reach towards rare processes and previously undetectable particles, eventually leading to the discovery of the last missing part of the Standard Model, the Higgs Boson. However, many questions still remain unanswered like the matter/anti-matter asymmetry in the universe. In the search for answers, the LHC will once more push the limits of technology with its high luminosity upgrade. New technological advancements are not only necessary for the accelerator complex, but also for the experiments which will have to cope with elevated radiation levels, data rate and pile-up.

For the inner tracking system of ATLAS, one of two experiments that discovered the Higgs Boson, this will mean a major detector upgrade. The currently silicon and gaseous tracker will be replaced by a purely silicon based one (Chapters 2 and 3) permitting to introduce novel technologies and concepts. With the availability of High Voltage CMOS (HV-CMOS) processes, a new way of producing silicon sensors for High Energy Physics applications emerged. The prospects of fast, radiation hard detectors, produced cost effectively in large volumes and simplifying detector construction sparked an extensive R&D programme within the ATLAS collaboration.

The characterisation of detector prototypes in laboratory measurements (Chapter 5) goes hand in hand with beam based experiments. For the latter, so-called beam telescopes provide precise particle trajectory measurements, allowing to explore the prototypes' behaviour in the particle beam with high spatial and time resolution. A new telescope based on the modules of the latest addition to the ATLAS Pixel Detector, the Insertable B-Layer (IBL) and with measurements on HV-CMOS prototypes in mind, was constructed and characterised (Chapter 4). It facilitated measuring the properties of a multitude of HV-CMOS sensors with encouraging results (Chapter 6) contributing to establishing this technology as a candidate for the ATLAS ITk upgrade.

Chapter 1
Fundamental Physics at CERN

CERN is a nuclear and particle physics laboratory in Geneva, Switzerland. It was founded in 1954 as a European effort to re-establish particle physics in the years after World War II and to ensure a peaceful application of the gained knowledge. Throughout the years the organization expanded constantly and includes, as of 2018, 22 member states, several associated member states and international observers from all over the world. CERN assumed a leading role in fundamental physics and contributed with various discoveries and high precision measurements to the establishment of the Standard Model of particle physics, recently culminating in the discovery of the long sought Higgs Boson by the ATLAS and CMS experiments at the LHC. Our understanding of the universe, however, is still incomplete. The matter/anti-matter asymmetry in the universe, the presence of Dark Matter and Dark Energy are just some examples of open questions which are tackled by current particle physics experiments. CERN's research is mainly backed by accelerators, beginning in 1957 with the Synchrocyclotron, which accelerated protons up to an energy of 600 MeV and reaching to the Large Hadron Collider (LHC) breaking records with a peak energy of 6.5 TeV per beam in 2015.

1.1 The Standard Model of Particle Physics

During the 1960s, a quantum field theory, known as the Standard Model of Particle Physics, was established, describing the fundamental particles and the corresponding interactions: the electromagnetic, the weak and the strong interactions. Matter is composed of combinations of 12 elementary fermions (particles with spin 1/2) and their anti-matter counterparts. The elementary fermions are grouped into three families with increasing mass. Interactions between these particles are described by three forces which are mediated by the exchange of gauge bosons (integer spin particles). An overview of the elementary particles and their coupling to gauge bosons, hence their participation in the corresponding interactions is summarised in Figure 1.1.

The Standard Model describes six quarks, organised in doublets: the up and down (u,d), charm and strange (c,s) and top and bottom (t,b) quark. Each quark carries a

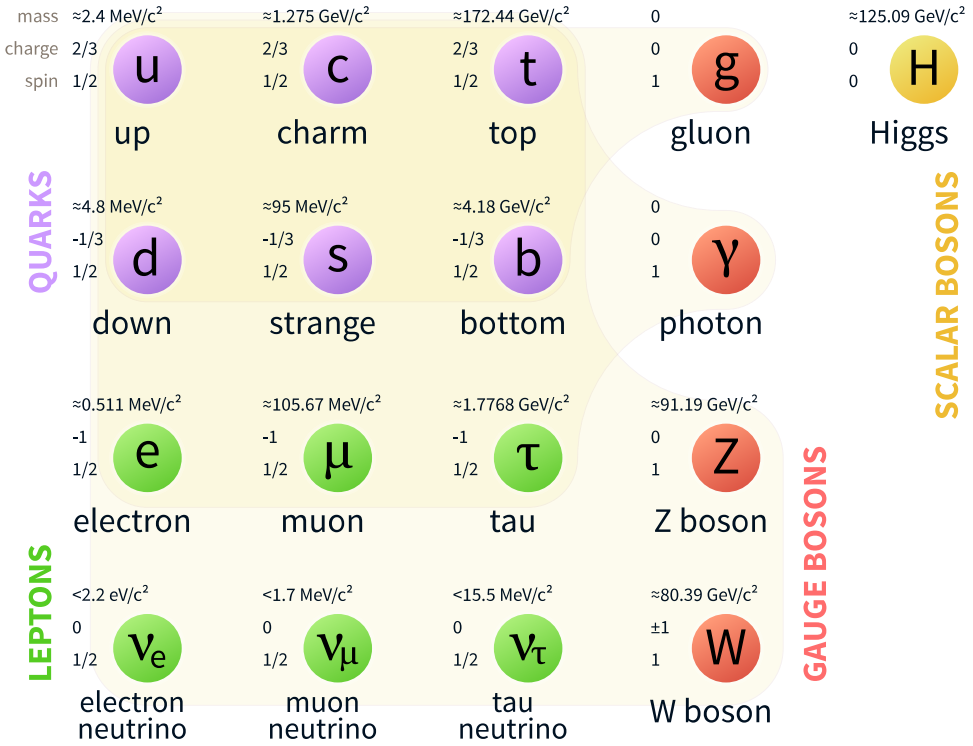

Figure 1.1: Diagram of the elementary particles of the Standard Model. Shown are the three generations of fermions in both the lepton and quark sectors, the gauge vector bosons and the Higgs boson. The yellow fields group the particles with participate in a given interaction. Data for this graphic was taken from [1], the actual graphic is adapted from [2].

fractional electric charge, a weak charge (isospin) and one of the three charges of the strong force called colour (red, green and blue). Therefore quarks take part in all, the weak, the electromagnetic and the strong interactions. Due to carrying colour charge, they cannot exist isolated but only appear in bound states of usually three quarks called baryons (e.g. protons, neutrons, etc.) or quark-antiquark pairs called mesons (e.g. pions, kaons, etc.).

Leptons are fermions which do not take part in strong interactions. The three families comprise singly charged particles called electron (e), muon (μ) and tau (τ) and their neutral and light counterparts, the neutrinos (ν_e, ν_μ, ν_τ).

Interactions between fermions are described by the exchange of gauge bosons. The weak force is mediated by the $W^\pm$ and Z bosons. They interact with all fermions discussed above, but limited to a range in the order of 10^{-18} m due to their high mass.

In contrast, the mediator of the electromagnetic interaction is the neutral and massless

photon (γ), which therefore has infinite range. It couples to all charged particles.

Finally, the massless gluons (g) act as mediators of the strong force between particles carrying colour charges. By being colour-doublets, they couple to themselves as well as to quarks. The strong force increases with distance of the participants, which forbids free quarks in nature. In fact, trying to separate quarks in a bound state would increase its energy to a point where a pair of particles is generated from the vacuum. These particles would hadronise with the original ones, replacing their initial bond.

The Standard Model unifies the electromagnetic and weak force into the electro-weak force and postulates the electro-weak symmetry group. It introduces mass to the fundamental particles by the Higgs Field to which all massive particles couple. In this framework the mass of the mediators of the weak force, the $W^{\pm}$ and Z bosons, can only be explained by breaking the electro-weak symmetry, as otherwise they would be massless under the gauge theory. This in turn requires an additional massive spin-0 particle, the Higgs Boson, which, although predicted in the sixties, would not be discovered until 2012. Its mass was an unknown parameter in the Standard Model and was determined to be $(125.09 \pm 0.24)\,\mathrm{GeV/c^2}$ in 2015 from the combined data of the ATLAS and CMS experiments at the LHC at CERN [3].

The Standard Model was thoroughly tested since its postulation and so far agrees with the experimental results. However, there are still open questions it cannot answer. Two examples are the origin and nature of Dark Matter and the hierarchy problem. Observations of galaxies revealed a huge discrepancy between the luminous mass and the mass distribution needed to explain their movement. This is accounted to the presence of Dark Matter, a type of matter which only interacts gravitatively and contributes 84 % to the mass of the universe [4]. The hierarchy problem results from the immense ratio between the scale of the gravity field and the weak force of around 10^{16}, hence requiring a very fine tuning of the Higgs mass calculation which is deemed unnatural. Therefore research towards additions to the Standard Model is conducted. These theoretical models usually postulate new particles which might be found at colliders like the LHC.

1.2 The Large Hadron Collider

The Large Hadron Collider (LHC) is CERN's largest storage ring and commenced operation in 2008. It is designed to accelerate protons and ions in two counter-rotating beams, eventually bringing them to collision in four points along the ring. The protons reach energies up to 7 TeV with a design peak instantaneous luminosity of $\mathscr{L} = 10^{34}\,\mathrm{cm}^{-2}\,\mathrm{s}^{-1}$, which is defined by reference [5] as

$$\mathscr{L} = \frac{N_b^2 n_b f \gamma}{4\pi\varepsilon_n \beta^*} F \tag{1.1}$$

The equation requires ideal circular beams and is derived entirely from the beam parameters: the number of particles per bunch (N_b), the number of bunches in the beam (n_b), the revolution frequency (f), the normalised transverse beam emittance (ε_n), the beta function at the collision point (β^*) and the geometric luminosity reduction factor due to the beams crossing angle at the interaction point:

$$F = \left(1 + \left(\frac{\Theta_c \sigma_z}{2\sigma^*}\right)^2\right)^{-1/2} \tag{1.2}$$

It is defined by the full crossing angle (Θ_c), the RMS of the bunch length (σ_z) and the transverse RMS of the beam size (σ^*) at the interaction point.

The LHC is the final stage of a cascade of accelerators as sketched in Figure 1.2. Protons are obtained from ionised hydrogen gas and start at the linear accelerator LINAC2. They traverse a radiofrequency quadrupole which bunches and pre-accelerates the beam particles before the LINAC2 increases the energy to 50 MeV. The protons are then accumulated and accelerated to 1.4 GeV by the PS Booster (PSB). The booster injects into the Proton Synchrotron (PS) which ramps up the beam energy to 25 GeV and sends the protons to the Super Proton Synchrotron (SPS). Inaugurated in 1976 as a proton accelerator, the SPS was transformed to a proton/anti-proton collider in 1981 at which crucial discoveries, like those of the W and Z bosons were made. With the construction of the Large Elecron-Positron Collider (LEP) the SPS was transformed into an injector for LEP, as well as for fixed target experiments like the North Area beam lines that will be discussed later in this thesis. In the SPS, protons reach an energy of 450 GeV before being transferred to the LHC.

Installed in the 26.7 km long tunnel of the Large Elecron-Positron Collider (LEP), the Large Hadron Collider is located between 45 m and 170 m below surface. The ring is divided into eight sections, each isolated in terms of cryogenics and powering, and accessible from the surface via shafts. Four access points are located at long straight sections hosting the four large experiments ATLAS at point 1, ALICE at point 2, CMS

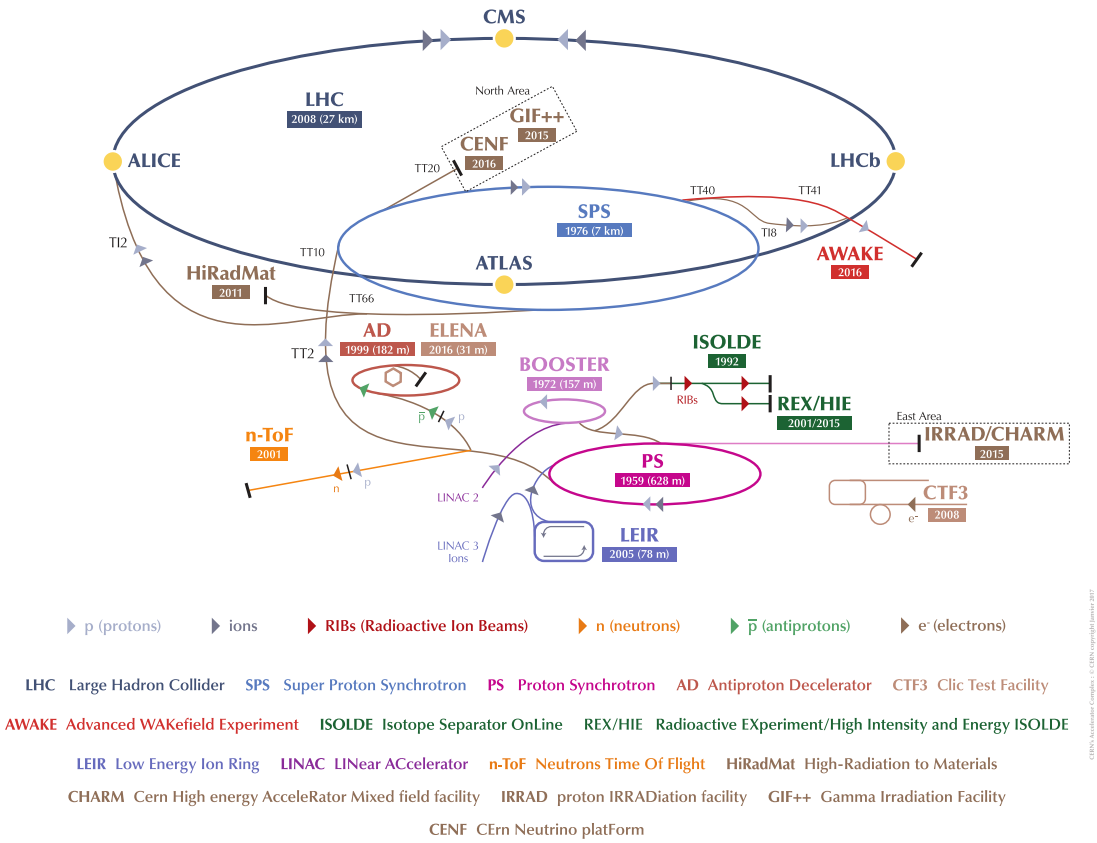

Figure 1.2: The CERN accelerator complex in 2016/17 [6]

at point 5 and LHCb at point 8. The other points host the beam injection, acceleration and cleaning stations as well as the beam dump.

In order to reach the design energy of 7 TeV per beam, a dipole field of 8.33 T is needed, which can only be generated by superconducting magnets. Due to space constrains of the tunnel, they were realised as two-bore magnets, meaning that both counter-circulating proton beams share a unique magnetic field. The magnetic field is generated by NbTi coils, cooled to 1.9 K with superfluid helium. Design luminosity is reached with 2808 bunches, each containing $1.15 \cdot 10^{11}$ protons with 25 ns bunch spacing, but particles collide in the four experiments with different instantaneous luminosities. ATLAS and CMS are designed as multi-purpose experiments to search for the Higgs Boson and new particles. They are therefore operated at maximum luminosity, while the two high precision experiments, LHCb for b-physics and ALICE for heavy ion physics, receive a lower luminosity.

LHC commenced operation in 2008 but was damaged soon after by an electrical failure. A faulty connection between two superconducting dipole magnets lead to a spark

that pierced the magnet's cryostat and resulted in an explosive decompression of the stored helium that ripped several magnets out of their anchorage [7]. The LHC had to undergo extensive repairs and was offline for 14 months before resuming operation in November 2009 at a reduced centre of mass energy of $\sqrt{s} = 7\,\text{TeV}$ (3.5 TeV per beam). After consolidation of the magnet interconnects, the machine was able to deliver collisions at $\sqrt{s} = 13\,\text{TeV}$ and the design luminosity of $1 \cdot 10^{34}\,\text{cm}^{-2}\,\text{s}^{-1}$. Although the maximum beam energy is limited by the magnetic field of the bending magnets, this does not necessarily limit the luminosity, which was raised in 2016 to $1.37 \cdot 10^{34}\,\text{cm}^{-2}\,\text{s}^{-1}$, exceeding all expectations.

1.2.1 Upgrades of the LHC

As of 2018 the LHC has already undergone a major upgrade (see Figure 1.3). During Run-1 (2010 to 2013) the LHC was operated routinely at a reduced luminosity of $10^{33}\,\text{cm}^{-2}\,\text{s}^{-1}$ and a maximum energy of 3.5 TeV per beam. In 2013 and 2014 this restriction was limited after checking and repairing the 10000 superconductive solder joints between the dipole magnets. This intervention, called Long Shutdown 1 (LS1) allowed to reach a peak energy of 6.5 TeV during Run-2, initially still at a reduced luminosity of $5 \cdot 10^{33}\,\text{cm}^{-2}\,\text{s}^{-1}$. Optimisations during operation increased the peak luminosity up to $2.14 \cdot 10^{34}\,\text{cm}^{-2}\,\text{s}^{-1}$ in 2018 and further increases are expected until the end of Run-2.

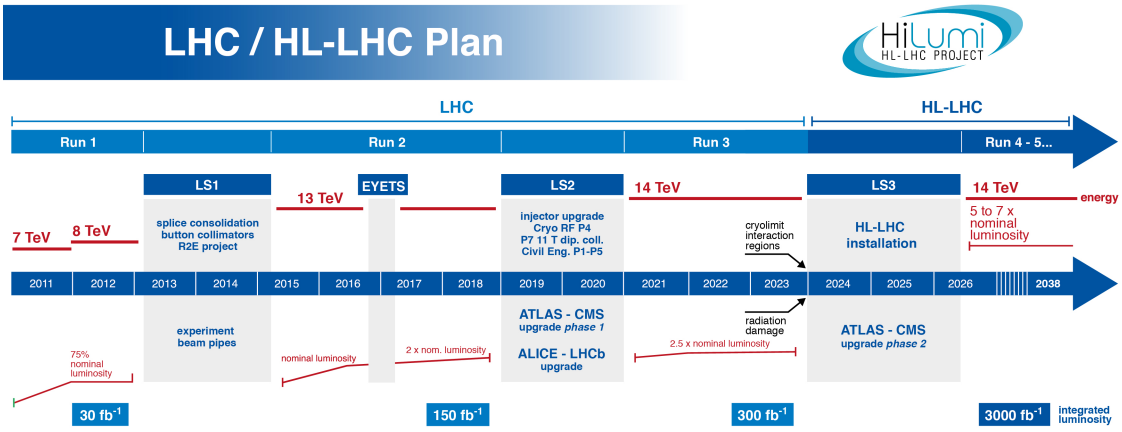

Figure 1.3: Schedule of the LHC run periods and upgrades including to be reached energies and luminosities [8]

The LS2 shutdown will introduce two major changes to the machine. The current linear accelerator LINAC2 will be replaced by the newly built LINAC4 leading to an increase in brightness in the PSB. Additionally, the LHC collimation system will be upgraded which will improve the focusing at the collision points. Both interventions will lead to an increase in luminosity, allowing the LHC to deliver a planned integrated luminosity of up to $400\,\text{fb}^{-1}$ during Run-3. In the light of the recent performance of the LHC, this value is likely to be exceeded.

Between 2024 and 2026, during LS3, the accelerator complex will once more be stopped for major upgrades. The goal is to retrofit the machine for an increase in luminosity by an order of magnitude enabling it to deliver up to $3000\,\text{fb}^{-1}$ of integrated luminosity in the following ten years. Such an endeavour will introduce upgrades to the whole injector chain and new technologies like crab cavities and NbSn based final focus quadrupole magnets. At these luminosities the proton-proton collisions would quickly burn-up the injected beam. The large difference in instantaneous luminosity between the beginning and the end of a fill would introduce stress to the experiments and require a considerable over-design of some detector components. Therefore, mitigating techniques are under investigation to level the instantaneous luminosity over a fill.

1.3 The ATLAS Detector

ATLAS[a] is one of the two general-purpose detectors at the LHC built for searches of new particles and physics beyond the Standard Model [9]. As such, it is designed to detect preferably all particles emerging from a collision and identify them by measuring their charge, energy and momentum as precisely as possible. This also allows to identify particles which are not detectable (e.g. neutrinos) as missing energy in the observed physics processes. The detector is therefore cylindrically shaped, forward-backward symmetric and composed of several sub-systems, each specialised in measuring a specific property of the produced particles. Sub-systems are realised as cylinders with additional end-caps, which provides a large angular acceptance.

The whole ATLAS detector is 46 metres long, 25 metres in diameter with a weight of ~ 7000 tons. A 3D rendered view of the detector can be found in Figure 1.4. In the following sections, an overview of the sub-detectors and the triggering system will be given.

[a] A Toroidal LHC ApparatuS

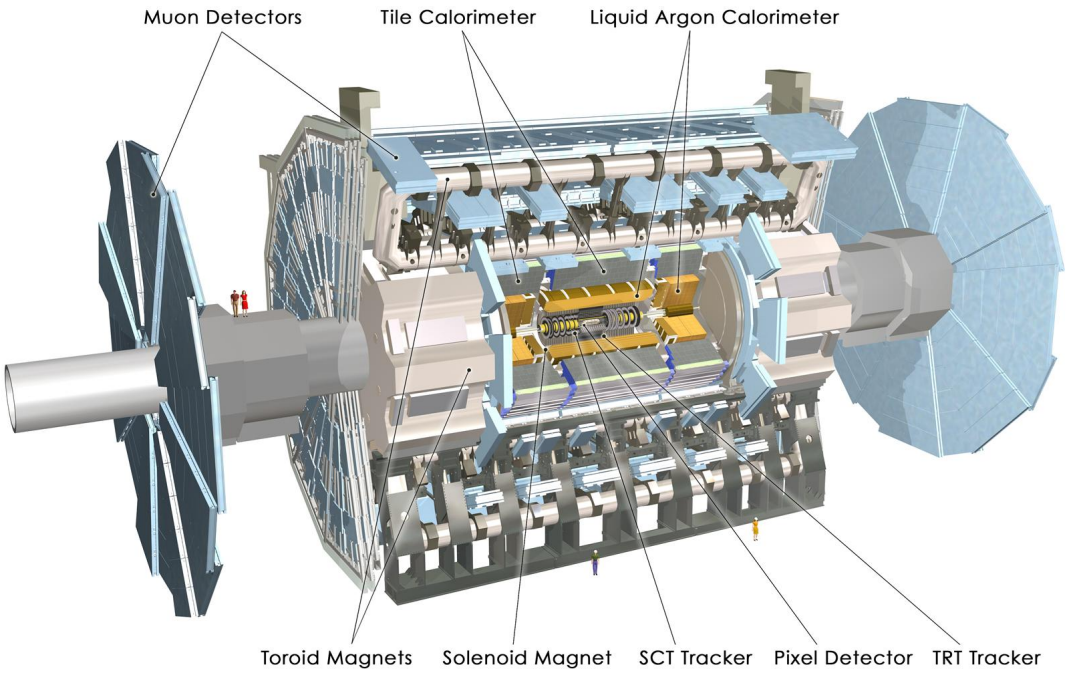

Figure 1.4: Schematic view of the ATLAS detector showing the various subsystems and a couple of persons for scale [10].

Inner Detector At the core of the experiment is the so-called Inner Detector (ID), a stack of position sensitive devices located in a 2 T solenoidal magnetic field. It is used to obtain tracking information of charged particles, which allows to locate vertices and measure the particles momentum and charge. A restricted particle identification is possible by exploiting the measurement of energy, deposited in the detector. Every bunch crossing releases on the order of 1000 charged particles within its acceptance. In order to operate in such an environment and provide reliable tracking, the ID is composed of fine granularity detectors with high radiation tolerance. It consists of (ordered by the distance to the particle beams) the Pixel Detector, the microstrip Semi-Conductor Tracker (SCT) and the straw-tube Transition Radiation Tracker (TRT).

The Pixel Detector is located closest to the interaction point and contains the highest granularity sensors mounted in three barrel-shaped layers and three end cap discs at each extremity. It provides a spatial resolution of 115 µm in z-direction and 10 µm in $R\phi$ direction and is essential for vertex reconstruction and b-tagging. The sub-detector was upgraded during the Long Shutdown 1 when a new inner layer, the Insertable B-Layer (IBL) was inserted, improving both detection efficiency and resolution. A detailed description will follow in Chapter 3.

The Pixel Detector is surrounded by the Semi-Conductor Tracker which comprises four barrel layers and nine end-cap discs at each side, amounting to a total of 60 m^2 of silicon detector surface. It hosts p-in-n microstrip sensors which are organised in doublets with a stereo angle of 40 mrad in order to obtain 2D hit coordinates. The SCT reaches a resolution of 580 µm in z-direction and 16 µm in $R\phi$.

The Inner Detector is completed by the Transition Radiation Tracker, a xenon-based gas detector consisting of about 300000 straw-tubes. It provides on average 36 spatial points per traversing particle with a resolution of 130 µm. Apart from tracking, it contributes to the identification of electrons (e/π separation), which emit transition radiation when passing from the active gas volume to the passive material embedding the straw-tubes.

The ID is surrounded by the inner solenoid magnet, which separates the inner tracking from the calorimetric system.

Calorimetric system The calorimetric system measures the total energy of particles by absorbing them. Depending on their sensitivity to the kind of particles, two types of sampling calorimeters, the Electromagnetic and Hadronic Calorimeter, are located around the solenoid.

The Electromagnetic Calorimeter absorbs particles mainly by eletromagnetic interaction. It covers the pseudorapidity[b] region of $|\eta| < 3.2$ and is composed of an accordion shaped stack of lead-stainless-steel foils as converters with copper-polyimide multilayer readout boards in between, located in a bath of liquid argon which acts as active medium. Electrons and photons traversing the calorimeter release most of their energy in this detector. The segmentation of the calorimeter allows to distinguish between electrons, photons and early hadronic showers based on the shape of the shower. As photons are not detectable in the inner tracking system, the innermost calorimeter layer is finely segmented to measure their direction.

Hadrons, which penetrate the electromagnetic calorimeter, are absorbed by the Hadronic Calorimeter. In this system three technologies are used for this purpose. The Tile Calorimeter at $|\eta| < 1.7$ uses steel for absorption and plastic scintillators for detection. At higher pseudorapidities, liquid Argon acts again as active material due to its high radiation tolerance. While the region of $1.5 < |\eta| < 3.2$ is covered by the Hadronic End-cap Calorimeter with copper as absorbing material, the Forward Calorimeter, based on a tungsten matrix, covers $3.1 < |\eta| < 4.9$. This detector is highly granulated to enable measuring the substructure of jets.

[b] The pseudorapidity is defined as $\eta = -\ln(\tan\Theta/2)$ with Θ being the polar angle relative to the beam axis.

The calorimetric system ensures efficient detection by a total thickness of between 22 and 24 interaction lengths of the electromagnetic calorimeter and around ten interaction lengths of the hadronic calorimeter.

The Muon Spectrometer The Muon Spectrometer encloses the calorimetric system. Its purpose is to measure the momentum of muons, the only detectable particles that can pass the calorimeters, and provide trigger information. For this, the Muon Spectrometer is immersed in a toroidal magnetic field up to $|\eta| < 2.7$, which is formed by eight superconducting air core coils, providing between $B = 0.5\,\mathrm{T}$ and $3\,\mathrm{T}$. Four gas detector types are used for different occupancies and speed requirements.

Three layers of high spatial resolution detectors form the barrel and end-cap region. Close to the interaction point and at pseudorapidities of $\eta \geq 2.0$, Cathode Strip Chambers (CSCs), multi-wire proportional chambers with strip cathodes, are used, reaching a spatial resolution of 40 µm. At larger radii, Ar/CO_2 filled Monitored Drift Tubes (MDTs) with a resolution of 35 µm are placed.

For triggering, Resistive Plate Chambers (RPCs) are located in the central region at $|\eta| < 1.05$ and Thin Gap Chambers (TGCs) at $1.05 < |\eta| < 2.7$. RPCs are narrow gas gap chambers, formed by two high-resistive plates which are separated by insulating spacers. Operated in avalanche mode they reach a timing resolution of 1.5 ns. TGCs are multi-wire proportional chambers with a smaller cathode-anode distance than anode-wire pitch, which leads to short drift times thus a good time resolution. They are placed in the forward region as they can cope with higher counting rates at the expense of a lower timing resolution of 4 ns.

Luminosity Monitoring The accurate knowledge of the delivered luminosity is a key requirement for many measurements of cross sections and branching ratios at the LHC. In ATLAS this is fulfilled by two dedicated forward detectors, LUCID[c] and ALFA[d].

LUCID measures the luminosity by counting the mean number of charged particles that are produced in inelastic pp collisions. Two modules of Cherenkov counters surround the beam pipe 18 m from the interaction point in both directions, covering the pseudorapidity region of $5.6 < |\eta| < 6.0$. Each station consists of 200 cylindrical, gas filled Cherenkov tubes with Photomultiplier Tube readout which point to the nominal interaction point. This allows discriminating protons originating from the primary interaction point from background. Fast electronics allow a bunch per bunch measurement with a relative uncertainty of 2.1 %.

[c] Luminosity measurements Using Cherenkov Integrating Detector
[d] Absolute Luminosity For ATLAS

LUCID is calibrated with data from the ALFA detector which measures the cross section for Coloumb scattered protons. It consists of two stations, placed $\sim$240 m from the interaction point in both directions and covering the region of $|\eta| > 8.5$. Each station hosts two groups of scintillating plastic fibres, placed perpendicular to each other in so called Roman Pots that can be moved down to a distance of $\sim$1 mm to the beam. ALFA measures the absolute luminosity with a precision of 2 to 3 %, but needs a special optics configuration of the LHC including a low luminosity ($\sim 10^{27}\,\mathrm{cm}^{-2}\,\mathrm{s}^{-1}$), a high β^* value and parallel-to-point focussing. Calibration constants from these special LHC runs are then extrapolated to the nominal luminosity for LUCID. In addition, the luminosity is estimated from machine parameters and by measuring and comparing the cross sections for well known physics processes.

Triggering System The LHC collides bunches with a frequency of 40 MHz. Recording data from the $\sim$100 million readout channels within ATLAS at that rate is impossible with the current technology. A three level triggering system therefore preselects potentially interesting events, reducing the amount of data by five orders of magnitude.

In a first stage, the purely hardware based Level-1 trigger selects events with a rate of $\sim$75 kHz. It combines data from the calorimetric and muon systems for decision making and defines Regions of Interest for the subsequent triggering levels. A decision is taken in less than 3 µs, which is the maximum time an event can be stored by the ATLAS low-level readout electronics. The so called Level-1 Accept (L1A) signals the electronics to transfer their data to readout buffers, making them accessible by the High Level Trigger (HLT).

The HLT comprises two stages of filtering running on a commercial PC farm: The Level-2 trigger and Event Filter. The Level-2 trigger uses data from the full detector in the Regions of Interest defined by the first stage for event building. It reduces the event rate to below 3.5 kHz with an average processing time of $\sim$40 ms. The Event Filter then fully reconstructs events using simplified algorithms close to those from the off-line analysis. This takes around four seconds after which the selected events are transferred to mass storage producing a final event rate of $\sim$200 Hz.

Chapter 2
Particle Tracking with Silicon Detectors

Silicon tracking detectors are usually implemented in the innermost systems of a collider experiment. By providing high resolution space points, they measure the trajectory of particles and locate the vertices of an interaction. When placed in a magnetic field, the particles charge and momentum can be estimated from the trajectory curvature. In this chapter, the detection principles of silicon sensors will be introduced. The implementation as hybrid pixel detectors, as used in the ATLAS tracker, will be discussed along with the effects of radiation on electrical and detection parameters.

2.1 Energy Loss in Matter

For particles to be detected, they have to transfer a certain amount of energy to the detecting material by elastic and inelastic scattering. In general, particles will interact more than once with the surrounding material if they are not absorbed. The following describes the energy loss mechanisms for charged particles and photons, which can be detected by silicon trackers.

Charged Particles For charged heavy particles ($m \gg m_e$, where m_e is the electron mass), the main energy loss processes are ionisation and Cherenkov radiation, which are described by the Bethe-Bloch formula

$$-\left\langle \frac{dE}{dx} \right\rangle = K\rho \frac{Zz^2}{A\beta^2} \left[\ln \left(\frac{m_e \gamma^2 v^2 W_{\max}}{I^2} - \beta^2 - \frac{\delta}{2} - \frac{C}{Z} \right) \right] \tag{2.1}$$

($K = 4\pi N_{\mathrm{a}} r_{\mathrm{e}}^2 m_{\mathrm{e}} c^2 = 0.307\,\mathrm{MeV\,cm^2\,g^{-1}}$, N_{a}: Avogadro's number, r_{e}: classical electron radius, m_{e}: electron mass, ρ: material density, Z: atomic number, A: atomic weight of the absorbing material, z: charge of the incident particle, $W_{\max}$: maximum energy transfer per interaction, I: mean excitation potential, δ: density correction, C: shell correction).

The Bethe-Bloch formula shows a minimum for a broad range of $\beta\gamma$ around a value of $\beta\gamma \approx 3$ (see Figure 2.1):

$$\left\langle \frac{dE}{dx} \right\rangle_{\text{MIP}} = -\frac{1}{\rho}\frac{dE}{dX} \approx 1.5\,\frac{\text{MeV}}{\text{g}\,\text{cm}^2} \tag{2.2}$$

In this region, particles are called minimally ionising. They loose the least amount of energy, thus generate the smallest signals in the detectors, but as they are mostly not influenced by the material, they represent the optimal particles for a tracking detector. Particles considered for tracking experiments are usually Minimum Ionizing Particles (MIPs).

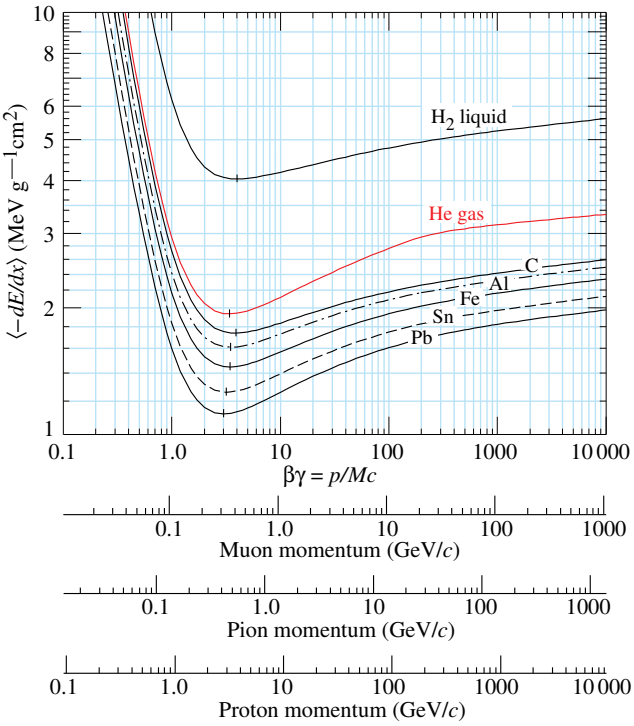

Figure 2.1: Mean energy loss rate in different materials around the minimum of the Bethe-Bloch formula [1]

While equations (2.1) and (2.2) describe the average energy loss in matter, the actual energy transfer per length $\Delta E/\Delta x$ is a statistical process resulting from multiple scattering in the medium. Its probability density function for thin absorbers, like silicon tracking detectors, is an asymmetric function resembling a gaussian distribution with a pronounced tail towards large energy transfers. The gaussian part results from many ionisation processes with small energy transfers, the tail from hard scattering where atomic electrons gain enough energy to be ionising particles themselves (δ-electrons).

The resulting Landau-Vavilov distribution is parametrised as [11]:

$$f(\lambda) = \frac{1}{\pi}\int_0^\infty e^{-t\ln t - \lambda t}\sin(\pi t)dt \tag{2.3}$$

with

$$\lambda = \frac{\Delta E - (\Delta E)_{\mathrm{MPW}}}{\xi} - \lambda_m \qquad \text{and} \qquad \xi = \frac{1}{2}K\rho\frac{Zz^2}{A\beta^2}\Delta x \tag{2.4}$$

$(\Delta E)_{\mathrm{MPW}}$ is the most probable energy loss which is found at $\lambda_m = -0.22278$.
Figures 2.2a and 2.2b show the energy loss distribution and the most probable energy loss for MIPs in different thicknesses of silicon.

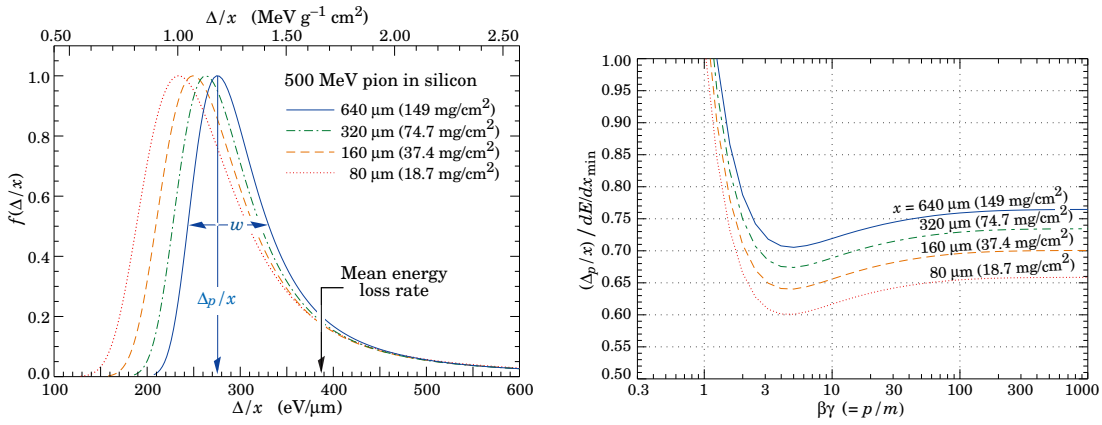

(a) **(b)**

Figure 2.2: (a) Energy loss distributions in silicon for 500 MeV pions, normalised to unity at the most probable value Δ_p/x [1] (b) Most probable energy loss in silicon scaled to a MIP (388 eV/μm) [1]

Photons In contrast to charged particles, photons interact with matter via the Photoelectric effect, Compton scattering and pair production. In the former, if its energy exceeds the binding energy of the electron, the photon is absorbed entirely by an electron in the atomic shell which is hereby released from the atom. The Compton effect describes the inelastic scattering of a photon on a free electron[a]. The photon is absorbed and a new one emitted with a reduced energy E'_γ depending on the scattering angle Θ:

$$E'_\gamma = \frac{E_\gamma}{1 + \frac{E_\gamma}{m_e c^2}(1-\cos\Theta)} \tag{2.5}$$

[a] An electron can also be considered free if its binding energy is exceeded considerably by the photon energy.

Due to multiple scattering in the detector, the photon energy can be gradually absorbed up to the point where the energy deposit in the material matches those of the photo-electric process. The third way of energy-deposition is by conversion into an electron-positron pair in the presence of a nucleus when the photon's energy exceeds 1.022 MeV, the rest mass energies of the electron and positron pair.

2.2 Semiconductor Detectors

Tracking detectors located close to the collision point have to provide high resolution measurements of positions of the particle trajectory while being able to survive the harshest radiation environment in the detector. Combined with the requirement to alter the particles energy the least possible, thus keeping a low material budget[b], thin segmented silicon detectors are the most common choice.

The detection process for silicon detectors is the generation of electron-hole (e-h) pairs by particles which transfer energy to the detector material as described in the last section. Electrons from the valence band can thereby be excited into the conduction band, leaving a vacant state in the valence band (a so called "hole") that acts as a positively charged pseudo-particle. In silicon, the average energy deposition to create such a pair is $E_{e-h} = 3.6\,\text{eV}$ leading to the generation of roughly 20 000 e-h pairs by MIPs in 250 µm of silicon. In undoped and unbiased silicon, such a charge would be easily shadowed by the intrinsic free charge carriers which have a density of $10^{10}\,\text{cm}^{-3}$. Therefore these charges have to be removed from the detector material and the generated charges have to be separated quickly before they can recombine in order to record a signal. This is facilitated by pn-junctions or diodes, operated in reverse bias mode.

2.2.1 The pn-junction as Particle Detector

By introducing impurities into the silicon lattice, its electrical properties can be altered. Replacing silicon atoms usually by those from the III. (p-type) or V. (n-type) main group of the periodic system of elements, a local excess of a charge carrier type (electrons for n-type and holes for p-type doping) is created. At the interface between n-doped and p-doped materials, the difference in charge carrier concentration leads to a diffusion of the respective carriers to the oppositely doped area. There they recombine with their counterparts forming a region without free charge carriers, the depletion zone. In this zone, the dopant ions are deprived of their reversely charged free carriers leading to a

[b] The material budget is the amount of material in the path of the particles, usually given in units of radiation length.

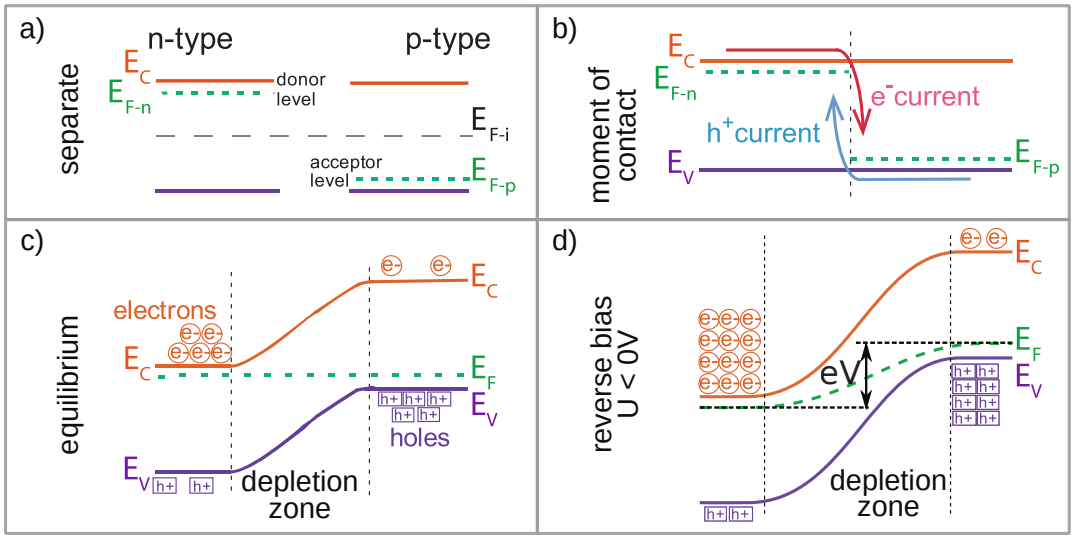

Figure 2.3: Formation of a pn-junction. Shown are the energy levels in the p- and n-doped regions (a) when both regions are separated, (b) at the moment of contact and (c) in a state of equilibrium where a space charge region has developed at the interface of the doped regions. Additionally in (d) the situation after application of a reverse bias is shown, which shifts the Fermi levels and enlarges the space charge region. Adapted from [12]

space charge region and thus an electric field which counteracts the diffusion. As it is formed at the material transition from p-doped to n-doped materials, this interface region is called pn-junction (see Figure 2.3).

The width of the depletion zone in the junction can be calculated from the equilibrium of the diffusion of charge carriers and the counteracting electric field in the space charge region as

$$d \approx \sqrt{\frac{2\varepsilon_{Si}\varepsilon_0(U_{ext} - U_i)}{e|N_{eff}|}} \tag{2.6}$$

with $\varepsilon_{Si} = 11.75$: the dielectric constant of silicon, ε_0: the vacuum permittivity, U_{ext}: the voltage applied externally to the junction, U_i: the intrinsic voltage originating from the space charges and $N_{eff} = N_D - N_A$: the difference in dopant concentration of the junction. This means that a low doping of the junction combined with a high reverse bias voltage yields a large depletion zone which can extend over the whole detector bulk. For very high voltages however, thermal effects, tunneling and the onset of avalanche multiplication lead to a breakdown of the junction. In this mode the junction conducts a large current that can damage the lattice and induce noise, but also exhibits a large

gain factor. Dedicated silicon devices (e.g. Silicon Photo-Multipliers) are capable to operate in this regime but are unsuited as tracking detectors in the LHC environment. The sensors, discussed in this thesis, cannot withstand high currents and are therefore limited by their breakdown voltage.

Particles depositing energy in the depletion zone generate a perceivable excess of electron-hole pairs in the pn-junction. By applying an electric field the pairs are separated, thus hindered from recombining and their motion induces a current on the readout electrodes. In addition, electron-hole pairs generated close to the depletion zone have a probability of reaching it by thermal motion (diffusion) instead of recombining and can therefore contribute to the signal. In the next section the signal generating charge carrier motion, usually called *Charge Collection* will be discussed.

2.2.2 Motion of Charge – Diffusion and Drift

Free charge carriers in a semiconductor, including induced electron-hole pairs, will move through the bulk by drift and diffusion. The current densities for electrons and holes are derived from the Boltzman Transport Equation as:

$$\vec{J}_h = q\mu_h \rho_h \vec{E} \; - \; qD_h \vec{\nabla}\rho_h \tag{2.7}$$

$$\vec{J}_e = \underbrace{q\mu_e \rho_e \vec{E}}_{\text{Drift part}} \; + \; \underbrace{qD_e \vec{\nabla}\rho_e}_{\text{Diffusion part}} \tag{2.8}$$

with the electric field ($\vec{E}$) and the carrier concentration ($\rho_{e/h}$), charge (q) and mobility ($\mu_{e/h}$). D is the diffusion constant calculated from Einstein's relation for electric mobility

$$D_{e/h} = \frac{k_B T}{q} \mu_{e/h} \tag{2.9}$$

including the temperature (T) and the Boltzmann constant (k_B).

Diffusion is a process that occurs whenever there is a gradient of carrier concentration in order to restore this system to uniformity. The gradient, combined with thermal motion of the carriers, forces them to move towards lower concentration areas. Initially point-like charge accumulations will therefore spread out and result in a Gaussian distribution with a standard deviation after a time t given by the diffusion length L_D [13]:

$$\sigma = L_D = \sqrt{Dt} \tag{2.10}$$

In silicon, at room temperature and low electric fields, the mobility for electrons and holes is found to be $\sim$1450 and $\sim$500 $\mathrm{cm^2\,V^{-1}\,s^{-1}}$ [14]. This translates to a diffusion length of $\sim 10\,\mu\mathrm{m}$ for electrons and $\sim 6\,\mu\mathrm{m}$ for holes in 25 ns which is the time between

bunch crossings in the LHC. As semiconductor sensors have an active depth of usually more than 100 µm (ATLAS Pixel sensors: 250 µm), signal generation based only on diffusion would greatly exceed the timing constraints of ATLAS. Furthermore diffusion induced signals degrade quickly after irradiation due to the charge trapping effect as will be discussed in Section 2.4. Charge collection by diffusion is therefore not suitable for an environment like ATLAS.

In contrast to diffusion, drift is a forced motion generated by an external electric field as it is present in the depletion zone of a pn-junction. Charge carriers follow the electric field lines but collide with lattice atoms on their way, leading to a mean drift velocity which is limited by the charge carrier mobility:

$$\vec{v}_{e/h} = \mu_{e/h}\vec{E} \tag{2.11}$$

For high electric fields apporaching several kV/cm (i.e. 40 kV/cm for unirradiated ATLAS Pixel sensors in nominal condition) charge carriers gain enough energy between collisions to excite the lattice. The mobility factor becomes inversely proportional to the applied field, counteracting the acceleration of the electrical field and leading to a saturation of velocity. For silicon, a value of $v_{\text{sat}} = 100\,\text{km/s}$ is found. Compared to the 25 ns, in which diffusion would transport charge carriers 10 µm into the bulk, a drift based collection would take around 100 ps being compatible with the LHC requirements. Additionally, as drift is a directed motion depending on charge, all charge carriers are directed towards the electrodes, generating a strong signal. The recombination of electron-hole pairs is as well prevented as electrons are pulled in the opposite direction of the holes.

A drift based collection is in particular important after irradiation where the short drift times reduce the probability of trapping (see Section 2.4), making this mechanism a requirement for efficient detection. As drift occurs only in the depletion zone, high bias voltages are necessary to produce a large enough depletion zone, ensuring an efficient and fast detection.

2.3 Hybrid Pixel Detectors

The main task of semiconductor detectors in the LHC experiments is the high precision measurement of particle trajectories. For this purpose, the detectors are segmented to a matrix of rectangular pixels with a size in the order of some ten microns in each direction. By extending one length to macroscopic sizes one obtains a so called strip detector. These strip detectors have less stringent requirements on the readout and are cheaper to build at the expense of a reduced resolution in direction of the long edge. Consequently they are employed in the outer layers of a semiconductor tracker like the ATLAS SCT.

Pixel detectors on the other hand reach channel densities of $1 \cdot 10^3$ to $1 \cdot 10^4$ Ch/cm^2 which can only be read out by dedicated Integrated Circuits (ICs). Each sensor pixel is connected individually to the corresponding readout cell on the Front-End by means of solder bumps. In the case of the ATLAS Pixel Detector these are silver-tin or indium solder balls which are deposited on the readout chip and connected in a reflow process. A sketch of a sensor bonded to a readout cell can be found in Figure 2.4.

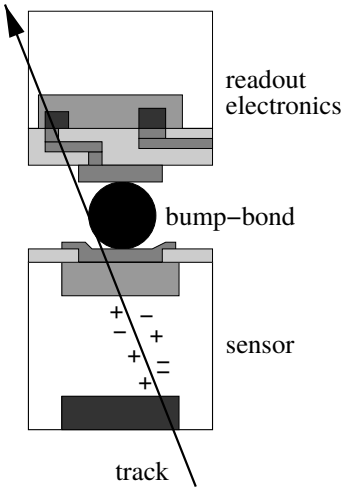

Figure 2.4: Cross section of a hybrid pixel detector, showing the sensor, the readout cell and the connecting bump bond together with a particle generating a signal [15].

Pixel detector readout chips usually comprise an analogue part following the Krummenacher architecture [16] for amplification, signal shaping and discrimination and a digital signal processing part as sketched in Figure 2.5.

Signals generated in the detector are amplified by a Charge Sensitive Amplifier (CSA) and then discriminated before being registered as a hit by the digital logic. In order to prevent saturation of the amplifier, its capacitance has to be discharged by means of a feedback current. In the ATLAS design a constant feedback has been chosen which has

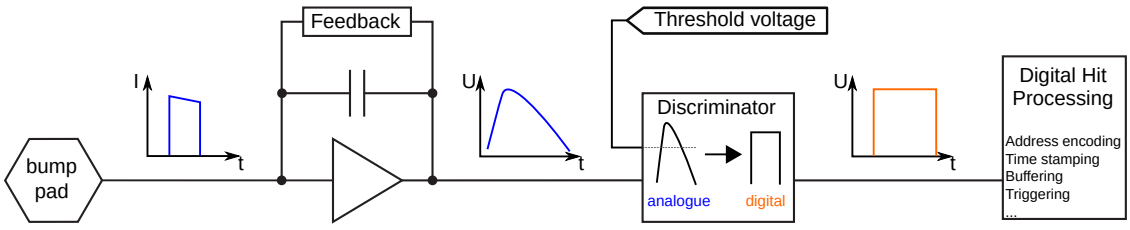

Figure 2.5: Sketch of an analogue readout chain for hybrid pixel detectors

the advantage that the deposited charge is accessible as the width of the output signal, measured as Time over Threshold (ToT). The discriminated signal is further processed by the digital logic. Hit information like pixel position, Time of Arrival (ToA) and ToT are stored in buffers and either piped out to the higher level readout as they are recorded (data-driven readout) or when requested (triggered readout). An actual implementation in the case of the FE-I4[c], the current pixel readout chip for the ATLAS IBL, will be discussed in Section 3.2.

Spatial resolution

As pixel detectors are used for precise particle tracking, the spatial resolution of the sensors is of paramount importance. It is defined by the segmentation of the detector, the charge sharing with neighbouring pixel cells and the efficiency of the readout electronics. Assuming a uniform and fully efficient detector without charge sharing and a perfect read out, the resolution can be calculated as follows:

Given an uniform illumination over the whole pixel length p, thus a constant occupancy distribution $f(x) = 1/p$ between $-p/2$ and $p/2$ the error on the hit position measurement x is the standard deviation of $f(x)$:

$$\sigma = \frac{\int_{-p/2}^{p/2} x^2 f(x) dx}{\int_{-p/2}^{p/2} f(x) dx} = \frac{\int_{-p/2}^{p/2} x^2 dx}{\int_{-p/2}^{p/2} dx} = \frac{p}{\sqrt{12}} \tag{2.12}$$

(The center of the pixel is defined as origin of the coordinate system).

This value represents an upper limit on the hit position error which can be reduced by considering multi-hit clusters and measuring the collected charge.

Multiple scattering

In a detector system, comprised of multiple planes of position sensitive detectors, the tracking resolution is determined by the resolution of the single planes, by the geometry of the detector and by the interactions of the particles with matter.

While the Bethe-Bloch formula describes ionisation effects, charged particles also undergo Coulomb scattering in the vicinity of a nucleus[d]. This effect is described by the Rutherford formula, which peaks at small angles. A macroscopic effect usually occurs when the particle is scattered many times ($\gtrsim 20$) in a layer of material. The resulting

[c] The original ATLAS Pixel readout chip FE-I3 implements a similar scheme in the analogue circuit.
[d] Elastic scattering on electrons is negligible for $E \gg m_e c^2$.

scattering angle θ is approximately gaussian distributed around zero where the standard deviation is given by the Highland-Formula

$$\sigma_\theta = \frac{13.6\,\mathrm{MeV/c}}{p\beta} z \sqrt{\frac{x}{X_0}} \left(1 + 0.038 \ln \frac{x}{X_0}\right) \tag{2.13}$$

(p, z: momentum and charge of the incident particle, x, X_0: thickness and radiation length of the scattering target)
As this effect can deteriorate the performance of a tracker severely, the material budget in and before the tracker has to be minimised.

Time-Walk

The accuracy of the time of arrival and the charge measurement as Time over Threshold may suffer from imperfections of the amplifier like time-walk and a not entirely constant discharge rate. Time-walk originates mainly from the finite rise time of the amplifier, which is dependent on the induced signal size. This means that the amplitude defines the time between signal generation and the signal reaching the discriminator threshold. The amplifier rise-time is dominated by the detector capacitance and the preamplifier bias current. As the pixel capacitance is proportional to its size, small pixel sizes are therefore preferred.

A second contribution to time-walk emerges from the discriminator itself. While switching, the comparator needs to charge a parasitic capacitance at its output. The available current for this operation is set by the discriminator bias current but depends also on the input signal size which again leads to delays of small input signals. High bias currents can mitigate somewhat the time-walk issue but at the expense of an elevated power consumption, which is not always tolerable as it increases the material budget of the detector due to the necessary powering and cooling services.

2.4 Radiation Damage in Silicon Detectors

Particles losing energy while crossing the detector generate a recordable signal, but can also damage the detector material. One usually distinguishes between the damage of interfaces and surfaces of silicon devices, mostly affecting the properties of electronic circuits, and the damage affecting the crystal itself, impacting the signal generation.

Surface damage occurs usually on Si-SiO_2 interfaces as they are common at Metal-Oxide-Semiconductor Field-Effect Transistor (MOSFET) gates. Impacting particles can ionise the interface material, thus create e-h pairs, but as in this area the electric fields are high, the charge carriers are prevented from recombination. Due to the low mobility

of holes compared to that of electrons, electrons are quickly evacuated while holes move slowly to the interface and get trapped in shallow energy levels. These fixed charges remain trapped for an extended period of time and move the threshold point of MOS transistors, disturbing the functionality of the circuit. This is somewhat mitigated by a small feature size as here the gate oxides are only some nanometres thick. The amount of charge induced in the oxide is thereby reduced and the trapped charges can be neutralised by the tunneling of electrons into the gate. In critical parts of a circuit, usually Enclosed Transistors (ELT) are used, which have proven a higher radiation tolerance than the standard linear ones [17]. They are built in a circular design where the drain is enclosed by the source and the gate implemented as a ring on top (see Figure 2.6).

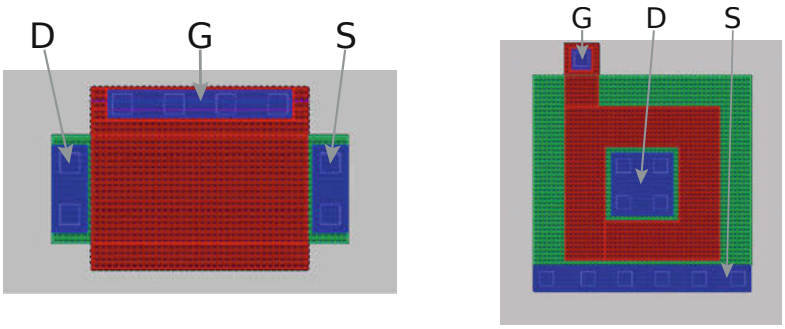

Figure 2.6: (a) Linear and (b) Enclosed (ELT) designs of a MOSFET transistor. The Drain-Source (D, S) channel is coloured in green, the Gate (G) in red and the metal contacts in blue [14].

The accumulated holes at the Si-SiO_2 interface also impact the interpixel insulation. The holes will attract free electrons from the bulk and as only few carriers can cross the interface by tunneling, a charge layer, called inversion layer, will form at the interface. This layer is conductive and would short the pixel implants if not accounted for. Three techniques have been developed to interrupt the conductive channel by introducing a p-implant (usually Boron) into the interpixel region called p-stop, p-spray and moderated p-spray as shown in Figure 2.7. In the P-stop process, which is a dedicated litographic step in the wafer processing, a highly doped p-well is implanted between the pixels that interrupts the inversion layer. P-spray is a layer of lower p-type doping that is applied to the whole wafer. As the inversion layer saturates at a concentration of $1 \cdot 10^{11}$ to $1 \cdot 10^{12}\,\mathrm{cm}^{-2}$, the amount of p-spray doping can be chosen such, that it compensates all accumulated charge carriers. Other implants for electronics or charge collection are much strongly doped and shadow the effects of this technique. The moderated p-spray

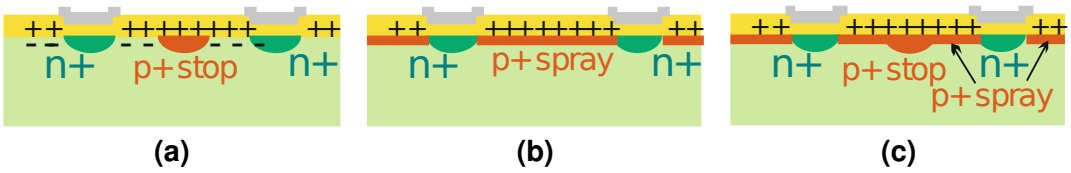

Figure 2.7: Sketch of interpixel insulation techniques, showing the trapped holes in the oxide and the effect of the insulation on the inversion layer for (a) p-stop, (b) p-spray and (c) moderated p-spray [12].

is a combination of both techniques. The thickness of the lithographic mask applied in the p-stop process is chosen such, that it allows a fraction of Boron ions to penetrate it. By this, a low doping layer is implanted over the whole wafer like in the p-spray process with a deeper and stronger doping in the opening of the mask between the pixel implants.

In contrast to effects of ionising radiation, Non Ionizing Energy Loss (NIEL) processes do not have an effect on the electrical properties of the circuit. Instead, the impinging particles can dislocate lattice atoms if the energy transfer exceeds a value of 25 eV and create vacancies and interstitials. Atoms, knocked out of the lattice, travel the silicon bulk and can cause ionisation and further displacement until they leave the bulk or come to a rest at any given position in the crystal. The resulting defects are shown in Figure 2.8.

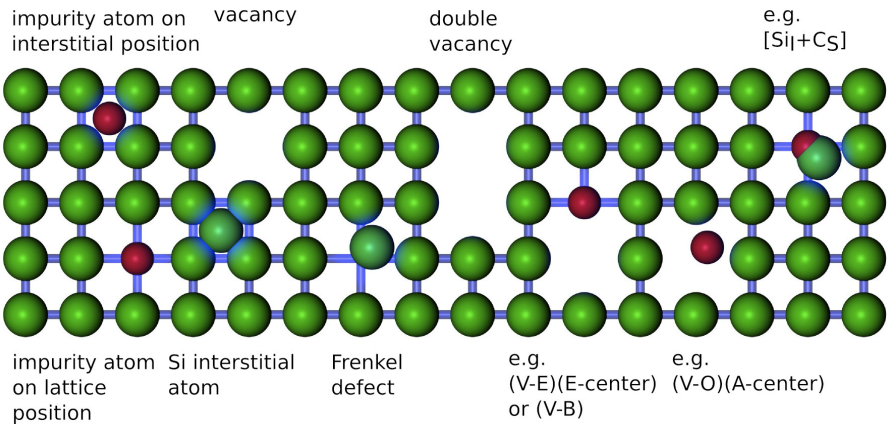

Figure 2.8: Representation of different types of crystal lattice damages induced by radiation [18]

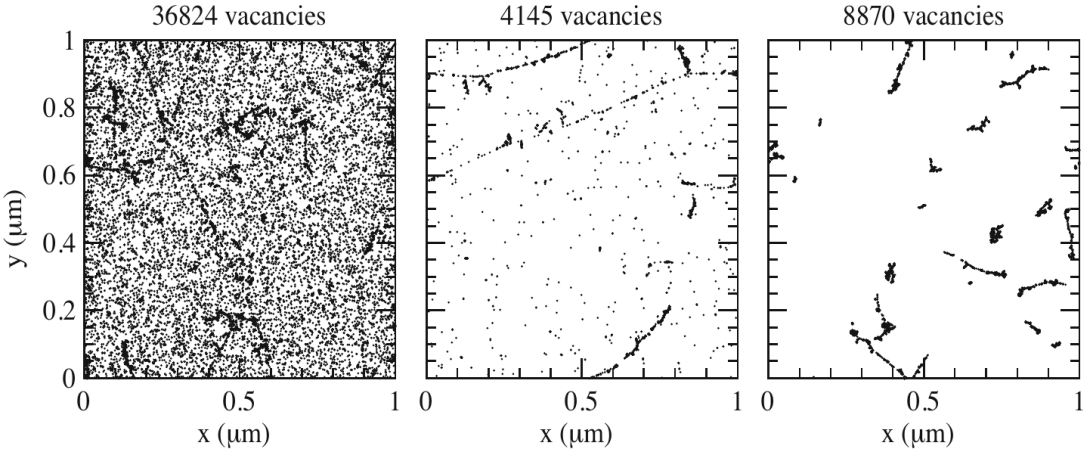

Figure 2.9: Simulated distribution of lattice damages in $1\,\mu m^3$ of silicon after $1 \cdot 10^{14}$ particles per cm^2 for 10 MeV protons (left), 24 MeV protons (centre) and 1 MeV (right) neutrons [14]

Depending on the particle type, point defects or cluster damages occur. While ionising particles like protons mostly cause point defects, neutrons generate cluster defects. Figure 2.9 shows the different types of damages after a fluence of $1 \cdot 10^{14}$ particles per cm^2 for protons and 1 MeV neutrons.

The effects of NIEL processes are usually normalised to the equivalent damage produced by a fluence of 1 MeV neutrons ϕ_{eq}. A hardness factor κ translates the actual fluence of the damaging particles ϕ_{irr} to the equivalent fluence:

$$\phi_{eq} = \kappa \phi_{irr} \tag{2.14}$$

with e.g. $\kappa = 0.6$ for 24 GeV protons and $\kappa = 1.85$ for 25 MeV protons [19].

Interstitials and vacancies can move through the silicon bulk, recombining thus healing the lattice or combining to more complex damages. This process, called annealing, depends highly on temperature and the time under heat. Thermal treatment of irradiated semiconductors can therefore be used to counteract the damages. One distinguishes between the beneficial annealing and the reverse annealing which leads to the formation of unwanted acceptor levels. The reverse process occurs on time scales orders of magnitude higher than annealing and can be effectively frozen out at temperatures below 0 °C. Irradiated devices have therefoere to be operated cold to prevent reverse annealing but thanks to the difference in time scales can be heated for short periods (e.g. during maintenance) to enhance the beneficial annealing.

Radiation damage can introduce new states in the band gap of the bulk, which can generate or absorb free charge carriers. They therefore act as induced donors or acceptors

with complex effects which are hard to predict. The observed effects are usually a change of effective doping concentration, increased leakage current and introduction of trapping centres.

Doping Concentration

As bulk damages act like donors or acceptors, they affect the effective doping concentration $N_{\text{eff}} = N_{\text{D}} - N_{\text{A}}$ ($N_{\text{A/D}}$: acceptor/donor concentration). In turn, this changes the bias voltage needed to reach a certain depletion depth, leading to high full depletion voltages ($>$1000 V) for fluences in the order of $1 \cdot 10^{15}$ to $1 \cdot 10^{16}$ $\text{n}_{\text{eq}}/\text{cm}^2$. In high resistive n-type bulk ($\mathcal{O}(\text{k}\Omega\,\text{cm})$), the introduction of donors leads to a lowering of the N_{eff} and at around $2 \cdot 10^{12}$ $\text{n}_{\text{eq}}/\text{cm}^2$ eventually to type inversion, where the sensor bulk starts behaving like p-doped silicon. The effect on the depletion voltage of and the formation of the depletion zone in a 300 µm thick n^+-in-n sensor can be seen in Figure 2.10.

In highly doped p-type substrates, like those used for HV-CMOS sensors, a so-called acceptor removal effect occurs [20]. It depends on the initial acceptor concentration in the bulk and leads to the removal of all effective acceptors up to a fluence of $1 \cdot 10^{15}$ to $2 \cdot 10^{15}$ $\text{n}_{\text{eq}}/\text{cm}^2$. This in turn enlarges the depletion zone as described by equation (2.6) and shown in Figure 2.11a, meaning that sensors with usually small depletion zones can gain a significant improvement in performance after irradiation. In contrast to the effects in n-type substrate, here the bulk remains p-typed. After the removal of all effective acceptors, the generation of stable deep acceptors slowly decreases the resistivity again.

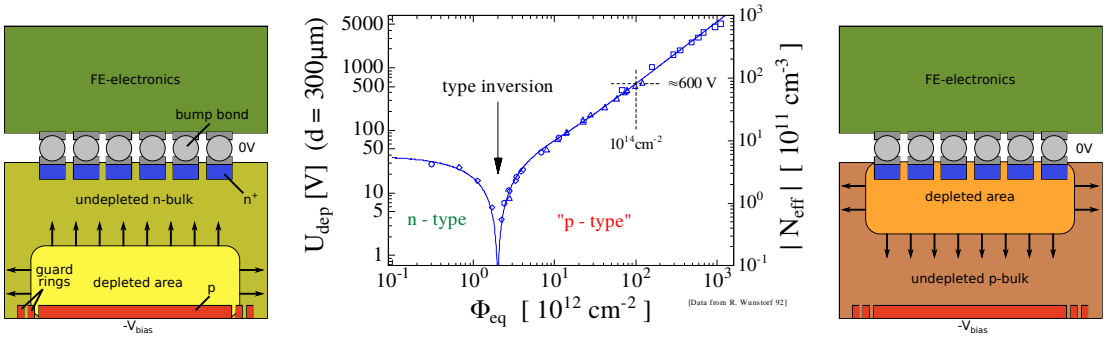

Figure 2.10: Growth of the depletion zone in (a) unirradiated and (c) type inverted n^+-in-n sensors. Before irradiation the depletion zone forms at the p-implant (bottom) while after type inversion it grows from the n+ electrodes (top). (b) Graph depicting N_{eff} versus the equivalent fluence [18].

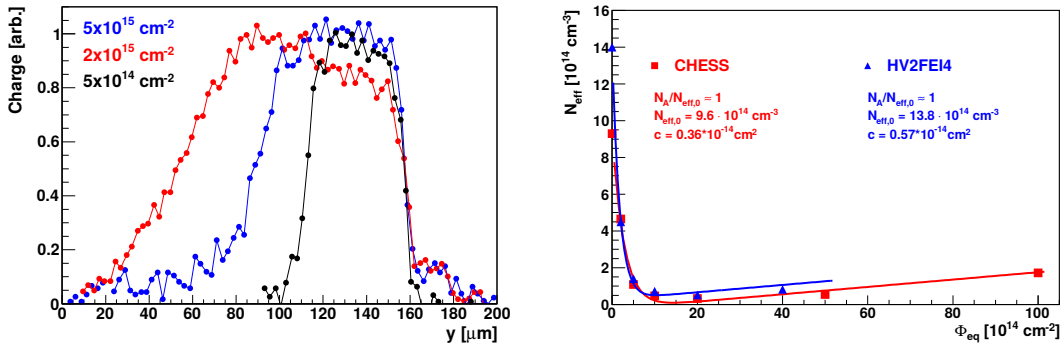

(a) (b)

Figure 2.11: (a) Charge collection profiles for single pixels at the same reverse bias voltages after irradiation up to $5 \cdot 10^{15}\,\mathrm{n_{eq}/cm^2}$ uncovering the growth of the depletion zone with fluence. (b) Effective doping concentration for sensors on low resistivity bulks irradiated up to $1 \cdot 10^{16}\,\mathrm{n_{eq}/cm^2}$ [20].

The effective doping concentration as shown in Figure 2.11b is described by

$$N_{eff} = N_{eff,0} \cdot \exp(-c \cdot \Phi_{eq}) + g_C \cdot \Phi_{eq} \tag{2.15}$$

with N_{eff}: the initial effective doping concentration, c: the removal constant, Φ_{eq}: the radiation fluence in units of 1-MeV neutrons and $g_C = 0.02\,\mathrm{cm^{-1}}$: the generation rate of stable deep acceptors. The removal constant has been found to be $c = 0.57 \cdot 10^{-14}\,\mathrm{cm^2}$ [20].

Leakage Current

Radiation induced states in the middle of the band gap can act as generation centres. Electron hole pairs can either be generated thermally via this interstitial state or recombine there. This leads to an increased leakage current in the bulk which in turn induces noise into the detector. Furthermore, it adds to the heating of the sensor which increases the danger of a thermal runaway that can potentially destroy the lattice. The increase of current is directly proportional to the fluence ϕ:

$$\Delta I_{\mathrm{leak}} = \alpha \cdot \phi \cdot V \tag{2.16}$$

with V being the volume under the electrode and α a universal constant that includes only the post-irradiation treatement of the material (annealing), but is independent of the type of silicon and the particles used for radiation.

Trapping and Charge Collection Efficiency

Energy states close to the valence or conducting bands tend to act as trapping centres, locations in which charge carriers can be captured for a certain amount of time, which can exceed the shaping time of the detector. The result is a reduced charge collection and eventually detection efficiency. The amount of charge decreases over time due to trapping as

$$N_{\mathrm{e,h}}(t) = N_{\mathrm{e,h}}(0) \exp\left(\frac{-t}{\tau_{\mathrm{eff_{e,h}}}}\right) \tag{2.17}$$

with $N_{\mathrm{e,h}}(0)$ being the initially generated elecron-hole pairs and $1/\tau_{\mathrm{eff_{e,h}}}$ the effective trapping probability, which can be described by

$$\frac{1}{\tau_{\mathrm{eff_{e,h}}}} = \beta_{\mathrm{e,h}} \phi_{\mathrm{eq}} \tag{2.18}$$

The proportionality constants were measured to be [21]

$$\beta_{\mathrm{e}} = (4.2 \pm 0.3) \cdot 10^{-16}\,\mathrm{cm^2\,ns^{-1}}$$
$$\beta_{\mathrm{h}} = (6.1 \pm 0.3) \cdot 10^{-16}\,\mathrm{cm^2\,ns^{-1}}$$

Figure 2.12 shows the fraction of electrons induced in the sensor bulk versus time after irradiation up to $1 \cdot 10^{15}\,\mathrm{n_{eq}/cm^2}$. It is evident that a fast charge collection, thus high electric fields are necessary for efficient detection of particles after irradiation.

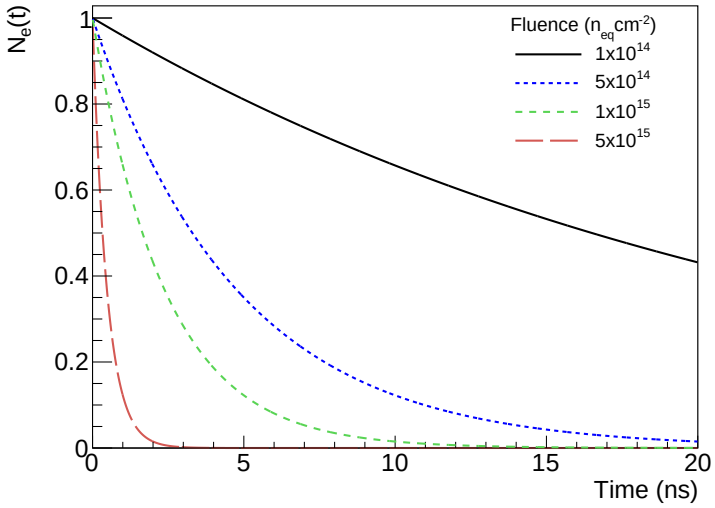

Figure 2.12: Fraction of electrons still available after drifting a certain amount of time in a sensor bulk, damaged by irradiation.

2.5 Summary

Pixelated silicon detectors are an integral part of modern tracking detectors. Being sensitive to charged particles with high granularity and radiation tolerance, they are usually employed as the innermost system of a collider experiment.

Silicon sensors exploit the availability of a depletion zone, generated by a pn-junction in which particles generate a signal by ionisation. Strong electric fields and a large depletion depth, generated by the operation of the junction in reverse bias mode, ensures a fast signal generation with high amplitude. In addition to this drift-based charge collection, the diffusion of free charge carriers, generated outside the depleted area can contribute to the signal, though at a reduced collection speed.

Silicon detectors for high radiation and high speed environments are usually constructed as hybrid detectors, where the sensing part is built independently of the readout. The high granularity of silicon sensors requires dedicated integrated circuits to which each pixel cell is connected via solder bumps. These circuits comprise per-pixel analogue and digital signal processing and provide hit coordinates and charge information to the higher level readout.

With irradiation, the properties of the detectors can deteriorate, whereas the type of radiation (ionising or non-ionising) influences different parts of the detector. Ionising radiation impacts electrical circuits which therefore have to be designed using dedicated techniques like enclosed transistors, thin oxide layers and small feature sizes. Also special isolation techniques like p-stop and p-spray were developed to prevent radiation-induced electrical shorts. Non Ionizing Energy Loss (NIEL) causes damage to the crystal lattice changing the signal generation of the sensor. Charge trapping leads to a degraded charge collection and the suppression of the diffusion component of the signal. A strong, drift-based collection, thus a large depletion zone is necessary for efficient operation. However, the necessary high voltage might not be reachable after high irradiation as the doping concentration changes with fluence. For low resistivity p-type substrates on the other hand, the acceptor removal effect leads to an increase of collected charge up to fluences of $10^{15}\,\mathrm{n_{eq}}/\mathrm{cm}^2$. By optimising the sensor design and choice of production technology, silicon sensors can be adapted to a variety of use cases.

Chapter 3
Pixel Detector Technologies in ATLAS

As described in Section 1.3, the ATLAS Inner Detector provides precise particle tracking with the Pixel Detector being at its core. In addition to tracking, the Pixel Detector's main purpose is the precise determination of the location of vertices and the tagging of heavy flavour jets.

One of the key requirements for many analyses at the LHC is the correct identification of bottom quark induced jets. This is necessary for all measurements and searches involving top quarks, as they predominantly decay into a b quark and a W boson. In the Higgs sector, the channel with the largest branching ratio of 58 % is the decay to a $b\bar{b}$ pair and searches for Beyond Standard Model physics also include processes with b-quarks in their final states, just to name a few. As mesons containing b-quarks are relatively long lived, they can travel a measurable distance in the detector (e.g. $\sim$0.3 mm at an energy of 50 GeV) before they decay, forming a secondary interaction point or vertex. Being able to distinguish these vertices from the primary ones presents a strong handle on the identification of bottom quarks and hence jets originating from these quarks. This is also important for the reduction of all backgrounds that involve b-quarks. Furthermore, in a high pile-up environment like ATLAS, locating vertices with high precision is necessary for keeping concurrent but uncorrelated events apart. For high precision measurements of the vertex position and the displacement of a possible secondary one (so called impact parameter), high granularity detectors close to the interaction point are necessary. These requirements, combined with a strong radiation hardness and low material budget are fulfilled by pixel detectors (Chapter 2).

In this chapter, the implementation of the Pixel Detector as part of the inner tracking system of the ATLAS experiment will be discussed. The original Pixel Detector will be introduced, along with its first upgrade, the Insertable B-Layer (IBL). As part of this upgrade the design of a new readout chip, the FE-I4, and the improvement in tracking performance will be reviewed. Finally, the high luminosity upgrade of the ATLAS Inner Tracker (ITk) will be presented and a candidate technology based on High-Voltage CMOS processes introduced. For the latter, the significance for the ITk in terms of sensor properties, detector construction and operation will be analysed.

3.1 The ATLAS Pixel Detector

The ATLAS Pixel Detector [9, 22] is the innermost system of the ATLAS experiment. As core of the inner tracker, it is designed to provide tracking and vertexing information with a resolution of 10 µm in the $R\phi$-direction and 115 µm along the beam axis up to a pseudorapidity of $|\eta| < 2.5$. The proximity to the interaction point and the high granularity makes it the most important detector for reconstruction of secondary vertices and b-tagging of jets.

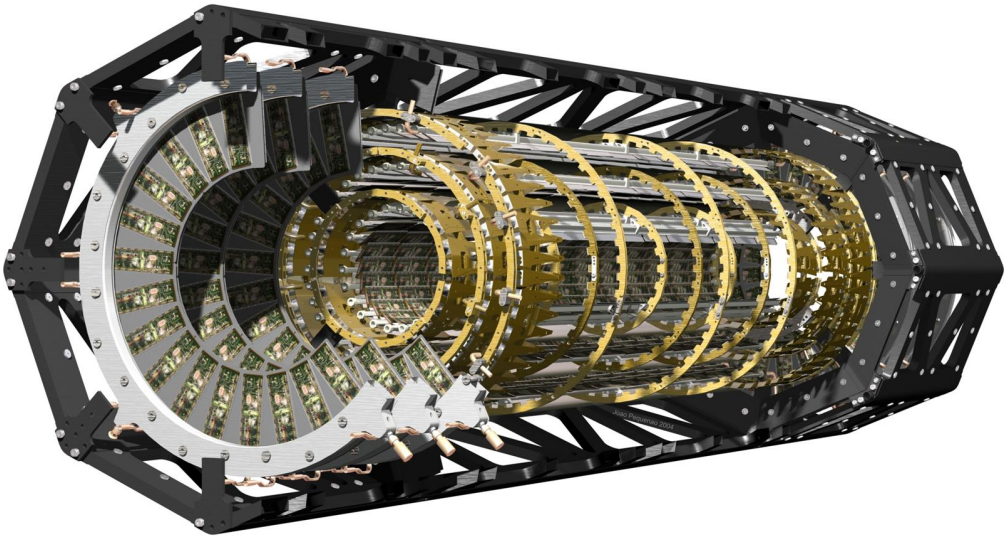

Figure 3.1: 3D image of the ATLAS Pixel Detector and its support structure [22]

The Pixel Detector (see Figure 3.1) is divided into three cylindrical layers (barrel region) at radii of 50.5, 88.5 and 120.5 mm which are closed up by three discs (end-cap region) in the forward and backward direction providing a hermetic coverage along the full η range. It hosts around 80 million pixels on 1744 hybrid modules. Each module comprises a single 250 µm thick n^+-in-n silicon sensor covering an area of $\sim 2 \times 6\,\mathrm{cm}^2$. The 47232 rectangular pixels are mostly $50 \times 400\,\mu\mathrm{m}^2$ sized and read out by 16 Front-End (FE) chips with the intermediate gaps being covered by longer pixels with a size of $50 \times 600\,\mu\mathrm{m}^2$. The hybrid module is supported by a flexible PCB, glued to the back side of the sensor. It hosts passive circuits for powering and the Module-Control Chip which facilitates the communication between the 16 FE chips and the off-detector readout system. Digital signals are transmitted optically to the outside of the detector thanks to optoelectrical converters close to the modules. During the Long Shutdown 1 of the LHC these converters were moved outside the Inner Detector cryostat, allowing for com-

parably simple access in case of failure [23].

The pixel detector was designed for luminosities up to $1 \cdot 10^{34}\,\mathrm{cm}^{-2}\,\mathrm{s}^{-1}$. It was anticipated that the LHC will greatly surpass that value, leading to increased pileup and radiation [24]. To account for failure of the current innermost pixel layer (B-layer) due to radiation and the increase in data rate, a fourth pixel layer, the Insertable B-Layer (IBL) was installed at a radius of 33 mm close to the interaction point.

3.2 The FE-I4 Pixel Detector Readout Chip

The harsh environment from radiation and pile-up, expected for the readout of the IBL sensors, demanded the design of a new readout chip, the FE-I4 [25, 26, 27]. It had to handle 5–6 times the hit rate of the original ATLAS Pixel readout chip FE-I3 [28] while being compatible with the two proposed sensor technologies (Planar Pixel Sensor (PPS), 3D) and the detector readout and control system [29]. Additionally, the dead region and power consumption of the chip had to be kept low in order to allow its employment on a small radius detector like the IBL. This lead to the following design decisions:

- Reduced feature size of 130 nm (250 nm for the FE-I3)
- A pixel size of $50 \times 250\,\mu\mathrm{m}^2$ for improved single point resolution
- Enlarged chip size of $19 \times 20\,\mathrm{cm}^2$ ($\sim$4 times the FE-I3 size) with a reduced fraction of inactive area ($\sim$25 % with FE-I3 to $\sim$10 %)
- Large sensor capacitance range (0 to 0.5 pF), thus compatibility with different sensor technologies and designs
- Low power consumption: $240\,\mathrm{mW/cm}^2$
- Radiation tolerant design for TID up to at least 200 Mrad (e.g. Enclosed Layout Transistors (ELTs), triple redundant latches, etc.)

The chip comprises three parts, the pixel matrix hosting the per-pixel analogue and digital signal processing, shared digital pixel regions at the periphery called End Of Column Logic (EOCL) and the End of Chip Region.

Analogue cell The analogue cell, as depicted in Figure 3.2, contains the analogue signal processing and delivers a discriminated signal to the digital logic of the readout chip.

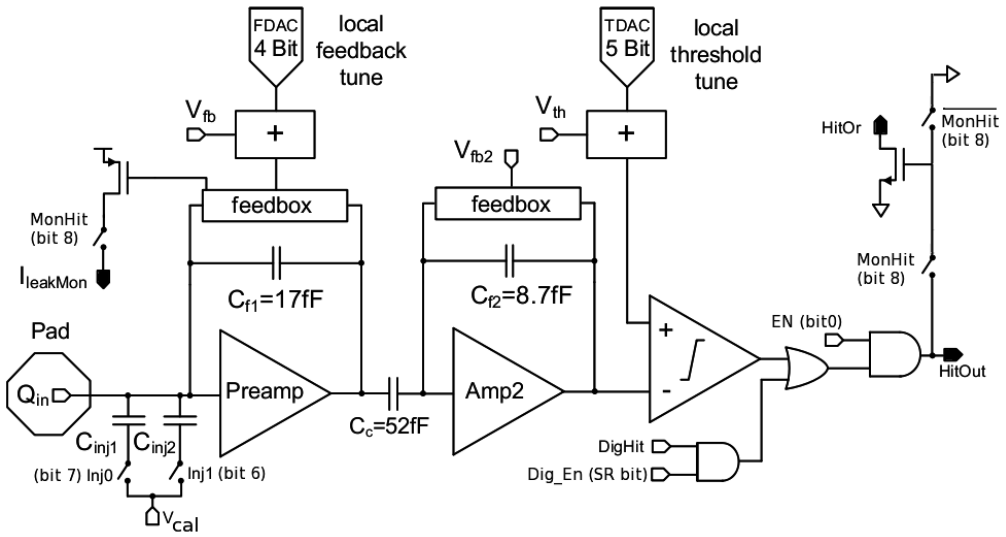

Figure 3.2: Schematic diagram of the analogue pixel cell showing the two stage amplifier, the discriminator and supporting circuits [29]

Charge collected by the sensor is initially amplified by two stages (Preamp and Amp2 in Figure 3.2) of a Charge Sensitive Amplifier which are AC coupled. For both amplifiers, the feedback current can be adjusted globally, while for the Preamp, per-pixel corrections can be applied via a 4-bit Digital to Analogue Converter (FDAC). This allows to fine tune the charge measurement, thus the charge to Time over Threshold (ToT) conversion factor. The Preamp contains furthermore a compensation for leakage current, originating from the sensor, up to 100 nA. After amplification, the signal is compared to a threshold voltage, which again is set globally with per-pixel corrections via a 5-bit DAC (TDAC). The output of the discriminators can be gated individually, allowing the masking of misbehaving pixels. All pixel outputs can be configuered to connect to the global HitOR bus where each connected pixel will pull down the bus when a signal over threshold has been detected. The so generated HitOR signal is internally used for self-triggering of the readout or debugging and triggering of an external readout system if evaluated externally via a wire bond pad. An implementation of the latter will be discussed in the scope of test beam measurements in Section 4.2.4. Finally, a charge injection circuit allows to test and calibrate each pixel by charging up to two capacitors at the amplifier input with an on-chip generated and configurable voltage. The capacitor discharge then injects a well known signal into the analogue cell.

Digital part and readout In the pixel matrix, four pixels share a digital cell for further hit processing as sketched in Figure 3.3. Charge information is extracted from the discriminated signal by one of four per-pixel ToT counters, while the hit timestamp is stored in an array of latency counters that is global to the digital cell. The cell is therefore capable of keeping up to 5 hits per 4 pixels ready for readout. This is a major difference in data handling compared to the FE-I3 readout chip of the ATLAS Pixel Detector. In the latter, a detected hit would be stored at the chip's periphery or End Of Column Logic (EOCL), meaning that at high occupancies the per column hit information bus could lock up easily. It was shown that this so called column-drain-scheme of the FE-I3 is not capable of delivering a satisfactory performance in case of high pile-up events [30]. In contrast, when a hit is detected by the FE-I4, the next free latency counter of the 4 pixel digital cell is started. It counts down from a configured latency in units of LHC bunch crossing times (25 ns). A Level-1 Accept (L1A) trigger in coincidence with the expiring of a counter initiates the transfer of hit information to the periphery and the allocated cells are freed. If no such signal is received before the counter expires, the hit information is deleted and the resources can be used for another hit.

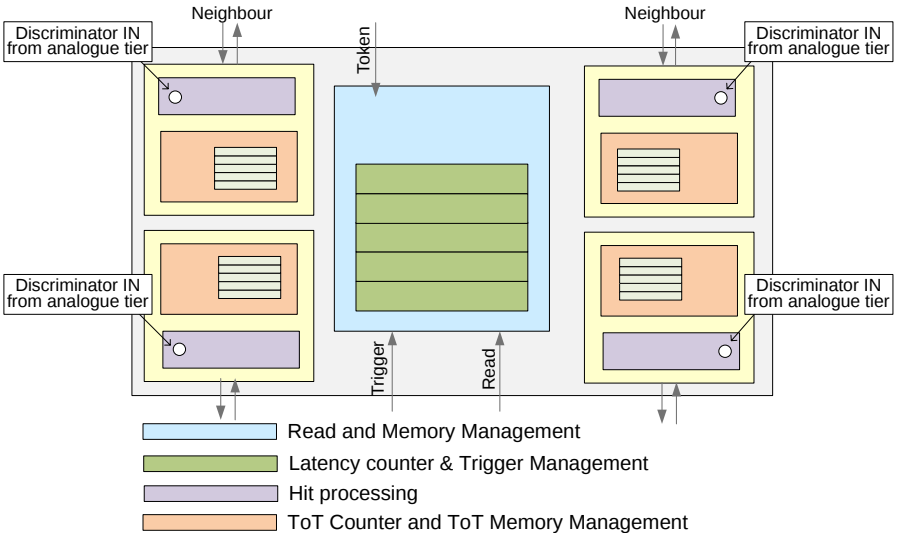

Figure 3.3: The 4-pixel regional digital logic [26]

The End of Chip region hosts voltage regulators, bias current and voltage generators, the interface to the readout system and the command and triggering system. The chips readout can be triggered either by the HitOR signal as described above, by an externally generated pulse or by the command encoder upon reception of a signal from the higher level readout system. When such a Level-1 Accept is received, the End Of Column Logic sends up to 16 consecutive triggers with decreasing latency information to the

pixel matrix. By this, an up to 400 ns wide time window can be read out. Data is then piped out to the higher level readout via LVDS with a speed of up to 160 Mbps. The integrity of the FE-I4 data is ensured internally by means of Hamming Encoding, while all outgoing data are 8b10b[a] encoded.

Calibration The FE-I4 has internal circuits for functional tests and individual calibration of each pixel. A scan over the pixel matrix is usually divided into multiple steps in which only a part of the matrix is active in order to avoid overloading the 4-pixel digital cells.

The basic functional test is the *Digital Test*, in which a number of digital pulses (usually 50–250) are injected right after the discriminator output of the analogue cell. If all pulses are correctly registered as hits, the digital part is considered sound.

The functional test of the analogue cell is called *Analog Test*. Instead of a digital pulse generator, the configurable *PulserDAC* injects a charge which is considered well above threshold (typically 16000 electrons) into the preamplifier. Again, the number of injected pulses is compared to the number of registered ones. The test allows for detecting malfunctions of the amplifiers and discriminators or an excess of noise which would render calibration useless.

The relevant information provided by the analogue cell is if the threshold has been exceeded and for how long the signal remained over threshold. This Time over Threshold is measured in units of LHC bunch crossing times (25 ns) and provides an estimator for the deposited charge as discussed in Section 2.3. For a well defined response to a signal, the single analogue cells can be tuned by per-pixel DACs (FDAC for the feedback current and TDAC for the threshold correction).

Figure 3.4a shows the dependency of the amplifier and discriminator output signal on the DAC parameters and the input signal. As both the discriminator threshold and the ToT depend on the setting of both the TDAC and FDAC, an iterative calibration is used. For determining the threshold of the discriminator, pulses from a range of charges are injected into the preamplifier. A perfect circuit would register no signals below threshold and all injected pulses above threshold – the activation curve would describe a step function. Due to electronic noise following a Gaussian distribution, the response is smeared to an error function with a signal detection probability of

$$P(q) = \frac{1}{2}\mathrm{erf}\left(\frac{q_{\mathrm{thr}} - q}{\sqrt{2}\,\sigma_n}\right) \tag{3.1}$$

with q: injected charge, q_{thr}: discriminator threshold, σ_n: standard deviation of the

[a] 8b10b is a line code that maps 8-bit words to 10-bit symbols achieving DC-balance, limited error correction and allowing for clock recovery [31].

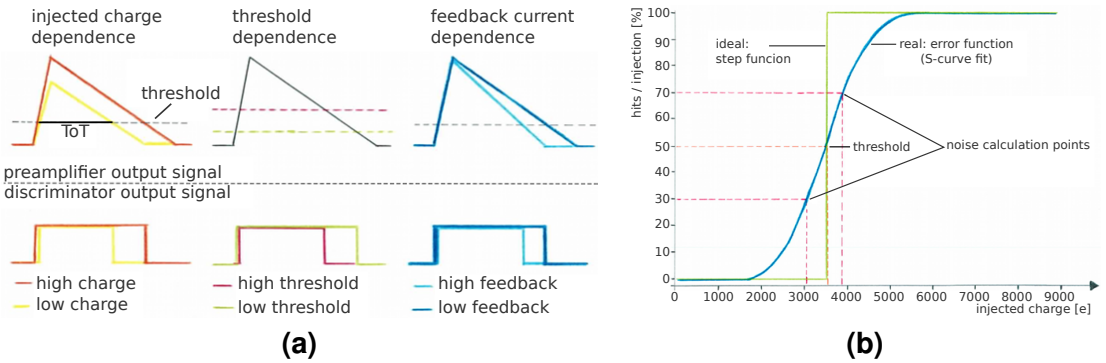

Figure 3.4: (a) Response of the FE-I4 preamplifier and discriminator to low and high signals at different calibration settings, (b) Expected activation curve of the discriminator: a step function convoluted by Gaussian distributed noise [32].

electronic noise distribution. Figure 3.4b shows the definition of the threshold as the point, where 50 % of the injected charges are detected and the value for electric noise as width of the 30 to 70 % interval.

Example threshold and ToT distributions for an FE-I4 module bonded to a 200 µm thick planar silicon sensor before and after equalisation are shown in Figure 3.5. The ToT distribution is obtained by injecting a defined charge into the pixels and recording the returned ToT value. Accordingly a set of calibration constants is referred to by the threshold value in electrons and ToT at a given charge, e.g. a threshold of 1600 e and a ToT of 10 bx for a charge of 20 000 e.

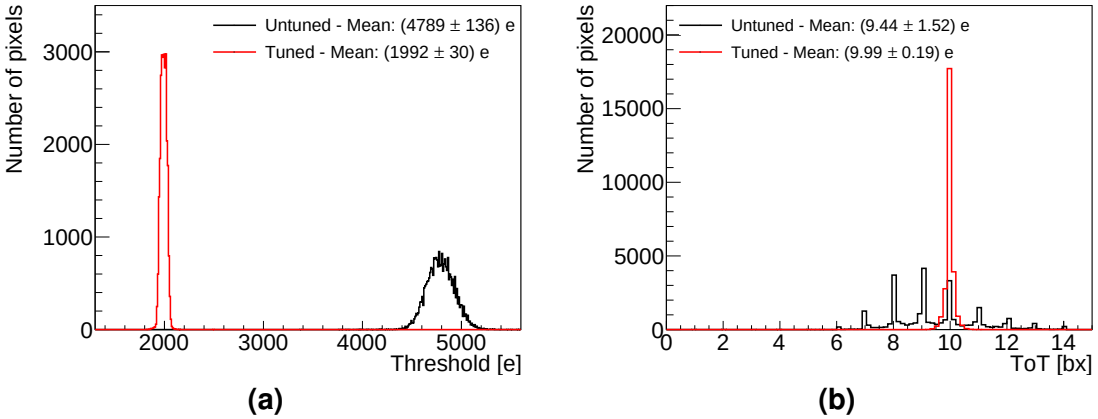

Figure 3.5: (a) Threshold and (b) ToT distributions before and after tuning for an FE-I4 and planar pixel sensor assembly.

3.3 State of the Art: The Insertable B-Layer

The ATLAS Pixel Detector showed great performance during its first years of operation, but it became soon evident, that the LHC would exceed its contemplated luminosity of $1 \cdot 10^{34}\,\mathrm{cm}^{-2}\,\mathrm{s}^{-1}$ for which the Pixel Detector was constructed. This would eventually lead to inefficiencies in the innermost layer due to high occupancy and radiation damage. Also at that time, some Pixel Detector modules were observed failing. In order to restore and improve the performance of the detector, the Insertable B-Layer (IBL), a new barrel layer was constructed and inserted into the centre of the detector (see Figure 3.6).

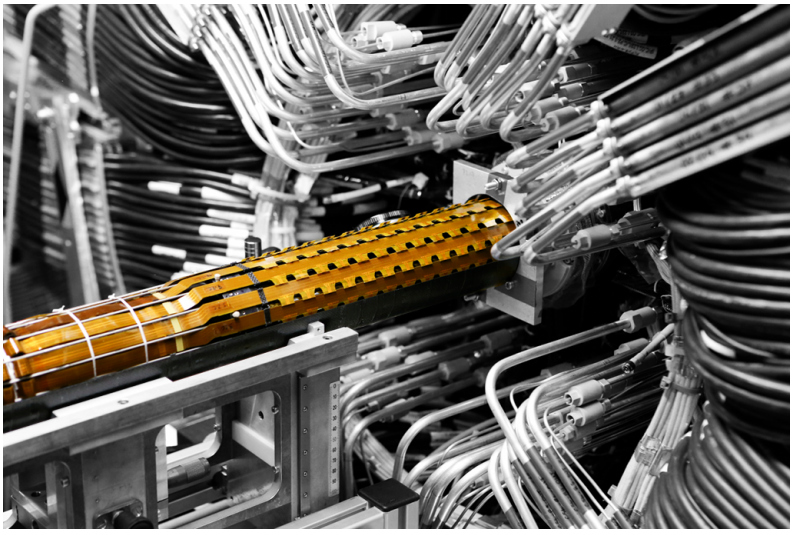

Figure 3.6: Picture of the IBL during installation into the ATLAS Pixel detector [32]

The IBL consists of fourteen staves that were mounted inside the innermost pixel layer at a nominal radius of 33.25 mm from the beam. The installation of an additional layer around the original beam pipe was not possible so it was replaced by a smaller one made of berillium, opening a gap of 9 mm for the installation of the detector and services. To fulfil its requirements in terms of occupancy and increased radiation levels, two new sensor designs and the aforementioned readout chip FE-I4 were developed.

The tight space constraints prohibited tilting of the sensors on a stave, requiring to minimise the inactive area between sensors by an appropriate design. Two sensors made in planar n^+-in-n and 3D technology were therefore built in a slim-edge or slim-fence design, ensuring an inactive edge as low as 200 µm.

Having proven reliable during its operation in the original Pixel Detector, the planar n^+-in-n technology was chosen for the central 75 % of the IBL surface. The original design was modified towards the IBL specifications by decreasing the pixel size from

$400 \times 50\,\mu m^2$ to $250 \times 50\,\mu m^2$ and by enlarging the outermost pixel columns towards the edges by 200 µm. In order to keep the material budget minimal, the readout-chips were thinned down to 150 µm and the sensors to 200 µm. Thinner devices were in principle possible, but the hybridisation process by bump bonding would have then required to mount the fragile sensors on handling wafers, increasing significantly the cost of production. As in the original design, the pixel matrix is surrounded by multiple guard rings to attenuate the high voltage towards the edges which are conductive due to the crystal damages introduced by wafer cutting. However, the demand for a thin inactive edge required a reduction of the number of guard rings from 16 to 13, thereby reducing the guard ring area length from 1100 µm to 450 µm (see Figure 3.7) [33]. For a further decrease in inactive area, the outermost pixels were prolonged to a length 450 µm, reaching 250 µm under the guard rings. For the IBL, $18.8 \times 41.3\,mm^2$ sized double-chip sensors were built that are read out by two adjacent FE-I4 chips. The unavoidable gap between the FEs was bridged by 450 µm long pixels that are bonded to both chips.

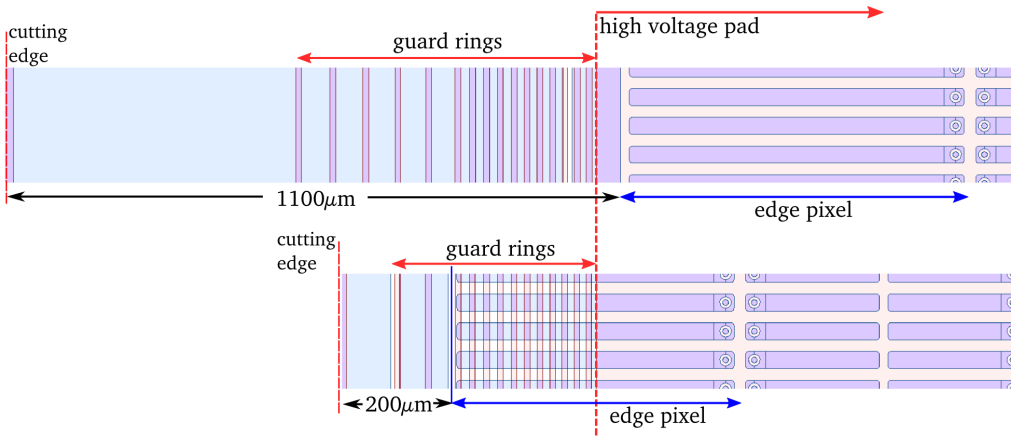

Figure 3.7: Design of the edge region of the planar n^+-in-n ATLAS Pixel and IBL sensors. The top part shows the original design with a wide guard ring section, the bottom one the slim-edge design with a reduced number of guard rings and prolonged outer pixels. Adapted from [34]

For the outer regions of the IBL staves, a new design called 3D was implemented. Instead of processing electrodes on the surface of the wafers, pillars are etched through the bulk by means of Deep Reactive Ion Etching (DRIE). The pn-junction is then formed by doping these pillars alternately. A double sided 3D design with a thin inactive edge (slim fence) was chosen for the IBL, where the n^+ electrodes were etched from the front and the p^+ ones into the backside of the 230 µm thick silicon bulk (see Figure 3.8).

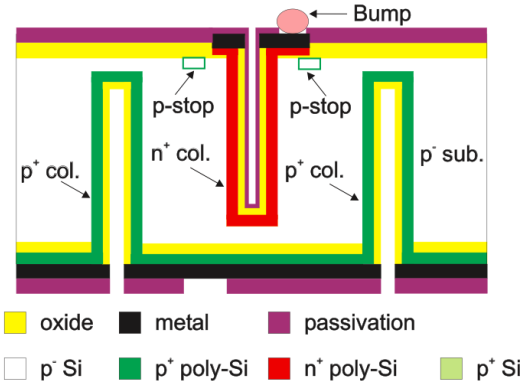

Figure 3.8: Schematic of the double sided 3D sensor design, showing the electrode implants reaching from the front- and backside of the wafer into the silicon bulk [29].

3.3.1 Performance of the Upgraded Pixel Detector

The impact of the introduction of the IBL to the ATLAS Pixel Detector was estimated during the LHC Run-2 in 2015 by evaluating the efficiency and resolution of the additional detector layer. The measurement was performed using a set of $Z \rightarrow \mu\mu$ events, selected from approximately $150\,\mathrm{pb}^{-1}$ of 13 TeV data.

Evaluating the probability to associate an IBL cluster to a track showed that the IBL works at an efficiency of over 98 % over a wide range of p_T as shown in Figure 3.9a. The slight decrease towards low p_T tracks is attributed to non-primary particle tracks with a softer p_T spectrum. In order to estimate the intrinsic hit efficiency of the IBL, the tracks were required to pass through the regions where IBL modules overlap. By requiring that at least the innermost module of the overlapping pair has detected a particle, the efficiency of the other module can be estimated.[b] The result shown in Figure 3.9b confirms the expected high overall detection efficiency and demonstrates the expected drop in efficiency along the z-direction due to the gaps between the modules on staves.

Requiring the track passing through overlapping modules and being detected by both, the hit resolution of the modules was estimated. This allows exploiting the full resolution of an IBL module surpassing the precision of a reconstructed track and lead to the resolution estimate of (10.0 ± 0.1) µm in $r\phi$ and (66.5 ± 0.8) µm in z direction [35].

Following these results, the improvement of the combined pixel tracking has been studied by comparing early LHC Run-2 (2015) to late Run-1 (2012) data. The inclusion of IBL increased the vertexing precision by over 70 % over its whole acceptance

[b] This is similar to the technique in test beam measurements where a dedicated sensor provides a reference for the devices under test to be compared with.

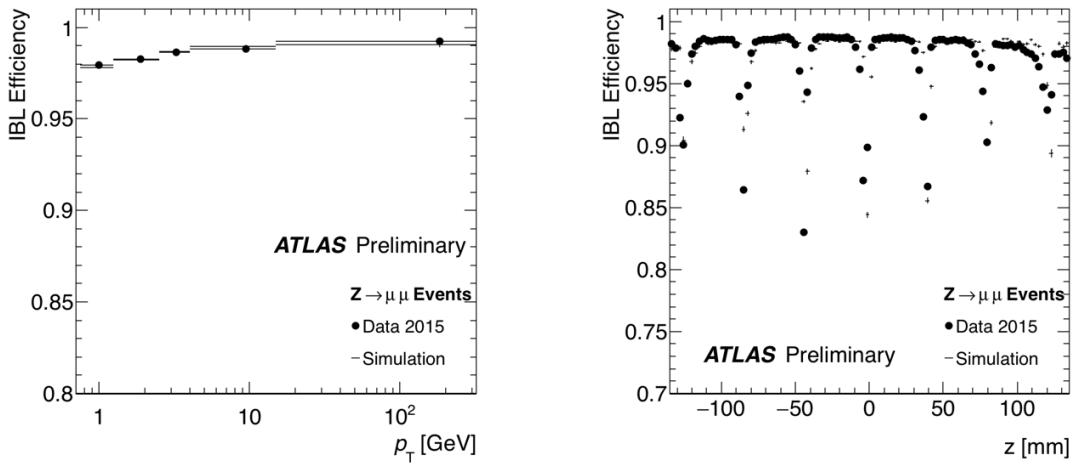

(a) **(b)**

Figure 3.9: (a) Efficiency of associating an IBL hit to a track as a function of the longitudinal z coordinate, showing the performance of the module and the efficiency drop at the boundary between modules. (b) Efficiency of associating an IBL hit to a reconstructed particle track as a function of the particle p_T [35].

for tracks with $p_T < 20\,\text{GeV}$ as shown in Figure 3.10. This is of special importance as it increases the tagging performance for *b*-flavoured jets, which is necessary for many analyses for example involving the Higgs boson, top quarks or searches for Beyond Standard Model physics. Due to efficient light- and *c*-jet rejection, the insertion of IBL has improved the *b*-tagging efficiency by 10 % [36]. Furthermore, it improves the identification of *B*-hadrons which thanks to their life time of 1.5 ps can travel several millimetres before decaying. High-resolution tracking of particles can therefore disentangle the vertices and enable to identify *B*-hadrons efficiently. Finally, during its operation in the first part of Run-2 2016, the upgraded Pixel Detector has shown a performance of almost 99 % sustained at high trigger rates of up to 85 kHz thanks to a maximum dead time of about 2 % [37].

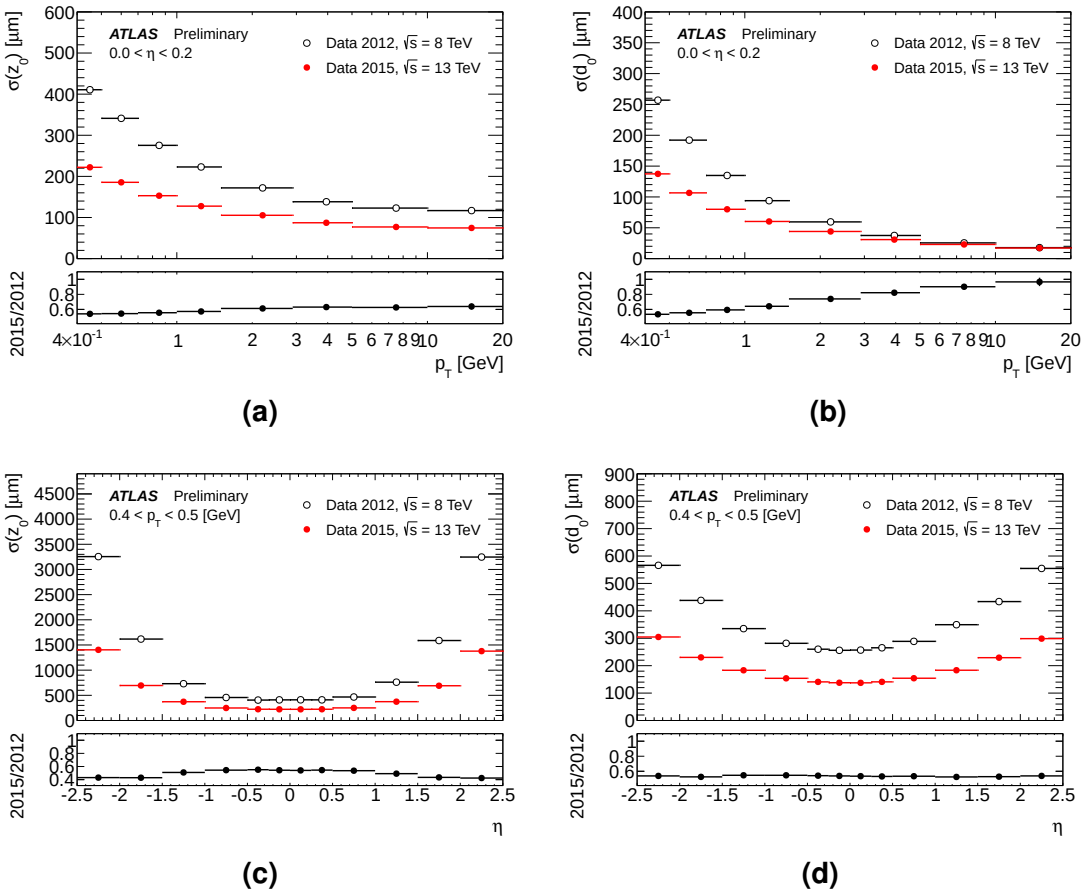

Figure 3.10: Comparison of (a)/(c) the longitudinal and (b)/(d) the transversal impact parameter resolution of the upgraded (IBL included) to the original Pixel Detector as function of p_T for $0 < \eta < 0.2$ and η for $0.4 < p_T < 0.5\,\text{GeV}$ [38].

3.4 High Luminosity Upgrades of the ATLAS Pixel Detector

The Inner Detector was designed for ten years of operation at an instantaneous luminosity of $1.0 \cdot 10^{34}\,\mathrm{cm}^{-2}\,\mathrm{s}^{-1}$ with an average pile-up of 23 interactions per 25 ns bunch crossing and a peak trigger rate of 100 kHz. In 2016 the LHC already exceeded these parameters and as of 2018 delivered luminosities up to $2.14 \cdot 10^{34}\,\mathrm{cm}^{-2}\,\mathrm{s}^{-1}$ with a pile-up of $\sim$60 [39]. The current Inner Detector however was able to cope with the new environment after upgrades to the Pixel Detector readout system [40].

With its upgrades during Long Shutdown 3 (LS3), the LHC is supposed to deliver beams at unprecedented intensities. The instantaneous luminosity will increase up to $\sim 7.5 \cdot 10^{34}\,\mathrm{cm}^{-2}\,\mathrm{s}^{-1}$ with an average pile-up of $\sim$ 200, pushing the particle rate up to $1\,\mathrm{MHz/mm}^2$. This also means that a trigger rate of several MHz has to be sustained in order to be efficient. Furthermore, the end-of-lifetime integrated luminosity will increase tenfold for the upgraded tracker to around $4000\,\mathrm{fb}^{-1}$. Pushing the requirements beyond what is sustainable with the current tracker, the Inner Detector will be exchanged during LS3 for a purely silicon-based one, replacing the current TRT by strip detectors and extending the Pixel Detector.

The layout under discussion early 2018 as seen in Figure 3.11 comprises five layers of pixel detectors in the barrel region closed up by end-caps for high pseudorapidities.

To cope with the dense tracking environment, the pixel size will be reduced from $250 \times 50\,\mu\mathrm{m}^2$ like for the IBL sensors to $50 \times 50\,\mu\mathrm{m}^2$ or $25 \times 100\,\mu\mathrm{m}^2$. Together with the elevated radiation levels and trigger rates, a complete redesign of the pixel readout chips is required. The new chip will be built in TSMC 65 nm CMOS technology and is, as of early 2018, in design by the RD-53 collaboration [42]. As the ITk Pixel Detector will strech over $\sim$ 30 cm in radius, the radiation environment will differ significantly between the layers as can be seen in Figures 3.12a and b.

While the innermost layer will have to sustain a Total Ionising Dose (TID) up to 1 Grad and NIEL fluences up to $2 \cdot 10^{16}\,\mathrm{n_{eq}/cm}^2$, the requirements for the outermost layer are relaxed to 50 Mrad and $1 \cdot 10^{15}\,\mathrm{n_{eq}/cm}^2$. This means in turn that the design decisions of the inner layers are dominated by the requirements from radiation, hence hybrid pixel detectors in planar and 3D technology are the necessary choice. The outer layers on the other hand leave space for novel technologies which can bring benefits in terms of module production and cost reduction. A candidate technology are HV-CMOS based sensors which will be discussed in the next section and are the main focus of this thesis.

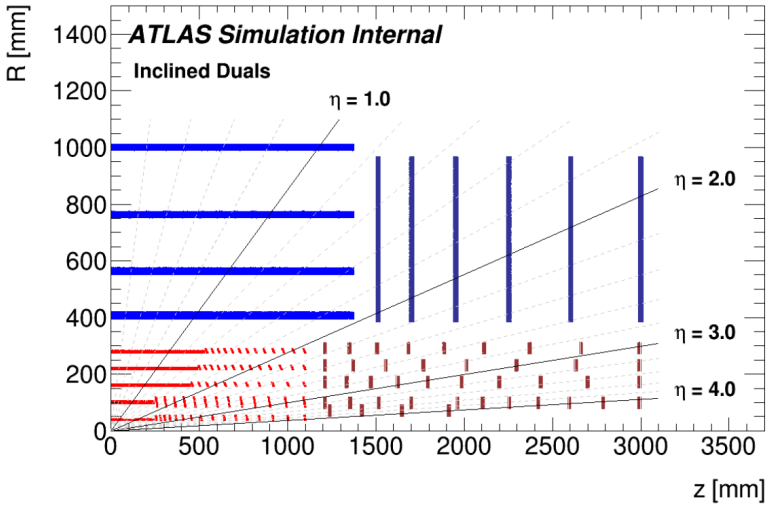

Figure 3.11: Schematic layout of the ITk detector for the HL-LHC upgrade, showing the upgraded strip detector (at $R > 350\,\text{mm}$, in blue) and the pixel layers ($R < 350\,\text{mm}$, in red). Only a quarter of the detector is depicted as it is symmetric around the interaction point [41].

3.5 High-Voltage CMOS Sensors for the Upgraded Inner Tracker

Complementary Metal-Oxide-Semiconductor (CMOS) is a technology for integrated circuits developed in 1963 and nowadays widely used in High Energy Physics (HEP) experiments for readout circuitry – the FE-I4 chip for example is fully implemented in CMOS technology. Being an industry standard it is available by a multitude of foundries around the world and chips can be produced relatively cheap in large quantities. Building detectors in CMOS technology enables to implement the full readout on the same substrate as the sensor itself, forming a Monolithic Active Pixel Sensor (MAPS). Such devices have been in use for some time in particle physics experiments, however they are not suitable for a high rate and high radiation environment like the ATLAS Pixel Detector. Here classical hybrid detectors have the advantage that by separating the sensing part from the readout, both components can be highly specialised to complementary tasks: in the case of the sensor, fast signal generation and tolerance against bulk damaging radiation, hence drift-based charge collection, and in the case of the readout chip, fast analogue and digital signal processing and tolerance against ionising radiation. This comes at the expense of complex interconnection techniques, namely bump bonding with impact on cost, production time, material budget, detector assembly and the necessary services.

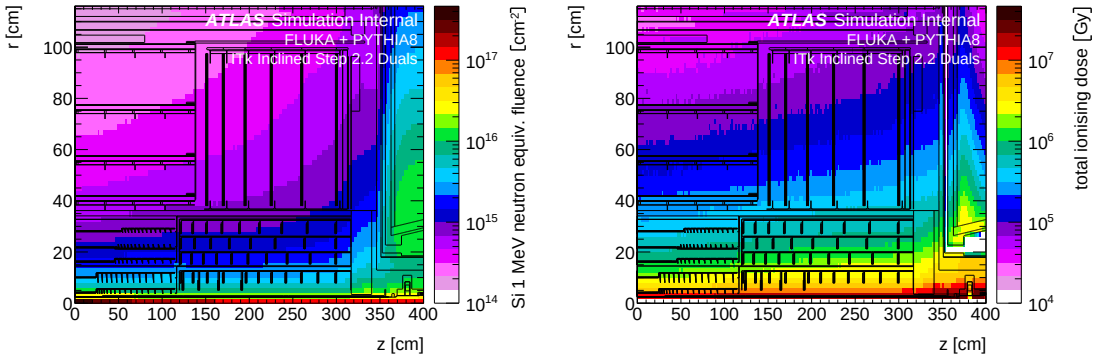

Figure 3.12: End-of-lifetime radiation levels as simulated for the ITk Pixel Detector: (a) shows the NIEL fluence and (b) the total ionising dose [41].

High Voltage CMOS (HV-CMOS) processes offer a possible solution by extending standard CMOS processes to allow low voltage electronics to be implemented on a substrate which is biased with high voltage. Typically this is realised by placing the low voltage electronics in deep implants which separate the circuitry from the high voltage in the bulk as sketched in Figure 3.13. Sensors built in such a technology can therefore host fast signal processing circuits while at the same time enduring bias voltages up to more than 160 V which enables a fast, drift-based charge collection.

Several use-cases as pixel detectors are possible for this technology ranging from a passive sensor which needs a dedicated readout chip to a so called Depleted MAPS (DMAPS), a fully monolithic device. A step in between is the hybrid active pixel sensor, which hosts certain signal processing electronics but still relies on a dedicated readout chip. These chips are used to investigate the capability of HV-CMOS sensors for the ATLAS detector without the overhead of a full-blown readout chip, allowing fast and comparably cheap prototyping. Additionally, low-cost interconnection techniques become available thanks to the on-sensor electronics. Sensors investigated in this work were entirely built as hybrid active sensors.

In contrast to classical sensors which rely on specialised processes, HV-CMOS is an industry standard process provided by a multitude of foundries and available for structure sizes down to 65 nm. The concepts and perspective of HV-CMOS will be discussed by way of example of the H18 process by the Austrian foundry ams AG [43] as this thesis concentrates on this technology. H18 is a 180 nm process implemented on low substrate resistivity p-type wafers ($\rho \sim 10\,\Omega\,\mathrm{cm}$). It introduces high voltage capabilities up to $\sim$160 V by means of a deep n-well for shielding the electronics and forming a charge

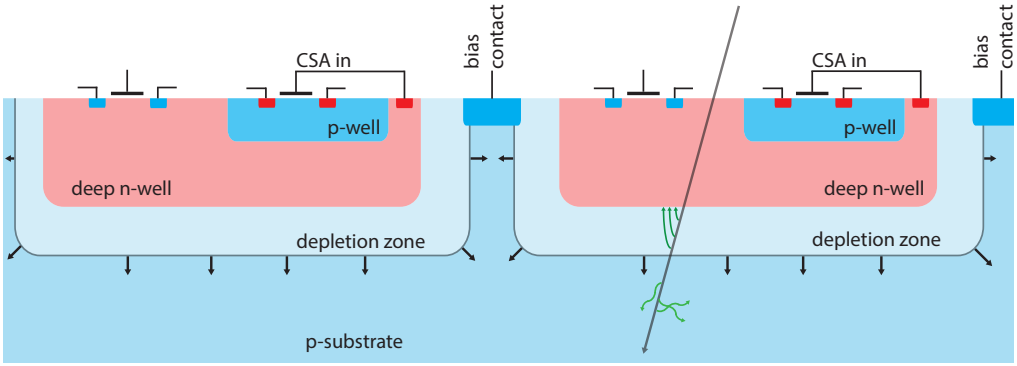

Figure 3.13: Simplified cross section of an HV-CMOS sensor. The highly sensitive depletion zone is growing from the deep n-well implants that shield the electronics sitting on the surface of the chip from the high voltage in the bulk [44].

collecting pn-junction. Thanks to the triple-well feature it allows implementing both NMOS and PMOS transistors in the n-well.

3.5.1 Sensor Properties

The potential of HV-CMOS sensors for their application in ATLAS relies on their ability to collect charge by drift, which depends highly on the size of the depleted zone. As this is proportional to the wafer resistivity, HV-CMOS sensors have intrinsically a smaller depletion zone compared to classical sensors which are built on high resisitivity ($\mathcal{O}(\mathrm{k\Omega\,cm})$) substrates. At full bias of 160 V this translates to a depleted depth of $\sim$10 to 20 µm in the H18 process, hence to a charge signal in the depletion zone of less than 1200 electron-hole pairs for Minimum Ionizing Particles (MIPs). This signal, being too low to be transmitted to an external readout chip[c], can nonetheless be amplified and processed by on-sensor electronics. The thin depletion zone on the other hand has the advantage of short collection times and helps disentangling tracks with shallow incidence angle like boosted jets.

In terms of radiation tolerance, the sensors profit from a drift based collection of electrons. Short collection times of well below 1 ns are expected which greatly counteracts charge trapping after high fluences of radiation. As the bulk material is of p-type, no type inversion can occur. Instead, the high initial doping concentration leads to the so-called acceptor removal effect which causes an increase of substrate resistivity with irradiation

[c] On the FE-I4, the minimum achievable threshold without sensor is around 700 e and with a bump-bonded sensor typically 1600 e is reached.

up to $5 \cdot 10^{15}\,\mathrm{n_{eq}/cm^2}$. The effect flattens out for high fluences and is counteracted by a slow acceptor introduction. Measurements however have shown that for $1 \cdot 10^{15}\,\mathrm{n_{eq}/cm^2}$, the target fluence of the outer layer of the ITk Pixel Detector, an 80 % higher signal amplitude compared to unirradiated sensors is to be expected, with still 90 % of the initial charge collected after $2 \cdot 10^{16}\,\mathrm{n_{eq}/cm^2}$ [45]. Also the tolerance against Total Ionizing Dose effects, which damage the on-chip circuitry, is expected to be high thanks to the small feature size, hence thin transistor gates, and the availability of advanced radiation hardening techniques like guard rings and enclosed transistors. Finally, the triple-well structure allows for implementing PMOS transistors which are intrinsically more radiation tolerant compared to NMOS ones.

Depending on the functionality necessary in the pixel cells, smaller pixel sizes can be achieved. A monolithic sensor in the ams 350 nm HV-CMOS process was implemented with $21 \times 21\,\mu\mathrm{m}^2$ sized pixels as a demonstrator for HEP applications [46]. Smaller pixel sizes lead to small electrode capacitances which translates to a better Signal to Noise ratio, benefiting especially low signal sensors like the HV-CMOS ones. In terms of tracking, they exhibit an improved single point resolution and a lower occupancy which is especially important for high pile-up environments like the ATLAS ITk. Furthermore, very small pixels permit a purely binary hit making where the consideration of the exact deposited charge would not contribute considerably to an improved resolution. This can be used to simplify the sensor design, the readout and the reconstruction process.

3.5.2 Implications on Module and Detector Construction

The availablity of on-chip electronics on a radiation hard sensor also impacts the possibilities for detector construction. Pixel cells can be designed with the exact amount of circuitry needed for their purpose: depending on the external readout scheme this might be only amplifiers, but can be extended by discriminators and further analogue and digital signal processing. For hybrid detectors this means that the output signal can be amplified large enough to allow to capacitively couple the sensor to the readout chip. The complex and costly hybridisation process by bump-bonding can therefore be replaced by a simpler scheme like gluing, where a thin glue layer acts as dielectric between the pixel signal pads of the sensor and the readout chip.

In contrast to classical sensors, the pixel size of HV-CMOS sensors is not limited by the pixel cell of the readout chip. Several small pixel cells can be connected to one readout pad and thanks to configurable outputs transmit the exact position of a hit in the group in their output signal. This can then be subsequently decoded by the readout chip and therefore increase granularity while keeping compatibility to other sensor technologies.

The discussed features of HV-CMOS sensors also have direct impact on the mate-

rial budget of a possible detector. As the depletion zone reaches only some 10 µm into the bulk, most of the detector material does not contribute to the charge collection and therefore can be thinned away. Prototype sensors for the CLIC experiment built in ams H18 technology have shown promising results after being thinned down to a thickness of 50 µm [47]. After irradiation, classical sensors like planar pixel devices need substrate biasing reaching 1000 V and beyond in order to deplete the bulk. Although n-in-p sensors and, after type inversion, also n-in-n sensors can be operated at lower voltages, the reduced depletion depth lowers the signal size which is especially critical with the onset of trapping. As leakage current scales with the size of the depleted volume, the full depletion of a planar sensor leads to an order of magnitude higher current compared to HV-CMOS sensors. The requirements for biasing and cooling services for HV-CMOS sensors are therefore relaxed. However, this has to be put into perspective with respect to the powering and I/O connections necessary for the signal processing circuitry on HV-CMOS sensors.

In general, being produced in single-sided processes, the interfaces of the sensor and readout chip face each other after hybridisation, complicating module assembly considerably. Industrial technologies like Through Silicon Vias would allow to bring the electrical interface of the readout chip to its back side providing a solution. The feasibility of such an approach and its implication on cost are currently under study.

The discussed advantages would be further augmented by a fully monolithic design which would also mitigate some of the identified issues. By eliminating the need for a dedicated readout chip and hybridisation, the material budget would be lowered and the module concepts greatly simplified. Also by unifying all electronics on one substrate, the circuitry can be optimised leading to lower power consumption and simpler, more lightweight services. On the other hand, designing a monolithic device for an environment like ATLAS is a challenging tasks due to tight constraints on timing, readout speed and power consumption. Especially fast digital circuitry tend to cross-talk into the analogue sensor part, introducing noise which has to be accounted for. First results on devices built in the ams H35 process for ATLAS ITk are promising [48] and sparked further research on DMAPS in ams H18 technology.

3.5.3 Conclusions

The HV-CMOS technology introduces novel concepts and opens an interesting perspective for usage in the ATLAS ITk upgrade. Drift based charge collection promises a fast and radiation tolerant detection up to ITk end-of-lifetime fluences. The possibility of on-sensor electronics enables cheap and simple hybridisation and the implementation of pixel geometries outside of limits given by the layout of the corresponding readout chip.

A reduced material budget, simpler module assembly and cost reduction is expected, which would be greatly enhanced by a possible implementation as a Depleted MAPS device.

As a new technology however, there is no previous experience in terms of large scale production, long term operation and stability. For hybrid detectors also new module concepts have to be developed, taking the electrical interfaces of two active devices into account. This might cancel out some of the expected simplification of detector construction and eventually cost reduction. Finally and more essentially, the sensors have to prove that they suffice to the ATLAS requirements for a pixel sensor in laboratory and beam based characterisations which is the subject of this thesis.

Chapter 4
The FE-I4 Beam Telescope Setup

Test beam experiments with charged particle tracking have proven an indispensable tool for detector characterisation. Although many parameters of a prototype can be assessed in a lab measurement, exposing a detector to a high energy particle beam simulates an environment close to operation in the actual experiment. These measurements take place in the secondary beam of synchrotrons like CERN SPS or DESY II which have a well known composition and energy. The beam lines are usually equipped with so called beam telescopes, providing trajectory measurements of the beam particles. Tracks are extrapolated to the prototype's position and projected on its plane, therefore by comparing the impact position on the prototype with its response, properties like detection efficiency, spatial resolution and timing can be assessed.

The following chapter elaborates on the construction and performance of a new beam telescope setup, based on the ATLAS IBL readout chip FE-I4. An overview of the detector planes, the Data Acquisition system and the integration of devices under test will be given, including the accompanying electrical, mechanical and monitoring services and their upgrades. The particle track reconstruction framework will be introduced, followed by a performance assessment of the telescopes tracking capabilities. This includes a discussion about the data taking rate with different configurations, the pointing resolution at the device under test and the suitability of the setup for various silicon detectors and beam conditions. This chapter follows in parts our publication in JINST [49].

4.1 The CERN SPS H8 Beam Line

The SPS, built in 1976 at CERN, is a 6912 m long synchrotron and the last accelerator in the injector chain to the LHC. It accelerates protons up to an energy of 450 GeV before delivering the beam to various experiments or the LHC. The SPS operates in pulsed mode where it is filled multiple times per minute, extracting its beams towards different experiments and experimental areas one at a time. Such a scheme of fills and extractions is called supercycle and lasts between half a minute and a minute, before being repeated. An example can be found in Figure 4.1.

The CERN North Area Experimental Hall houses several beam lines which are served by the SPS. The 400 GeV primary proton beam is slowly extracted over 4.8 s on the 30 cm thick beryllium target T4 resulting in a secondary beam that consists mainly of attenuated protons from the primary beam, pions and electrons. Particle and momentum selection and further splitting up into various beam lines is achieved by wobbling (directing the primary beam at the target at different angles). For the measurements presented in this thesis, the H8 beam was set to deliver a π^+ beam with an energy of 180 GeV. It can be steered and tuned by the user by means of magnets and collimators. For small prototypes, a focused beam with a diameter of $< 5\,\mathrm{mm}_{1\sigma}$ can be set up to increase the particle rate in the region of interest.

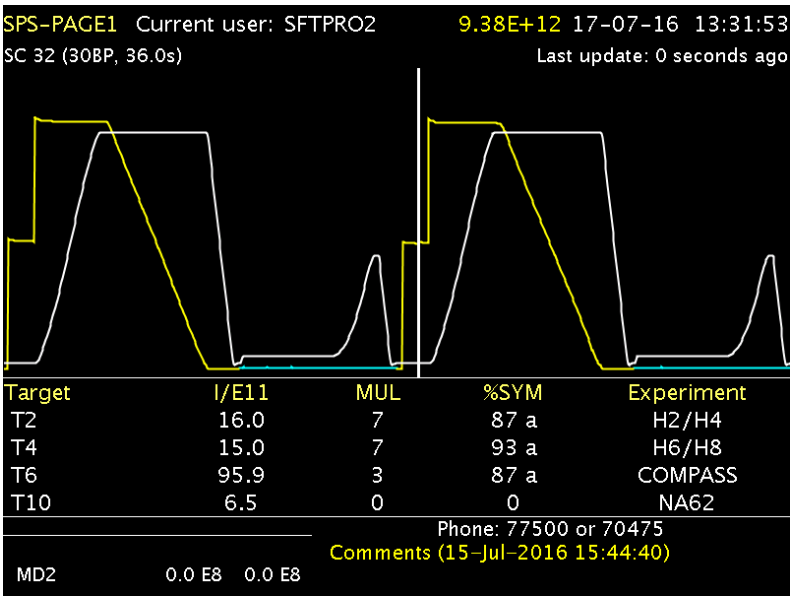

Figure 4.1: The SPS supercycle overview page (Vistar) showing a typical operation mode of the SPS with two fills and slow extractions towards the test beam areas. The yellow/blue line shows the beam intensity in the accelerator and the white one the magnet current or beam energy.

4.2 The FE-I4 Telescope

R&D for ATLAS ITk pixel sensors is currently performed on the FE-I4 readout ASIC which was mainly used for building the ATLAS Insertable B-Layer (see Chapter 3.3) [24]. The availability of hybrid pixel detector modules from the IBL construction allowed the development of a beam telescope. It is designed as a fully synchronised system for fast data taking (trigger rates of several kHz) with prototypes as small as few mm^2.

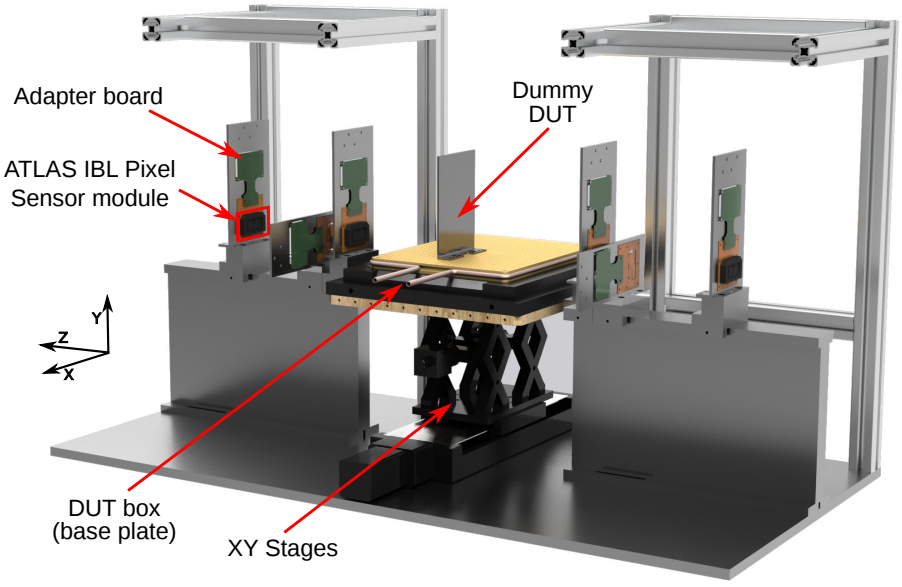

Figure 4.2: 3D image of the FE-I4 telescope

The FE-I4 telescope is a modular setup comprising two arms, each equipped with three detector planes, between which a box with detector prototypes is mounted on XY-stages for positioning in the beam. A movable half height rack hosts the DAQ, power supply, control and monitoring systems which will be described in the following sections. The setup is complemented by a silicon oil chiller for cooling the Devices Under Test (DUTs). The arms are implemented as rails on which detectors can be mounted on cars, allowing for easy positioning in the beam.

4.2.1 The Telescope Planes

All six planes of the telescope use IBL Double Chip modules as detectors with a Module Adapter PCB as interface to the DAQ system, both mounted on an aluminium frame which slides on one of the telescope arms as shown in Figure 4.3.

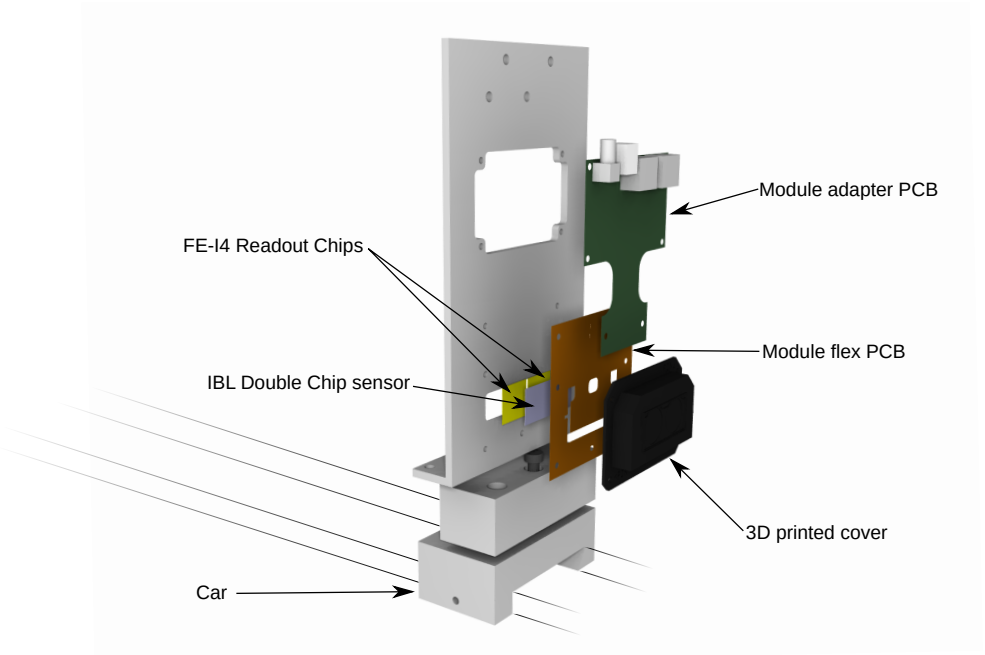

Figure 4.3: 3D Rendering of a telescope plane showing the different mechanical and electrical components

The aluminium frame is an L-shaped bracket with a $62 \times 14\,\mathrm{mm}^2$ sized opening at the position of the sensor. In order to minimise multiple scattering on the supporting material only two thin blades reach below the edges of the detectors as support. This in turn means that the thermal load of the FE-I4 has to be fully diverted on the periphery of the chips. The mounting profits from the good thermal conductivity of silicon and the fact that the heat is mostly generated at the FE-I4 Low Drop-Out Regulators (LDOs) which are located at the periphery. A finite element simulation in which the FE-I4 was modelled as a block of silicon with a heat generator of $0.8\,\mathrm{W/FE}$ close to the periphery validated the design. At an ambient temperature of 25 °C and in thermal equilibrium the FE-I4 stayed below 30 °C as shown in Figure 4.4, thus in a safe region for operation.

Each 200 µm thick n^+-in-n planar pixel sensor comprises 160×336 pixels with a pixel pitch of $250 \times 50\,\mu\mathrm{m}^2$, except for the central and outermost columns. As Double Chip modules, every sensor is read out by two Front-Ends bonded to it and placed as closely as possible to each other. However, as the FEs have an inactive edge and cannot be positioned touching each other, a 205 µm gap emerges. The central column pixels are therefore prolonged to 450 µm to bridge this gap. Equally, to keep the inactive area low at the edges of the module in the long pixel direction, the outermost pixels are 500 µm

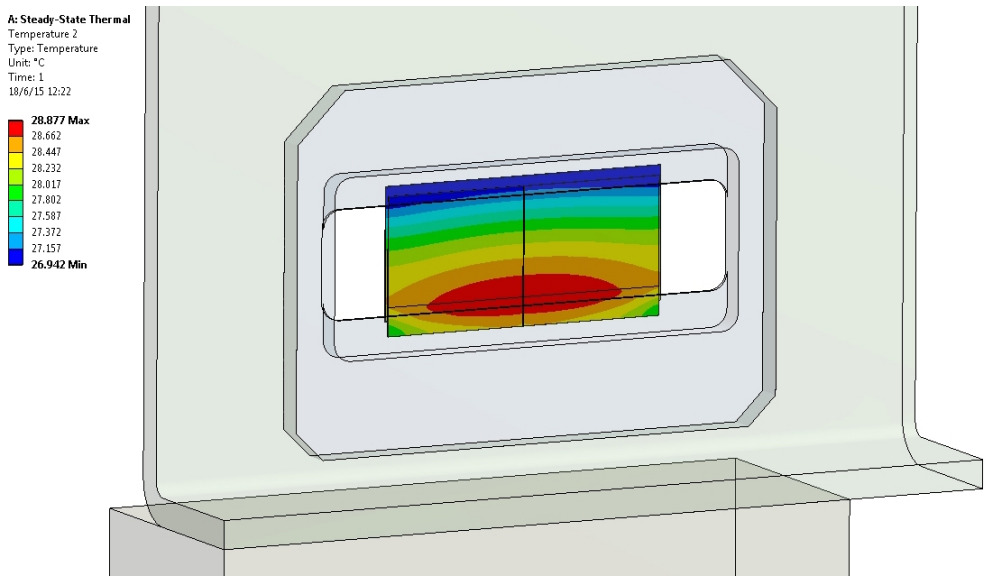

Figure 4.4: Finite element simulation of a telescope plane with two active Front-Ends, each dissipating 0.8 W, and an ambient temperature of 25 °C. The graphic shows the temperature distribution over the detector which is thermally connected to the aluminium support frame [50].

long and reach below the guard rings. For detector operation a higher noise output for these pixels has to be taken into account. To avoid these noise based effects and coping with the different geometry during reconstruction, the outermost columns of the FE are deactivated during data taking at the expense of $\sim$4 % of the telescope's acceptance.

In order to achieve a comparable spatial resolution in horizontal as vertical direction, despite the oblong shape of the pixels, every middle plane of the telescope arms is rotated by 90° around the beam axis. This in turn means that the overlap of the telescope planes along the beam is defined by the short side of the sensor in both dimensions which reduces the acceptance of the telescope to approximately the size of one Front-End. Therefore only one FE per plane is activated during data taking, but the mechanics allow for quickly changing to the other chip in case of failure.

The IBL Double Chip modules are loaded with a flexible PCB (module flex) which provides access to the bias wirebond pad of the sensor and the FE-I4 powering and I/O pads by means of a 50 pin PCB-to-PCB connector. An additional Module Adapter PCB acts as breakout board providing standard Molex Mini-Fit series, LEMO type 00 and RJ45 connectors for attaching the plane to power supplies and the DAQ system.

4.2.2 The Data Acquisition System

The Data Acquisition (DAQ) is a modification of the readout system developed for qualification tests of the IBL. It is based on the HSIO/RCE system, designed by SLAC[a]. The general layout is sketched in Fig. 4.5. It comprises the High-Speed Input Output (HSIO) FPGA board, the Reconfigurable Cluster Elements (RCEs) and the ATLAS Trigger and Data Acquisition (TDAQ) framework running on a dedicated PC.

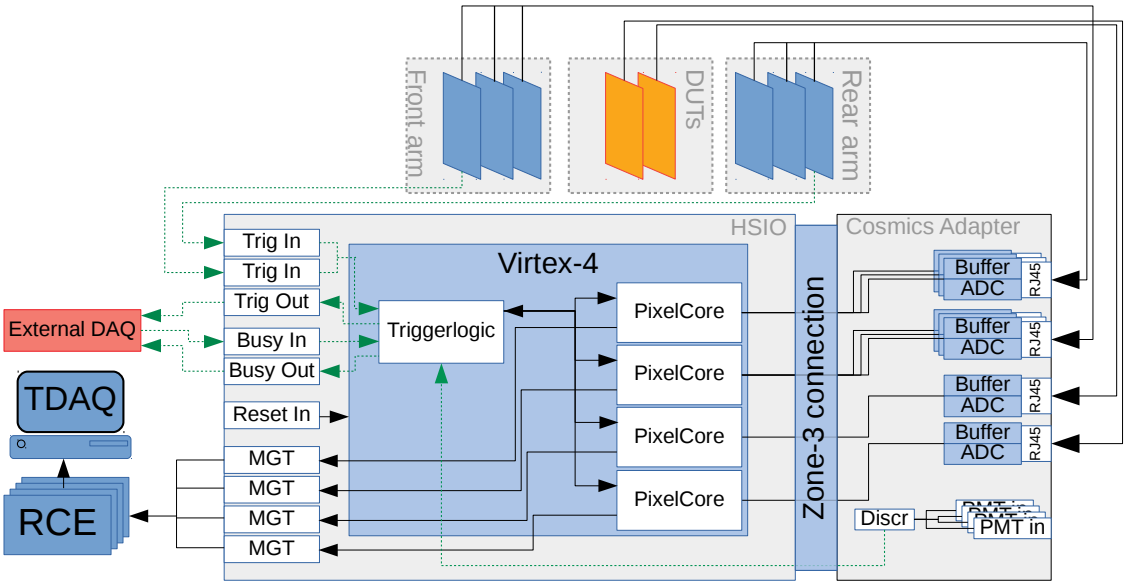

Figure 4.5: Structure of the telescope DAQ system. Shown are the data and trigger (green dashed lines) connections between the detectors, the low level (HSIO) and high level (RCE, PC) readout system.

The HSIO is a custom-made FPGA board, based on the Xilinx Virtex-4 integrated circuit. As a general-purpose readout board, it hosts a large number of I/O channels and communicates with up to four RCEs via optical links. It implements the low level communication to the detector Front-Ends and the evaluation of trigger signals from various sources. In case of the FE-I4 telescope, the HSIO is used in conjunction with the CosmicBoard, a custom made PCB that interfaces the HSIO via an ACTA Zone-3 connector. This board hosts LVDS buffers and connectors for up to 16 Front-Ends. Four discriminator signals, which are served by LEMO inputs can be used for triggering readout via external detectors like scintillators. Each Front-End connection (RJ-45

[a]Stanford Linear ACellerator Laboratory

socket) comprises the buffered Clock (CLK) and Command (CMD) output; and a data input line. An analogue input line, connected to on board Analogue to Digital Converters (ADCs) allows reading out temperature sensors on the detectors. In the following, the joint HSIO/CosmicBoard will be simply referred to as HSIO.

Its FPGA is partitioned into several modules allowing to adapt to different scenarios in a convenient way. The main ones are the *PixelCore* and *TriggerLogic*. The PixelCore hosts the necessary logic to communicate with the FE-I4 Readout Chip (ROC) using its custom protocol, to ensure data integrity via 8bit/10bit encoding and to buffer and send out the data stream to the RCE unit. Each RCE is served by one instance of the PixelCore which in turn can handle multiple FEs. Thanks to that scheme, the size of the system is only limited by the space on the FPGA and the configured size of the per-Front-End FIFOs. Load balancing is achieved by splitting the connected FEs into up to four PixelCores - the number of Multi-Gigabit Transceivers (MGTs) being the limiting factor. As shown in Figure 4.5, the splitting can be inhomogeneous in order to account for different readout modes of the FEs and in general one would choose the balancing according to the amount of data that has to be sent to and processed by the RCEs per trigger. Finally, the PixelCore modules act as interface between the RCEs and the TriggerLogic module, allowing to reconfigure the triggering scheme on-the-fly.

The Reconfigurable Cluster Element is a generic computational unit based on a 350 MHz PowerPC System On Chip (SOC). It runs a RTEMS Real-Time kernel as operating system. Software packages, which define the actual tasks of the system, are uploaded as part of the boot-up procedure. An RCE can handle up to 24 high-speed serial I/O lanes at speeds up to more than 40 Gb/s. Four RCEs share the workload of reading out the six telescope planes and up to two DUTs. One RCE is assigned to each triple of telescope modules and each of the DUTs. This scheme (3:3:1:1) proved most efficient as the DUTs are usually operated with a four times wider readout window compared to the telescope planes and as they are more likely to be noisy, a higher data output from the FEs is expected.

The DAQ PC is a standard x86 64 bit computer, running the ATLAS TDAQ [51] system for communication and data handling on a Scientific Linux OS version 6. A modular, custom-made software, built on top of the framework implements a user-friendly control and configuration interface. The software communicates via the Common Object Request Broker Architecture (CORBA) over Ethernet with the RCEs. Each action on the Front-End is implemented as a scan. The software sends scan configurations to the RCEs which then prepare the needed data interpretation infrastructure and Front-End commands and relay these to the HSIO. The user can operate the system in calibration mode via the CalibGui (see Figure 4.6a) or in data taking mode via the CosmicGui (see Figure 4.6b). In both cases the user has to provide human-readable detector configura-

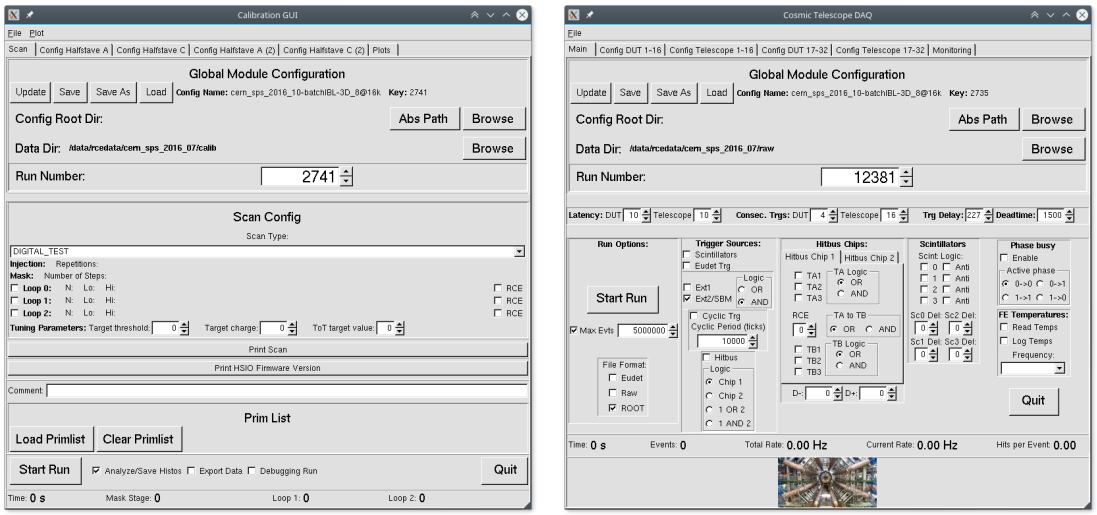

(a) **(b)**

Figure 4.6: The two user interfaces of the RCE system: (a) CalibGui for detector calibration and (b) CosmicGui for data acquisition.

tion files which contain all settings for the registers of the given detector and can freely assign the configuration to one of the readout links of the attached RCEs.

With the CalibGui, the user can run the full calibration and validation of the FE-I4 including basic functional tests of the analogue and digital parts of the pixel cells, threshold and ToT response equalisation and self-triggered data taking. A batch mode via primitive lists (each scan or change of setting is considered a primitive action) allows for automated tests. The scan result can immediately be evaluated from ROOT histograms.

The CosmicGui enables the user to set the detectors in data taking mode and adjust parameters like readout window sizes, delays and an artificial dead time which ensures that the DAQ was given enough time to receive all FE data. Here also the trigger scheme is set, which comprises several inputs that can be combined using logic operators:

- **HSIO:** Digital input lines (LEMO), which can be used individually or combined via AND or OR operators. Usually this input is used to read out the HitOR signal of one or two Front-Ends.
- **Cyclic trigger:** Issues a trigger signal every $n \times 25\,\text{ns}$. Mainly for debugging purposes.
- **Scintillators:** Uses the up to four scintillator inputs on the CosmicBoard. Each input delay can be set individually and all channels can be used as trigger veto.

The Eudet and Hitbus trigger are meant for other detector systems and will not be considered here.

4.2.3 Integration of Devices Under Test

The current reference readout chip for the ATLAS Pixel community is the FE-I4 chip. Therefore also CMOS Pixel prototypes are usually characterised with this chip and as the telescope is to be used mainly for these devices it was designed accordingly. The integration of DUTs in this case is straight-forward as they can be considered as additional telescope planes, thus being in principle transparent to the DAQ. In usual telescope operation, the telescope planes are well characterised and tuned, so they can be operated as one unit. The DUTs however may have different characteristics and require different delay settings and readout windows than the telescope planes. Therefore, the DAQ was extended to allow for these parameters to be set independently for telescope planes and DUTs.

The readout for non-FE-I4 DUTs (so called "external" DUTs) is not implemented in the telescope DAQ. These devices have to bring their own control and readout system and can synchronise their data stream to the telescope via the two schemes sketched in Figure 4.7. A basic requirement, however, is that data can be assigned to a trigger signal.

In the first scheme (*Trigger/Busy scheme*) the telescope processes its trigger inputs independently from the external device and sends out a TTL or CMOS trigger signal to the external DUT. The DUT DAQ then raises a busy signal, that halts the consideration of further triggers by the telescope while it reads out the DUT. It has to ensure that all incoming triggers are accepted and processed in order for the events to be synchronised.

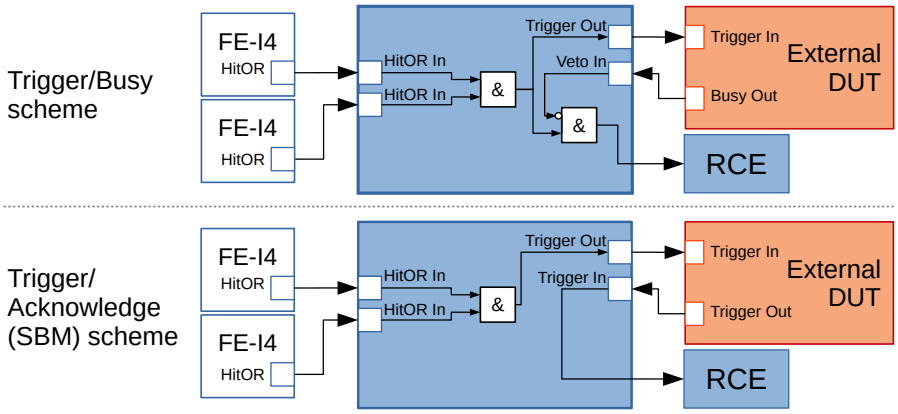

Figure 4.7: Trigger schemes for non-FE-I4 (external) DUTs ensuring synchronised data streams which can be merged off-line for analysis [49].

The second scheme (*Trigger/Acknowledge scheme*) is needed in case the DUT is incapable of delivering a busy signal or does not reliably accept triggers. Here, the HSIO evaluates its trigger inputs and in case the telescope DAQ is ready for a trigger and a signal arrives, it is sent out to the external DAQ without triggering the telescope readout. If the DUT accepts the trigger, it sends the signal back to the HSIO, triggering the telescope readout and starting its own. This is the more robust scheme, as it checks for both systems' readiness, before starting the readout.

4.2.4 Region of Interest Triggering

The FE-I4 telescope was primarily designed for measuring prototypes of very small sizes (few mm^2) compared to the telescope acceptance ($\sim 3\,cm^2$). Given a fairly uniform illumination of the telescope, only few percent of all recorded tracks would pass through the DUT. Although these tracks can be used to determine accurately the position of the telescope planes, most tracks will be discarded after the initial alignment, as they are irrelevant for the characterisation of the prototype. The FE-I4 chip offers a solution for this issue in form of the Hitbus or HitOR. As described in Section 3.2, the discriminator output of each pixel can be connected to a global bus which is accessible via a wirebond pad and can be used to trigger the readout of the whole telescope. The per pixel

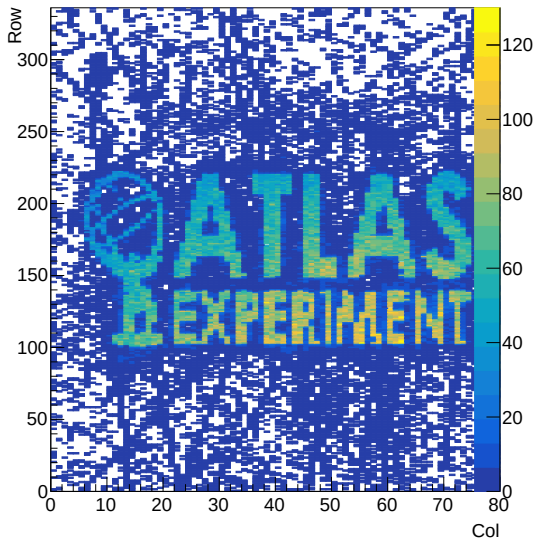

Figure 4.8: Hit map of the first telescope plane in a data set with a complex ROI mask derived from the logo of the ATLAS Experiment. The low occupancy background around the logo originates from delta electrons and nuclear interactions with the sensor.

configuration register holds a bit which defines if a particular pixel is connected to that bus allowing to restrict triggering to an arbitrary number of pixels. The Region Of Interest (ROI) is usually found either by triggering on the DUT and reading the mask from the hit occupancy map of the telescope trigger planes or by observing correlations of hit positions on the DUT and trigger planes. Usually rectangular shapes resembling the prototypes form the ROI, but arbitrary shapes are also possible as depicted in Figure 4.8.

4.2.5 Test Beam Timing

In an experiment like ATLAS with high multiplicity events, it is of great importance to assign the detected particles to the right bunch crossing, i.e. the time they pass the detector. As it is impossible to read out the whole pixel detector every bunch crossing due to the maximum trigger rate of the ROCs being in the order of 100 kHz, only hits, detected in the 25 ns time bin that is selected by the Level-1 trigger, are read out. This means that although the ROCs buffer all detected hits locally, the signal has to be generated and cross the discriminator threshold fast enough to be associated with the right bunch crossing. The performance of detectors is therefore estimated by the detection efficiency in one time bin or in-time efficiency.

The FE-I4 chip samples all pixel cells every 25 ns and stores hit information in buffers shared by four pixels. The hits are timestamped with the Bunch Crossing ID (BCID), which is a 10 bit counter, that is increased every clock cycle. A trigger or L1A, issued by the DAQ system, requests hit information for a certain BCID and the up to 15 following clock cycles. Internally this is translated into up to 16 consecutive triggers that are sent into the pixel matrix. Ideally, hits originating from a particle that triggered the readout of the detector, would occupy exactly one time bin[b], meaning that the delay between trigger and particle detection is fixed. In reality however, the distribution of delays called *LV1 distribution* is smeared like depicted in the left (grey) part in Figure 4.9 due to two effects

- Timewalk of the Front-End amplifier
- Arrival of particles asynchronous to the Front-End clock

The former is an intrinsic problem of CSAs, whose rise time is always dependant on the input charge. Especially for values close to the threshold, this effect is highly pronounced. The issue can be somewhat mitigated by a lower threshold or faster electronics, but this approach is limited by constraints on the maximally allowed power consumption and noise occupancy.

[b]The time when the signal crosses the discriminator threshold defines the timing of the particle.

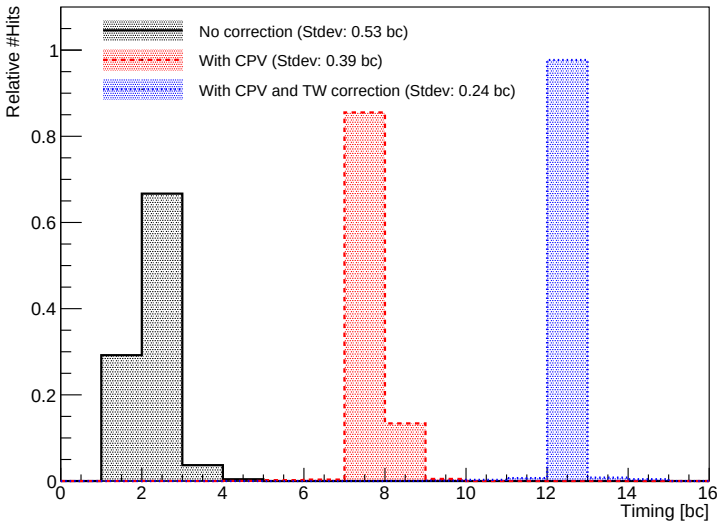

Figure 4.9: Hit timing of an FE-I4 plane in a non-synchronous beam in units of LHC bunch crossings (25 ns), without any correction, with the Clock-Phase Veto (CPV) and additionally with the FE-I4 Time-Walk (TW) correction. The three distributions were normalised and artificially shifted for visual clarity.

ATLAS requires a perfect in-time efficiency[c] which cannot be reached by the analogue part of the IBL modules. Therefore, a digital signal processing scheme was implemented in the Front-End. Most of the low signal hits originate from charge sharing. Here the particle traversed the pixel close to its boundaries, so that the induced charge is not completely collected by the hit pixel, but also by the neighbouring one. The distribution of charge depends on the hit position and the electric field configuration and can lead, in case of high asymmetry, to a pixel with high signal (big hit) and a neighbouring one with a signal close to the threshold (small hit). In that case it is likely that the small hit is detected one bunch crossing later than the big hit, which would lead to the loss of that hit if the Front-End is configured for only one consecutive trigger per L1A (usual detector operation). A deteriorated efficiency and wrongly reconstructed hit positions would be the result. In order to cope with that issue, the FE can be set to a mode where small hits, that are located next to a big hit and are registered in the next clock cycle after the big hit, will be moved into the timing bin of the big hit. This is a reasonable scheme, as the actual hit timing is much better provided by the big hit, which is less effected by time-walk. The effect of moving small hits, which have a ToT of one or two clock cycles, to the timing bin of the big hit can be seen in the second (red) and third (blue) distribution

[c] Hit detection efficiency restricted to 20 ns integration time

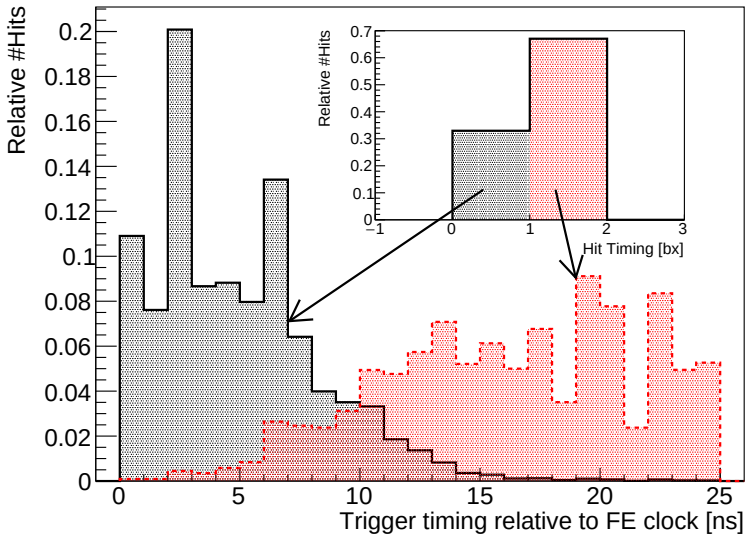

Figure 4.10: Time of arrival of a trigger/particle with respect to the FE-I4 clock for single hits. It shows that the asynchronous beam is the main effect for the smearing of the hit timing distribution.

in Figure 4.9. Small hits, which do not accompany a big hit, are discarded, which can lead to an artificially lowered overall efficiency of the sensor. In consequence the scheme is not applied to test beam measurements.

The time structure of the test beam poses another source of smearing of the timing distribution. In the LHC experiments, the FEs are driven by a clock which is synchronous to the particle collisions, meaning that the particles always arrive in a narrow interval around the same phase of the FE clock.The phase is tuned for most hits to be detected in one time bin.

The SPS secondary beam is not bunched, but continuous over the spill length of 4.8 s. As the particle detection is not locked to the clock phase of the FE, there is a fairly high probability that a particle will be detected in the time bin next to the actual time of arrival. Figure 4.10 shows that the smearing of the hit timing distribution originates from the different times of arrival of the particles with respect to the Front-End clock.

To counteract this effect a measure called Clock-Phase Veto (CPV) (alternatively Phase Busy) was implemented. The CPV is a system, that rejects all triggers, which arrive outside a given interval of the Front-End clock phase as shown in Figure 4.11. By this, an artificial bunching is achieved where the timing is known with a precision of 6.25, which is given by the 160 MHz system clock instead of 25 ns. The effect of the CPV, with and without the hit moving mechanism of the FE can be seen in Figure 4.9.

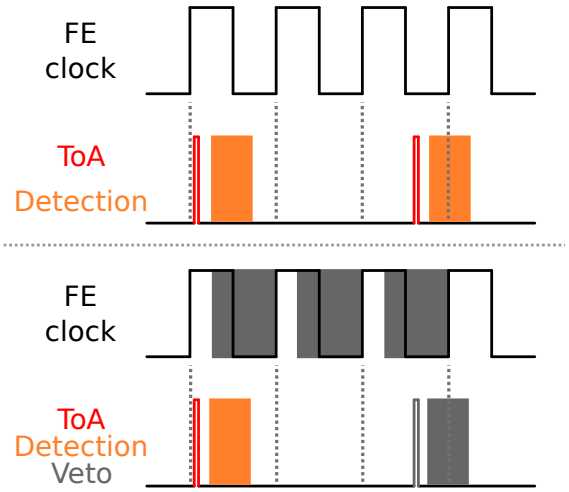

Figure 4.11: Schematic of the Clock-Phase Veto. Triggers from particles arriving late in the FE-I4 clock cycle are discarded, effectively restricting the time of detection close to the leading edge of the Front-End clock.

A disadvantage of this scheme is a reduced trigger rate as 75 % of the potential triggers will be discarded. However, as the dead time of the system is dominated by the readout of the FEs, only a reduction by around 50 % was observed.

4.3 Services and Detector Control System

Two mechanical structures, the telescope itself and a movable rack containing the DAQ and Detector Control System (DCS) form the test beam setup like sketched in Figure 4.12. The setup is based on a passive dampening table on which the two telescope arms, two linear stages and the DUT box are mounted. Each arm can be freely moved along the beam axis allowing to position the telescope planes as close as possible to the DUT box, independently of its size.

The DUT box is a styrofoam cube which encloses fully the DUTs to shield them thermally and optically. It is accurately positioned in the beam via two high-precision linear stages with a travel range of 110 mm in the vertical and 50 mm in the horizontal direction perpendicular to the beam. The stages are equipped with stepper motors which are controlled by an OES ALLEGRA-2-10-02 programmable control system driver. The driver allows for up to 256 micro-steps per motor step to increase the positioning resolution. With a typical setting of 10 micro-steps per step, the nominal positional accuracy is $\sim$2 µm. The stages are interlocked on both ends of the range by single-pole single-throw switches, preventing the carriages from hitting the mechanical limits of the stages.

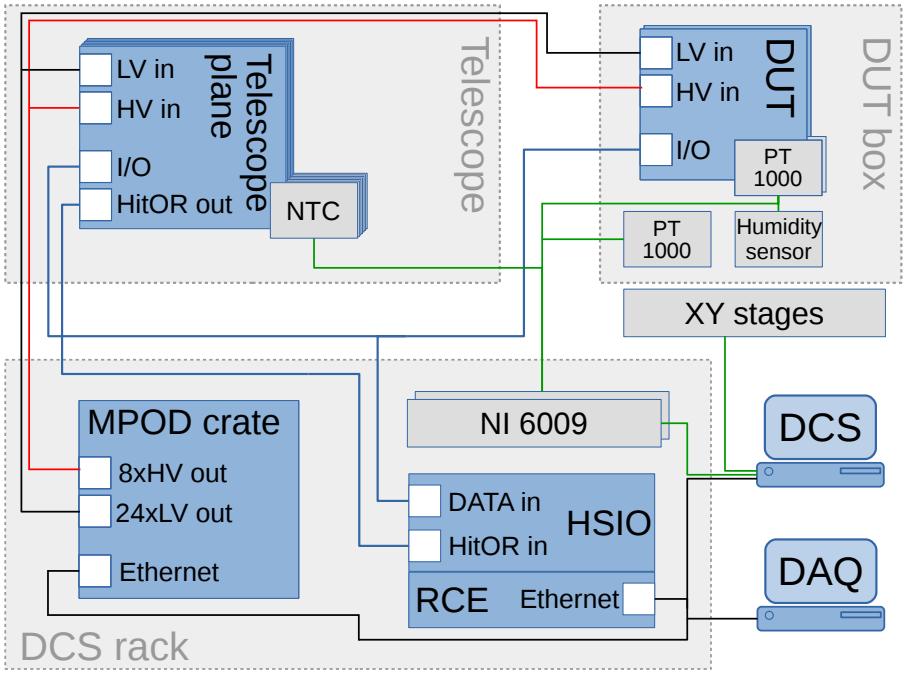

Figure 4.12: Schematic view of the telescope setup including the DCS system [49]

Power Supply

The telescope itself and especially the various DUTs need a variety of high and low voltages for operation. It was therefore decided to use a modular mixed Low Voltage (LV)/High Voltage (HV) system by WIENER. The MPOD mini-crate is a compact 19 ” chassis that is equipped with four power supply cards in the 6U Eurocard format: one ISEG EHS-8210n-F 1 kV HV module for biasing the telescope plane sensors and DUTs, two WIENER MPV 8008D LV modules for powering readout ASICs and supplying additional bias voltages up to 8 V and a WIENER MPV 8210D LV module that provides up to 120 V, which can be used for biasing of sensors like Silicon Photo-Multipliers (SiPMs) or LV powering. All channels have a floating ground and are monitored in terms of output voltage and current. HV channels are interfaced via built-in SHV BNC connectors, while each 4 LV channels share a 37-pin sub-D connector which additionally hosts sensing lines and an interlock loop. Finally, the modules are managed by an integrated crate-controller which can be accessed remotely via Ethernet, CAN bus or USB for monitoring and control, while an integrated LCD display and two rotary controls allow to manage the crate locally.

Cooling

The telescope planes themselves are operated without need of active cooling as shown in Chapter 4.2.1. DUTs are located in an insulated styrofoam box, which is kept at low humidity by means of a constant flow of cold nitrogen gas. Devices are mounted on a $30 \times 25\,\mathrm{cm}^2$ aluminium base-plate, holding a 1 cm pitched grid of M5 holes. The base plate is the interface between the chiller and the DUT. A copper pipe runs along the sides of the base plate which is connected to a HUBER UNISTAT 705 silicon oil chiller that reaches temperatures down to $-75\,^{\circ}\mathrm{C}$. It can be controlled locally by means of a touch screen or remotely via an RS-232/485 interface.

DUTs can be thermally coupled by direct contact to the base plate or by means of adhesive copper tapes that are clamped on the base plate. For further cooling or if a direct thermal contact to the base plate is not feasible, the nitrogen gas is cooled as well by being directed through a U-shaped chuck running another copper pipe around the edges of the plate. Figure 4.13 shows the open DUT box with the cooling system.

Temperatures of down to $-46.1\,^{\circ}\mathrm{C}$ on the baseplate, leading to the cooling of an FE-I4 based sensor to $-26.6\,^{\circ}\mathrm{C}$ have been reached. A study of the thermal properties of the box can be found in reference [52].

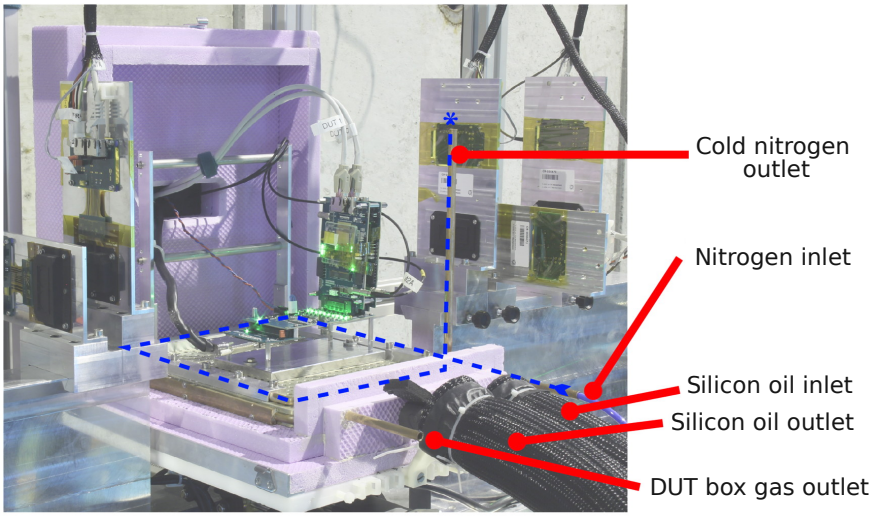

Figure 4.13: Picture of the open DUT box showing two mounted sensors and the base-plate and air cooling system [53].

Environmental Monitoring

Each flexible PCB, that is glued to the detectors of the telescope planes, is equipped with a Negative Temperature Coefficient (NTC) temperature sensor which is continuously

read out by a National Instruments (NI) USB-6009 OEM 14-bit Analogue to Digital Converter. A second NI device can be used to read out further temperature (NTC or PT1000) or humidity sensors. Typically, humidity sensors are placed close to the DUT in the box and recorded along with temperature sensors on the DUT, floating in the box, on the base plate and at the exit of the dry air pipe.

Slow Control Software

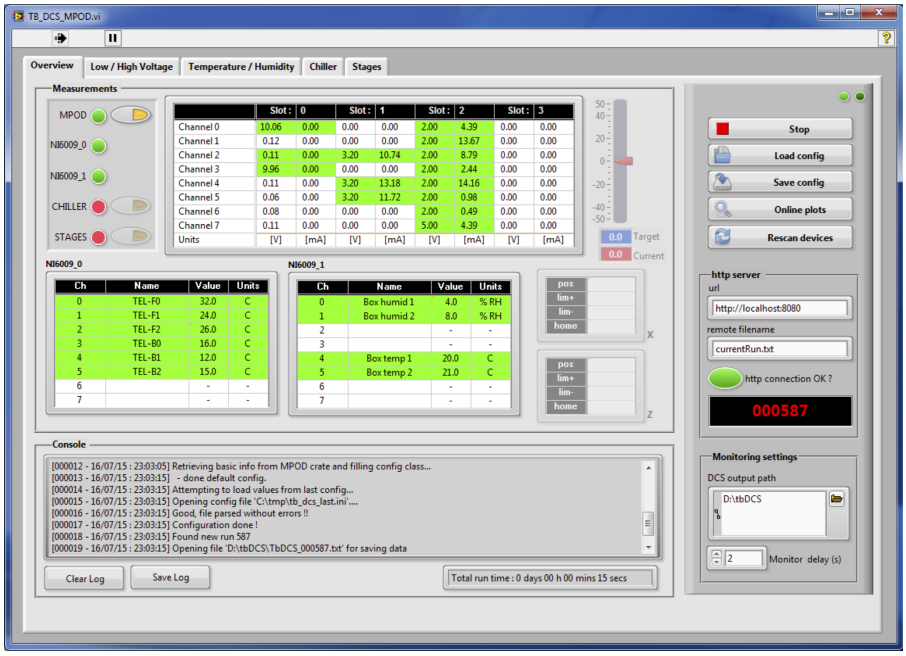

Figure 4.14: Graphical user interface of the slow control software. The screenshot shows the overview tab reporting about the connection of the various DCS devices, their current configuration state, current readout of environmental and electrical parameters, as well as the status of the logging and synchronization to the DAQ system [49].

A standard x86 Laptop acts as control for the MPOD crate, the linear stages and the chiller, while recording temperature and humidity data from the NI ADCs. The slow control software, as shown in Figure 4.14, has been implemented in the NI LabVIEW 2012 Development System. Upon startup, the various devices described above are probed and connected to the interface. An HTTP connection is established to the DAQ PC to obtain the current run number. The MPOD crate is accessed via SNMP, which gives full control of the crate via request packages. SNMP offers a notification mechanism called Traps, usually used for quickly informing about failure states. As the MPOD crate does not support Traps, a continuous polling has been implemented to promptly detect possible

failures, like tripped channels. Users have full control over the usually needed functions of the PS modules, including safety limits on and setting of currents, voltages and ramp speeds. Certain devices may require a defined power-up procedure which can be defined in the GUI. In so-called *Channel Sequences* single channels or groups are powered up or down in a given order with a user-defined delay. Channels of different modules can be mixed in any step of the sequence. The nominal state of the DCS (PS channel names, limits and nominal values, activated temperature sensors, set temperatures and channel-sequences) is stored in human readable configuration files. Finally, all read out values are saved to human readable space separated value files with a user defined delay (typically some seconds).

4.3.1 Data Taking Automation

Test beam campaigns usually contain scans over one or several parameters of the detector like bias voltages, threshold levels or other settings. This requires a frequent change and logging of settings between data taking runs which is usually performed by the operator. As most components of the telescope setup are connected via Ethernet, an automation scheme was implemented including logging and sending of alert messages in case of errors in the data taking. Figure 4.15 shows the control and data flow in the automated test beam runs, the core being a Python based scan supervisor which can communicate with all relevant components of the DAQ and DCS system. It runs a configurable scan loop that comprises the change and control of settings, running and monitoring the actual data taking, reporting to a log file and, upon finishing a parameter sweep, analysing the

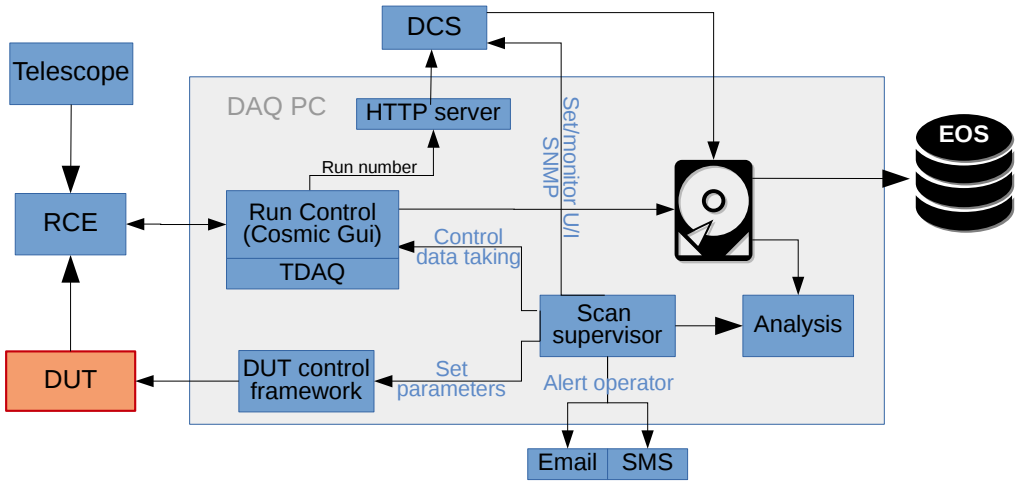

Figure 4.15: Scheme of the control and data streams in the automatic data taking with the FE-I4 telescope

collected data to provide a continuous data quality monitoring. On-DUT parameters are set by directly sending commands to the DUT controlling software framework while bias voltages provided by the Wiener crate are modified via SNMP[d]. Data is taken with the telescope specific DAQ system which is invoked in a sub shell and monitored by means of interpreting log files and exit codes. The gathering of statistics can be split up in multiple runs to minimise data loss due to failures. Upon finishing a run or at the occurrence of an error, the operator is informed by email and/or SMS and can react promptly. The system does not attempt to fix failure modes as it would add complexity to the system with the small benefit of decreasing the already low amount of intervention necessary by the operator. In fact, the system can be run several days with the operator merely performing monitoring tasks. All data is saved centrally on the DAQ PC and backed up in CERN's central storage EOS.

4.4 Track Reconstruction

Raw data from the telescope and DUTs are saved in ROOT files. For each trigger and each detector all hits that were recorded along with the timestamp and if available, information about the charge, are stored in ROOT TTrees. For an FE-I4 detector, this is the row and column position, the delay of the detection with respect to the trigger and the approximate deposited charge in ToT.

The raw data is handled by the Judith reconstruction software [54], which performs cleaning, track reconstruction and analysis. It is an object oriented framework written in C++, initially designed for telescopes based on the MIMOSA26 [55] sensor and later adapted to cope with FE-I4 modules. With the upcoming use of small size pixel detectors (O(few mm^2)) with unusual pixel geometries (see Chapter 5) the framework was increasingly modified, eventually leading to a fork called Proteus [56]. In the following, the workflow of the reconstruction frameworks, based on Judith will be described with selected developments towards Proteus pointed out. The usual workflow from raw data to results is shown in Figure 4.16.

Preprocessing

Detectors are rarely free of noise. Although sophisticated tuning procedures aim for a uniform and quiet detector, there are usually at least a few pixels which cannot be properly tuned. Especially after irradiation, detectors tend to display elevated noise levels. Such pixels are unsuited for characterization as they can disturb alignment and analysis

[d] Simple Network Management Protocol

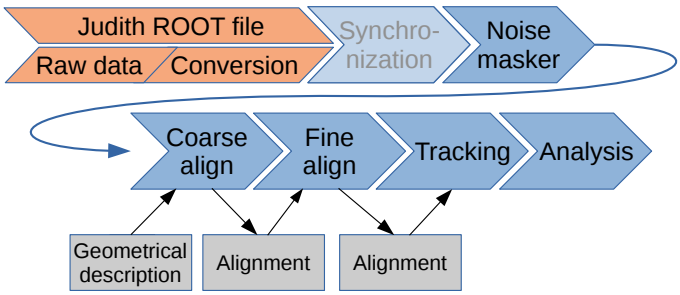

Figure 4.16: Analysis flow in the Judith reconstruction framework [49]

algorithms. Therefore the first step of the data handling is the identification and masking of such pixels.

Judith calculates per pixel occupancies and excludes from further analysis those pixels which exceed a user defined threshold (usually a hit frequency between $1 \cdot 10^{-5}$ to $1 \cdot 10^{-3}$ hits/pixel/event). This method is effective when the sensors are illuminated uniformly, but can be confused if e.g. a tight Region of Interest Trigger is used.

Proteus mitigates beam inhomogenity effects by calculating an expected local occupancy at position of the analysed pixel cell via a kernel density estimator. The pixel's occupancy is then stated as local significance which yields a robust variable for a cut.

Clustering

Particles traversing a detector plane can trigger more than one pixel by physically passing through multiple pixels and/or by charge sharing, forming a so called hit cluster. Pixels triggered by the same particle have to be identified in order to calculate the actual hit position. A recursive procedure starts with a random hit as seed of the cluster and adds all neighbouring hits to it. For each of the added hits the neighbours are added until no further hits in the vicinity of the cluster are found. A maximum distance for the next neighbour can be defined to cope with broken clusters, which occur when detector inefficiencies lead to missing hits.

For clusters consisting of more than one pixel, the actual hit position on the sensor has to be reconstructed. The basic method, called binary or digital hit making, is calculating the barycentre of the hits

$$p_{x,y} = \frac{1}{n} \sum_i p_i \tag{4.1}$$

For detectors which deliver information about the deposited charge q_i, like FE-I4 devices, this information can be taken as linear weight of hits, improving cluster position

estimates:

$$p_{x,y} = \frac{\sum_i q_i p_i}{\sum_i qi} \tag{4.2}$$

With good knowledge of the electric field in the detector, thus being able to model charge sharing between pixels accurately, a correction function can be defined which shifts the digital hit position depending on the fraction of charge collected by two neighbouring pixels. The so called η-correction [57] can yield an even more refined hit position compared to linear weighting. Due to the geometry of IBL sensors on the telescope planes, their operation above full depletion voltage, and the positioning perpendicular to the beam, only minimal charge sharing is observed. Therefore digital hit making was chosen as preferred algorithm.

Detector Alignment

For precise tracking of particles to the level of microns the exact position of detectors with respect to each other and the beam is paramount. Although the telescope mechanics and planes were manufactured with great care, a precision to such levels is not achievable for a system that shall be modifiable on the spot. DUTs are often assembled with even greater tolerances. A software based system to account for deviations from an optimal position is therefore needed.

The Judith and Proteus frameworks contain two processors for offline detector alignment. For a first coarse alignment 2D inter-plane hit correlation distributions are calculated. Given a mostly parallel beam and perfectly aligned detectors the correlation would form a straight line through origin with a slope equal to the ratio of the pixel pitches. Shifts perpendicular to the beam are reflected in the axis intercept while deviations from the calculated slope are directly proportional to rotations. In this step, only lateral shifts are corrected by calculating the mean of distances of the in-plane coordinates. For this scheme the first plane is defined as origin of a global coordinate system to which the position of the other planes is referenced. Planes are also only aligned to their direct upstream neighbour in order to minimise the effects of scattering.

The coarse alignment is usually sufficient to allow the generation of tracks. To further refine the alignment a fine tuning procedure based on unbiased residuals is performed. Residuals are defined as the difference of the reconstructed point of entry in a detector and the hit position calculated from a cluster that was associated to the track. By excluding the plane under consideration from tracking, unbiased residuals are obtained.

The Judith framework calculates the alignment constants by slicing the sensor under consideration along the X-axis and for each slice computing the unbiased residuals of all hits that fall into that interval as sketched in Figure 4.17. The mean and spread of

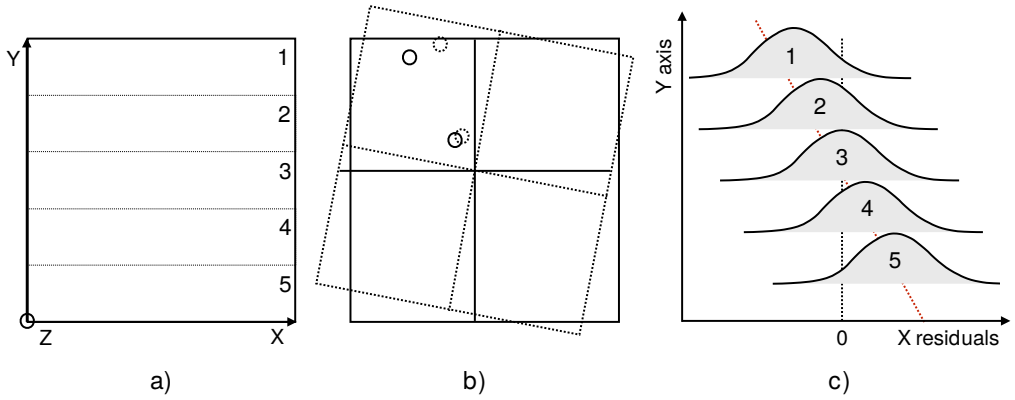

Figure 4.17: Schematic representation of the fine alignment procedure of Judith. a) The sensor is divided into a number of slices (here 5) b) shows the calculated and projected positions of the particles and the misalignment of the detector. c) shows the unbiased residual distributions for each slice versus their position on the sensor. By fitting a straight line through the mean positions of the distributions the angular and lateral displacement is calculated [50].

the displacement of the slice with respect to the track is obtained by fitting a Gaussian function to the distribution. A linear fit of the displacements with respect to their X-position yields the rotation along the Z-axis (slope) and shift (offset) of the plane.

Although the approach by Judith shows good results, it is sensitive to the choice of binning parameters and the beam profile. In the Proteus framework the calculation of alignment constants is performed by using the residuals on a track by track basis. Here the measured residuals ε_x and ε_y in the local coordinates of the plane are calculated by a projection of the displacement Δx, Δy and $\Delta\gamma$, the first two being the lateral displacement, the last one the rotation around the beam axis, on the reconstructed hit position (x,y):

$$\begin{pmatrix}\varepsilon_x\\ \varepsilon_y\end{pmatrix} = \begin{pmatrix}1 & 0 & -x\\ 0 & 1 & y\end{pmatrix} \cdot \begin{pmatrix}\Delta x\\ \Delta y\\ \Delta\gamma\end{pmatrix} \tag{4.3}$$

Rotations are described using the small angle approximation. The linear system of equations in eq. (4.3) is under-determined, but can be approximately solved by requiring a χ^2 minimization as:

$$\begin{aligned}\Delta x &\sim \varepsilon_x(1-x^2)+\varepsilon_y xy\\ \Delta y &\sim \varepsilon_y(1-y^2)+\varepsilon_x xy\\ \Delta\gamma &\sim \varepsilon_y x-\varepsilon_x y\end{aligned} \tag{4.4}$$

The so calculated displacement distribution should be centred around zero in case of a perfect alignment, so the mean of the displacements is the sought after alignment correction. To further stabilise the algorithm, a dampening factor (default being 0.8) is applied to the alignment correction. A progression of the alignment constants for a telescope plane over several iteration steps with 100000 events can be seen in Figure 4.18. Except for the initial overshoot of the first steps, all trends converge and after less than thirty steps a stable set of alignment constants is found.

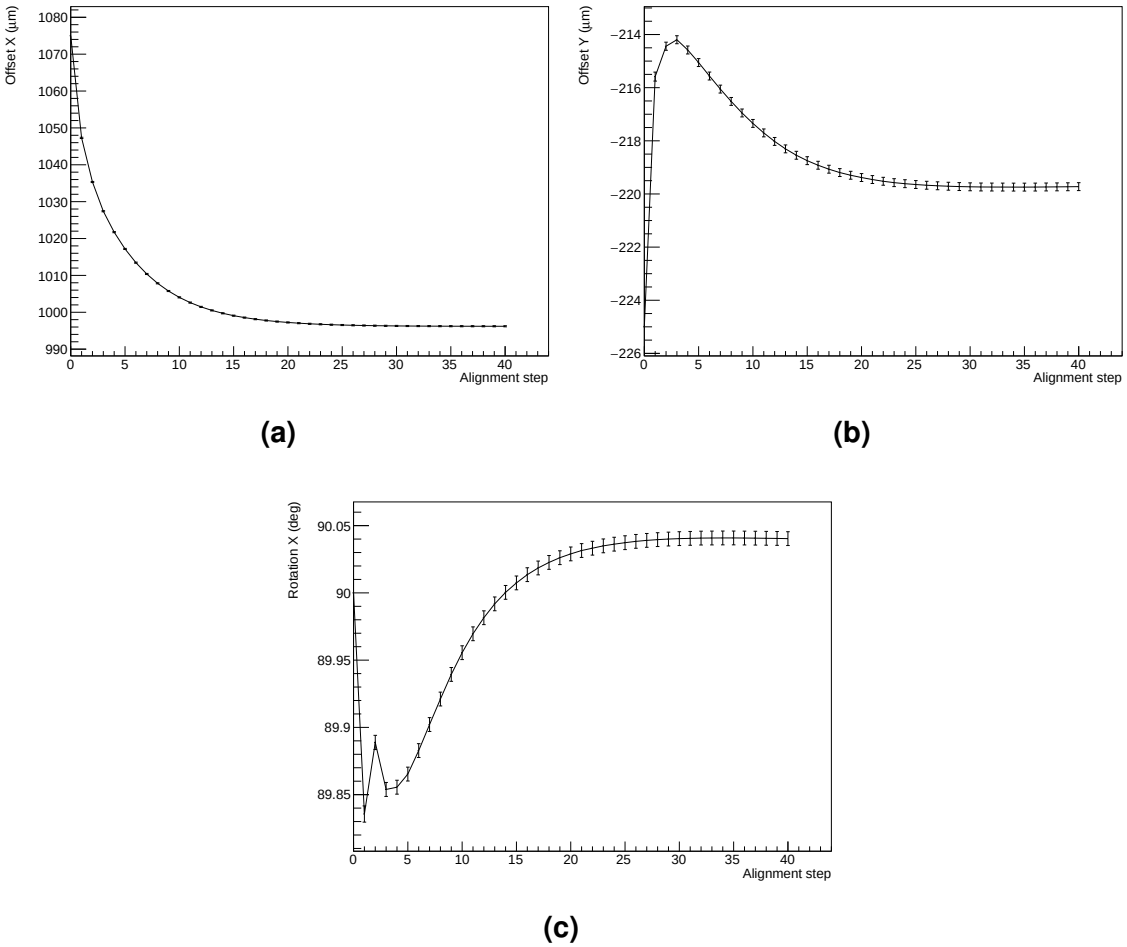

Figure 4.18: Example of a progression of the alignment constants over 40 steps of the fine alignment algorithm for the second telescope plane (the first one is fixed as reference). Shown are (a) the horizontal displacement, (b) the vertical displacement and (c) the rotation around the beam axis.

Track Finding and Fitting

Starting from a seed cluster, usually on the first plane, the track finding algorithm searches for associated clusters on consecutive planes. Assuming a mostly parallel beam, the search region is defined by projecting a cone starting at the last hit position with a user defined opening on the next plane as sketched in Figure 4.19.

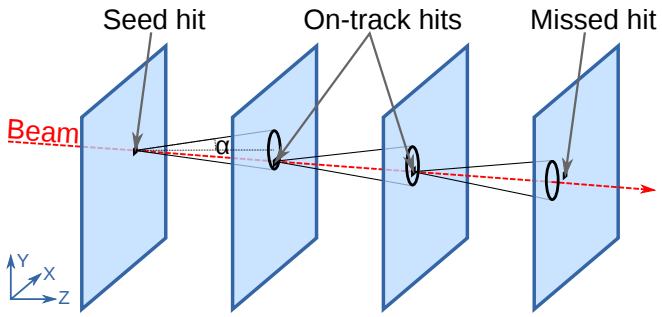

Figure 4.19: Diagram of the track finding algorithm of Judith showing the formation of a slightly inclined track with the initial assumption of a parallel beam

The opening angle has to account for multiple scattering and should be chosen depending on the conditions during data taking. While adding hits to the track, the beam angle is adapted. If multiple clusters are found within the search region, the track bifurcates and further searches continue in both directions. Candidate tracks containing the largest number of associated clusters are kept and after linear regression, the track with the least χ^2 is selected. Clusters which were associated to a track are excluded from further searches to prevent double usage. The algorithm handles data with large amounts of scattering well, given a low track density. In this case tracks are likely to be separated clearly, thus ambiguities of assignment of clusters to tracks are negligible. A χ^2 cut removes tracks which are highly disturbed due to scattering or nuclear interaction with the telescope material.

4.5 Performance of the FE-I4 Telescope

The FE-I4 telescope was designed to quickly gather data for small devices with high resolution. To assess the performance of the system, the telescope was tested in a high energy 180 GeV beam at CERN SPS. For comparison some measurements were also performed at a low energy (<10 GeV) beam at CERN PS. During these periods, full FE-I4 size as well as small scale DUTs were characterised and served as a benchmark.

4.5.1 Trigger Rate

The speed of the telescope has been assessed in operation with different readout parameters like number of DUTs or readout window widths.

A readout window of four bunch crossings or 100 ns length for the telescope was found to be sufficient to collect all hits despite the asynchronous beam and amplifier timewalks. In this setting, the telescope achieves a trigger rate of around 18 kHz which defines an upper limit for data taking independently of the DUT readout. A higher trigger rate would require the exclusion of telescope planes which in turn would reduce spatial resolution and should therefore be avoided.

Initially the telescope and DUTs were readout by only one RCE, leading to all data being sent over one link and processed serially by one computing unit. In order to increase the telescope performance the data streams were eventually split up into four groups, where each arm of the telescope and each DUT is read out by one RCE as described in Chapter 4.2.2. The effect of different numbers of telescope planes connected to the RCEs is summarised in Table 4.1. It becomes evident that splitting the data stream and sending it to multiple RCEs has a marginal effect ($\sim$2 %) on the trigger rate whereas adding planes to an RCE reduces the rate by $\sim$26 %. The rate is further limited by the RCE with the highest load which supports distributing it symmetrically between the computing units.

Table 4.1: Trigger rate of a telescope only readout with different number of planes included in the data stream. The values in the first state the number of telescope planes connected to the first and second RCE.

Readout configuration	1:0	2:0	3:0	1:1	1:2	2:2	1:3	2:3	3:3
Relative trigger rate (%)	100	74	55	98	71	71	56	56	55

The FE-I4 data output is organised in 24-bit words, framed by two 8-bit words that mark the beginning and end of the frame. There are several formats implemented depending on the mode of operation. In data taking mode a trigger is followed by a number of *Pixel Data* frames. These consist of

- **SOF:** 8-bit Start of Frame word
- **DH:** 24-bit Data Header word holding a magic number, the LV1ID and BCID
- **DR (multiple):** For each hit pixel a 24-bit Data Record with the pixel position and ToT code. In case of two pixels, next to each other in a column being hit, the ToT

codes of both, but only the position of the first pixel is stored, reducing the amount of transmitted data.

- **EOF:** 8-bit End of Frame word
- **SR:** In case of an error state, a Service Record is sent along with the data

This means that for any trigger, at least the SOF, DH and EOF are transmitted and have to be decoded by the receiving end. Figure 4.20 shows that the average number of hits in a telescope plane is around 1.44 (5 % of events with more than two hits) per event, which defines the actual payload of the telescope integrated over the readout window, or number of consecutive triggers per L1A. The payload to overhead ratio is therefore

$$\eta = \frac{\text{nHits} \cdot \text{DR}}{\text{SOF} + \text{EOF} + \text{nL1} \cdot \text{DH}} = \frac{\text{nHits} \cdot 24\,\text{bit}}{(8+8+\text{nL1} \cdot \text{DH})\text{bit}} \tag{4.5}$$

As discussed in Chapter 4.2.5 (Figure 4.9) and even without any corrections, all hits detected by the telescope can be recorded in four bunch crossings, therefore this was set as the default readout window leading to an overhead of 69 % compared to 91 % for a full readout of 16 bunch crossings.

When adding an FE-I4 based DUT to the readout with the full readout window of 16 bx (400 ns), the trigger rate still reaches up to $\sim$6 kHz. There is no drop in trigger rate when including a second DUT as the workload for two DUTs is distributed to two RCEs, while in the case of one DUT one RCE remains idle. Small devices cover only a fraction of the telescope's acceptance, hence without appropriate restriction of the trigger acceptance most recorded tracks ($\sim$98 % in case of a 3 mm^2 device) would not cross the DUT and, except for the initial software alignment of the telescope, would be of no use. This number can be greatly reduced to around 30 % by choosing a Region of Interest trigger window which encloses just the DUT with a small additional safety margin. The effects of the different DUT geometries and the ROI trigger are summarised in Table 4.2.

4.5.2 Influence of Hit Occupancy on Reconstruction

The FE-I4 ROC was designed with fast readout and high hit occupancies in mind. For an effective reconstruction – at least one track is found in $>$98 % of recorded events – tracks have to be unambiguously separable. As described in Section 4.4, the reconstruction framework is capable of coping with multiple tracks per event given they are not close to each other. Figure 4.20 shows the hit frequency per event and the number of clusters after processing. With a mostly uniform illumination of the sensor in the SPS H8 beam, a mean hit occupancy after clustering of 1.07 clusters/event and

Table 4.2: Trigger performance of the telescope setup for different configurations: standalone, with FE-I4 and small sized DUTs. The telescope planes readout window was fixed at 100 ns [49].

Number of DUT	DUT readout window	ROI trigger	Trigger rate [kHz]	Fraction of in-DUT tracks
none	/	no	18.3	
1 (3 mm^2)	400 ns	no	6.3	$\sim$1 %
1 (3 mm^2)	400 ns	yes	6.0	$\sim$70 %
1 (FE-I4 size)	200 ns	no	5.7	$>$90 %
2 (FE-I4 size + 3 mm^2)	400 ns	no	6.3	$>$90 % / $\sim$1 %

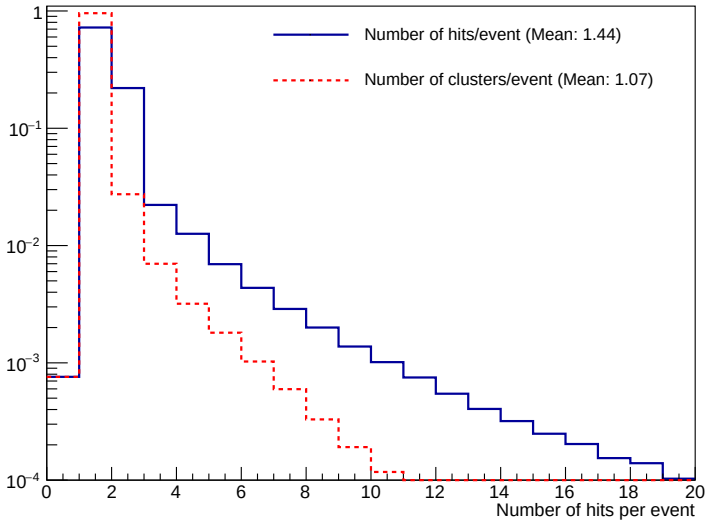

Figure 4.20: Raw number of hits per event for the last telescope plane (one of two trigger planes) and number of clusters after processing showing a mean occupancy of $<1 \cdot 10^{-4}$ hits/pixel/event.

$5.4 \cdot 10^{-5}$ hits/pixel/event was measured, therefore tracks originating from multiple particles are likely to be separable. The distribution however reveals, although suppressed, a tail towards high numbers of hits or clusters per event. Events with a high number of hits originate from delta electrons or nuclear interaction of the incoming particles with the sensor, where a nucleus is fragmented and successively deposits a large amount of

energy around its original position. Despite a high hit detection efficiency, parts of these long in-sensor tracks may remain undetected leading to discontinuous clusters which in turn will be considered as several individual ones. However, events with more than five hits account for only $\sim$2 % of the data set and large clusters are ignored in the track finding algorithm.

4.5.3 Pointing Resolution at the Device Under Test

In order to estimate the spatial resolution of the telescope, the errors of the track fit parameters are projected to the position of the DUT. For the following calculations, the telescope planes were oriented orthogonally to the beam direction according to Table 4.3.

Table 4.3: Positions of the telescope planes for the resolution measurement

Offset in beam direction (cm)	0.0	17.5	34.9	82.6	101.0	117.0
Rotation around beam axis (deg)	0	-90	0	0	+90	0
Rotation around vertical axis (deg)	0	0	0	180	180	180

As the hit position was calculated taking only binary information into account, only the position of the planes and the granularity of the sensors define the resolution of the telescope. The pointing resolution of the telescope is deduced from the errors of the track fit projected to the position of the DUT z:

$$\sigma^2(z) = \sigma_o^2 + z^2\sigma_s^2 + 2zC(o,s) \tag{4.6}$$

with σ_o being the uncertainty on the track's origin, σ_s the uncertainty on the track's slope and $C(o,s)$ the covariance between the track parameters. Although the tracking algorithms do not directly account for alignment imprecisions and multiple scattering, these uncertainties are present in the distribution of calculated hit positions and consequently absorbed in the fit parameter uncertainties. This leads to a pointing resolution at the centre of the telescope, the usual position of a DUT of

$$\sigma_{X,DUT} = 11.7\,\mu\text{m} \qquad \text{and} \qquad \sigma_{Y,DUT} = 8.3\,\mu\text{m}$$

These values were compared to the prediction of the analytical model for broken line fitting as introduced in reference [58]. It assumes a beam that is parallel and perpendicular to the sensors which themselves are thin compared to the distance between each other and takes into account multiple scattering in the detector material. For a given geometry

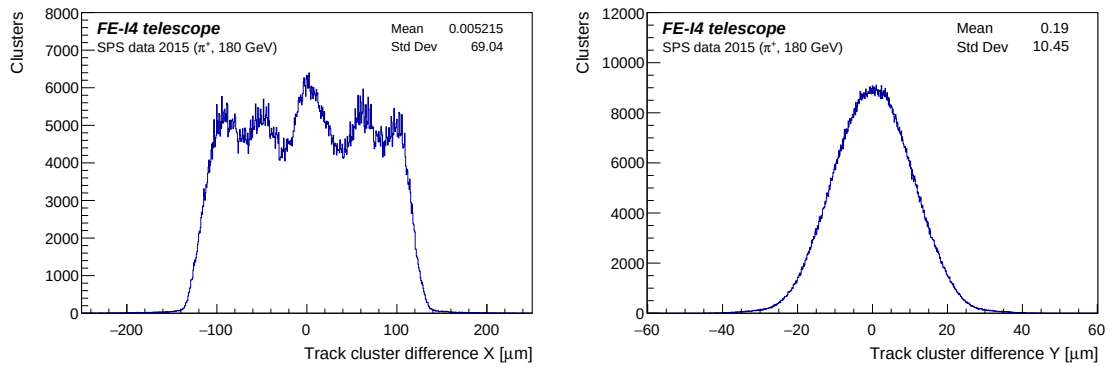

(a) **(b)**

Figure 4.21: Residual distribution in (a) X and (b) Y directions for the third telescope plane after alignment [49]

and material distribution, the model yields an analytical solution to the resolution at each position in the telescope. For the presented setup it predicts a value of 13.0 µm (horizontal) and 9.4 µm (vertical), which underestimates the telescopes performance by $\sim 12\,\%$. The reason for this discrepancy can be found in the resolution enhancing charge-sharing effect, which is not accounted for in the model and will be discussed now in the scope of the obtained residual distributions.

Figures 4.21a and 4.21b show the residual distributions (distance of the track projected on the plane and the calculated particle position from the hit cluster) for the telescope's innermost plane of the front arm, which is also closest to the DUT box, in the horizontal (X) and vertical (Y) directions. The vertical distribution follows the expected shape of the convolution of a uniform with a Gaussian distribution, with the Gaussian part clearly dominating due to the telescope's resolution and the small pixel size. The horizontal one follows the same pattern but shows a five peak structure. This is a geometric effect, as will be shown below, that results from the increased granularity given by the rotated middle planes of the telescope arms.

Both distributions are centred around zero with a standard deviation (SD) of $\sigma_{X,res} = 69.0\,\mu\text{m}$ and $\sigma_{Y,res} = 10.5\,\mu\text{m}$. In the case of binary hit making, the SD of the residual distribution is given by eq. 2.12. For an FE-I4 sensor with a pixel pitch of $250 \times 50\,\mu\text{m}^2$ this yields a single hit resolution of

$$\sigma_{X,single} = 72.2\,\mu\text{m} \qquad \text{and} \qquad \sigma_{Y,single} = 14.4\,\mu\text{m}$$

The calculated values, especially in the vertical direction, exceed considerably those measured. This is attributed to the charge sharing effect, which for the telescope sensors leads to around 20 % of clusters containing more than one hit as shown in Figure 4.22a.

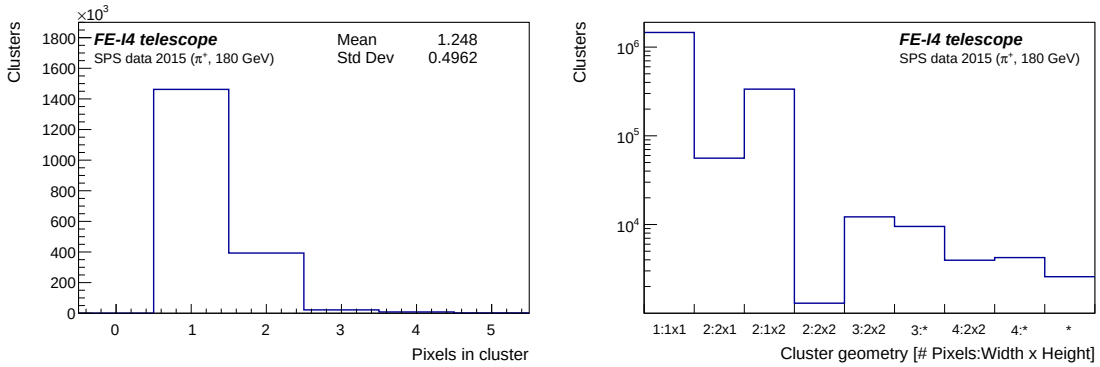

Figure 4.22: Distribution of (a) cluster sizes and (b) shapes of clusters for the third telescope plane. Cluster shapes, that are not explicitly listed for a given number of pixels, are merged in one bin, labelled with an asterisk [49].

The most-probable area for a particle to produce a one pixel cluster is smaller than the actual pixel size. This leads to a reduced effective pixel size, thus an increased resolution for single hit clusters, which is also reflected in the SD of their residual distributions $\sigma_{X,res,SP} = 70.2\,\mu\text{m}$ and $\sigma_{Y,res,SP} = 10.6\,\mu\text{m}$. The large signal produced by the planar sensors and low threshold of the ROC makes it improbable for a particle to fire less than two pixels when hitting within a zone of around 7 µm in X and 14 µm in Y around the perimeter of the pixels. This asymmetry can also be observed in the distribution of cluster geometries as shown in Figure 4.22b. Therefore the resolution of single sensors is overestimated and by this the given telescope resolution is merely an upper limit.

The Five Peaked Structure

To determine the origin of this effect, a simulation of the telescope was performed using the Geant4-based AllPix framework [59]. The model follows closely the active part of the FE-I4 telescope including two arms with three 200 µm thick FE-I4 sensors, the middle ones being rotated by 90°. All planes were perfectly aligned to each other and an 180 GeV π^+ beam was simulated without angular spread. The resulting data set was reconstructed like actual data using the Judith/Proteus software.

The resulting residual distribution in X direction as shown in Figure 4.23a shows five distinct and sharp peaks equally spaced over 250 µm, the pixel pitch in that direction. Due to the simplified model the result is lacking the effects from inefficiencies, misalignment and charge sharing which would lead to smearing of the peaks, eventually resulting in a

distribution similar to the one in Figure 4.21a. It shows however, that the observed effect is a purely geometrical one originating from the oblong shape of the FE-I4 pixels.

For simplicity, only single hit clusters and binary hit making are considered. Given a telescope geometry where all planes are oriented in the same direction, reconstructed particle tracks would follow exactly the centres of the hit pixels independently of the particle's position on the hit pixels as shown on the left hand side of Figure 4.23b. In that case the residual distribution would show a sharp peak centered at zero. By including the rotated telescope planes, granularity for tracking is increased by the aspect ratio of the pixels of $p_X/p_Y = 5$ in the X direction which allows to distinguish between tracks with a resolution of 50 µm as shown on the right hand side of Figure 4.23b. This leads to five possible track positions on the DUT, hence to the observed structure. In conclusion, this effect results from the finite resolution of the telescope and has, except from the unusual structuring of the residuals, no further consequence for tracking.

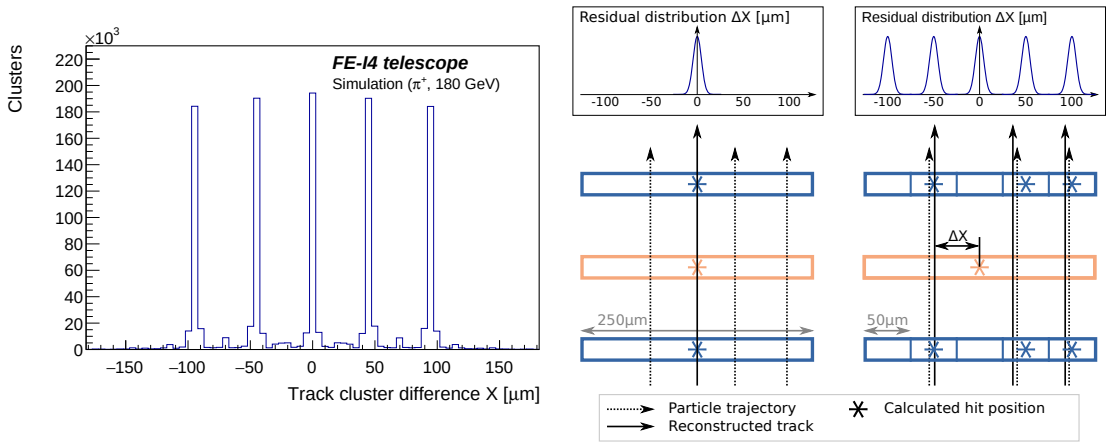

Figure 4.23: (a) Simulation of the residuals distribution for the third telescope plane in the X direction. All planes were perfectly aligned and no charge sharing between pixels was taken into account. (b) Schematic description of the origin of the five peaks structure in the residuals distribution. The blue boxes represent pixels of tracking planes, while the orange box stands for a pixel of the DUT. The residual distribution is calculated as the distance between the reconstructed track position and the calculated hit position on the sensor [49].

Material Budget

Compared to detectors in monolithic technology, the IBL modules have a considerable material budget which comprises 350 µm of silicon, a 100 µm thick aluminium holding structure at the edges of the detectors and ABS covers to shield the detectors from the environment. Therefore the multiple scattering effect was estimated by simulating the interaction of a 180 GeV π^+ beam with the telescope planes using the AllPix framework. The simulated geometry comprises six planes of the telescope and a seventh identical plane placed as DUT in the centre of the structure. A scattering angle of 14.8 mrad (6.6 mrad per plane) was calculated, leading to a deflection of $\sim$12 µm for a configuration with a total length of the telescope of 80 cm. For comparison the calculation was repeated excluding the outermost planes resulting in a total scattering angle of 14.7 mrad, which is comparable with the six planes setup. The resolution in this setup however is decreased by 1 µm in the X and 3 µm in the Y direction therefore nullifying any positive effect of the reduced material budget.

During commissioning of the telescope, some data was taken in the $\sim$10 GeV beam of the PS T9 beam line. A qualitative estimate of the telescopes performance in such conditions as compared to the SPS H8 beam can be obtained from the correlation between the hit pixel positions on the first and last telescope planes as they can be seen in Fig. 4.24.

It becomes immediately evident that the telescope's resolution is highly dominated by multiple scattering on its planes which would increase further by introducing a DUT and the surrounding box. For such a scenario advanced fitting methods like the General

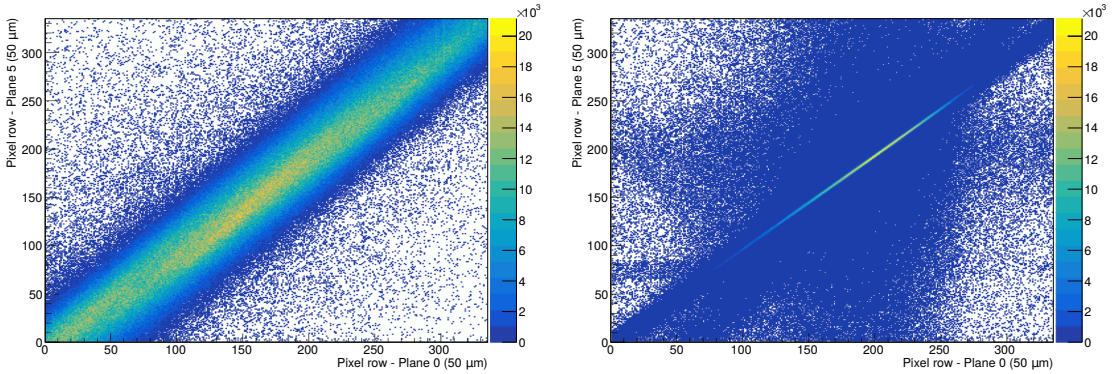

Figure 4.24: Hit positions of the first vs. last telescope planes showing the correlation between the two coordinates in (a) the 10 GeV beam of the PS T9 and (b) the 180 GeV beam of the SPS H8 beam line.

Broken Line fitter [60] could yield reliable results. However, the FE-I4 telescope was designed for a high energy beam and should be used in such in order to reach its full potential.

4.6 Summary

The FE-I4 Telescope, a setup with six IBL Double Chip modules at its core, was constructed in 2014 and since then successfully operated at CERN's PS T9 and SPS H8 beam lines and since 2017 also at the Fermilab Test Beam Facility, USA. It records tracks with a rate of around 18 kHz in stand alone mode and 6 kHz with up to two, FE-I4 based DUTs. The telescope was designed towards high energy beams like the SPS H8 180 GeV pion beam for which it reaches a resolution better than 11.7 µm and 8.3 µm in the X/Y plane at the DUT position.

As a fully integrated system it provides infrastructure for a variety of devices including LV and HV power supplies, temperature control and a remote and precise positioning of the DUT via an XY stage. All services are remotely manageable by the user with many parameters being accessible through a Python API providing a high level of automatisation including a preliminary data analysis. In case of very small devices, the Region Of Interest trigger yields a speed-up of data taking by a factor of over 30 compared to triggering on the full telescope acceptance. As the telescope is used in a non-bunched beam, the Clock-Phase Veto triggering scheme was developed to mitigate the effects of particles arriving non-synchronous to the readout clock, hence emulating an environment closer to the LHC experiments and allowing for a finer hit timing measurement.

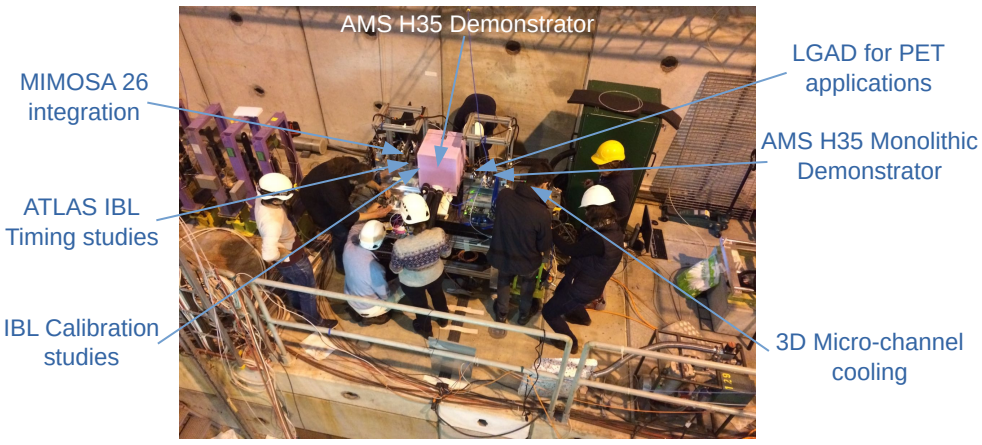

Figure 4.25: Photo of the telescope setup being in use by seven experiments in parallel

The track reconstruction and data analysis software Proteus (former Judith) has been developed towards FE-I4 based devices like the HV2FEI4 sensors, but has also already been used for applications with different readout systems like the TowerJazz Investigator [61]. Being open source, with a clear structure and support by the main developers and the community, Proteus is constantly evolving and expanding towards new devices.

The telescope enabled testing of various detectors, ranging from small and full size FE-I4 based sensors [62, 63] to strip modules and pad detectors [64]. Figure 4.25 shows the telescope being prepared for measurements with several FE-I4 and non-FE-I4 based devices. As a semi-permanent installation of a highly integrated system, the telescope setup is available to support detector development at the CERN SPS beam lines while remaining portable enough to be used in other facilities like Fermilab during a shutdown of the CERN accelerators.

Chapter 5

Active Hybrid Pixel Sensors in ams HV-CMOS Technology

Depleted active hybrid pixel sensors in CMOS technology are under investigation by several groups in the ATLAS collaboration ranging from passive sensors up to fully integrated Monolithic Active Pixel Sensors (MAPS). A general introduction and the prospects of CMOS sensors for ATLAS was given in Chapter 3.5. Technologies from three foundries were identified as candidates for a possible sensor implementation: ams AG [65], LFoundry [66] and TowerJazz [67]. In all technologies multiple prototypes were implemented to assess their suitability as pixel sensors for the ATLAS Inner Tracker (ITk) project. This thesis focuses on those in the 180 nm High Voltage CMOS (HV-CMOS) process H18 by ams AG.

The following chapter will introduce a possible implementation of active pixel sensors built in the H18 process as hybrid detectors. The design of the sensor including its analogue signal processing, supporting electronics and electrical interface will be given along with the specifics of the detector versions implemented in this framework. For detector characterisation and calibration, test benches and new parameter tuning procedures were developed and will be discussed. Finally, irradiation campaigns with x-rays, protons and neutrons will be presented and the effect on the sensor electronics assessed, while Chapter 6 will focus on the impact on particle detection.

The ams H18 process [43], formerly called IBM CMOS 7H, was co-developed by ams and IBM [68]. Being a High Voltage CMOS process, it allows combining electronics with operational voltages ranging from 1.8 V to 50 V (with extensions well above 100 V) by shielding low voltage electronics in deep n-wells. The process offers a maximum reticle size of $\sim 2 \times 2\,\mathrm{cm}^2$ implemented on p-doped wafers with a resistivity in the order of $10\,\Omega\,\mathrm{cm}$. Apart from the development for the ATLAS ITk, HV-CMOS sensors in this process are candidates for the tracking detectors of the μ3e (MuPix) and CLIC (C3PD) experiments [69, 70].

While the MuPix chip was designed with a full readout forming a MAPS from the start, the ATLAS development initially targeted at a hybrid detector where the fast digital electronics remains on a dedicated readout chip to which the sensor provides a discrim-

inated signal per pixel. A possible implementation is sketched in Figure 5.1. Prototypes in the early R&D phase were therefore designed to act as a drop-in replacement for the baseline passive sensors in Planar Pixel or 3D technology, hence relying on a readout by the ATLAS FE-I4 Readout Chip (ROC)[a]. Small scale prototypes, implementing various pixel designs, were produced in multi-project wafer runs in a search for a radiation tolerant, efficient and fast detector. These sensors were connected capacitively to the FE-I4 by gluing which omitted the complex and costly bump-bonding process and allowed to build a large number of samples in-house. Multiple versions of these sensors, called HV2FEI4, were characterised in terms of radiation tolerance, hit detection efficiency and timing.

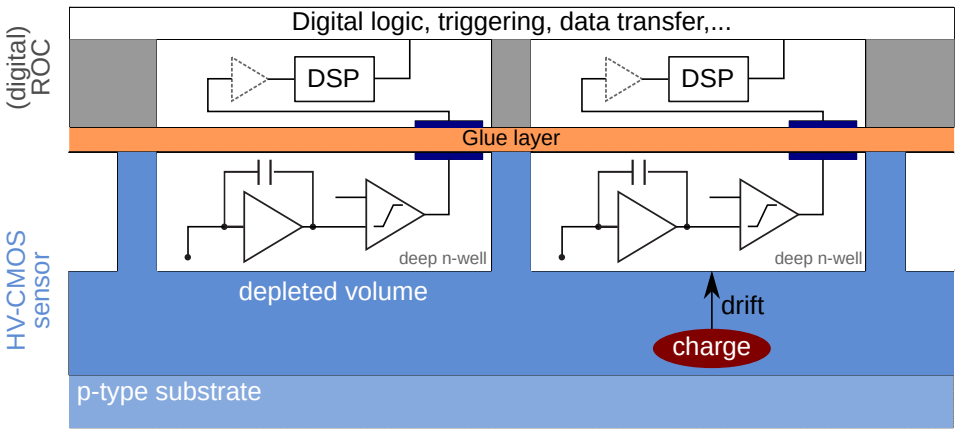

Figure 5.1: Sketch of an HV-CMOS hybrid detector with the sensor capacitively coupled to a readout chip (ROC). The sensor contains the anlogue processing chain implemented in the pixel deep n-well which acts as collecting electrode. Digital Signal Processing (DSP), higher level data handling and the interface to the trigger and DAQ systems is left to a dedicated chip.

5.1 HV2FEI4 - ams H18 Prototypes for the FE-I4 Readout Chip

The HV2FEI4 prototypes were designed around the specifications of the FE-I4 Readout Chip. The core functional block is the active pixel matrix, which hosts one or multiple flavours of active pixel cells, the main differences being the per-pixel signal processing

[a]The FE-I4 chip is described in detail in Section 3.2

electronics and the geometry of the readout electrodes. As the pixel cells are meant to act as individual units and be mostly transparent to the FE-I4, which expects an array of diodes at its inputs, the matrix is referred to as Smart Diode Array (SDA). The pixel circuitry is configured by a variety of bias signals and electronic switches. Bias voltages and currents are mostly provided by configurable on-chip generators with a few required to be supplied externally. Pixel by pixel settings, stored in memory cells throughout the matrix, allow to adapt to various use cases like a readout by the FE-I4 or calibration in stand-alone mode.

In the following, the general sensor design based on the HV2FEI4 version 2 prototype will be introduced. The HV2FEI4 version 2, as shown in Figure 5.2a, is a $4.4 \times 2.2\,\mathrm{mm}^2$ prototype hosting 1440 pixel cells, organised in 60 columns and 24 rows. With a size of $33 \times 125\,\mu\mathrm{m}^2$ the pixels are considerably smaller than the $250 \times 50\,\mu\mathrm{m}^2$ readout cells of FE-I4. In order to match the FE-I4 footprint the pixel matrix is divided into unit cells of six sensor pixels (two rows and three columns) of which three always share a Front-End readout channel as shown in Figure 5.2b.

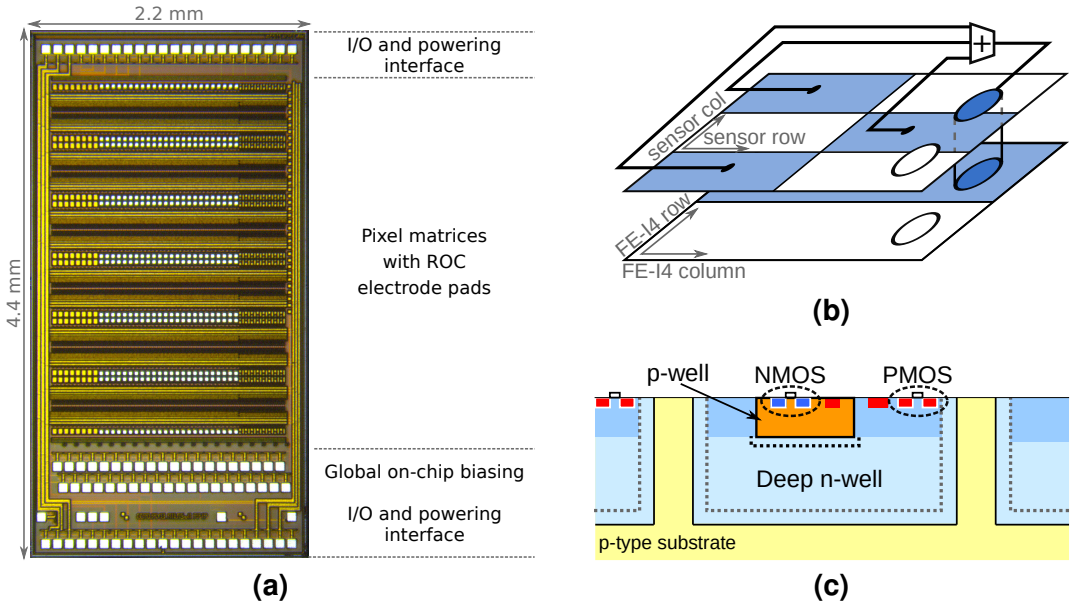

Figure 5.2: (a) Overview of an HV2FEI4 version 2 prototype chip. (b) Sketch of the multiplexing of an HV2FEI4 unit cell to two FE-I4 readout cells. The signals of three HV2FEI4 pixels are summed up and delivered to one readout pad. (c) Implant structure in the ams H18 process.

As with the other prototype versions, multiple flavours of pixel designs are implemented in this chip: the *Partially Radiation Hard* (main matrix), the *Fully Radiation Hard* and the *Simple Pixels*. The following descriptions are based on the Partially Radiation Hard matrix and other flavours will be discussed in the prototype overview in Section 5.1.5.

5.1.1 Smart Diode Array

In the ams H18 small scale prototypes, the pixels of the Smart Diode Array (SDA) contain a small amount of signal processing in form of an amplification and discrimination circuit. The circuitry for a pixel is placed inside a deep n-well which is processed on the p-doped substrate, thus forming the charge collecting pn-junction while shielding the circuitry from the high bias voltages of typically >80 V. Thanks to the tripple-well feature of the H18 process, additional large p-wells can be placed inside the deep n-well as shown in Figure 5.2c. This allows NMOS transistors in addition to PMOS transistors to be implemented on the same pixel.

Per pixel signal processing comprises a Charge Sensitive Amplifier (CSA), an RC-CR (low-pass/high-pass) filter, a discriminator and an output stage. Figure 5.3 shows the simplified schematics of a single pixel cell for the first two versions of the HV2FEI4 prototypes.

The first signal processing stage comprises the charge sensitive amplifier which is capacitively coupled to the charge collecting deep n-well. To provide a defined potential for the circuitry, the n-well it is connected via a transistor to the analogue supply voltage, which also acts as a slow drain for the collected charge that is reaching the amplifier. The amplifier is implemented with a non-linear feedback to ensure a nearly constant discharge of the integrating capacitor.

High frequency noise is filtered by a non-linear low-pass element, implemented as a source follower, before a capacitor decouples the amplification from the discrimination stage. Combined with an externally provided voltage, this establishes a well defined baseline level for the discriminator on top of which the amplified signal is added.

The discrimination stage is implemented only with NMOS transistors as they reside in an additional p-well. This shields against crosstalk of the fast digital switching in the comparator to the deep n-well. The comparator threshold is set by an external voltage which is fed through a transistor acting as adjustable resistor. Processing imperfections, leading to a slightly different behaviour of each pixel, can be mitigated by means of an additional 4-bit per pixel Digital to Analogue Converter (TDAC). It generates a current through the adjustable resistor that reduces the effective threshold.

The discriminated signal triggers the output stage which generates a current pulse

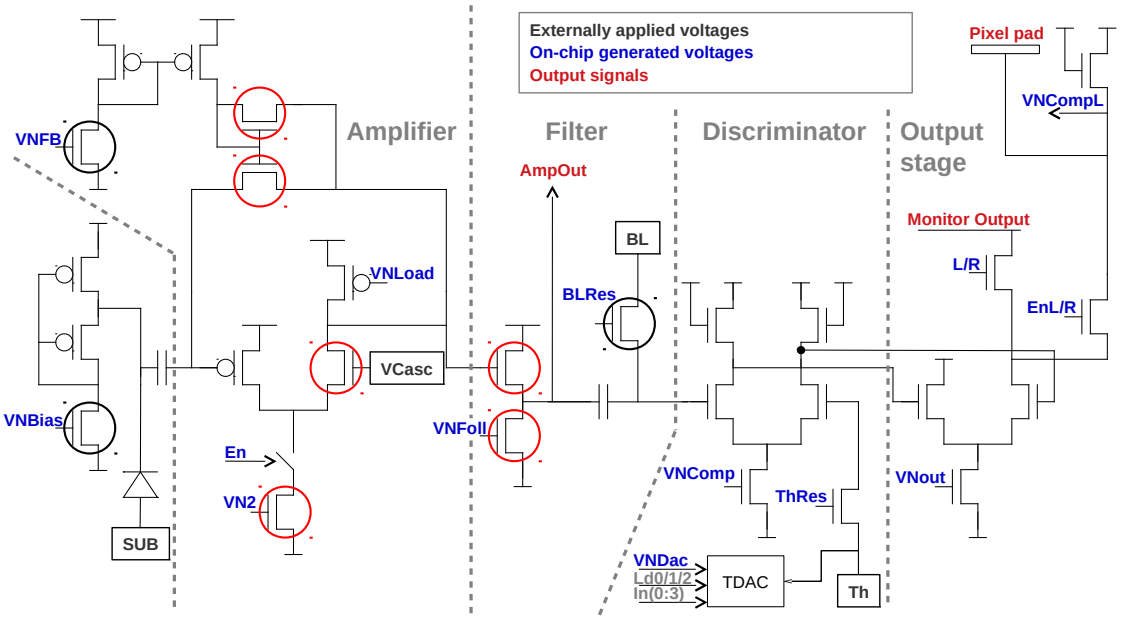

Figure 5.3: Simplified schematic of the main pixel cell for the first two HV2FEI4 versions. The black circles mark transistors which were linear in the initial design, but have been replaced by enclosed ones in the second version. In the *fully radiation hard* pixel matrix of version two also the red circled transistors are enclosed [71].

with an amplitude defined by a global setting and which is coupled to the readout chip for further processing.

Each pixel is surrounded by a metal trace connected to the substrate bias voltage. As the substrate resistivity is low ($\mathcal{O}(10\,\Omega\,\mathrm{cm})$), the potential spreads through the bulk and reaches well below the deep n-well, enlarging the charge collecting depletion zone.

The low resistivity of the substrate also leads to low signal sizes, for Minimum Ionizing Particles (MIPs) of less than 1200 e, an order of magnitude smaller than those of an IBL planar pixel sensor. As the signal amplitude on the amplifier is anti-proportional to the capacitance of the collecting electrode, a small pixel size is preferable. Therefore a size of $125 \times 33\,\mu\mathrm{m}^2$ was chosen for the HV2FEI4 sensors which is smaller than the FE-I4 pitch of $250 \times 50\,\mu\mathrm{m}^2$. To be compatible with the readout chip, two triples of sensor pixels are connected to two readout channels of the FE-I4 forming a $250 \times 100\,\mu\mathrm{m}^2$ unit cell, each readout channel receiving the summed signal of the triple. For each pixel of a triple, the output pulse amplitude can be selected by a global setting. Combined with the FE-I4's capability of recording the signal charge (in form of a Time over Thresh-

old (ToT)[b]) the hit pixels can be distinguished.

The HV2FEI4 pixels (or sub-pixels as seen by the FE-I4) were initially ordered in a chessboard pattern like shown in Figure 5.2b, minimising charge sharing between sub-pixels of one readout electrode in order to facilitate distinguishing the hit pixels on the FE-I4. This so called sub-pixel encoding feature was not used in this thesis and all pixel outputs were kept at the same value. An in-depth discussion about decoding the sub-pixel hit position with the FE-I4 can be found in a dedicated publication [72].

Additionally, test pulses can be injected into every pixel and their response observed on a global monitor line for calibration and testing. Some pixels in the lowermost row also implement an output after the source follower which is globally buffered and allows accessing the amplified analogue signal.

5.1.2 Bias and Configuration Circuitry

The HV2FEI4 sensors are configurable on a per-chip and per-pixel level by setting switches or modifying the working points of transistors by applying bias voltages.

For global biasing, a block of 6-bit Digital to Analogue Converters (DACs) is placed at the chip's periphery providing voltages and currents for the several stages in the pixel cells, the most important being listed with their default values in Table 5.1. They allow to shape the amplifier signal by setting its gain, feedback current and the bias of the source-follower. The speed of the comparator and the dynamic range of the threshold correction are also defined by dedicated DACs, as are the output levels of sub-pixels, connected to one readout channel.

The configuration of the pixel matrix is set by means of a column and row register with unit cell granularity that are daisy-chained into a long unit. Configurable parameters and their functions are listed in Table 5.2. As the register contains one set of parameters per column and one per row, the majority of parameters are shared by the unit-cells of one column or row. This has implications on the possible combination of configuration settings.

In general, the register allows to define which pixel cells, respectively their amplifiers, are activated in a unit cell via enable bits and which discriminator outputs are connected to the global monitoring bus. However, as the enable bits are stored globally per row, the masking of one potentially misbehaving pixel cell is not possible as it would deactivate all corresponding sub-pixels in the unit cells of the same row. A similar situation arises for the global monitoring bits, which are only defined in the column register. For calibration and testing however, single pixels can be addressed by connecting exactly one

[b] See Section 3.2

column to the global monitoring bus and enabling one pixel cell of one row. This also prevents disturbing effects from crosstalk during calibration.

Discriminator threshold levels are defined globally by an external voltage and can be corrected for local variances by means of a pixel per pixel DAC. Their settings are saved for each pixel in a Random Access Memory (RAM) that can be programmed by the column-row register. In order to keep the register compact, only the setting for two pixels per row can be manipulated at a time, so for each column the configuration has to be sent separately.

For calibration and debugging, the analogue outputs of a row of pixels can be connected to a dedicated output line. The column register allows to define which pixel's output is routed to the wirebond pad.

The HV-CMOS design has the feature to operate as a strip-like sensor where the pixel outputs, instead of being connected to their corresponding readout pads, are connected to per column lines in parallel. The pixels combined signal then becomes accessible by wirebond pads at the periphery. This mode of operation is not considered in this thesis.

Table 5.1: Overview of the global DAC settings commonly used for sensor tuning.

Name	Nominal value	Description
BLRes	1	Inverse time constant of the high-pass filter
ThRes	20	Resistivity of the ThRes transistor; inverse strength of effect of the TDAC output on the threshold
VN / VN2	60	Bias current of the preamplifier
VNFB	5	Feedback current of the preamplifier
VNFoll	20	Bias current of the source-follower in the filter stage
VNDAC	10	Bias current/step size of the TDAC
VNComp	10	Bias current of the comparator
VNCompL	0	Load transistor of the comparator; defines its recovery time
VNOut0	30	
VNOut1	30	Amplitudes of output stages for the corresponding sub-pixels
VNOut2	30	

Table 5.2: Elements of the pixel configuration register. Each register cell configures one unit-cell of 3 rows by 2 columns of pixels.

Name	Description
Row register cell	
EnR/EnL	Switch between pixel or strip operation for all sub-pixels of first/second triple
InR[3:0]/InL[3:0]	TDAC value for the first/second triple of sub-pixels
En[5:0]	Enable sub-pixel amplifier
Column register cell	
L0-2/R0-2	Connect sub-pixels to the global monitor line
Ld[0:2]	Write the TDAC values set in the row register cells to the sub-pixels
dc	Direct Coupling: bypass coupling capacitors before readout pad
ao	Connect this column's analogue output line to the corresponding wirebond pad

5.1.3 Electrical Interface

The HV2FEI4 chip exposes its powering lines and digital interface in two rows of wirebond pads as shown in Figure 5.4. The function of certain signal lines and some operational features are described below while an overview can be found in Table 5.3.

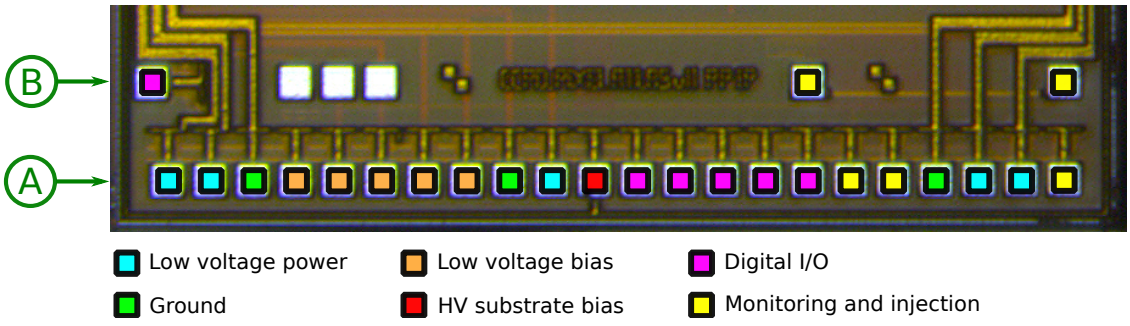

Figure 5.4: Bottom part of a HV2FEI4 version 2 sensor showing the two rows (A, B) of wirebond pads, populated for tests and operation as pixel detector

Low voltage powering As a prototype, the sensor has to be supplied with a variety of power and bias voltages. It is paramount that these inputs and supply lines are immune to possible electromagnetic interferences as some of them are directly fed to the amplifiers of the pixel cells.

Digital I/O The digital input/output block gives access to the global biasing and column-row registers. Both registers share a common serial data input and are programmed by applying a clock to the corresponding register. A pulse on a dedicated load input then initiates the transfer from the registers to the latches.

For verification and debugging, the global bias configuration can be reloaded from the latches to the global register and piped out to a dedicated wirebond pad.

SUBstrate This is the reverse bias voltage of the collecting diodes, applied to the sensor's substrate. It is a negative voltage limited to $-50\,\mathrm{V}$ according to the manufacturer. However most prototypes were able to sustain $-90\,\mathrm{V}$ before breakdown.

Mon This output is the main probe for functional tests and tunings. Each pixel output can be multiplexed to this pad allowing to evaluate the digital response of the whole pixel matrix.

Inj Calibration and functional tests require the ability to inject well defined electrical pulses into the preamplifiers of the pixel matrix. In contrast to more elaborate chips like the FE-I4, the HV2FEI4 does not comprise an internal pulse generator. The calibration charges have therefore to be generated externally and injected into this input. As integrated circuits are prone to imperfections during production, the conversion of the externally applied voltage to the injected charge has to be calibrated with reference signals as can be obtained from x-ray radiators like the Fe^{55} isotope.

AmpOut This pad allows for capturing the analogue signal after the source follower of a group of pixels in the lowermost pixel row. It allows to measure the spectrum of radioactive sources and hereby obtain the aforementioned calibration constants for the injection circuit. The output is buffered globally by an additional source follower to reduce load on the investigated pixel and further lower noise due to the long connections across the chip.

Table 5.3: Electrical interface of the HV2FEI4 version 2 prototypes. D1.8 means Digital input with 1.8V logic level and PD/U: Pull-down/-up. Rarely used signals are written in brackets.

Name	Wirebond pad	Nominal value (V)	Description
Powering			
VSSA	A1, A21	1.5	Amplifier voltage
VDDA	A2, A20	1.95	Pixel matrix analogue voltage
GNDA	A3, A19	0	Analogue ground
VDDD	A10	1.95	Pixel matrix digital and periphery voltage
GNDD	A9	0	Digital ground
Bias Voltages			
VCasc	A4	1.0	Amplifier cascode bias, generated on chip and can be left floating
(ThPLow)	A5	0.8	Threshold voltage for simple pixels
Gate	A6	2.1 - 2.3	Overvoltage for diodes; compensation for voltage drop
BL	A7	0.8	Base line voltage for the discriminator input
Th	A8	0.8 - $\sim$1.0	Global threshold voltage
SUB	A11	$\sim$90	Substrate bias
Digital Interface			
Sin	A12	D1.8	Serial data input for all registers
Ld	A13	D1.8	Load shift register to latches
CkChip	A14	D1.8	Clock for column/row register
CkDAC	A15	D1.8	Clock for global biasing block
(RB)	A16	D1.8	Read-back copying content of latches to global biasing register
(SO)	B1	PD	Output of global biasing register (1.8V logic level)
Testing Circuit			
Mon	A17	PU1.8	Global monitoring line
Inj	A18	<1.8	Global injection line (negative pulses)
AmpOut	A22	PD-1	Buffered analogue output
(MonP)	B5	PD	Differential monitor output
(MonN)	B6	PD	

5.1.4 Hybridisation with the FE-I4

The HV-CMOS development offers a potential reduction of cost in terms of hybridisation. Even though the HV2FEI4 prototypes require a dedicated readout chip to which they have to be bonded, a significant reduction in per-module cost can be achieved by avoiding the complex bump bonding procedure. As the on-pixel circuit allows for a controllable output signal, considerably higher than the collected charge, the sensors were glued to the FE-I4. The glue acts as a dielectric between the sensors and readout chip electrodes, forming Capacitively Coupled Pixel Devices (CCPDs).

Being a novel technique for bonding, extensive studies have been undertaken to find the optimal tools, procedures and materials. Following parameters were investigated:

- Thickness of the glue layer ($<10\,\mu m$)
- Precise 2D alignment ($\sim 1\,\mu m$) as there is no self-alignment due to adhesion like for bump-bonding
- Planarity over the sensor (uniform capacity for all pixels)
- Mechanical and chemical stability
- Radiation tolerance

Gluing studies were performed using glass plates and sensor dummies. As bonding material, adhesive tapes and two component glues were tested of which the Araldite 2011 and Araldite 2020 were identified as suitable. Bonding was initially performed by manual application of glue and simple flip-chipping machines, but was soon replaced by commercial machines like the FINEPLACER lambda, FINEPLACER pico [73] and the SET Accµra 100 [74]. An alignment precision of $\sim 1.5\,\mu m$ with a difference in glue layer thicknesses of $<100\,nm$ over a distance of 2 cm was achieved. Using commercially available machines allowed the rapid construction of prototype detectors ranging from small scale sensors up to full reticle size ($\sim 2 \times 2\,cm^2$) ones. Further details about the conducted studies can be found in dedicated publications [75, 76].

The sensor was designed to have its electrical interface on the side of the readout chip to enable wirebonding of both chips. This means in turn that there are separate coordinate systems for the two devices as shown in Figure 5.5b. While pixels of both devices are addressed by their row and column, as described in the previous section, the HV2FEI4 pixels can additionally be described in unit cells of three by two pixels which map to two FE-I4 cells.

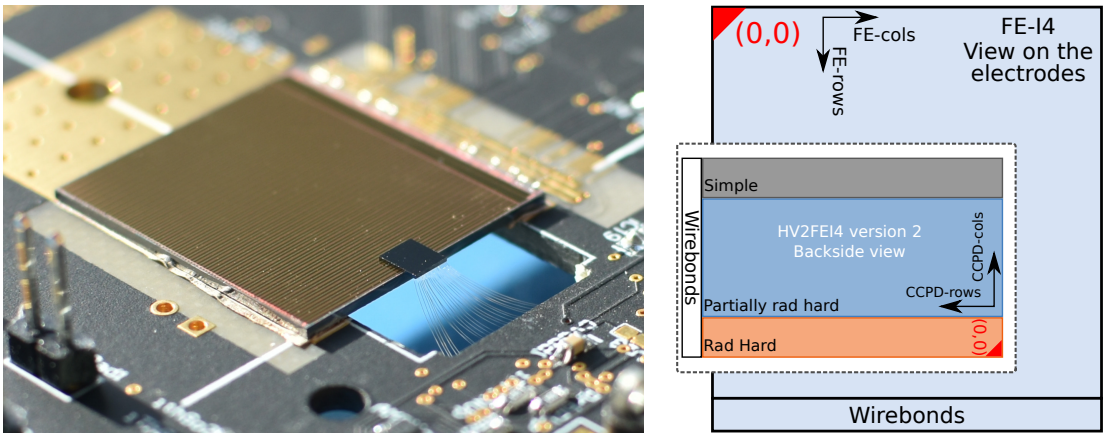

(a) (b)

Figure 5.5: (a) An HV2FEI4 sensor glued to an FE-I4 ROC. (b) Sketch of the HV2FEI4 hybrid assembly with the two coordinate systems of the sensor and ROC.

5.1.5 Small Scale Prototypes

During R&D, several pixel designs and improvements were implemented leading to six HV2FEI4 versions (also called Capacitively Coupled Pixel Devices (CCPDs)) as of 2018. While this thesis concentrates on the version 2 and 4, the following section shall give an overview of the various pixel designs and their differences to motivate the design decisions that drove the development.

HV2FEI4 version 1

The first version of the HV2FEI4 prototypes was a proof of concept, showing that it is possible to detect particles with an HV-CMOS sensor in this technology. On the $4.4 \times 2.2\,\mathrm{mm}^2$ chip 1440 pixels were placed implementing three layouts as shown in Figure 5.6a:

- **A (Columns 0 - 47):** This matrix dominates most of the chip area. The layout and pixel electronics correspond mostly to the pixel matrix of version 2, described in Section 5.1.1, with the exception that all enclosed transistors are laid out as linear ones using solely components from the manufacturer's design libraries. The unit cells form the chessboard pattern for interconnection with the ROC as already explained earlier.

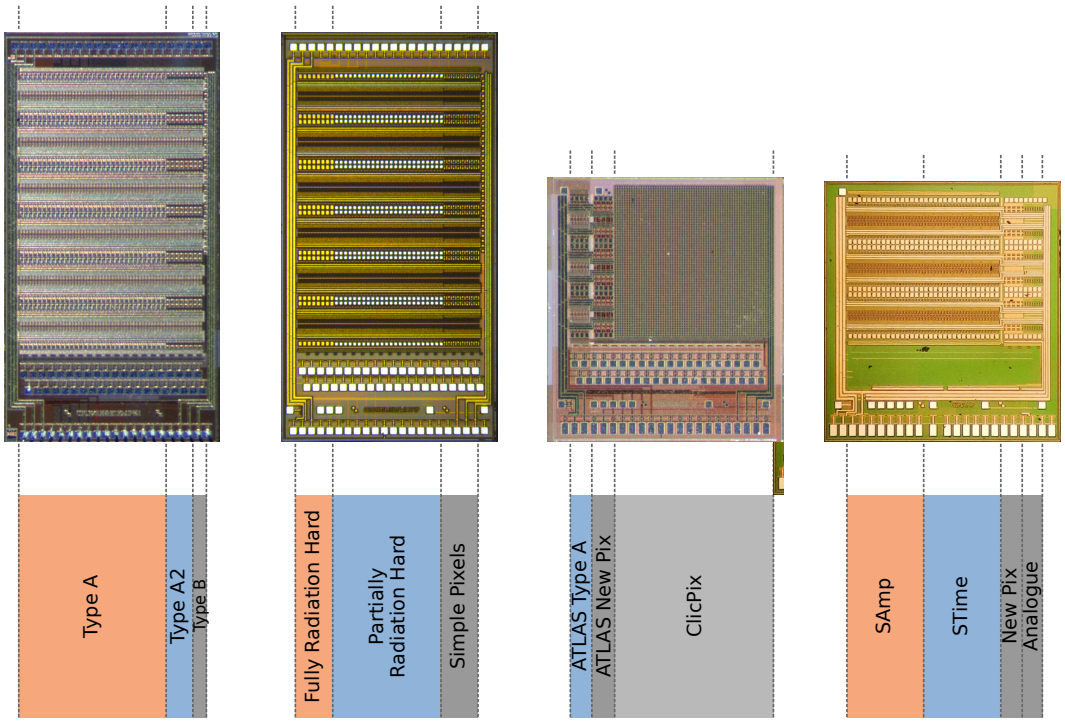

(a) Version 1 **(b)** Version 2 **(c)** Version 3 **(d)** Version 4

Figure 5.6: Pictures and overview of the matrices implemented on HV2FEI4 version 1 to 4 prototypes. The main focus of the investigations was laid on the blue and orange matrices.

- **A2 (Columns 48 - 56):** Electronically this matrix is identical to *A*. The main difference is that pixel pads do not have passivation openings which allows only for AC coupling to the ROC.
- **B (Columns (57 - 59):** These are simplified pixel cells with less amount of NMOS transistors, aimed at lower noise and better radiation tolerance. For this, the TDAC and source follower have been removed and a second amplifier stage was implemented to mitigate the threshold mismatch of the discriminators.

The pixel in column 19, row 12 exposes its source follower output to the buffered output *AmpOut* and can be used for calibrating the injection circuit. A dedicated pixel pad outside the pixel matrix is directly connected to the injection circuit and can be monitored by the bonded readout chip. It can be used to determine the coupling capacity of the active sensor to readout chip bonding.

HV2FEI4 version 2

This design was mostly described in the previous sections. It has the same geometry as the first version and also comprises three pixel types which can be seen in Figure 5.6b. The amplifier design was adapted using custom designed enclosed transistors to strengthen the radiation tolerance of the sensor.

- **Partially Radiation Hard (Columns 12 - 47)**: This is the main matrix and implements the pixel design shown in Figure 5.3. Compared to the pixel type *A* of the first prototype version, the transistors defining the CSA feedback, the bias of the deep n-well and the discriminator input baseline were all enclosed.
- **Fully Radiation Hard (Columns 0 - 11)**: This design is identical to the main matrix except that additionally the red encircled transistors in Figure 5.3 were implemented as enclosed ones. Also the pixels do not have passivation openings restricting the bonding to capacitive coupling.
- **Simple Pixels (Columns - 48 - 59)**: They share the same preamplifier design of the *Partially Radiation Hard* pixels, but contain a simplified discriminator and output stage.

In addition to the new pixel types, it is now possible to read back the global bias register and a total of eight pixels in row 12 provide access to the source-follower output.

HV2FEI4 version 3

In contrast to the first two versions, this $2.8 \times 2.4\,\mathrm{mm}^2$ chip contains mostly pixels adapted to the CLICpix readout chip [77]. There are two matrices for FE-I4 readout (see Figure 5.6c):

- **ATLAS Type A (Column 0 - 5)**: These pixels are based on the Radiation Hard type of version 2, however a long linear transistor instead of an enclosed one is used in the CSA feedback. The TDAC was redesigned to ensure constant current consumption and no current flowing through the global threshold line. Both were leading in the earlier versions to a dependence of one pixel's threshold on the setting of the other ones.
- **ATLAS New Type (Column 6 - 11)**: This type of pixels was a first attempt to separate the electronics from the charge collecting electrode. By this, the capacitance of the diode shall be reduced, leading to a higher signal. The substrate is kept at ground potential while the separated collecting n-wells are biased with a positive

high voltage. Finally the pixel size is reduced to $25 \times 125\,\mu m^2$ with four pixels being connected to one FE-I4 readout cell.

A $100 \times 100\,\mu m^2$ passive diode is placed close to the chip's edge allowing for laser based measurements of charge collection without the necessity and influence of on-chip electronics. Also the latches of the global bias block are improved in terms of ESD safety to mitigate the configuration loss observed on the former version of these prototypes.

HV2FEI4 version 4

The design has been revamped to improve the radiation hardness and to reduce the noise as well as to enhance the sub-pixel encoding capabilities. It has the same geometry as version 3 but incorporates the four pixel matrices depicted in Figure 5.6d:

- **SAmp (Column 0 - 23)**: Based on the *Type A* pixels of the version 3, it replaces some enclosed transistors with linear ones reducing the noise level of the amplifier. Also the input capacitor is enlarged and the collecting diode segmented, reducing its capacitance and leading to an improved signal amplitude.

- **STime (Columns 24 - 47)**: This type is identical to the SAmp except for the output stage which implements two new sub-pixel encoding schemes in which the output signal width is independent from the deposited charge. In the *Voltage Mode Amplitude Encoding*, the output voltage levels of the pixel triple are defined by external voltages. If multiple pixels are hit, the mean of the set voltages is transmitted. The *Pulse Length Encoding* keeps the amplitude fixed and makes the length of the output pulse configurable. As the FE-I4 has a Time over Threshold based charge resolution, this scheme can force the ROC amplifier to stay well over threshold for a defined amount of time. Here in case of multiple hits, the sub-pixel with the longest pulse width determines the output width.

- **New Pixels (Column 48 - 55)**: This design is based on the New Pixels in version 3 but has been improved in terms of noise by adding a low pass filter and replacing an enclosed transistor with a linear one.

- **Analog pixels (Column 56 - 63)**: These $25 \times 250\,\mu m^2$ sized pixels contain only amplification stages similar to the CLICpix matrix of the version 3 and provide analogue information to the ROC. A new summing scheme was developed to facilitate the sub-pixel encoding.

In this prototype, the chessboard like sub-pixel pattern is dropped out in favour of a linear one, simplifying the alignment for test beam measurements. The matrix allows to

electrically inject charges row wise instead into the full matrix and to disable discriminators column wise, allowing to reduce the activity on the chip to one pixel at a time for calibration.

HV2FEI4 version 5 and beyond

In test beam measurements, it was found that the time resolution of the earlier versions was beyond 25 ns resulting from time-walk of the preamplifier. To mitigate this, a compensation circuit is implemented mimicking the functionality of a constant fraction discriminator while avoiding the complexity of such a device. In principle, the overdrive of the input signal, exceeding the threshold, is fed into the comparator, increasing the propagation time with the signal strength. Big signals, which cross the threshold faster than small signals are therefore delayed and the timing distribution compressed. Further information can be found in reference [78]. The version 5 allows for setting parameters globally while the next generation implements per-pixel tuning DACs to account for production mismatches. These prototypes are not covered in this work, however characterisations and results with the time-walk compensating circuit can be found in reference [79].

5.2 Control and Measurement Setups

Operating and characterising HV2FEI4 sensors requires specific equipment for control and configuration. As described above, active sensors require several power and bias sources and need to be configured by an outside system. Two such systems, called *UX-IBO* and *CaRIBOu* have been developed in the last years to accommodate a multitude of sensor prototypes.

In operation, the HV-CMOS sensors are usually read out by the FE-I4 readout chip. As this is a well known and characterised device within the ATLAS community, there were already readout systems available when the HV2FEI4 sensors emerged. For laboratory measurements the *USBPix* setup, developed by the University of Bonn, was chosen for controlling the FE-I4. It is a well known system based on a Xilinx Spartan-3 Field Programmable Gate Array (FPGA) that allows functional tests, calibration and data taking with the FE-I4. The user controls the system either with the *STControl* graphical user interface or the *pyBar* Python framework. Further information can be found in reference [80].

5.2.1 The UXIBO Test Bench

The USB Xilinx Board (UXIBO) test bench was initially developed for the first version of the HV2FEI4 sensors. It is based on the eponymous FPGA board that was designed by the University of Heidelberg for teaching purposes. It hosts a Xilinx Spartan2E FPGA, which interfaces a PC via a USB-UART bridge. Being a tool for educational purposes, it contains a variety of periphery of which only the General Purpose Input Output (GPIO) connector is used for this setup. The test bench comprises the UXIBO itself and a carrier PCB implementing the necessary infrastructure for powering and biasing the sensor.

The PCB hosts the circuitries for both parts of the hybrid detector, the FE-I4 and the sensor, where the readout chip part has been adapted from the Single Chip Cards developed for characterisation of FE-I4 modules [80]. For the HV2FEI4 sensor, an independent circuitry was developed, which can be divided into the powering part, the biasing part and the I/O circuitry. A setup for a HV2FEI4 version 4 prototype is shown in Figure 5.7.

Low voltages for several powering lines and the Gate bias voltage are provided externally by laboratory power supplies, which also allow to monitor current consumption. As the prototypes do not contain sophisticated debugging infrastructure, the current of

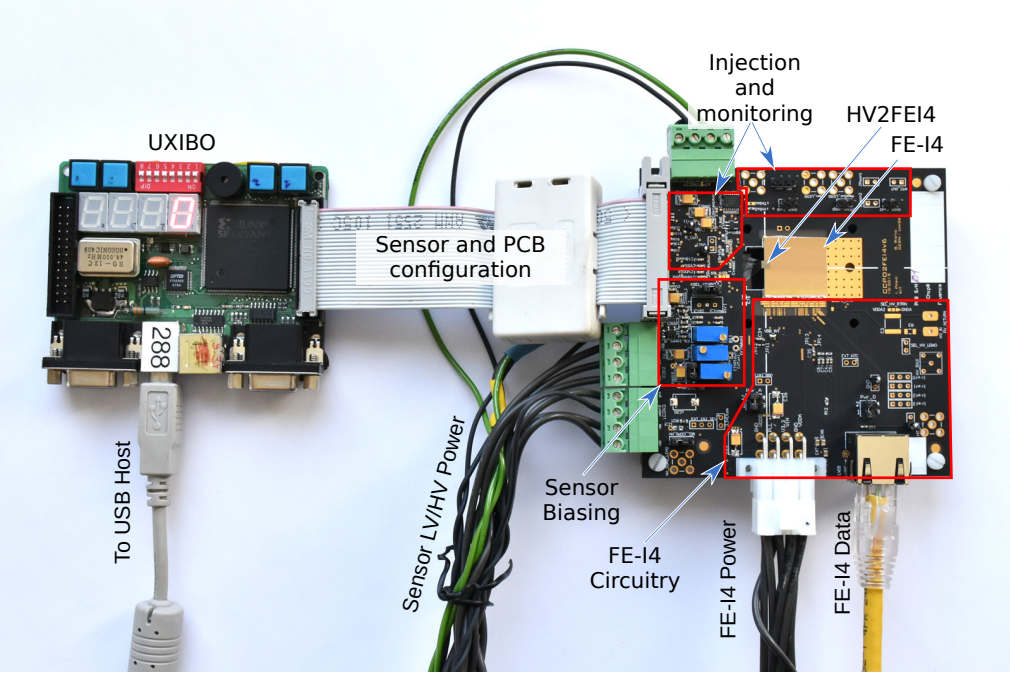

Figure 5.7: Photo of a UXIBO characterisation setup with for an HV2FEI4 version 4 prototype. Part of the biasing and I/O infrastructure are on the bottom side of the PCB.

the analogue part (IDDA) and especially the preamplifier (ISSA) are important probes to crosscheck the state of the sensor.

Bias voltages are generated on-board by means of variable voltage dividers or DACs. Some, like the discriminator input baseline voltage, are fixed and bias the gate of a MOSFET, drawing practically no current. They are therefore supplied by a 1 kΩ potentiometer referenced to VDDA. The global threshold voltage is generated by a 14-bit DAC as it has to be adjusted regularly and precisely.

For HV2FEI4 sensors, the injection circuit has to be implemented externally and was realised as a combination of another 14-bit DAC and a Fast Analogue Switch (switching time $<$150 ns) which on activation pulls the injection input to ground, generating the required negative pulse. As the monitoring output is a negative logic pulse, this signal is inverted using an operational amplifier with open feedback loop before delivering it to the FPGA.

The UXIBO connects to the sensor PCB via its CMOS 3.3 V GPIO connector. It interfaces directly the on-board DACs and the configuration and global biasing registers of the HV-CMOS sensor. For both interfaces a serial data input and clock is provided which program the settings into the corresponding registers. A signal to dedicated load inputs then issues the transfer from the registers to the configuration latches. For the HV-CMOS sensor these signal levels are shifted with voltage dividers to 1.8 V which is matching the requirements of the sensor.

In injection mode, the FPGA triggers the Fast Analogue Switch 128 times in a burst. During that time a counter is armed to receive pulses from the monitoring line. In low threshold operation and especially after irradiation the sensor can become noisy and distort the reading. To estimate the reliability of the read back value, a second counter is initialised to 128 and started after the injection pattern has been finished, running for the same amount of time as the first one. Each hit decrements the counter giving an indication of the amount of noise in the measured signal.

The UXIBO is connected via USB to a PC running a custom designed software written in Borland C++. The graphical interface allows to set all configuration values as well as to scan and tune the threshold settings of the pixel matrices. For this, the Binary and Noise tune, as they will be described in 5.3, were implemented.

5.2.2 The CaRIBOu Control and Readout System

The Control and Readout Itk BOard (CaRIBOu) is a custom made test bench for HV-CMOS detectors, based on the Xilinx Zync ZC706 [81] development board. It was designed for operating the sensor and the readout chip (the FE-I4 in our case) using one system while keeping it generic for flexible adaptation. The test bench is segmented in several boards as depicted in Figure 5.8 with:

- The ZC706 Central Interface FPGA board
- The CaR board: powering, monitoring and signal conversion
- The IBO: detector specific interface board
- Cable boards (optional) - not shown on the figure

CaRIBOu provides all the necessary power, bias voltages (except for the substrate bias HV) and the injection circuit on the dedicated **C**ontrol **a**nd **R**eadout board. It hosts 16 DACs for bias voltages and eight programmable low voltage regulators which can be

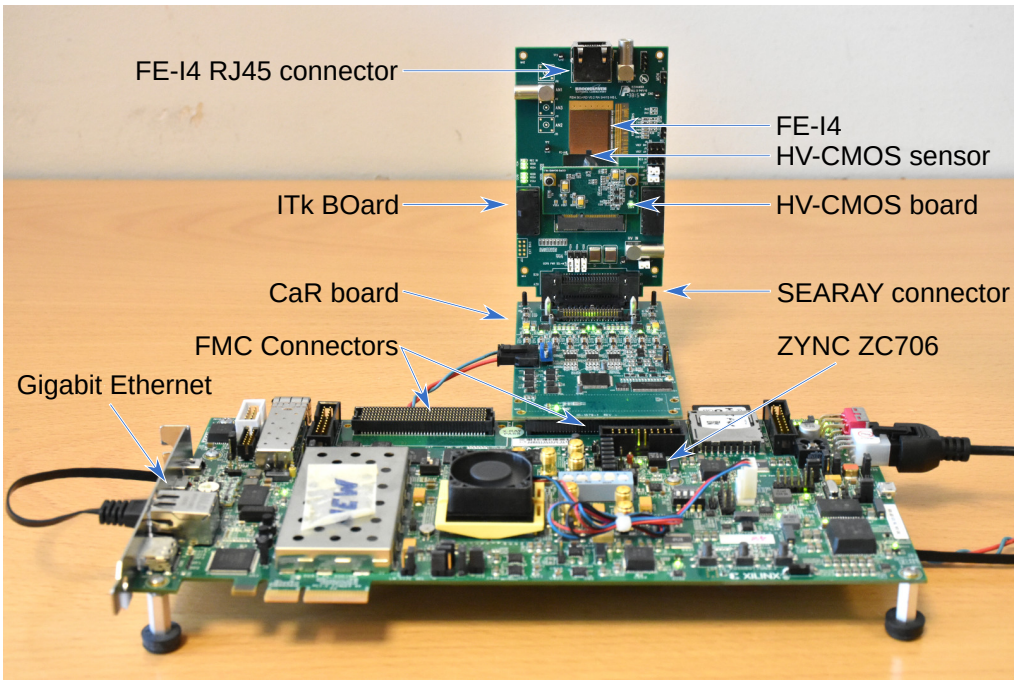

Figure 5.8: Photo of a CaRIBOu Setup with an HV2FEI4 detector. Shown are the ZC706, the CaR board and the IBO. In this setup the CaR board is directly connected to the ZC706 so no cable board is needed.

monitored in terms of current and power. Analogue signals are digitised by a 40 MHz 12 bit Analogue to Digital Converter (ADC) with eight channels and two pulse generators are used for injection. The board infrastructure is configured via an I^2C interface while all data lines are using the LVDS standard. The CaR board and the FPGA are interfaced via an FMC[c] connector using LVDS lines for the FE-I4 communication. LVDS to LVCMOS converters allow connecting to the HV-CMOS sensors. The board can be directly attached to the ZC706 or connected via a flexible VHDCI[d] cable for which adapter boards have been made. This is especially convenient when operating irradiated sensors which have to be cooled to temperatures as low as $-30\,°C$ while the FPGA board can be kept out of the cold environment. Thanks to the extensive infrastructure on the CaR board, it can host two detectors at the same time which are attached via Samtec SEARAY connectors.

The detectors themselves are hosted on the **I**Tk **BO**ards, which carry passive electronics. The FE-I4 specific circuitry is implemented on a carrier board that interfaces the CaR board. As the HV2FEI4 interface tends to vary with the protoype version, its interface is implemented on a mezzanine board which is connected to the carrier board via a mini-PCIe connector. The carrier board allows connecting the FE-I4 to an external readout system like the USBPix or RCE/HSIO (see Section 4.2.2).

The CaRIBOu system is controlled by the Central Interface board which is the Xilinx ZC706 off-the-shelf development kit. The FPGA can be interfaced by GBT [82] or, like used in this thesis, a Gigabit Ethernet link. It implements a command decoder as interface to the infrastructure on the CaR board and the connected detectors. In addition, it hosts a buffer in which data from the readout chip and the on-board ADCs can be stored.

The host software is implemented in Python running on a standard x86 PC and interfacing the ZC706 usually via TCP/IP over its Gigabit Ethernet Link. It allows the user to query and set all parameters of the CaR board and to configure and tune the attached detectors. A graphical interface has been implemented for easy configuration and monitoring of the CaR board infrastructure. It also allows configuring the HV2FEI4 sensors, whereas scans and tuning procedures are implemented as Python programs via the CaRIBOu API to exploit the full flexibility of the system. Further information has been reported in reference [83].

[c] FPGA Mezzanine Card
[d] Very High Density Cable Interconnect

5.2.3 Integration into the FE-I4 Telescope Setup

The FE-I4 Telescope allows several FE-I4 based devices under test to be read out and their data recorded transparently as the DAQ system is agnostic to the actual sensor. Being hybridised with the FE-I4, the HV2FEI4 prototypes directly profit from this feature. In terms of DAQ settings, only the latency of the hits with respect to the trigger signal has to be adjusted as the signal propagation time in the HV2FEI4 electronics add to the one of the FE-I4. Additionally, the maximum readout window of 400 ns (16 bx[e]) is set to ensure that also hits, delayed by effects like time-walk, are reliably recorded. The size of the prototype sensors requires setting a tight Region of Interest trigger mask, which typically comprised only few percent of the telescope's acceptance.

The telescope setup has no means of controlling the HV2FEI4 sensors themselves or monitoring them. In the UXIBO setup it is entirely the task of the shifter to log the status of the sensors and manually adjust settings or scan the desired parameters. This was improved with the introduction of the CaRIBOu system which is fully scriptable thanks to its Python interface. An automation based on the scheme described in Section 4.3.1 was developed, allowing to automatically take threshold and bias voltage scans without being limited to just these parameters. The settings of the sensors are logged during the run and subsequently a preliminary analysis is performed immediately after data taking.

5.3 Sensor Tuning Procedures

The HV-CMOS sensors can be configured by setting multiple parameters. For most of these parameters, optimal settings were found through simulation and lab tests leading to the nominal values listed in Table 5.1. Due to imperfections in the manufacturing processes, the behaviour of the pixels in the matrix is not uniform. Especially the discriminator threshold has to be adjusted precisely due to the small signal size of the sensors. The HV2FEI4 prototypes host a four bit DAC (TDAC) per pixel allowing to equalise the matrix. Three types of algorithms, the Binary Tune, the S-Curve Tune and the Noise Tune have been implemented and tested, targeting for an optimal threshold tuning.

The threshold setting of a pixel is verified by injecting electrical pulses into the amplifier and observing the response of the discriminator. As described in Section 3.2, by varying the input voltage the activation curve of the discriminator can be measured. The function follows a Gaussian Error Function where a signal detection probability of 50 % defines the threshold point and the width of the interval between 20 % and 80 % the electrical noise contribution[f] as shown for the FE-I4 in Figure 3.4a.

[e] The FE-I4 clock period, based on the time between LHC bunch crossings

[f] For the FE-I4, a smaller interval of 30 % to 70 % is used as an estimator for noise

In addition to the per pixel TDAC, global parameters have to be adjusted setting the range of the threshold tuning:

- **Th:** This bias voltage defines the global threshold level. It has to be set to a value that allows all pixels to be adjusted to the target threshold via their TDACs.
- **VNDAC (usually) or ThRes:** Set the step size of the TDAC parameter and should be adjusted such that after tuning, the distribution of TDAC values occupies the whole parameter range. A too low value would lead to many pixels being outside the target threshold range.

In the following section, the optimisation of the global and per pixel parameters with the aforementioned algorithms and their performance will be discussed.

5.3.1 Algorithms - The Binary, S-Curve and Noise Tune

Binary Tune

In the Binary Tune, the optimal TDAC per pixel is found using a binary search. As a first step, the TDACs of all pixels are set either to a low value (high threshold) or their middle value of 7 or 8[g]. A charge, corresponding to the target threshold, is injected and the response probability of all pixels recorded. In case of an initially low TDAC setting, the global threshold is set so that no pixel shows a higher detection probability than 50 %. For a middle TDAC setting, the global threshold is varied to center the obtained threshold distribution around the target value.

For each pixel at a time, the same charge as in the previous step is injected and the TDAC value for a response, closest to 50 %, is used for a binary search pattern. Finally, a threshold scan verifies the settings by measuring the discriminator activation curves as described above.

This algorithm has the advantage of being fast as a solution is found after maximally five[h] injection steps. Noise or other malfunctions of the pixel that lead to the measured threshold not depending monotonously on the TDAC settings generate biased results.

S-Curve Tune

This tuning algorithm uses a full threshold scan, as described above for verification, to find the optimal TDAC value per pixel. The global threshold is found as for the *Binary Tune* or has to be set manually to a reasonable value. All TDAC settings are

[g] The HV2FEI4 TDAC has a 4-bit resolution.

[h] Number of steps in the search: $\lfloor \log_2(n) + 1 \rfloor = 5$, with $n = 16$ the number of possible TDAC settings.

reset to a middle value of five and a per pixel threshold scan is performed. A Gaussian Error function is fitted to each activation curve and the threshold value extracted. The TDAC is then varied until a threshold inside the user defined tolerance interval is found. Alternatively the activation curve for each TDAC setting is recorded, and the threshold vs. TDAC plotted. Interpolating the resulting curve provides the optimal value.

The algorithm is more robust than the Binary Tune as single outliers during injection have a weaker effect on the result and the quality of the fit offers a robust estimate for the quality of the pixel. Due to the required large number of threshold scans, this procedure has the inconvenience to be slow.

Noise Tune

The goal of this algorithm is to find the minimal possible threshold value where the pixels are still free of noise. For this, no signal is injected into the pixel matrix and instead the activity of the pixel discriminator in its idle state is observed over a certain amount of time. If no hit has been detected, the pixel counts as noise free to the level of recording time.

Initially the local threshold correction is set to the highest value. The global threshold is set such that the pixel with the highest noise level is still free of noise. In the per-pixel correction step the local threshold is lowered until noise hits are observed and then increased by one step, setting the discriminator just above the noise level. Once completed, a matrix verification scan is done and if noise in a pixel is found the local threshold is increased.

The Noise Tune is a valuable alternative to the injection based algorithms if the pixel matrix is not uniform in terms of noise behaviour or if the noise levels are in general high. Injection based algorithms may get confused and would require a high target threshold to find proper discriminator parameters. In this case the Noise Tune would find the working point where the sensor would be most efficient, with the disadvantage of a non-uniform threshold setting. As this is in general unfavoured the algorithm is scarcely used.

5.3.2 Performance of the Tuning Algorithms

Previously introduced algorithms were extensively used for laboratory and test beam measurements. The binary and noise tune were implemented first and were mostly used for version 2 prototypes until the S-curve tune was developed. Although the latter in general yields a more uniform and low threshold distribution, the binary tune achieves comparable results on “well behaved” (low noise, good linearity with respect to TDAC settings) sensors with a significant time saving.

The binary and S-curve algorithms have been extensively studied and reported in reference [84]. Figures 5.9a and 5.9b show that using the S-curve method a significant equalisation of the pixel thresholds down to a standard deviation of 76 e for version 2 and 38 e for version 4 with a threshold as low as 403 e can be reached. The electronic noise levels on the S-curve were stated for both sensors around 75 e. For the version 4 sensor, the binary tune yielded a comparable mean value.

It should be noted that these measurements were performed in a laboratory. In the environment of a beam experimental area with extensive installed infrastructure like magnets, pumps and heavy lifting devices, the level of induced noise is generally higher impacting the lowest achievable threshold.

The Noise Tune was so far only used on version 2 samples, mostly in test beam experiments. A threshold distribution with a most probable value of ~ 500 e was obtained in the SPS H8 beamline at CERN [85]. Thanks to improvements of the discriminator and the threshold setting circuitry of the version 4 prototypes the noise tune did not show significant advantages over the binary tune and thus was not used. Further developments are pursued with novel algorithms based on noise occupancy measurements as reported in [84].

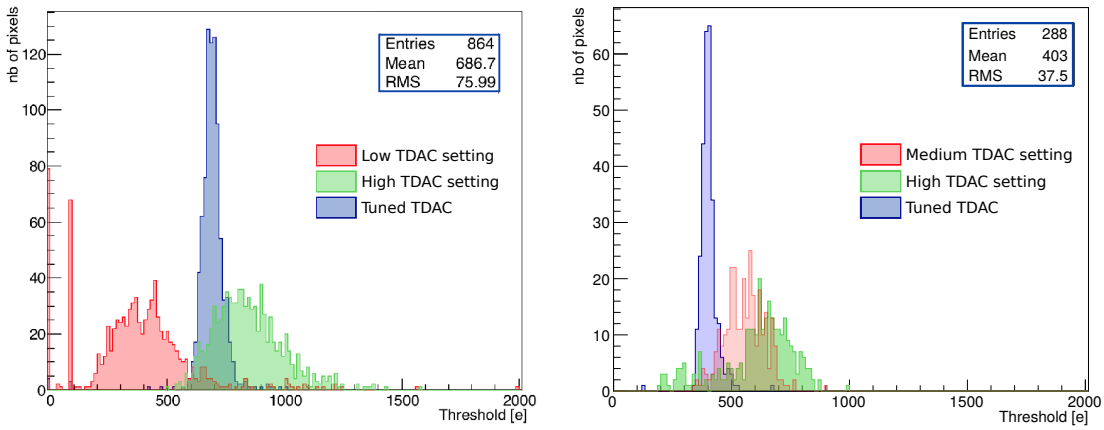

Figure 5.9: Threshold distributions before and after the tuning of (a) a version 2 and (b) a version 4 sensor. The broad (green and red) distributions were obtained before tuning with a uniform TDAC setting of 3(4) and 9, respectively. The narrow (blue) curve shows the result of an S-Curve tuning. The two peaks below 200 e in (a) result from failed S-Curve fits [84].

5.4 Irradiation with Hadrons and X-rays

High energy physics experiments for high luminosity colliding beams usually require materials suitable for a heavy radiation environment. As stated in Section 3.4, sensors for the ATLAS Inner Tracker upgrade will have to sustain TIDs up to 1 Grad and NIEL fluences up to $2 \cdot 10^{16}$ n_{eq}/cm^2 in the inner and a factor $\sim$10 less for the outer pixel layers.

CMOS sensors for HEP applications have been around for quite some time (see Section 3.5), but they are not capable to sustain operation in the radiation environment of the ATLAS ITk. With HV-CMOS sensors the goal is to demonstrate their suitability with the various prototypes.

Each prototype generation has to undergo an extensive irradiation campaign proving their radiation tolerance in several steps towards the ultimate ITk dose and fluence. As HV-CMOS sensors implement the collecting diode and sensitive electronics on the same substrate, they were tested separately - the electronics after irradiation with protons and x-rays and the charge collection of the sensing part after irradiation with protons and neutrons.

5.4.1 Influence of Ionising Radiation on Sensor Electronics

To estimate the radiation tolerance of the sensor electronics, prototypes were exposed to ionising radiation up to 1 Grad. By using electrical injection of charge into the pixel cell, the effects on the sensor bulk, hence the charge collection was disentangled and only the electronics investigated. As a cross-check, source scans with Fe-55 x-ray and Sr-90 beta radiators were performed. The focus was on the amplifiers as due to the low signal from the pixel diode, they define the hit detection and noise behaviour.

The irradiation campaigns took place at CERN using a 10 keV x-ray source and the 24 GeV proton beam of the IRRAD facility [86] at CERN PS. For all campaigns the sensors were operated at room temperature with nominal conditions: fully biased and configured. The two main amplifier designs of HV2FEI4 version 2 and 4 prototypes (as described in Section 5.1.5) were tested. They are based on the *Partially Radiation Hard* design as a compromise between radiation hardness, gain and noise levels and differ in the implementation of their feedback transistor as linear (LT) or enclosed (ELT) type (see Section 2.4).

Results for an HV2FEI4 version 4 prototype after x-ray irradiation up to 1 Grad are shown in Figure 5.10a. The chip was irradiated in multiple steps with a dose rate of 103 krad/min and after each step annealed at 70 °C for two hours. Both amplifiers were found to be functional after the maximum dose, but with a drop in amplitude of the order of 12 % for the LT and 55 % for the ELT type. While further annealing for 26 days

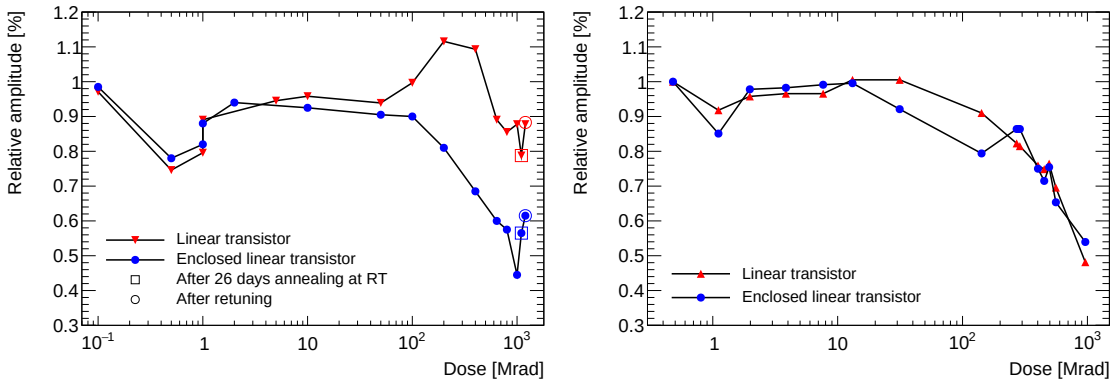

Figure 5.10: Response of two types of amplifiers, with linear and enclosed feedback transistors to an 1.2 V injection pulse after irradiation (a) by X-rays up to 1 Grad and (b) with protons up to 962 Mrad. The last three points in (a) were taken after 1 Grad, but separated for better visibility [88].

at room temperature slightly recovered the ELT amplifier's relative amplitude to 57 %, the LT one worsened. However, fine tuning of the biasing DACs allowed to recover the performance to 88 % for the LT type and 62 % for the ELT. Although the LT amplifier showed less degradation with dose and even exceeded its initial amplitude after 100 Mrad[i], it became significantly noisy after 200 Mrad dominating the measured noise spectra as presented in reference [87]. For the ELT type, the signal remained visible up to the target dose with the signal to noise ratio reduced from 60.3 to 27.5. Comparable results were obtained from the HV2FEI4 version two prototypes [87].

The prototypes showed a similar behaviour when exposed to the proton beam at the IRRAD facility. The results in Figure 5.10b show a steady performance up to 100 Mrad, with a degradation up to 50 % when reaching the maximum dose of 962 Mrad. However, reference [89] shows that with retuning also here the amplitude can be restored up to over 80 % of the initial value. As for the x-ray irradiation, the LT type became noisy after 200 Mrad leading to the ELT type being the clearly preferred design.

For both irradiation campaigns, a dip in the amplitude around 1 Mrad was observed. This effect was also measured on the FE-I4 ROC and attributed to an increased leakage current of NMOS transistors in this region of TID and feature size. Detailed studies related to low TID effects can be found in references [75] and [90].

In conclusion, the HV2FEI4 amplifier designs have proven to be radiation tolerant up

[i]This effect is still to be understood.

to the TID expected for the inner layer of ATLAS ITk. Even if degradation of performance is observed with high irradiation, it can be mostly recovered by annealing and proper retuning. In addition, the HV-CMOS technology is considered a candidate primarily for the outer layers of the ITk, where a TID of up to 50 Mrad is expected. All prototypes qualified for this region as they kept a good performance up to 100 Mrad even without retuning.

5.4.2 Hadron Irradiation at Accelerators and Reactors

While ionising radiation causes surface damages which influences electronic circuits, it has little effect on the charge collection in the sensor bulk and the pn-junction properties as described in Section 2.4. Sensors in HEP experiments, additionally to ionising radiation, are exposed to high particle fluences causing Non Ionizing Energy Loss (NIEL) which can damage the crystal lattice, inducing charge trapping and changing the substrate resistivity as discussed in Section 2.4.

Prototype sensors are therefore tested by irradiation with hadrons from particle accelerators or nuclear reactors. In contrast to studies of the electronic circuitry, which is independent of radiation effects in the sensor bulk, irradiation of the sensor bulk always induces a certain amount of TID in the circuitry. If only the properties of the pn-junction are tested like in Transient Current Technique (TCT) measurements, the ionising dose does not influence the result as the signal is directly extracted from the junction. When the HV-CMOS sensor is operated as designed and signals are processed by its on-chip circuitry, it is important to disentangle TID based effects when interpreting results from NIEL-focused irradiations. However, as discussed in the previous section, the hadron induced TID decreases the analogue cell performance by no more than 15 % for doses up to 100 Mrad which in turn can be mitigated by tuning the global bias parameters. Up to this dose, the NIEL induced effects can be mostly disentangled from the TID ones.

HV2FEI4 sensors were irradiated with neutrons at the TRIGA Mark II reactor of Joseph Stephan Institute in Ljubljana, Slovenia and with protons at the medical cyclotron at Bern University Hospital (Inselspital), Switzerland.

The TRIGA reactor at JSI

The research reactor at JSI is a 250 kW TRIGA[j] Mark II reactor [91]. It is a light water pool type reactor, cooled by natural convection which output power can be regulated in a wide range down to few watts. The reactor has been extensively characterised and the delivered neutron flux was found to be in agreement with simulation models within few

[j] Training, Research, Isotopes, General Atomics

percent. The core permits inserting devices for irradiation at several positions between the fuel rods which allows to chose the neutron energy spectrum. For irradiation of HV2FEI4 sensors, the TIC channel was selected. It has an approximately elliptic shape with axis lengths of 7 cm and 5 cm and recieves devices up to a length of 15 cm. At this position 38 % of the incoming flux is composed of fast neutrons ($> 0.1\,\mathrm{MeV}$) which are the cause of $\sim$98 % of NIEL damage in this channel. The fluence is measured by Neutron Activation Analysis on aluminium sheets which are irradiated alongside the prototypes. This measurement is stated to be accurate to 10 %.

The Bern medical cyclotron

The cyclotron at the Bern University Hospital is a commercial IBA Cyclone 18/18 HC device accelerating H^- up to 18 MeV [92]. Being a device for medical purposes, the cyclotron is used for isotope production over night, while being available for research during daytime. It can provide a beam current up to 150 µA using one or both of its H^- sources, whereas operation down to the pA level is possible. This translates to a dose rate ranging from 0.1 to 1000 Mrad/h. Protons are extracted by stripping off the electrons from the H^- ions with pyrolytic carbon foils. A beam transfer line transports the protons into a dedicated research bunker which hosts the apparatus used for detector irradiation [93]. The extraction line is set up to deliver a flat beam with a uniformity of 80 % within 40 mm in both transverse directions. In contrast to neutron irradiations in a reactor, the irradiation apparatus can already be accessed a few minutes after switching off the beam and is suited for devices as large as $30 \times 30\,\mathrm{cm}^2$.

The beam profile is measured by a two-dimensional beam profiler developed by University of Bern, using a fluorescence screen. The beam current density is measured by an active collimator which is connected to a high precision ammeter. It allows to determine the delivered dose with a relative uncertainty of 6 %. Further information on the beam instrumentation and the irradiation setup can be found in reference [93].

5.4.3 Overview of HV2FEI4 Prototypes

Table 5.4 shows an overview of the samples that are discussed in this thesis. All prototype sensors were glued to an FE-I4 readout chip and mounted to PCBs as discussed in Section 5.2. For both the HV2FEI4 version 2 and 4 there are unirradiated reference samples (402, CaribouP) for comparison. The version 2 prototype C22 along with the version 4 prototypes 404 and CaribouN1 and N5 were irradiated at JSI prior to being characterised in the lab. This was necessary due to the limits in size of the available irradiation channel and to avoid irradiating the PCB therefore limiting the activation of the samples.

Table 5.4: List of HV2FEI4 samples

Sample	Particle type	Irradiation fluence (10^{14} n_{eq}/cm^2)	Approximate TID (Mrad)	Facility
HV2FEI4 version 2				
C19	/	0	0	/
C22	n	10	1	JSI
HV2FEI4 version 4				
402	/	0	0	/
404	n	10	1	JSI
CaribouP	p	0, 1.3, 5	0, 6, 22	Bern
CaribouN1	n	10	1	JSI
CaribouN5	n	50	5	JSI

In contrast, the Bern cyclotron allows irradiating already assembled detectors as they can be freely positioned in the beam and the beam itself well collimated. CaribouP was therefore assembled as a fresh module and characterised before and after two irradiation steps up to $5 \cdot 10^{14}$ n_{eq}/cm^2.

Irradiated prototypes were cooled during operation, but stored at room temperature. It should be noted that for all irradiations, the influence of the TID with 22 Mrad or below remains in a region which can be either neglected or mitigated by tuning of the sensors. In the next chapter, the performance of these sensors as measured in test beam experiments will be presented.

5.5 Summary

The prospects of active pixel sensors in HV-CMOS technology for the ATLAS high luminosity upgrade has lead to the development and characterisation of various prototypes, implementing different amounts of signal processing electronics and pixel geometries. HV2FEI4 sensors, built in the ams H18 180 nm process have been investigated as hybrid detectors with the FE-I4 readout chip. The sensors implement per-pixel signal processing circuits to amplify the collected charge and discriminate against noise. In contrast to passive sensors, the HV2FEI4 sensors are capacitively coupled to the readout chip by a thin glue layer that acts as a dielectric and replaces the complex bump-bonding process. Several versions of HV2FEI4 sensors were developed targeting higher radiation tolerance, faster detection, efficiency improvements and elevated calibration capabilities.

Two milestones were reached by the second and fourth generation designs. The usage of Enclosed Transistors in parts of the analogue circuitry introduced radiation tolerance to the electronics and a revamped amplifier and discriminator design improved the noise and speed performance and lead to a stable signal transmission to the FE-I4.

HV2FEI4 prototypes are highly configurable by a number of on-chip current and voltage generators and externally supplied bias voltages. For the configuration and control of the sensors, two systems were designed, the UXIBO and the CaRIBOu. Both systems implement the full feature set of the prototypes and allow operation and calibration by means of dedicated software, running on a standard PC. UXIBO is a lightweight FPGA board, interfacing a dedicated PCB that carries the necessary circuitry for the operation of and the interface to the FE-I4 and the sensor. Several carrier PCB versions have been designed to accommodate the changing interface and feature set of the sensors. With the development of CaRIBOu, a more flexible system was established, based on an off-the-shelf FPGA board. The necessary electronics was implemented on a dedicated PCB, which leaves only simple circuitry to the carrier board, making it highly adaptable while a Python programming interface allows to quickly implement new and automatic procedures. Both systems were integrated into the FE-I4 Telescope setup for test beam experiments. Thanks to the CaRIBOu scripting interface, automated scans were added to the telescope framework (see Section 4.3.1) to facilitate data taking.

As the sensors have to cope with a low signal size, fine tuning of the discriminator threshold levels is paramount for efficient operation. Three algorithms were developed and implemented in both control systems, the Binary, S-Curve and Noise Tune. While the former two aim to equalise the threshold settings over the pixel matrix, the Noise Tune finds the lowest possible threshold per pixel, just above the noise regime. All algorithms were tested and showed that a uniform threshold setting as low as 400 e (a MIP signal has a most probable value of $\sim$1200 e) is feasible with the HV2FEI4 prototypes.

The radiation tolerance of the sensors was assessed in X-ray, proton and neutron irradiations up to end-of-lifetime doses and fluences for the ATLAS ITk. The electrical circuitry, as tested by the response of the amplifier to electrical test pulses, proved to tolerate total ionising doses up to 200 Mrad and was still operational at 1 Grad. As the HV-CMOS technology is targeted for the outer layers of the ITk Pixel Detector, it will only have to withstand a maximum dose of 50 Mrad. In this region, the circuitry operated properly, with a dip in performance around 1 Mrad as it was expected from observations of the FE-I4. However, the performance is restored by tuning bias voltages and currents.

In the next chapter, the detection performance after irradiation with protons and neutrons, that mostly damage the crystal lattice (NIEL processes), will be discussed.

Chapter 6
Test Beam Characterisation

Test beam measurements allow to assess the quality of a detector in an environment close to the final experiment. For operation in the future ATLAS ITk, candidate sensors have to prove a high hit detection efficiency combined with a fast detection. During test beam campaigns in 2014 to 2016, HV2FEI4 version 2 and 4 prototypes were thoroughly tested in the CERN PS T9 10 GeV proton and the SPS H8 180 GeV pion beams where particle tracking was provided by the FE-I4 telescope. They had to prove to be suited for a beam environment and their performance concerning hit detection efficiency and timing was evaluated in different operational conditions by variation of the set threshold and bias voltage. In contrast to the former generations of plain CMOS based sensors, the HV-CMOS prototypes are considered for a high radiation environment. The test beam campaigns therefore focused on assessing the detector performance before and after irradiation up to ITk end-of-lifetime fluences.

In this chapter, the test beam measurement methods and results for HV2FEI4 sensors will be presented. First, the operation of the sensors in the beam environment and the peculiarities during data taking due to the sensor geometry will be discussed. The analysis procedures will be introduced along with quality criteria on the reconstructed data. This will be followed by the measurement campaigns for different sensor versions. For each campaign, the operational parameters, the sensor calibration and limits of the measurement will be reviewed. The following analyses of the hit detection efficiency and timing will extract information about charge collection and signal processing in the sensor as well as possible advantages and shortcomings of the sensor design. Finally, an interpretation of the gathered results in view of operation and detector performance of the tested prototypes will be given.

For the measurements presented in this chapter, the *Partially Radiation Hard* matrix of the HV2FEI4 version 2 prototypes and the *STime* matrix of the version 4 devices (see Figure 6.1) were considered as these are the baseline implementations for an ATLAS ITk candidate in ams H18 technology.

Most results presented in this chapter have already been published in [50, 53, 63, 85] and [88].

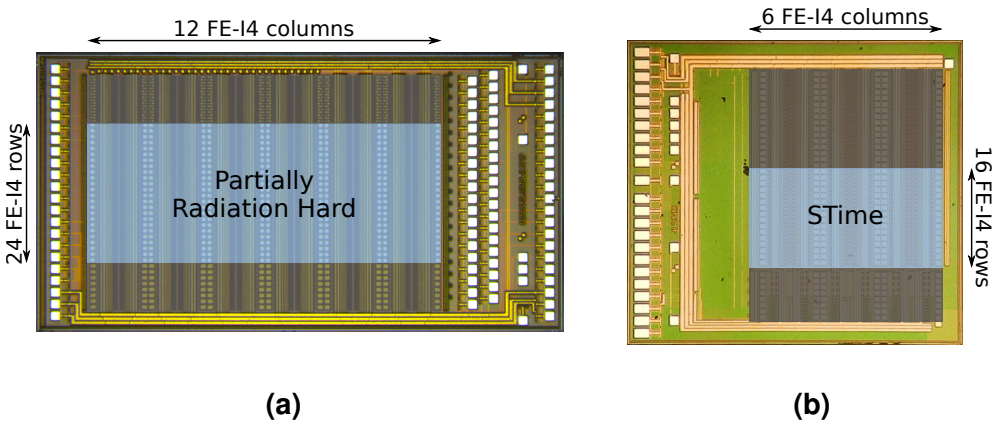

Figure 6.1: Pixel matrices of (a) HV2FEI4 version 2 and (b) version 4 prototypes investigated in test beams. The size of an FE-I4 row and column is 50 µm and 250 µm respectively. Please refer to Section 5.1.5 for further details about the prototype chips.

6.1 Data Taking and Analysis with Small Scale Prototypes

Test beam measurements with the HV2FEI4 prototypes are a challenging task due to their geometry. The small size and number of pixels requires special care while operating the sensors, setting up the beam and defining DAQ parameters.

For data analysis a proper alignment correction is essential. The performance of alignment procedures however is profiting on big active areas and large data sets, which in case of small size sensors requires careful and potentially manual tuning of the alignment parameters.

Data Taking

From the data taking point of view, the small active detector area of few mm^2 slows down the process of gathering enough statistics for a meaningful data analysis. The introduction of a Region Of Interest (ROI) for triggering, as described in Section 4.2.4, significantly increased the speed of data taking. Whenever possible the beam size was optimised reaching an approximately gaussian distribution with a standard deviation of around 5 mm.

Additionally, online monitoring is affected by the small number of pixel cells. Useful tools for monitoring the quality of the data taking are for example the display of correlations between pixel coordinates on the DUT and the telescope and the timing distribution

of the recorded hits with respect to the trigger. These distributions can be easily distorted by a few noisy pixels on the device under test.

Pixel Geometry

The pixel geometry of the HV2FEI4 sensors does not necessarily correspond to the FE-I4 readout geometry as described in Section 5.1, which has to be taken into account for data taking and analysis. The first two prototype versions implemented a chessboard structure as shown on the left side of Figure 6.2, while as of version 4 the geometry was changed to a simpler, linear one as shown the right side of the same figure. As the sub-pixel encoding was not implemented, the hits could only be distinguished at the level of Front-End readout cells. A so called macro-pixel was therefore defined as basic geometry for data analysis. In case of the version 2 samples this is the $250 \times 100\,\mu m^2$ sensor's unit-cell which comprises two FE-I4 readout cells, while for the version 4 the unit cell can be cleanly split along its short axis. There, each FE-I4 cell was mapped to half a unit cell of $125 \times 100\,\mu m^2$ size.

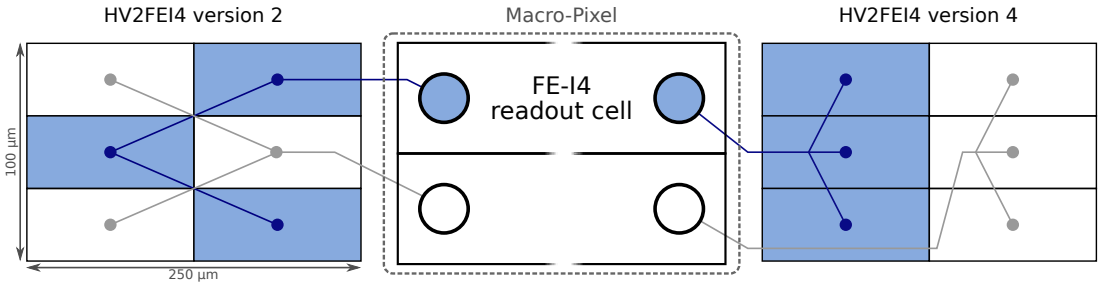

Figure 6.2: Mapping of a unit cell of the version 2 (left) and version 4 (right) sub-pixel geometry to a macro-pixel for analysis.

Noise Behaviour and Masking

HV2FEI4 sensors deliver a combined signal of three sub-pixels to an FE-I4 readout cell as shown in Figure 6.2. The sensors had therefore to be precisely calibrated to ensure a mostly noise-free operation[a], as already one noisy pixel would saturate the entire FE-I4 readout cell which would then be removed from data taking. This has further implications due to the telescope's finite resolution. A particle passing through a deactivated pixel can be wrongly reconstructed on the neighbouring pixel. As this pixel is not hit by

[a]This is particularly difficult for highly irradiated sensors.

the particle, it cannot detect it and therefore appears inefficient. For large size sensors, tracks reconstructed on the pixels next to the deactivated one would be ignored to prevent that effect. Due to their small size, this is not reasonable for HV2FEI4 sensors as it would quickly lead to a masking of a considerable part of the active area.

Additionally, the chessboard structure of the version 2 prototype necessitates that FE-I4 readout channels are masked in pairs. It results from the fact, that the three sub-pixels belonging to one FE-I4 readout cell are geometrically overlapped by two. Figure 6.3 shows the situation for an HV2FEI4 unit cell where only one readout cell (the top one in the drawing) was masked. Three regions can be identified from the geometry of the FE-I4 pixels: Region I is geometrically covered by the deactivated readout cell (upper orange frame) while region II and III are covered by the still active one. Under the active cell, region II stands for all tracks that hit a sub-pixel connected the still activated readout cell and region III for those connected to the deactivated one. From this three possible cases arise:

- The track hits region I: As the readout cell is masked, the track is simply discarded and the analysis remains unperturbed.
- The track hits region II: In this case the track can be detected by an active sub-pixel and the event can be analysed normally.
- The track hits region III: The particle hits an active readout cell but cannot be detected by the sub-pixel as it belongs to a deactivated cell. A reduced measured efficiency is the result.

To prevent this artificial degradation of efficiency in the case of region III, always a unit cell as a whole, meaning pairs of FE-I4 channels in a column, should be masked.

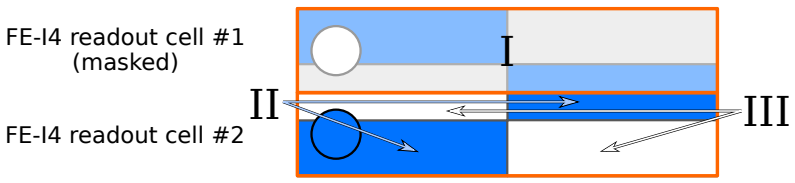

Figure 6.3: Effect of masking one readout cell of an HV2FEI4 version 2 unit cell. The orange frames show the two FE-I4 readout cells, the white (blue) rectangles, the HV2FEI4 pixels read out by the top (bottom) FE-I4 cell. Tracks hitting area I and II are unproblematic, while a hit in region III would lead to an apparently lower detection efficiency.

6.1.1 Efficiency Assessment

The assessment of detector parameters like hit detection efficency and time resolution in a test beam experiment is performed by extrapolating the particle trajectory, reconstructed with the external telescope planes, to the DUT and by evaluating its response at the position of impact. Section 4.4 explains in detail how tracks are formed and how the telescope planes and DUTs alignment is established. The track position on the DUT, however, is only defined in the limits of the telescope resolution which in turn requires to not only take into consideration the exact point of impact but also its surroundings, according to the resolution. For the HV2FEI4 sensors, an elliptic region with axis length of 1.5 times the pitch of the macro-pixel was chosen for matching possible hits to tracks as sketched in Figure 6.4. The efficiency of the pixel is then defined as

$$\varepsilon = \frac{N_{matched}}{N_{reconstructed}} \tag{6.1}$$

with $N_{matched}$ being the number of tracks matched to a hit and $N_{reconstructed}$ the number of reconstructed tracks on a pixel cell. This estimate relies on a noise-free detector, as noise hits can be misleadingly matched to a track hence artificially increase the measured efficiency at that point.

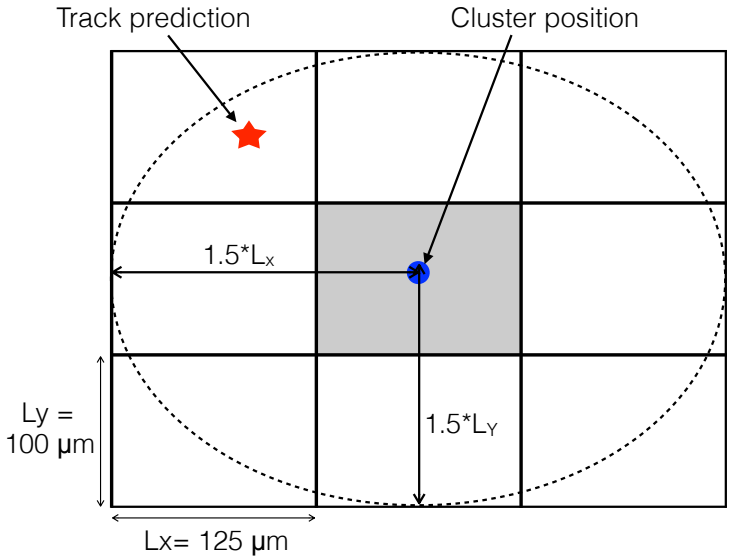

Figure 6.4: Definition of the area used to calculate the efficiency of HV2FEI4 sensors. Each $125 \times 100\,\mu m^2$ macro-pixel (gray area) is formed by three single HV-CMOS $125 \times 33\,\mu m^2$ pixels. For the version 2 prototype the macro-pixel covers a full unit cell reaching a size of $250 \times 100\,\mu m^2$ [53].

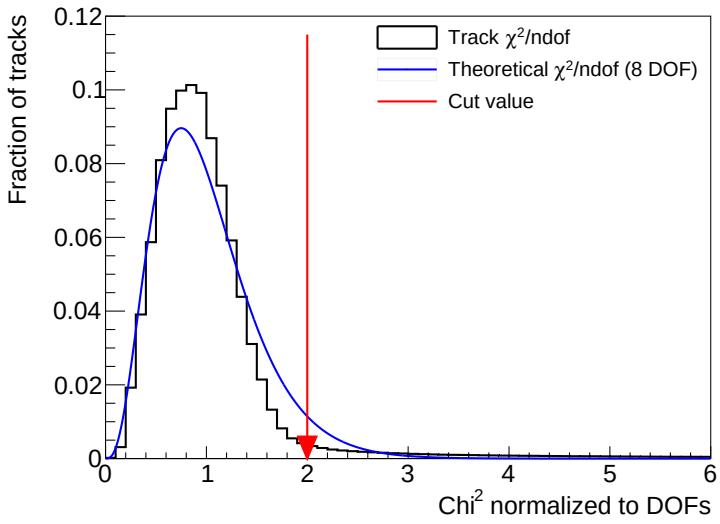

Figure 6.5: Distribution (normalised to unity) of linearly fitted tracks from SPS H8 beam data. The vertical line marks the cut applied to tracks considered for analysis.

In the vicinity of the sensor edge, tracks that have missed the DUT can falsely be reconstructed on the sensor due to the finite resolution of the telescope. To avoid a possible artificial degradation of efficiency, tracks reconstructed close to the sensor edge were rejected.

In order to reach a high accuracy, which is especially important for the in-pixel measurements, only tracks with associated hits in all planes[b], a $\chi^2/n_{\mathrm{dof}} < 2$ and a shallow angle with respect to the beam axis were selected for analysis. The χ^2/n_{dof} distribution of data taken in the SPS H8 beam and the cut value are shown in Figure 6.5.

Although the sub-pixel hit position could not be decoded at the time of the data taking, the average response of single sub-pixels can be estimated by overlaying the efficiency maps of all unit cells. The so called in-pixel efficiency maps display the average response to a particle hitting a central sub-pixel or the inter-pixel region.

6.1.2 Timing Measurements

While assessing the suitability of a pixel detector for an environment like the ATLAS ITk, fast hit detection is as important as a high detection efficiency. In fact, only hits that are detected in usually one to two bunch crossings ($1\,\mathrm{bx} = 25\,\mathrm{ns}$) can be read out in time and otherwise are discarded. This strict requirement is not posed on test beam

[b]The pointing resolution at the DUT for tracks reconstructed with a missing plane is reduced approximately by half.

measurements, where all hits in the maximum recording interval of the FE-I4, 400 ns or 16 bx are read out. However, the advantage of HV-CMOS sensors over former CMOS sensors is the fast charge collection by drift which can be measured in the test beam.

As with the efficiency, the hit timing measurements rely highly on the correct assignment of a track to a valid hit. The FE-I4 measures the hit timing as the delay of the detection of a hit with respect to the trigger with the resolution of 25 ns being defined by its 40 MHz clock. Section 4.2.5 shows however, that this measurement suffers from a non-bunched beam like at the PS T9 and SPS H8 beam lines. The Clock-Phase Veto (CPV) scheme was therefore developed and used for the irradiated version 4 prototypes.

Furthermore, due to the sampling frequency of the FE-I4, sub-structures of less than 25 ns width can not be resolved, leaving the measurements vulnerable to misalignment between the sampling point and the mean latency of the hits that can artificially enlarge the distribution. In all cases, the timing of DUTs can be compared to that of the telescope planes. As these are detectors of a type that was used to build the ATLAS IBL detector, they meet the timing criteria of ATLAS and are influenced by the non-bunched beam same as the DUTs.

6.2 Performance of HV2FEI4 Version 2 Prototypes

The version 2 devices were the first samples to be operated in the FE-I4 telescope setup after its commissioning in summer 2014. Two samples, C19 (unirradiated) and C22 ($1 \cdot 10^{15}$ n_{eq}/cm^2, neutrons) were measured where for C19 two million triggers in the PS T9 beam and for C22 4.5 million triggers were collected in the SPS H8 beam. They were configured by the UXIBO system (Section 5.2.1) and their threshold tuned in the beam area. For the following measurements, the substrate bias voltage was held at -80 V.

Test beam areas are usually equipped with various devices (e.g. pumps, magnets, cranes, etc.) which lead to a significant amount of electromagnetic interference. The version 2 prototypes were prone to pick up these signals as noise, especially via the high voltage substrate bias. A stabilisation of the bias was tried by increasing the filtering capacitances close to the bias input and replacing the high voltage power supply with a battery pack. However, the leakage current would not allow for a stable voltage level with batteries over a time span of hours which was necessary for gathering the necessary amount of data. The best possible solution was therefore to use as short as possible and shielded cables to the high voltage supply. With such a setup, a threshold tuning that would equalise the matrix (Binary Tune) would have lead to a high threshold. The matrix was therefore tuned to a mean value between 500 and 600 e using the Noise Tune algorithm (see Section 5.3).

At the time of data taking the telescope setup was still under heavy development and certain features were not available yet. In particular, the cold box was not optimised yet and the Clock-Phase Veto mechanism not implemented. The incoming dry gas was not cooled and the thermal connection between the sample PCB and the cooled base plate established by means of a copper tape. Despite a temperature of the base plate of below $-35\,^{\circ}\mathrm{C}$ only a temperature of $\sim 0\,^{\circ}\mathrm{C}$ was measured on sensor.

6.2.1 Efficiency and Timing Assessment

The efficiency for C19 and C22 per macro-pixel is plotted in Figure 6.6. A low efficiency region of four rows can be found at the bottom of both plots which corresponds to the Radiation Hard pixels. These pixels cannot be operated in parallel to the Partially Radiation Hard pixels as their threshold is intrinsically higher and thus incompatible. However, they remained active during data taking and were used for alignment, but yield no reasonable efficiency as they were untuned.

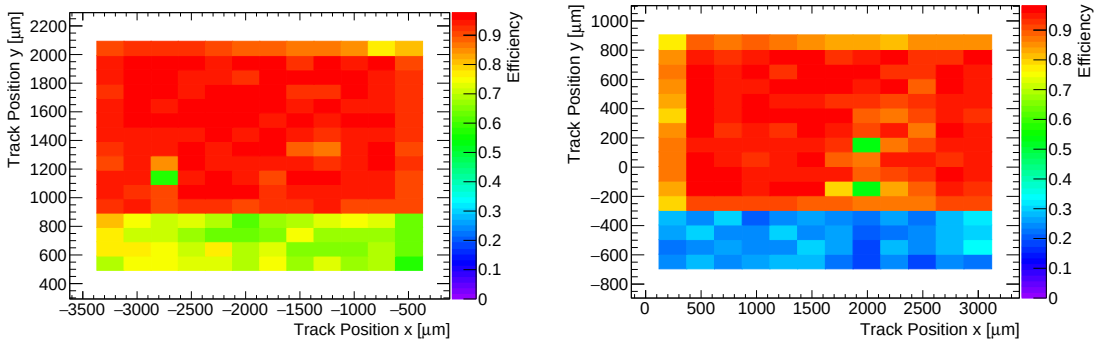

Figure 6.6: Detection efficiency maps for (a) the unirradiated sample C19 and (b) the $1 \cdot 10^{15}\,\mathrm{n_{eq}/cm^2}$ sample C22. The low efficiency regions at the bottom side of the plots originate from another pixel type with a higher threshold [85].

The Partially Radiation Hard pixel matrix of C19 shows a uniform distribution with a mean detection efficiency of $\sim 97\,\%$, excluding the edge pixels which suffer from the telescope's finite resolution. After irradiation to $1 \cdot 10^{15}\,\mathrm{n_{eq}/cm^2}$, the efficiency drops to $95\,\%$. Certain pixels show an efficiency of around $50\,\%$ hinting at a failure of a subpixel triple that was connected to one Front-End cell. Also the neighbouring pixels are affected, as tracks passing through the faulty pixels can be reconstructed on the neighbours without a possibility of being detected by the sensor. Given a significantly larger

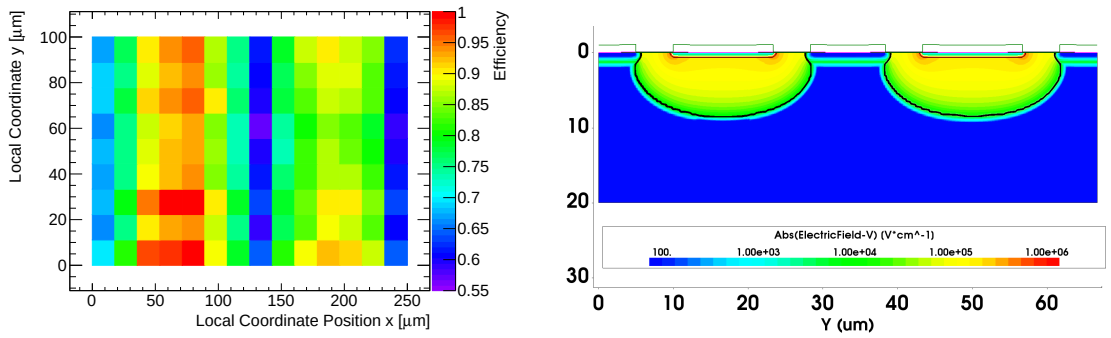

Figure 6.7: (a) Efficiency map of all pixels of C19 overlayed into one cell, showing intra-pixel inhomogeneities. (b) Simulation of the electric field distribution at $U_{Bias} = -80\,\mathrm{V}$ for the inter-pixel region of an HV2FEI4 version 2 sensor [85].

pixel matrix, this effect would be mitigated by ignoring all tracks reconstructed on the pixels around the affected one. For the HV2FEI4 sensors however this would lead to a inacceptable reduction of useable data.

Nevertheless, these considerations do not fully account for the loss in efficiency for the unirradiated sample. In order to investigate the response of the unit cell with respect to the hit position, an in-pixel efficiency map can be seen in Figure 6.7a. This map was taken deliberately with a high threshold of around 2000 e to enhance possible features. It becomes evident that the inter-pixel region in the horizontal direction suffers from a significant efficiency drop. The actual value is not representative due to the high threshold. At this position a ring electrode is implemented that distributes the high-voltage into the bulk. A TCAD simulation of this region is shown in Figure 6.7b. The plot depicts the electric field distribution under two adjacent pixel implants with the depletion zone marked by a fine black line. It confirms that the sensor bulk under the metal layer is not depleted hence the charge collection is not efficient in this region. Furthermore the in-pixel plot shows an asymmetry between the first and second column of the sensor. This has been attributed to a powering issue in the sensor design and was also observed on the ams H18 sensor for the CLIC detector, CLICpix [47].

During the campaign, a low time resolution of the sensors was observed which cannot be explained by the asynchronous beam[c]. Figure 6.8a shows the distributions for both sensors at nominal conditions. For these plots the noise baseline[d] was subtracted and

[c]For this measurement the CPV was not available yet.

[d]Noise hits introduce a constant baseline to the timing distribution as they are not correlated with the trigger.

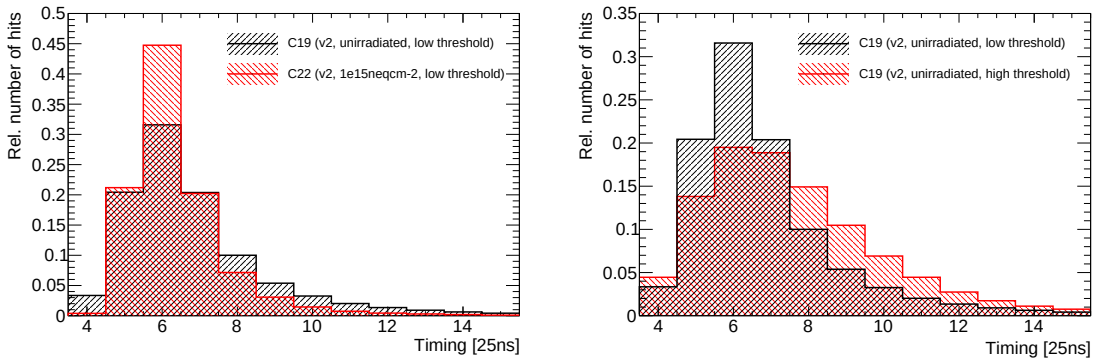

Figure 6.8: (a) Comparison of hit timings between C19 and C22. (b) Hit timing for C19 with low and high threshold settings [85].

the resulted histogram normalised to unity in order to allow comparability. The C19 timing distribution shows an RMS of 50 ns with a long tail from late hits which even exceed the FE-I4 time acceptance. This hints at a strong diffusion component in the charge collection of the sensor. Although it has been designed as a drift based sensor, the depletion zone reaches only $\sim$10 to 20 µm into the bulk due to the low substrate resistivity [45]. The Most Probable Value (MPV) for charge deposition of a MIP is around 1000 e after this length in silicon which is close to the tuned threshold. For an efficient detector of this design, a diffusion component seems necessary. This assumption is supported by the timing distribution of the irradiated sensor C22, which is compressed to a standard deviation of 33 ns and shows a greatly suppressed tail. After irradiation to $1 \cdot 10^{15}\,\mathrm{n_{eq}/cm^2}$ diffusion becomes a highly inefficient process due to trapping.

The presence of the tail after such a fluence also hints to an intrinsically low time resolution of the sensor as the charge collection via drift takes only a few ns. Figure 6.8b shows the timing distribution for the unirradiated C19 prototype operated in high (2000 e) and low ($\sim$ 550 e) threshold settings. The broadening of the distribution with the threshold level supports the assumption that the sensor is limited by its electronics. Studies conducted in reference [72] show that the response time of the CSA of the HV2FEI4 raises rapidly for low signal amplitudes.

6.3 Performance of the HV2FEI4 Version 4 with the UXIBO Setup

The HV2FEI4 version 4 samples were characterised in the SPS H8 beam in 2014 – 2016. First measurements on these samples were conducted using the UXIBO setup until it was superseded by the CaRIBOU system. As the samples were differently configured and operated with UXIBO, compared to the CaRIBOu system, their results will be discussed separately.

6.3.1 Overview and Operation of the UXIBO System

In 2014, the unirradiated sample 402 and the $1 \cdot 10^{15}$ n_{eq}/cm^2 irradiated sample 404 were measured in the SPS H8 beam. For these sensors, parameter scans of the global threshold and substrate bias value were performed. As with the version 2 samples, discussed in the last section, their discriminators were tuned to a threshold close to the noise edge (Noise Tune), resulting in an MPV of the threshold distribution of about 300 to 500 e ($\sim$0.83 to 0.84 V). However, as only a rough calibration of the injection voltage to the actually injected charge exists, the threshold will be stated in mV for the remainder of this section.

Both samples suffered from early breakdown leading to a maximum bias voltage of 12 V for the unirradiated sample and 35 V for the irradiated one as compared to 95 V that was often reached in the lab. The reason for this effect is presumably to be found in the chip's design, where the close proximity of high voltage carrying metal traces to the low voltage components leaves very little margin to manufacturing imperfections. Apart from that, the substrate bias pad is located between LV pads with a narrow spacing of 70 µm also leaving little margin for wire bonding. The fact that sample 404 was destroyed later by a spark from the HV line [94] hints at a wire bonding issue.

Between one and two million triggers were taken per data point with a tight Region Of Interest trigger mask. Figure 6.9 shows the residuals for both sensors which are comparable, but although their mean is close to zero, the obtained RMS of $\sim 145 \times 84\,\mu m^2$ stands in contradiction to the values, expected from the size of the macro-pixel. Given the telescope resolution of $11.7 \times 8.3\,\mu m^2$ and the single point resolution of the unit cell as $p_{x,y}/\sqrt{12}$ ($p_{x,y}$: unit cell pitch) the expected RMS is calculated by summation in quadrature to $\sim 73 \times 30\,\mu m^2$. This points to an issue with the calculation of the alignment, most likely a rotation. Rotations are difficult to handle for small sensors, which cannot produce an appropriate handle for corrections (lever arm) and also no procedure for rotations other than those around the beam axis were available in the reconstruction framework. Even though the limits of this particular setup have been hit, the resolution is still sufficient for an analysis of the sensor's global efficiency and timing capabilities.

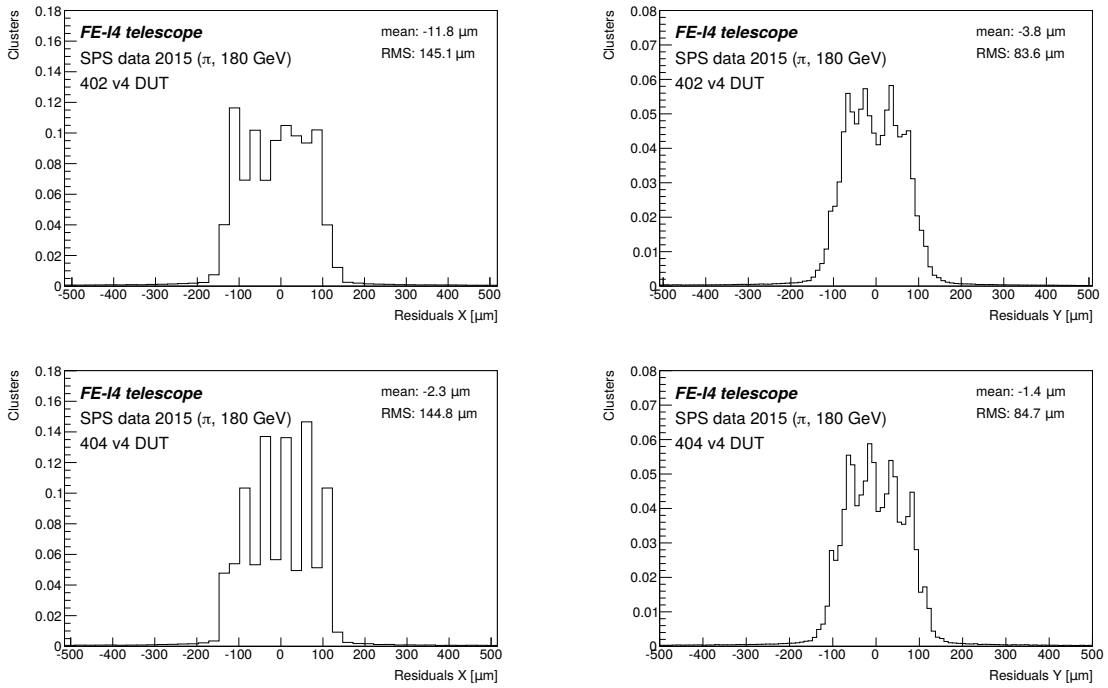

Figure 6.9: Residual distributions in X (left) and Y (right) for the analysed samples 402 (top) and 404 (bottom). Note the multi-peak structure, discussed in Section 4.5.3, which is also visible here due to the size of the macro-pixel [50].

6.3.2 Efficiency and Timing Assessment

The global efficiency maps for both sensors at a global threshold of 0.84 V are shown in Figure 6.10. As in previous measurements, the outermost pixel cells have to be excluded from analysis to avoid edge effects due to the telescope resolution. Figure 6.10a shows only the part of the matrix which is used for the analysis for 402, while the relevant parts for 404 are framed in black in Figure 6.10a. Although the sample was functioning normally, a misconfiguration during data taking lead to the deactivation of certain pixels in the two columns around 2200 µm in the vertical direction which were consequently removed from analysis. The detection efficiency of the matrices is uniform yielding a global efficiency of 99.5 % for 402 and 96.2 % for 404.

For both matrices, high voltage bias and threshold scans were performed and plotted in Figure 6.11. The high efficiency of $\sim 98\,\%$ for the unirradiated sensor without biasing strongly indicates that a big fraction of the charge is collected by diffusion, which should deteriorate after irradiation as supported by the efficiency of $\sim 30\,\%$ for the unbiased irradiated sensor. Although diffusion is strongly suppressed by trapping, detection is sup-

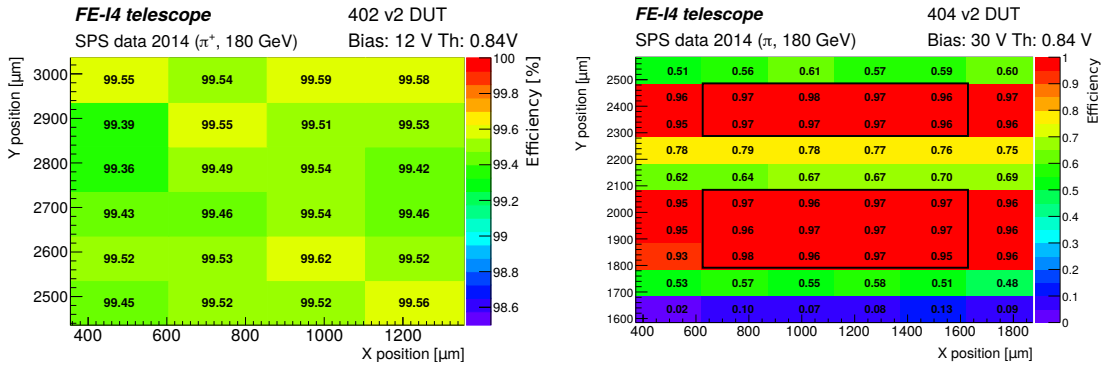

(a) **(b)**

Figure 6.10: Efficiency map of (a) the non irradiated sample 402 [88] and (b) the $1 \cdot 10^{15}\,\mathrm{n_{eq}/cm^2}$ irradiated sample 404 [50]. For 402 only the central region of the characterised matrix is shown, excluding edge pixels, which cannot be measured reliably due to the finite resolution of the telescope. For 404 only the framed regions were taken into account for the efficiency estimate for the same reasons.

ported by the intrinsic depletion zone which is greatly enhanced after $1 \cdot 10^{15}\,\mathrm{n_{eq}/cm^2}$ due to the acceptor removal effect as seen in Edge TCT measurements [45]. The performance of the irradiated sensor was mostly restored by applying a bias voltage, showing that the detector now collects charge predominantly by drift. Especially the data for the irradiated device indicates that an improvement is to be expected with higher voltage as a plateau has not been reached for 35 V. This should also mitigate the strong dependency of the efficiency on the set threshold and lead to a plateau for low thresholds.

The observations on the detection efficiency are supported by timing measurements. Figure 6.12 shows a considerable tail in both timing distributions which is suppressed for the irradiated sample as expected from the loss of the diffusion component. The remaining distribution still spans over 9 bx indicating that the time-walk observed for the version 2 samples is not entirely solved for this generation of sensors. It is also evident that the detector is limited by the integration window of the FE-I4 as there are clearly hits arriving after its upper limit.

Measurements with the version 4 sensors 402 and 404 proved that a high detection efficiency can be reached even after irradiation to fluences $1 \cdot 10^{15}\,\mathrm{n_{eq}/cm^2}$. However due to the limited biasing of the sensors and the non-uniform threshold tuning via the Noise Tune algorithm a final conclusion cannot be drawn. The measurements were therefore repeated and greatly expanded using the CaRIBOu system.

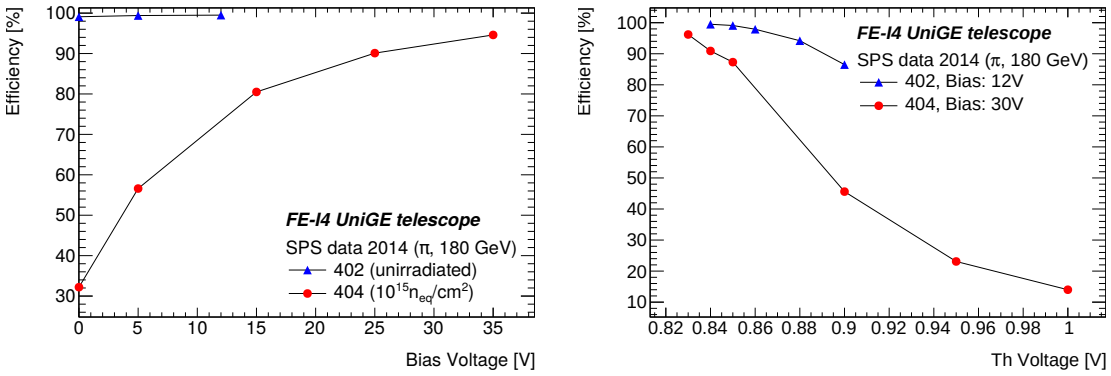

(a) **(b)**

Figure 6.11: Efficiency of 402 and 404 vs. (a) applied bias voltage and (b) threshold for the highest possible bias voltages for these samples [88].

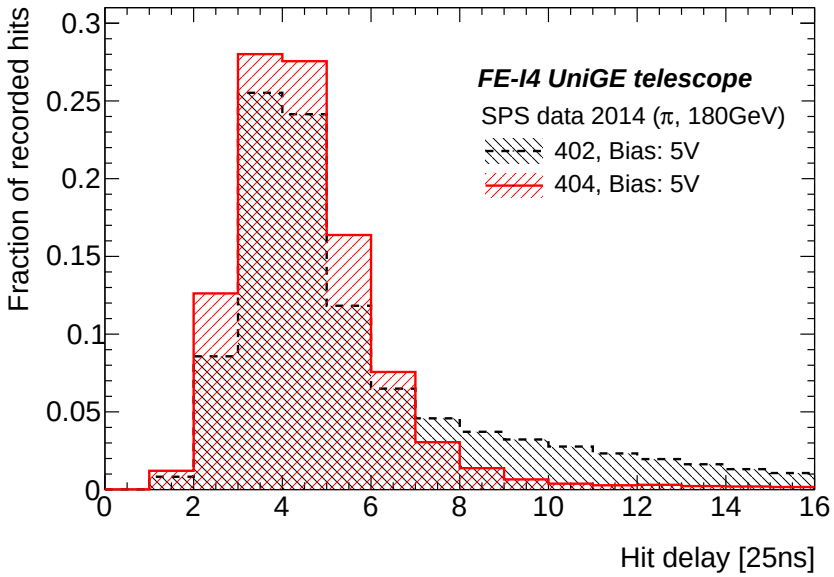

Figure 6.12: Distribution of the delay time between the telescope trigger and detection in the sensor in units of 25 ns for the 402 and 404 HV2FEI4 samples. Both distributions have been normalised to unity [88].

6.4 Performance of the HV2FEI4 Version 4 with the CaRIBOu Setup

With the availability of the CaRIBOu setup (see Section 5.2.2), as of 2015 all samples were measured using that system, effectively replacing the UXIBO test bench. The CaRIOBu setup and its inclusion in the automatic data taking of the FE-I4 telescope allowed to perform parameter sweeps efficiently, leading to a wealth of data being acquired.

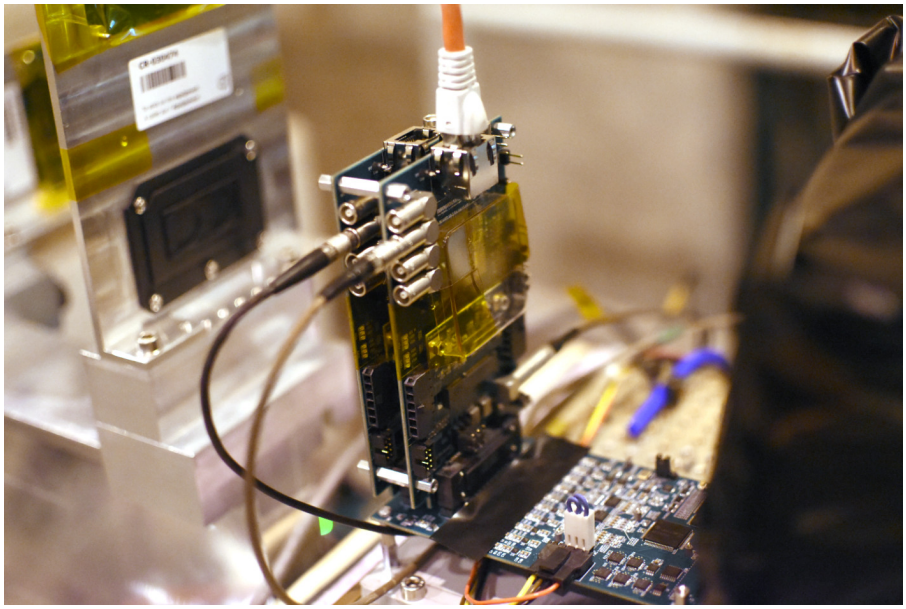

Figure 6.13: Photo of the CaRIBOu system with two HV2FEI4 version 4 samples inside the FE-I4 telescope and the first plane of the telescope's rear arm in the background.

6.4.1 Overview and Operation of the CaRIBOu System

In 2015 and 2016, multiple samples, unirradiated and irradiated up to $5 \cdot 10^{15}\,\mathrm{n_{eq}/cm^2}$, were characterised, tuned and controlled with the CaRIBOu system. Figure 6.13 shows a photo of the CaR board, installed into the FE-I4 telescope and carrying two HV2FEI4 version 4 samples. The FE-I4 Readout Chips of the samples (in the photo only the front one) were connected directly to the telescopes DAQ system although CaRIBOu is capable of reading out the FE-I4 directly, which in that case would render data taking and synchronisation difficult. All samples were thermally stabilised by air cooling. The unirradiated ones were held at room temperature (20 °C), while the irradiated prototypes were cooled to $\sim -28\,°\mathrm{C}$ to suppress the leakage current due to the bulk damage.

In terms of noise performance, a significant improvement over the UXIBO based setup was observed. This is likely to be the result of the generation of powering and bias voltages close to the chip and heavy filtering on both the CaR and the chip carrier board. The system allowed for equalising the discriminator thresholds using the Binary Tune algorithm to 607 e for the unirradiated detector and ∼600 to 860 e for the irradiated ones[e]. For the latter the injection voltage to charge calibration could not be performed. This calibration requires recording the analogue signal from the pixel cells, however the buffers of these lines saturated even for low injected charges, rendering the measurements useless. The threshold for these samples is therefore only an approximation using the calibration constant of the unirradiated sample (8.6 e/mV [63]) and will henceforth be given in mV over the baseline voltage . In contrast to prior measurements all samples were able to be biased up to 80 to 85 V.

[e]The values per sensor are noted in the diagrams or will be stated where appropriate.

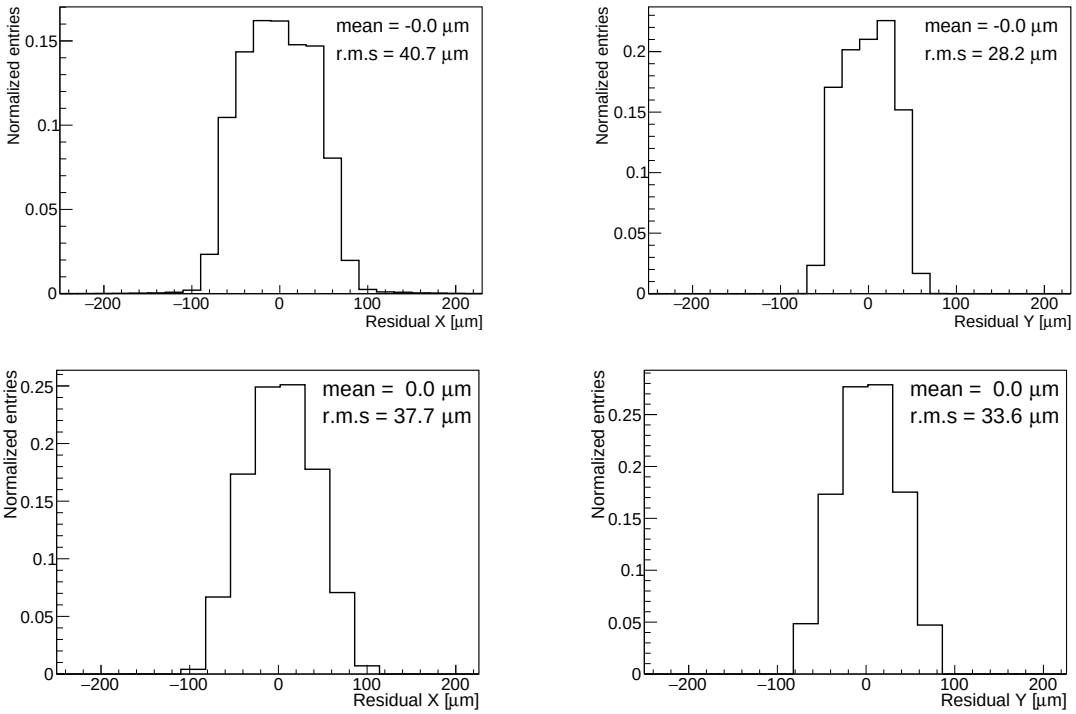

Figure 6.14: Residual distributions for the $125 \times 100\,\mu m^2$ sized unit cells in the horizontal (left) and vertical (right) plane for the unirradiated (top) and $1 \cdot 10^{15}\,n_{eq}/cm^2$ irradiated prototype (bottom). The RMS is compatible to the expected values of 37 µm (horizontal) and 30 µm (vertical).

Between 3 and 4 million triggers were taken per data point for the unirradiated and 5 million triggers for the irradiated sensors. Figure 6.14 shows the residual distributions obtained for the unirradiated and the $1 \cdot 10^{15}\,\mathrm{n_{eq}/cm^2}$ irradiated samples as example for the data taking with the irradiated detectors. All distributions are well centered around zero and their RMS agrees within few µm with the expected value of $\sim 37\,\mu\mathrm{m}$ in the horizontal and $\sim 30\,\mu\mathrm{m}$ in the vertical plane meaning that the full resolution of the telescope can be exploited for analysis.

6.4.2 Results of the Unirradiated Prototype

The efficiency map of the unirradiated sample, biased to 85 V and the discriminators tuned to 600 e, is shown in Figure 6.15a. It reached an average value of 99.7 % excluding the outermost pixels to avoid edge-effects. As with the version 2 samples, the in-pixel efficiency was evaluated by projecting the data for all *STime* pixels into one macro-pixel. In Figure 6.15b the resulting efficiency map is plotted which shows a slight attenuation in efficiency towards the edges hinting at charge sharing.

A measure for charge sharing is the distribution of cluster sizes as shown in Figure 6.16a. In the SPS H8 beam line, particles hit the detector almost perpendicularly. However only $\sim 78\,\%$ lead to single-hit clusters, while in $\sim 20\,\%$ of the cases two-hit clusters

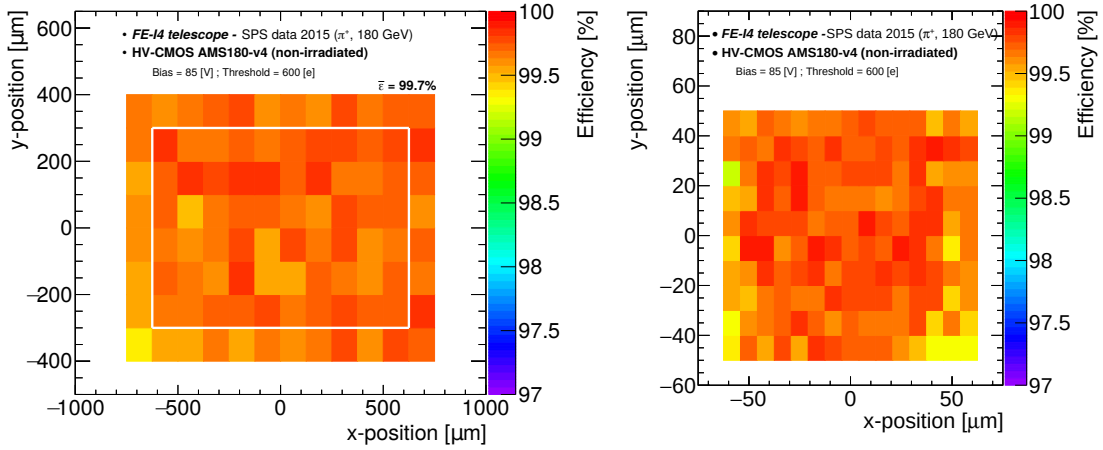

Figure 6.15: (a) Efficiency map of an unirradiated HV2FEI4 version 4 sensor. For the computation of the average global efficiency only the pixels inside the white box are used to avoid edge effects. (b) Efficiency inside a *macro-pixel* of $125 \times 100\,\mu\mathrm{m}^2$, corresponding to three single HV-CMOS pixels connected to one FE-I4B readout cell [63].

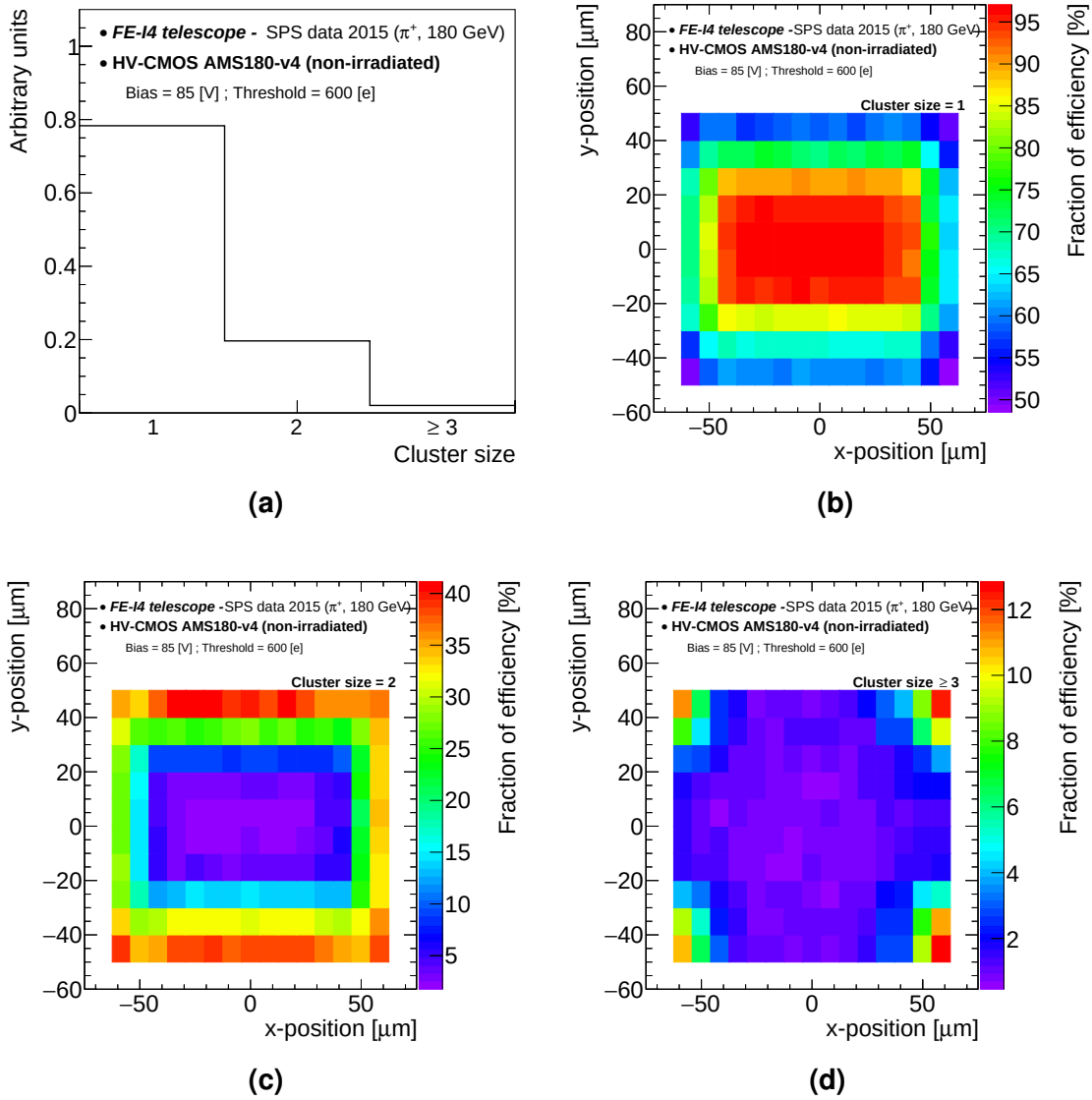

Figure 6.16: (a) Cluster size distribution for normal incidence tracks and nominal operating conditions. The distribution has been normalised to unity. (b) to (d) Relative contributions to the efficiency inside a *macro-pixel* according to their cluster sizes [63].

were formed. The occurrence of a significant fraction of two-hit clusters is attributed to diffusion which was already shown to contribute significantly to the signal of unirradiated devices during the UXIBO campaign.

The contribution to the in-pixel efficiency versus cluster size is shown in Figures 6.16b to d. It is evident that the high efficiency of the central part results mainly from clusters with one hit. The edges are populated by two-hit clusters which is expected from charge sharing while the remaining cluster sizes contribute to the corners of the pixel cells.

For this sample, threshold and bias voltage scans were performed. The efficiency versus threshold can be seen in Figure 6.17 for which three regions were identified and their approximate edges marked by red lines. For a low threshold, the detector cannot be operated properly as more and more pixels become noisy, while for a too high threshold smaller charge deposits remain undetected. Between these two regions a plateau emerges in which the detector can function efficiently. The broad width of the plateau of $\sim 300\,\mathrm{e}$ indicates that it is operated far from its limits which relaxes the requirements on the threshold equalisation as the reached sigma of the threshold distribution remains with a value 73 e well within the plateau.

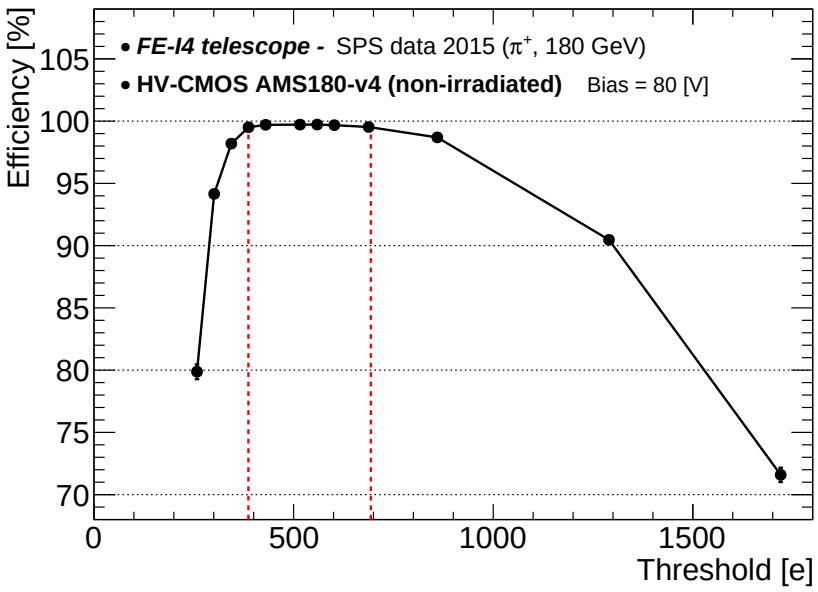

Figure 6.17: Efficiency as a function of threshold. The two vertical dashed lines enclose the interval in which the sensor's efficiency exceeds 99.5 % [63].

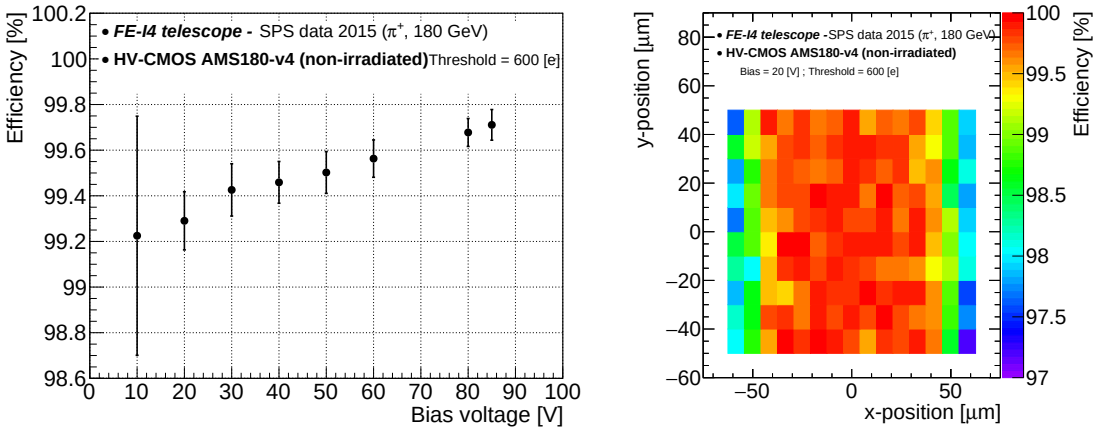

(a) **(b)**

Figure 6.18: (a) Efficiency as a function of bias voltage and (b) in-pixel efficiency map for a bias voltage of 20 V [63].

Figure 6.18a shows the sensor behaviour with respect to high voltage [f]. Even for a bias voltage as low as 10 V the detector is highly efficient with over 99 % detection probability as it is expected from a diffusion dominated signal. The performance increases with high voltage as also the depletion zone grows, placing the results in good agreement with those from the unirradiated UXIBO sample 402. By observing the in-pixel efficiency for a low bias voltage of 20 V, as plotted in Figure 6.18b, regions of inefficiency at the edges of the pixel column appear. This effect was already observed at the version 2 prototypes and attributed to the biasing metal traces implemented in that region. In view of the version 2 results, the width of these traces was reduced which explains why the effect is less pronounced in this sensor generation.

Timing properties of the prototypes have been evaluated with respect to cluster size, bias voltage and threshold. Figure 6.19a shows the timing of the recorded hits with the sensor fully biased and at a threshold of 600 e. Although most hits fall into four bins, a long tail from late hits is visible. By plotting the distributions for single-hit and double-hit clusters separately (Figures 6.19b and 6.19c) it becomes evident that the tail is dominated by the latter.

For single-hit clusters the charge is deposited centrally in the pixel and in case of high bias voltage the drift part of the signal can quickly drive the discriminator over threshold.

[f] The large statistical uncertainty for the first data point is due to a mistake during data taking where the ROI triggering was not activated so that only a small fraction of the recorded tracks passed through the sensor.

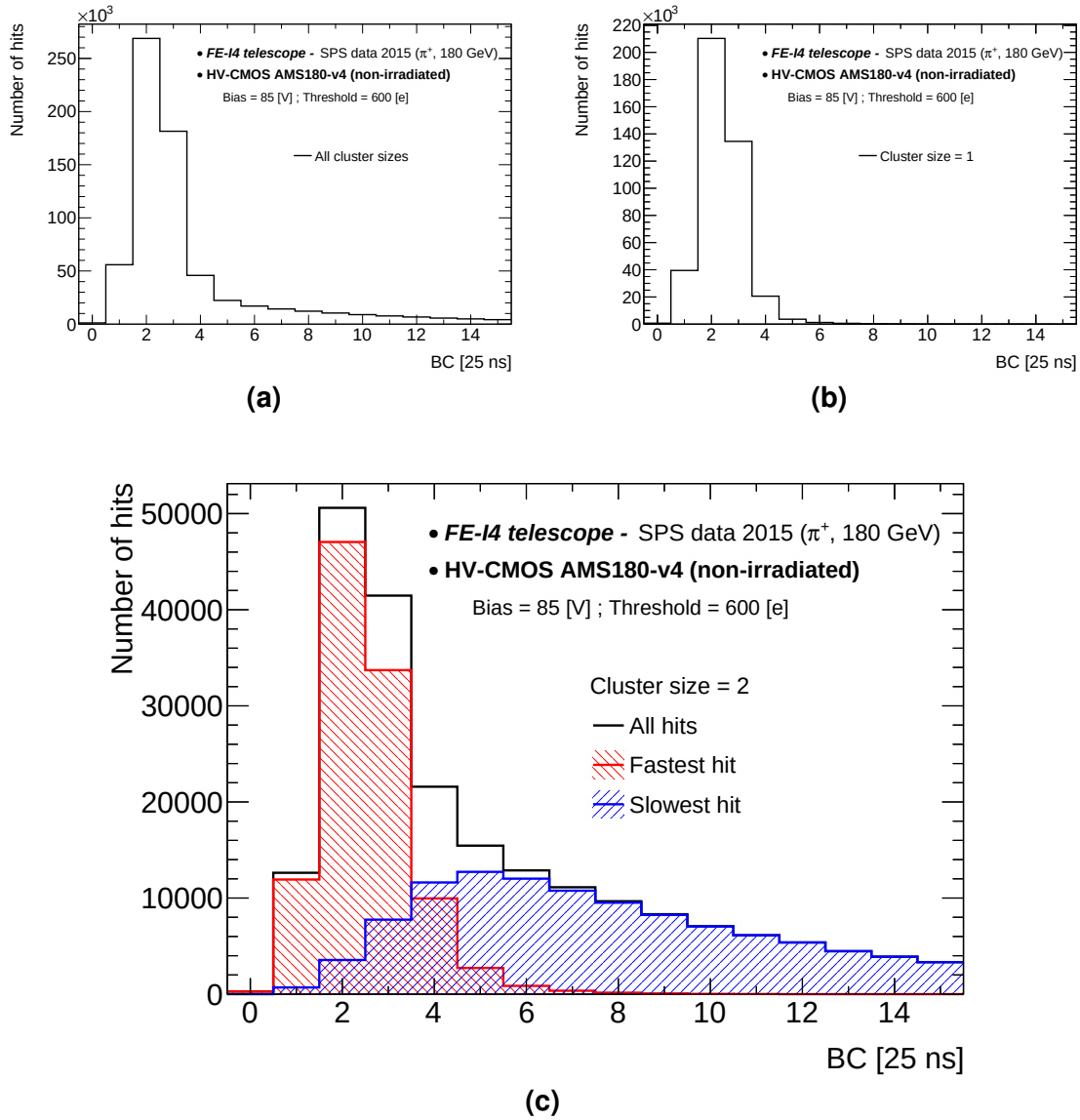

Figure 6.19: Timing distribution of the DUT hits in units of 25 ns for (a) all cluster sizes, (b) cluster size one and (c) two. In the latter, the distribution to the measured time from each of the two pixels in the cluster is shown [63].

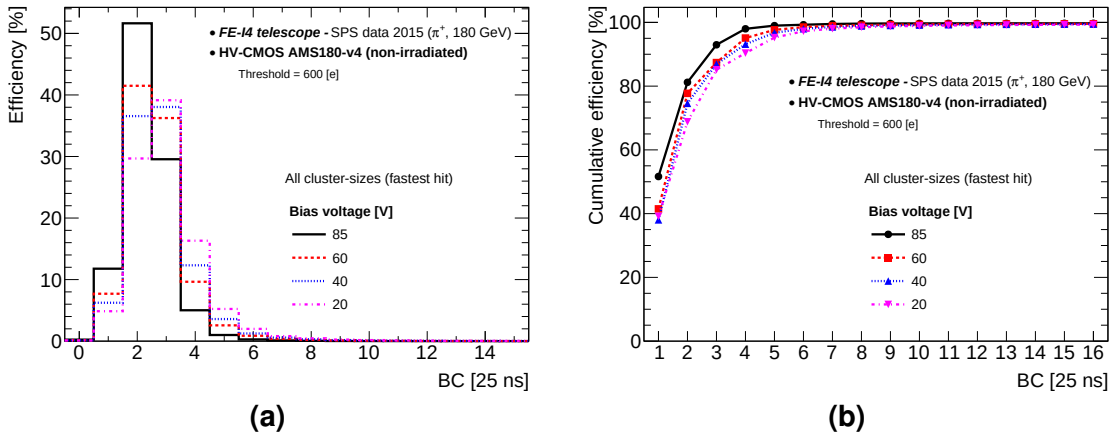

Figure 6.20: (a) Efficiency and (b) cumulative efficiency versus hit timing for different bias settings. For multi-hit clusters only the fastest hit is shown [63].

In case of two hit clusters, a part of the charge has to diffuse to the neighbouring pixel and depending on the impact of the particle in the primary one, only a fraction of the deposited charge reaches the secondary one. Due to the time-walk of the amplifier, this signal is then detected late. In order to investigate the drift part of the signal collection, especially as diffusion will be highly suppressed after irradiation, the following analysis considers only the fastest hit in a cluster.

In Figure 6.20a the efficiency contribution with respect to the detection time and the bias voltage is plotted. The dispersion decreases with rising bias voltage and the mean is shifted towards earlier times. Both observations can be explained by the fraction of charge being collected by drift which rises with bias voltage. Another way to assess the timing capabilities, is to interpret the cumulative efficiency versus integration time which is shown in Figure 6.20b. For this plot the efficiency contributions were accumulated starting at the maximum efficiency bin and adding the neighbours sorted by their value, hence containing the necessary integration time for a certain efficiency. It shows that at full bias an efficiency over 90 % is reached after three bx with the trend flatting out after five bx. Although the raise in efficiency between 20 V and full bias is only around 0.4 % a high voltage is needed in order to compress the timing distribution.

Figure 6.21 demonstrates the effect of the threshold on the timing distribution for a bias voltage of 80 V. It shows a clear dependence of hit detection latency with threshold which again is an indicator for time-walk of the amplifier signal. In case of a constant rise time for all signal sizes, the threshold would merely influence the detection efficiency. The distribution however is compressed for lower thresholds even in the high efficiency

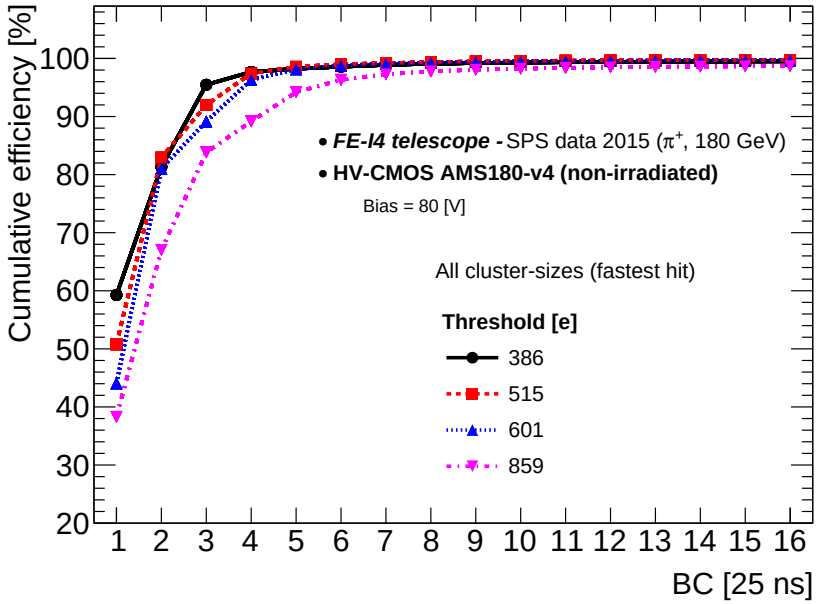

Figure 6.21: Efficiency vs. hit timing in units of 25 ns for different threshold settings [63].

plateau (lowest three threshold settings in this figure) identified in Figure 6.17.

The measurements on the unirradiated HV2FEI4 version 4 sensor using the CaRIBOu system confirmed and greatly expanded the findings of the UXIBO based campaign. A high efficiency of 99.7 % was reached with a fully biased sensor, operated at an equalised threshold of 600 e. It could be shown that the requirements on the bias and threshold settings with respect to efficient hit detection are relaxed. A 300 e wide plateau of almost constant efficiency was identified for the threshold settings and increasing the bias voltage from 10 to 85 V improved the efficiency by $\sim 0.7\,\%$. However, as expected for a sensor with a shallow depletion zone in the order of 10 µm, a significant fraction of charge is collected by diffusion. Together with the identified time-walk of the amplifier this has a significant impact on the time resolution of the detector. In terms of timing, a high bias voltage and a low threshold are therefore necessary for efficient detector operation.

6.4.3 Results after Irradiation to HL-LHC Fluences

In this study, conducted in 2016 at the SPS H8 beam line, three samples were measured with two previously neutron irradiated at JSI to $1 \cdot 10^{15}$ and $5 \cdot 10^{15}\,\mathrm{n_{eq}/cm^2}$ and one initially proton irradiated in Bern to $1.3 \cdot 10^{14}\,\mathrm{n_{eq}/cm^2}$. The last sample was measured in the beam and again irradiated to a total fluence of $5 \cdot 10^{14}\,\mathrm{n_{eq}/cm^2}$ before being re-measured. Discriminator thresholds of all samples were equalised by the CaRIBOu system. However as NIEL effects from irradiation induce a high leakage current thus noise, the minimum achievable threshold varies between the samples. In order of increasing fluence, global thresholds of 0.07 V($\sim$ 600 e), 0.09 V($\sim$ 690 e), 0.08 V($\sim$ 770 e) and 0.1 V($\sim$ 860 e) were set. Values in electrons are mere approximations as a calibration was not possible as described earlier. All samples could be fully biased up to 85 V, however the $5 \cdot 10^{14}\,\mathrm{n_{eq}/cm^2}$ irradiated one experienced elevated noise levels at voltages higher than 60 V and was therefore operated at that voltage for the detailed studies.

In general, sensors have to prove to be operational at the target fluence of the ITk outer pixel layers of $1 \cdot 10^{15}\,\mathrm{n_{eq}/cm^2}$ on which the focus will be laid during this study. The global efficiency map at this fluence is shown in Figure 6.22a. The prototype, biased to 85 V and tuned to 80 mV, is uniformly sensitive with a mean efficiency of 99.7 %. This value has been taken rejecting tracks up to 20 µm from the sensor edge to prevent the influence of reconstruction artifacts. Also the in-pixel efficiency plotted in Figure 6.22b demonstrates a very uniform response of the macro-pixel with no visible structures at the level of 1 %.

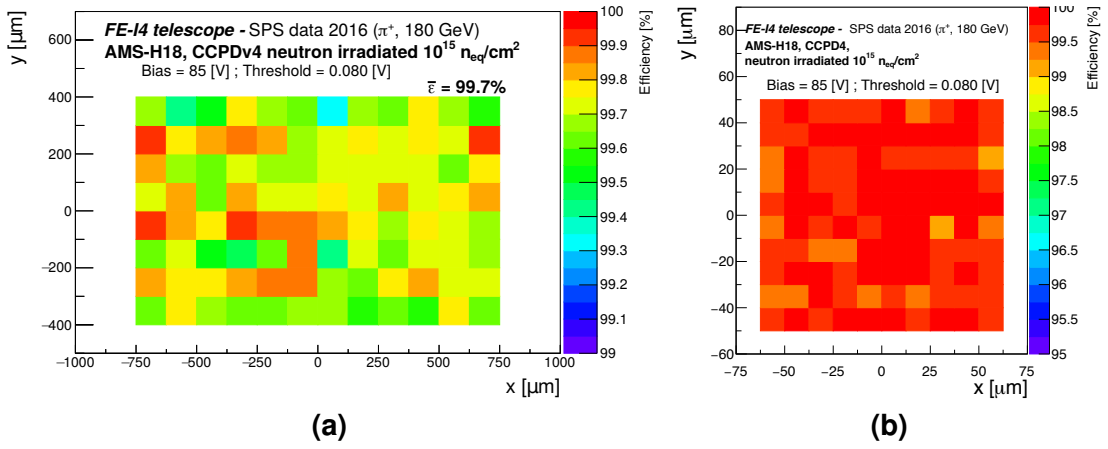

(a) (b)

Figure 6.22: (a) Hit efficiency map for an HV2FEI4 version 4 sample, neutron-irradiated to $1 \cdot 10^{15}\,\mathrm{n_{eq}/cm^2}$. (b) Overlay of all central pixels showing the in-pixel hit efficiency [53].

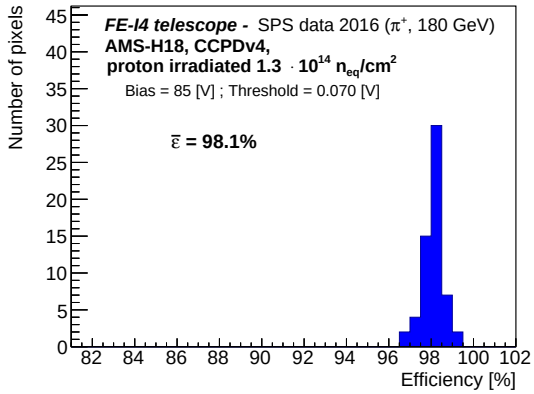

(a) Hit efficiency for $1.3 \cdot 10^{14}\,\mathrm{n_{eq}/cm^2}$ (p)

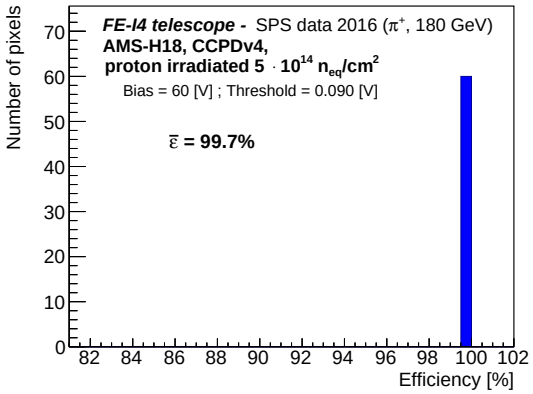

(b) Hit efficiency for $5 \cdot 10^{14}\,\mathrm{n_{eq}/cm^2}$ (p)

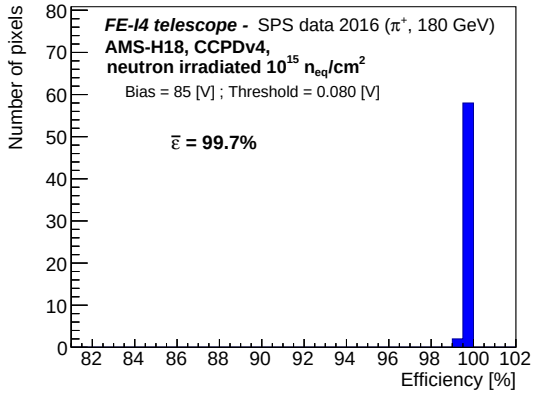

(c) Hit efficiency for $1 \cdot 10^{15}\,\mathrm{n_{eq}/cm^2}$ (n)

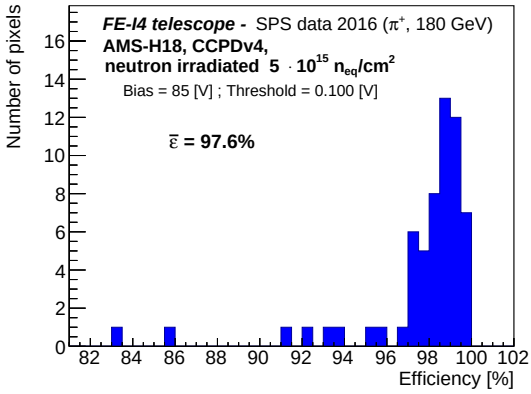

(d) Hit efficiency for $5 \cdot 10^{15}\,\mathrm{n_{eq}/cm^2}$ (n)

Figure 6.23: Hit efficiency histograms for HV2FEI4 version 4 prototypes irradiated to different fluences of protons (upper row) and neutrons (lower row). The thresholds of 70, 80, 90 and 100 mV are assumed to be equivalent to 600, 690, 770 and 860 $\mathrm{e^-}$, respectively [53].

For comparison with other fluences and easier identification of outliers, the efficiency of all prototypes is histogrammed in Figures 6.23a-d. All prototypes demonstrated high detection efficiencies with a mean of (in order of increasing fluence) 98.1 %, 99.7 %, 99.7 % and 97.6 %. For $1 \cdot 10^{15}\,\mathrm{n_{eq}/cm^2}$ the distribution shows several outliers ranging down to 83 %. At these fluences the silicon crystal is already heavily damaged and single pixels may become unexpectedly noisy or loose efficiency due to a high leakage current. It should be noted that the $1.3 \cdot 10^{14}\,\mathrm{n_{eq}/cm^2}$ sample had a lower efficiency than the next higher irradiated ones. This is attributed to the low charge collection region seen by TCT measurements and which will be discussed further in the scope of parameter sweeps.

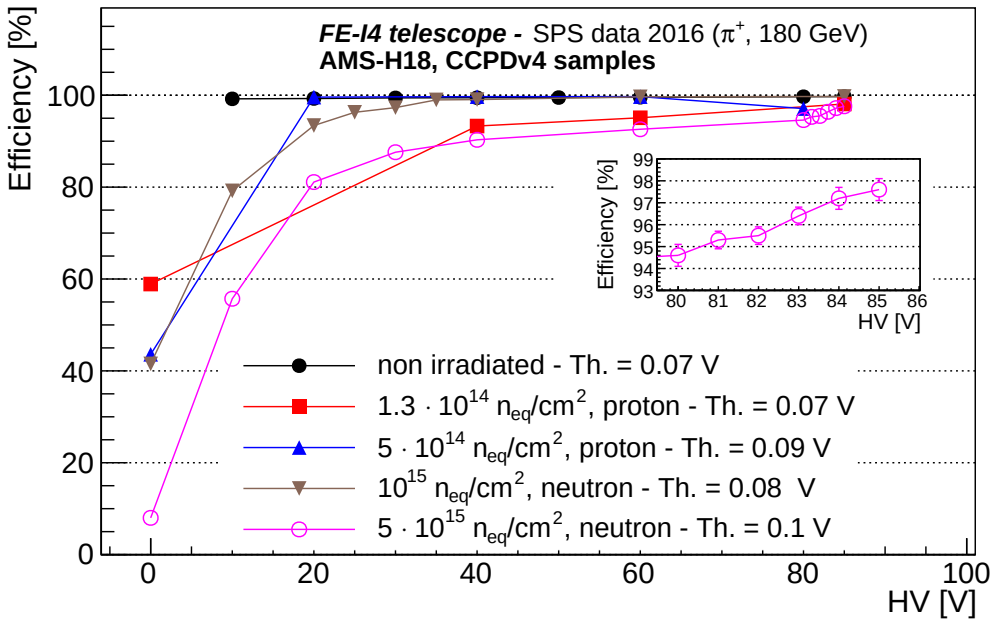

Figure 6.24: Average hit efficiency as function of bias voltage. The inset shows the sudden increase in efficiency between 80 and 85 V, which is attributed to charge multiplication. The thresholds of 70, 80, 90 and 100 mV are assumed to be equivalent to 600, 690, 770 and 860 e, respectively [53].

The efficiency values versus bias voltage can be found in Figure 6.24. A plateau is reached after 40 V, but especially for the lowest and highest fluences a significant improvement in detection can be reached by high bias voltages. Values for the lowest bias voltage show a decrease in efficiency with fluence, which is expected as the diffusion component deteriorates rapidly with irradiation. However the trend of the low voltage region up to the plateau shows a significant recovery of the sensitivity leading to a highly efficient plateau region. For these fluences the depletion zone is enlarged due to the acceptor removal effect that leads to an increase in substrate resistivity. After the highest fluences however, this effect cannot fully counteract trapping and the efficiency cannot be sustained. As described above, the $5 \cdot 10^{14}$ n_{eq}/cm^2 sample became noisy for the highest bias voltage which is also visible in the reduced efficiency of the 85 V data point for that sample.

For the highest fluence, a rapid increase in efficiency close to its breakdown voltage was observed. The inset in Figure 6.24 shows its behaviour between 80 and 85 V. This effect was also observed on other ams H18 detectors [95, 96] and was attributed to charge multiplication. It is known from highly irradiated ($>1 \cdot 10^{15}$ n_{eq}/cm^2) planar and 3D sen-

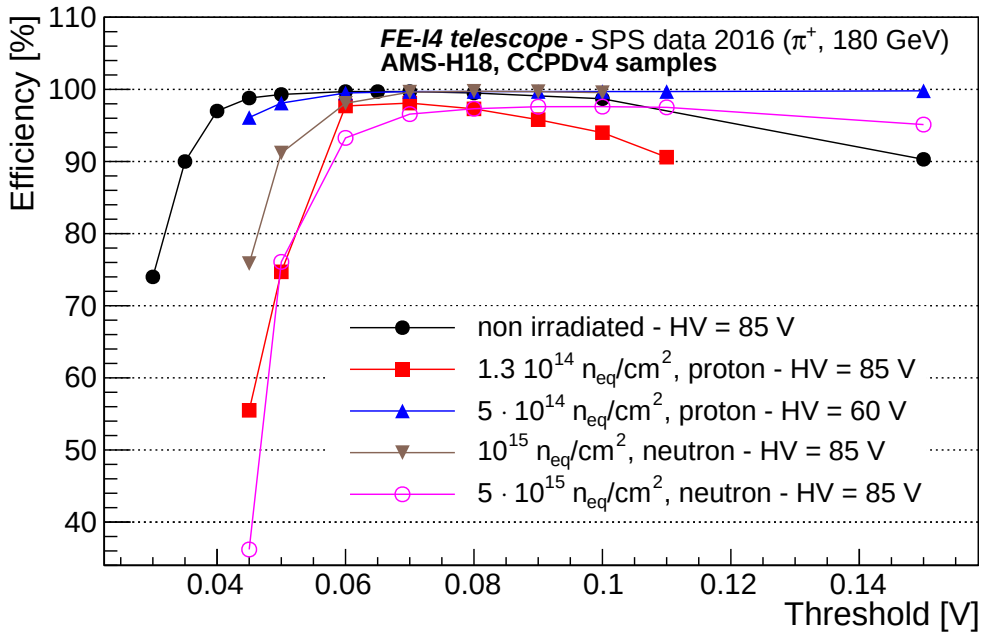

Figure 6.25: Average hit efficiency as a function of threshold voltage [53].

sors in the presence of a high electric field combined with trapping [97]. Here free charge carriers can obtain enough energy to ionise atoms on impact, leading to an amplification effect which is correlated with an increase in noise and leakage current for the passage of a particle. The increase of efficiency combined with an increase of the leakage current in this sensor indicates that indeed the charge multiplication effect is present in HV-CMOS devices.

Results from threshold scans in Figure 6.25 show again the threefold structure as discussed for the unirradiated sample. For high threshold settings there is a loss of efficiency due to low charges not being detected while for low thresholds the pixels become too noisy for operation. In between, plateaus of stable high efficiency appear with the highest width for the intermediate fluences. This is expected from observations of the HV scan as the highest signal after irradiation can be found for values where the charge trapping is compensated by the acceptor removal effect. In the low threshold region, before the reduction in efficiency due to noise, the minimum threshold rises with fluence (0.06 V, 0.06 V, 0.07 V, 0.09 V) which can be explained by the elevated levels of bulk leakage current after irradiation. This especially limits the $1.3 \cdot 10^{14}\,\mathrm{n_{eq}/cm^2}$ and $5 \cdot 10^{15}\,\mathrm{n_{eq}/cm^2}$ samples as they suffer from low signal sizes.

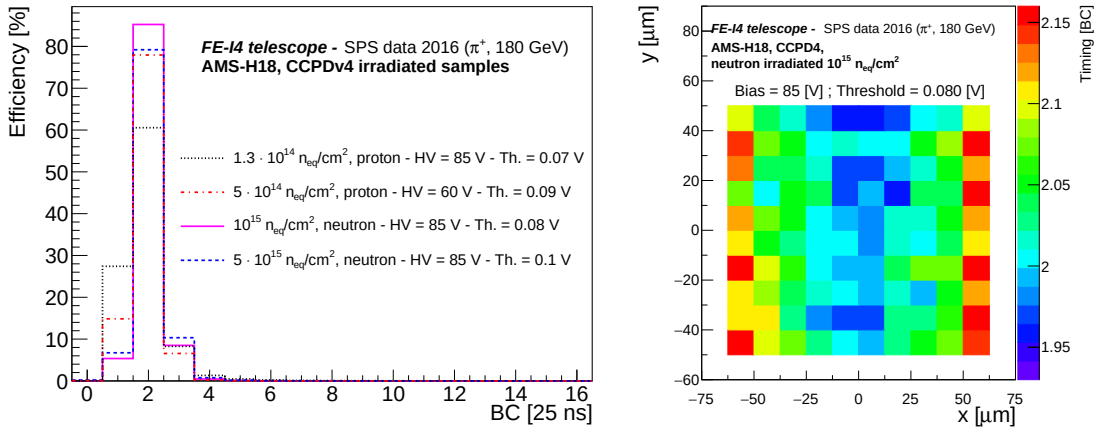

(a) **(b)**

Figure 6.26: (a) Hit timing distributions for the four irradiated HV2FEI4v4 samples at their operational bias voltages. (b) In-pixel timing map showing the mean timing of hit detection with respect on the particle impact position [53].

The reduced diffusion has also a clear impact on the distribution of cluster sizes. While for the unirradiated samples $\sim 20\,\%$ of the hits produced multi-hit clusters, the fraction of two-hit clusters is suppressed to 2 to 4 % after irradiation, with the fraction of greater cluster sizes staying well below 1 %. For the timing measurements again only the fastest hit of a multi-hit cluster was considered, however due to the predominant one-hit clusters this has little effect on the result.

The efficiency contribution with respect to the timing bin was calculated and can be seen in Figure 6.26a. In contrast to the campaign with the unirradiated sensors, for these measurements the Clock-Phase Veto (CPV) mechanism was activated. The timing resolution of the detectors improves with irradiation till $1 \cdot 10^{15}\,\mathrm{n_{eq}/cm^2}$, leading to an efficiency of $> 85\,\%$ for one bx and $> 95\,\%$ after integration over three bx for this value. Again, this can be explained by the elevated signal sizes after irradiation which mitigate the time-walk effect as seen before.

The effect of the signal size can be found in the timing distribution versus bias voltage in Figure 6.27. As the diffusion component after $1 \cdot 10^{15}\,\mathrm{n_{eq}/cm^2}$ is negligible and only the fastest hits in multi-hit clusters are considered, this plot directly shows the performance of the amplifier with signal size. The in-pixel mean timing map in Figure 6.26b demonstrates further that the late hits originate from the sides of the macro-pixel. As shown for the unirradiated sample, this is a region of low field which leads to a lower collected charge, thus to a degraded timing performance.

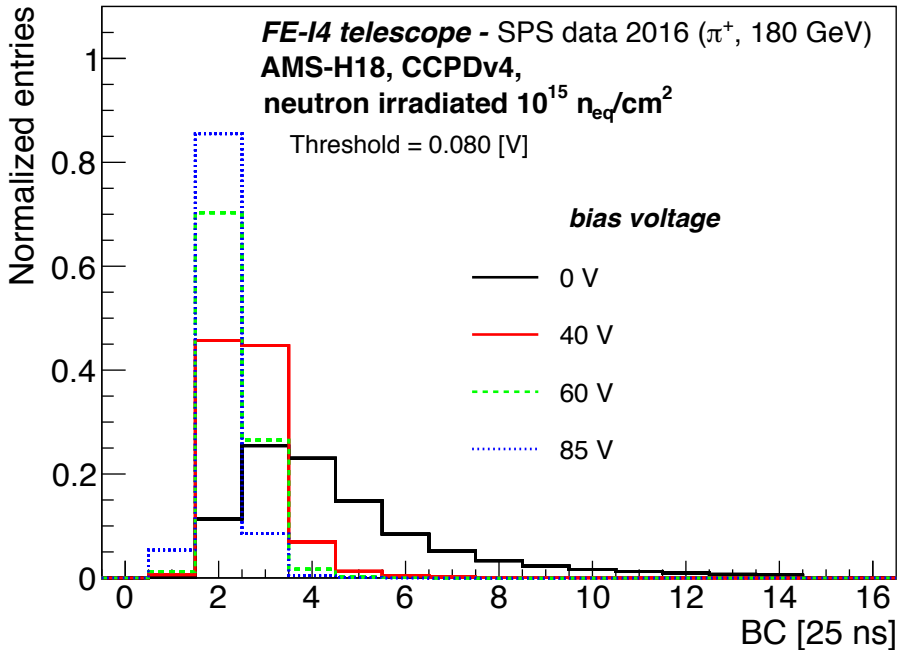

Figure 6.27: Hit timing distributions for the $1 \cdot 10^{15}\,\mathrm{n_{eq}/cm^2}$ irradiated HV2FEI4 version 4 sample at different operational bias voltages [53].

6.5 Summary - Evolution of HV2FEI4 Sensors

Since 2007 HV-CMOS sensors have been investigated as candidate sensors for the ATLAS ITk upgrade. As such, several generations of HV2FEI4 small scale prototypes were designed and characterised. The versions two and four mark milestones in this developments as the former introduced radiation hard designs and the latter a revamped signal processing chain and a stabilised signal transfer to the readout chip. Consequently these prototypes underwent a thorough investigation in the CERN PS and SPS test beams focused on their hit detection efficiency and timing properties.

6.5.1 Low Threshold Capabilities

HV2FEI4 sensors are built upon a low resistivity substrate, thus the signal size is inherently small (Most probable value for charge deposited by a MIP in the depletion zone is $\sim 1000\,\mathrm{e}$) as the depletion zone extends only up to some $10\,\mu\mathrm{m}$ into the bulk, compared to the full depletion of a $200\,\mu\mathrm{m}$ ATLAS IBL planar sensor. A low threshold setting is therefore paramount for efficient sensor operation. All HV2FEI4 sensor generations demonstrated a possible low threshold of $\sim 500\,\mathrm{e}$ or below. However, these thresholds

were reached with different tuning mechanisms depending on the use-case for the detector. The results presented in this chapter were entirely taken in a test beam environment which induces a lot of noise into the detectors. Tunings that were obtained in the lab could usually not be used directly in the beam area, so the samples were retuned in-situ which means that the given values can be considered upper limits for these detectors.

Due to the "dirty" environment of the beam area, initially detectors were tuned to their lowest possible threshold using the Noise Tune algorithm. The version 2 prototypes reached a level of 500 e using this tuning. With the redesign of the amplifier and discriminator the stability and noise performance of version 4 prototypes was improved leading to lower minimum thresholds of 300 to 400 e. Although low thresholds are necessary for efficient detection, the Noise Tune produces a non-uniform pixel matrix which is not favoured for actual detector operation and also limits comparability between devices. Furthermore the properties of a pixel detector tend to shift with time, temperature, occupancy and eventually radiation. Operating a sensor right at its noise edge would require a frequent recalibration.

Studies with the CaRIBOu system therefore switched to the Binary Tune method in order to obtain a uniform matrix. In general, the prototypes demonstrated a more stable and reproducible behaviour compared to the UXIBO based system. Stable points for unirradiated version 4 samples were found at 400 to 600 e which was shown to be still low enough for efficient operation.

After irradiation, the minimum threshold increased for all designs as expected due to the elevated noise levels, following the rise of leakage current. After $1 \cdot 10^{15}$ n_{eq}/cm^2 and with Noise Tuning, the version 4 samples reached a threshold of 500 e which is around 100 e lower than for equally irradiated version 2 prototypes. The CaRIBOu samples were again tuned to equilibrium and for $1.3 \cdot 10^{14}$ n_{eq}/cm^2 could remain in the threshold region of the unirradiated module with ~ 600 e. The consecutive irradiation up to $5 \cdot 10^{15}$ n_{eq}/cm^2 then required an increase up to ~ 860 e which is mitigated by the increase of collected charge thanks to the acceptor removal effect.

6.5.2 Hit Detection Efficiency

The detection efficiency of prototypes was measured with various discriminator threshold settings and substrate bias voltages. All prototypes demonstrated a high efficiency above 99 % before and above 95 % after irradiation. Although the HV2FEI4 sensors, in contrast to earlier plain CMOS based detectors, are capable of collecting a significant amount of charge by drift, the fraction collected by diffusion cannot be neglected.

The version 2 sensors For the unirradiated version 2 prototype initially an efficiency of $\sim 97\,\%$ was measured. This value was improved in later measurements to $\sim 99.6\,\%$ by a more careful tuning and increased bias voltage [98]. The improvement shows that for this sensor generation the performance is highly dependent on a careful choice of operational parameters. The region of lower efficiency was identified by in-pixel efficiency measurements, shown in Figure 6.7a, as a low field region between pixel columns, generated by the high-voltage distributing metal traces. This is in line with simulations of the electric field distribution under the pixel implants and can explain the degraded performance of the $1 \cdot 10^{15}\,\mathrm{n_{eq}/cm^2}$ irradiated sensor. Although the depletion zone should grow as suggested by TCT measurements, the shielding metal traces would prevent the development between the pixels. This was mitigated in the version 4 design by slimming of the metal traces.

The version 4 sensors The version 4 samples were measured with the UXIBO and CaRIBOu control systems. Full parameter sweeps of the high voltage and threshold settings were performed for fluences up to $5 \cdot 10^{15}\,\mathrm{n_{eq}/cm^2}$. The unirradiated sensor reached an efficiency of 99.7 % at full bias and low threshold. However, at low bias voltages the sensor is still highly sensitive with a value of 99.2 % indicating strongly at a high fraction of charge, collected by diffusion. This is further supported by the efficiencies obtained for irradiated sensors without bias of 60 % ($1.3 \cdot 10^{14}\,\mathrm{n_{eq}/cm^2}$), 42 % ($1 \cdot 10^{15}\,\mathrm{n_{eq}/cm^2}$) and 17 % ($5 \cdot 10^{15}\,\mathrm{n_{eq}/cm^2}$). For the highest fluencies the detector becomes greatly inefficient as the diffusion component is mostly suppressed by charge trapping. However by application of a high voltage the irradiated sensors recover up to the performance of the unirradiated one as shown in Figure 6.24. This results from a strong drift signal and the increased substrate resistivity due to the acceptor removal effect. For the intermediate fluence of $1.3 \cdot 10^{14}\,\mathrm{n_{eq}/cm^2}$ the onset of trapping reduces the collected charge while the acceptor removal effect is not yet pronounced sufficiently to compensate for that. This reflects the results obtained from TCT measurements [99]. All prototypes, but especially the unirradiated and intermediate fluence ones, produce an efficiency plateau with respect to high voltage in which the sensor can be operated conveniently. For the highest fluence, indications of charge multiplication were found.

In terms of performance versus threshold, wide regions of stable efficiency were identified in Figure 6.25 for all but the $1.3 \cdot 10^{14}\,\mathrm{n_{eq}/cm^2}$ sensor. This can again be explained by the strong signals generated thanks to the increase of the substrate resistivity, which sets in around $5 \cdot 10^{14}\,\mathrm{n_{eq}/cm^2}$. For most of a sensor's lifetime this means that a certain headroom for the requirements on the signal processing exists which is necessary for stable detector operation.

6.5.3 Timing Performance

The timing performance of HV-CMOS sensors is composed of the time it takes to collect sufficient charge to drive the discriminator over threshold and the signal propagation time in the pixel cell itself. Studies were done using the hit timing capabilities of the FE-I4 which has a resolution of 25 ns. A quantitative comparison of the performance of the various measured samples is difficult as it is subject to the sampling point, which was not adjusted during data taking and the introduction of the Clock-Phase Veto (CPV) for the irradiated CaRIBOu samples. However, the behaviour of the circuitry and the charge collection can still be estimated and values will be given where appropriate.

The version 2 sensors The version 2 samples demonstrated that although a fully biased and tuned sensor can efficiently detect particles, the timing resolution is sub-par to those of baseline planar or 3D detectors. The hit detection distribution shows a broad, 5 bx wide peak with an extensive tail of late hits as compared to a sharp, two to three bx wide distribution that was measured for the baseline sensors. It was established that the performance suffers from two effects: the diffusion component of the charge collection and the time-walk of the pixel amplifier as can be seen in Figure 6.8. Going from an unirradiated to a $1 \cdot 10^{15}\,\mathrm{n_{eq}/cm^2}$ irradiated sensor, more than 85 % of the registered hits fall into a 3 bx region and the tail towards late hits is suppressed, as it would be expected from the diminishing of the slow charge collection by diffusion. The amplifiers performance was evaluated by comparing the hit timing of the unirradiated sensor with low ($\sim 550\,\mathrm{e}$) and a very high ($\sim 2000\,\mathrm{e}$) threshold. For the high threshold the distribution broadened considerably and shifted towards later timing. This is a clear sign for time-walk of the amplifier as otherwise only the efficiency would have been influenced by the change in threshold.

The version 4 sensors As with the efficiency, the redesigned signal processing brought substantial improvement to the timing performance of version 4 sensors. The time distribution, as shown in Figure 6.19, was compressed leading to $\sim 94\,\%$ of hits being detected in 3 bx. However a tail of late hits, although suppressed, was still present.

The cause for the tail was found to originate from charge sharing in multi-hit clusters as it vanishes if only one-hit clusters are considered. However the tail towards later hits is still present when only taking fast hits into account, uncovering that also the version 4 circuitry suffers from time-walk. This is even amplified for the secondary hits in two-hit clusters as in addition to the latency due to diffusion, their collected charge is intrinsically lower than for the primary one. These clusters, forming 20 % of hits for the unirradiated sensor, are greatly suppressed already after $1.3 \cdot 10^{14}\,\mathrm{n_{eq}/cm^2}$. In fact, after

$5 \cdot 10^{15}\,\mathrm{n_{eq}/cm^2}$ where practically no diffusion is present, the sensor's sharp distribution from Figure 6.27, would develop a tail of late hits by reducing the bias voltage and with it the signal size. This can only be explained by the speed of signal propagation in the pixel cell. To disentangle the effect of multi-hit clusters and make results comparable to irradiated sensors, only the fastest hit was considered in the analysis. Also here, the distribution would shift to later detection times and its width would grow with a rising threshold, confirming the time-walk effect. In addition, the improvement of timing with rising high voltage, showed that with sufficient biasing the detector would predominantly collect charge by drift.

For the irradiated samples, the timing, plotted in Figure 6.26a, improved initially as the diffusion component was suppressed by trapping. This was further enhanced with fluence up to $1 \cdot 10^{15}\,\mathrm{n_{eq}/cm^2}$ as in this region the depletion zone is enlarged by the acceptor removal effect. As shown in the efficiency results, irradiation to $5 \cdot 10^{15}\,\mathrm{n_{eq}/cm^2}$ leads again to a degradation of signal size which is directly reflected in a reduced timing performance. In general, the version 4 prototypes reached a high efficiency of over 80 % with an integration time of one bx and 95 % with three bx, bringing them close to the performance of IBL sensors.

Remark on substrate resistivity The presented measurements have demonstrated that the HV2FEI4 sensors profit considerably from the acceptor removal effect and the consequential augmentation of the depletion zone with fluence. However, a range around $1 \cdot 10^{14}\,\mathrm{n_{eq}/cm^2}$ was identified where the trapping effect dominates charge collection which impacts both detection efficiency and timing. In general, a larger depletion zone would be desirable to mitigate this effect. Simulations based on TCT measurements suggest that a moderate increase of the initial substrate resistivity from 10 to 20 or 40 Ω cm would greatly reduce the attenuation of collected charge in this region without losing the benefits of the acceptor removal effect [99]. For the presented sensors, only a substrate with a resistivity of $\sim 10\,\Omega$ cm was offered by ams AG/IBM. As in the meanwhile the foundry implemented the H18 process in-house, a higher substrate resistivity has become available.

Chapter 7
Conclusions and Future Developments

Experiments at the Large Hadron Collider have lead to a wealth of precision measurements and discoveries. In the search for new physics, thus effects with weak couplings which are currently out of reach of the collider, it will be upgraded to raise its integrated luminosity by an order of magnitude. These upgrades, envisioned for the Long Shutdown 3 in 2024 to 2026, will once more push the limits of what is technologically possible, both for the accelerator and the experiments. For the ATLAS inner tracking system, this will necessitate a major upgrade with a completely redesigned and purely silicon based Inner Tracker (ITk). New technologies and techniques will be vital to fulfill the elevated requirements on tracking and vertexing whilst coping with an unprecedented pile-up and radiation scenario. For the inner layers of the Pixel Detector, the baseline sensor technologies, planar and 3D silicon, are set. The envisaged large area of pixel detectors for the outer layers combined with their lower radiation environment, however shifts the focus to cost effective production of sensors, module assembly and services.

High Voltage CMOS, although being a class of well established industrial processes, was only recently introduced as a potential technology for pixel sensors for HEP. The prospect of radiation hard detectors, produced in low cost industry standard processes and holding the potential for low-cost hybridisation or even fully monolithic devices resulted in an extensive R&D effort within ATLAS. While technologies from various chip foundries were investigated in parallel, this thesis concentrates on the H18 180 nm process by ams AG.

Initially aimed as a drop-in replacement for the baseline sensors, the HV2FEI4, a class of prototypes adapted to the latest ATLAS pixel readout chip, the FE-I4, was developed in H18 technology. Several generations of HV2FEI4 prototypes were designed and characterised in laboratory and test beam experiments with respect to their detection efficiency, speed, radiation tolerance and operation in the beam.

Hybridisation by gluing, replacing the costly and complex bump-bonding process and AC coupling the sensor to the readout chip, has proven to be effective. Studies with various gluing materials and bonding machines have lead to a stable and fast procedure and allowed to construct prototypes rapidly. The availability of on-sensor electronics

made possible to construct a finer granularity sensor – the HV2FEI4 has three times the granularity of the ATLAS IBL sensors.

An extensive hardware and software development was conducted to accommodate the feature set of the prototypes. The initial designs based on the UXIBO development board were extended and optimised for each generation of HV2FEI4 sensors before being superseded by the CaRIBOu system. Several sensor calibration algorithms were developed and tested, proving that the sensors can be operated at low thresholds. Especially as the prototypes are implemented on low resistivity substrates, thus have a comparably low signal size, this is necessary for efficient particle detection.

The sensors were extensively characterised in terms of radiation tolerance. The pixel circuitry proved to sustain Total Ionising Doses of up to 1 Grad from x-rays and protons. Although such high doses inflicted measurable damage to the circuitry, it was mitigated by careful retuning of the biasing parameters. In the target region for the outer layers of the ITk around 50 Mrad, this was not necessary as the sensors remained mostly unperturbed.

Effects of radiation on the sensor bulk and its ability to detect traversing particles were mainly assessed in test beam experiments. For this purpose, the FE-I4 Telescope, a new beam telescope was constructed with measurements on HV-CMOS sensors in mind. With six position sensitive planes, based on the latest technology from the ATLAS Insertable B-Layer (IBL), it reaches a pointing resolution of better than $11.7 \times 8.3\,\mu m^2$ at the device under test and can thereby resolve sub-pixel structures. Sensors like the HV2FEI4 are seamlessly integrated into the readout and a Region of Interest triggering facilitates fast data taking with such small sized devices. Combined with an extensive infrastructure including power supplies, cooling, positioning stages and monitoring, it forms a complete test bench for beam based detector characterisation. While all test beam results, presented in this thesis, were taken with HV2FEI4 sensors, further studies on various devices including other variants of HV-CMOS sensors, FE-I4 based baseline sensors and non-FE-I4 devices were conducted using this setup.

The test beam measurements on HV2FEI4 sensors demonstrated a high detection efficiency of over 99 % up to a fluence of $1 \cdot 10^{15}\,n_{eq}/cm^2$, the end-of-lifetime fluence of the outer layers of the ATLAS ITk pixel detector. It was shown that unirradiated sensors collect a significant fraction of charge by diffusion which changes dramatically with irradiation and the onset of the charge trapping effect. Parameter scans demonstrated that with high bias ($\sim$90 V) the hit detection efficiency can be completely restored, proving the sensors' large depletion zone and charge collection by drift.

The sensors profit highly from the acceptor removal effect which increases the bulk resistivity with irradiation up to $5 \cdot 10^{15}\,n_{eq}/cm^2$ as was also seen in Edge-TCT measurements. However, a fluence region of decreased efficiency ($\sim$98 %) was identified around

$1.3 \cdot 10^{14}\,\mathrm{n_{eq}/cm^2}$ where the acceptor removal effect is not enough pronounced yet to completely counteract the loss of diffusion by charge trapping. Laboratory measurements suggest that this can be mitigated by higher substrate resistivities as they recently became available by the foundry.

Despite the efficient detection up to high fluences, the sensors do not fully qualify for the ITk due to a sub-par timing behaviour. A considerable time-walk effect was found in the analogue circuitry which necessitates an integration time, longer than the LHC bunch crossing time (25 ns) for efficient detection of all hits. Especially in the unirradiated case, where diffusion leads to multi-hit clusters with asymmetric charge sharing, hits with a spread of over 400 ns were observed. As diffusion subsides with irradiation, the late hits are suppressed and the detector's timing performance reaches up to ITk requirements. An effective time-walk mitigation technique built into the pixel discriminator was developed and implemented in the later sensor generations [79].

Following the encouraging results of the HV2FEI4 sensors, a full reticle size sensor in the ams H35 350 nm technology demonstrated that an efficient large detector can be constructed and operated as a hybrid with the FE-I4 readout chip [76]. First measurements on the monolithic pixel matrices, implemented on the same chip, showed promising results [48] and lead to an ongoing development towards fully monolithic sensors in ams H18 technology for the ITk outer layers.

List of Figures

List of Tables

Bibliography

[1] C. Patrignani et al., *Review of Particle Physics*, Chin. Phys., vol. C40, no. 10, p. 100001, 2016. doi:10.1088/1674-1137/40/10/100001.

[2] Wikipedia contributors, *Standard Model of Elementary Particles*. `https://upload.wikimedia.org/wikipedia/commons/0/00/Standard_Model_of_Elementary_Particles.svg`. Accessed on 2018-05-01.

[3] G. Aad et al., *Combined Measurement of the Higgs Boson Mass in pp Collisions at $\sqrt{s}$=7 and 8 TeV with the ATLAS and CMS Experiments*, Physical review letters, vol. 114, no. 19, p. 191803, 2015. arXiv:1503.07589, doi:10.1103/PhysRevLett.114.191803.

[4] Planck Collaboration, *Planck 2015 results - I. Overview of products and scientific results*, A&A, vol. 594, p. A1, 2016. doi:10.1051/0004-6361/201527101.

[5] L. Evans and P. Bryant, *LHC Machine*, JINST, vol. 3, no. 08, p. S08001, 2008. doi:10.1088/1748-0221/3/08/S08001.

[6] E. A. Mobs, *The CERN accelerator complex*, Oct 2016. `http://cds.cern.ch/record/2225847`, Accessed on 2018-05-01.

[7] CERN, *Interim summary report on the analysis of the 19 September 2008 incident at the LHC*, Tech. Rep. EDMS 973073, CERN, Geneva, Oct 2008.

[8] High Luminosity Large Hadron Collider Collaboration, *The HL-LHC Project*. `http://hilumilhc.web.cern.ch/about/hl-lhc-project`. Accessed: 2018-03-06.

[9] The ATLAS Collaboration, *The ATLAS Experiment at the CERN Large Hadron Collider*, JINST, vol. 3, no. 08, p. S08003, 2008. doi:10.1088/1748-0221/3/08/S08003.

[10] J. Pequenao, *Computer generated image of the whole ATLAS detector*. `https://cds.cern.ch/record/1095924`, Mar 2008.

[11] L. Landau, *On the energy loss of fast particles by ionization*, J. Phys.(USSR), vol. 8, pp. 201–205, 1944. doi:10.1016/B978-0-08-010586-4.50061-4.

[12] F. Hartmann, *Evolution of silicon sensor technology in particle physics; 2nd ed.* Springer tracts in modern physics, Berlin: Springer, Dec 2017.

[13] K. K. Sze S.M., *Physics of Semiconductor Devices*. Wiley-Inerscience, 2006. doi:10.1002/0470068329.

[14] H. Kolanoski and N. Wermes, *Teilchendetektoren: Grundlagen und Anwendungen*. Berlin: Springer Spektrum, 2016.

[15] L. Rossi, P. Fischer, T. Rohe, and N. Wermes, *Pixel detectors: from fundamentals to applications*. Particle Acceleration and Detection, Berlin: Springer, 2006.

[16] F. Krummenacher, *Pixel detectors with local intelligence: an IC designer point of view*, NIMA, vol. 305, no. 3, pp. 527 – 532, 1991. doi:10.1016/0168-9002(91)90152-G.

[17] W. Snoeys et al., *Layout techniques to enhance the radiation tolerance of standard CMOS technologies demonstrated on a pixel detector readout chip*, NIMA, vol. 439, no. 2, pp. 349 – 360, 2000. doi:10.1016/S0168-9002(99)00899-2.

[18] G. Troska, *Development and operation of a testbeam setup for qualification studies of ATLAS pixel sensors*. PhD thesis, TU Dortmund, Feb 2012. doi:10.17877/DE290R-3375.

[19] G. Lindström, M. Moll, and E. Fretwurst, *Radiation hardness of silicon detectors–a challenge from high-energy physics*, NIMA, vol. 426, no. 1, pp. 1–15, 1999. doi:10.1016/S0168-9002(98)01462-4.

[20] G. Kramberger et al., *Charge collection studies in irradiated HV-CMOS particle detectors*, JINST, vol. 11, no. 04, p. P04007, 2016. doi:10.1088/1748-0221/11/04/P04007.

[21] G. Kramberger et al., *Determination of effective trapping times for electrons and holes in irradiated silicon*, NIMA, vol. 476, no. 3, pp. 645 – 651, 2002. Proc. of the 3rd Int. Conf. on Radiation Effects on Semiconductor Materials, Detectors and Devices. doi:10.1016/S0168-9002(01)01653-9.

[22] G. Aad et al., *ATLAS pixel detector electronics and sensors*, JINST, vol. 3, no. 07, p. P07007, 2008. doi:10.1088/1748-0221/3/07/P07007.

[23] S. Welch and J. Dopke, *The ATLAS Pixel nSQP Readout Chain*, Tech. Rep. ATL-INDET-PROC-2012-018, CERN, Geneva, Oct 2012.

[24] The ATLAS IBL Collaboration, *Production and integration of the ATLAS Insertable B-Layer*, JINST, vol. 13, no. 05, p. T05008, 2018. arXiv:1803.00844, doi:10.1088/1748-0221/13/05/T05008.

[25] M. Garcia-Sciveres et al., *The FE-I4 pixel readout integrated circuit*, NIMA, vol. 636, no. 1, Supplement, pp. 155 – 159, 2011. doi:10.1016/j.nima.2010.04.101.

[26] M. Barbero et al., *FE-I4 ATLAS pixel chip design*, PoS, vol. VERTEX2009, p. 027, 2009. doi:10.22323/1.095.0027.

[27] M. Barbero et al., *A new ATLAS pixel front-end IC for upgraded LHC luminosity*, NIMA, vol. 604, no. 1–2, pp. 397 – 399, 2009. Proceedings of the 8th International Conference on Position Sensitive Detectors. doi:10.1016/j.nima.2009.01.160.

[28] I. Perić et al., *The FEI3 readout chip for the ATLAS pixel detector*, NIMA, vol. 565, no. 1, pp. 178 – 187, 2006. Proceedings of the International Workshop on Semiconductor Pixel Detectors for Particles and Imaging. doi:10.1016/j.nima.2006.05.032.

[29] ATLAS IBL collaboration, *Prototype ATLAS IBL modules using the FE-I4A front-end readout chip*, JINST, vol. 7, no. 11, p. P11010, 2012. doi:10.1088/1748-0221/7/11/P11010.

[30] D. Arutinov et al., *Digital Architecture and Interface of the New ATLAS Pixel Front-End IC for Upgraded LHC Luminosity*, IEEE Transactions on Nuclear Science, vol. 56, pp. 388–393, April 2009. doi:10.1109/TNS.2009.2015318.

[31] A. X. Widmer and P. A. Franaszek, *A DC-balanced, partitioned-block, 8B/10B transmission code*, IBM Journal of research and development, vol. 27, no. 5, pp. 440–451, 1983. doi:10.1147/rd.275.0440.

[32] J. Jentzsch, *Pixel detector modules performance for ATLAS IBL and future pixel detectors*. PhD thesis, TU Dortmund, Jun 2015. doi:10.17877/DE290R-16400.

[33] M. Benoit, *Étude des détecteurs planaires pixels durcis aux radiations pour la mise à jour du détecteur de vertex d'ATLAS*. PhD thesis, 2011. presented 10 Jun 2011.

[34] S. Altenheiner et al., *Planar slim-edge pixel sensors for the ATLAS upgrades*, JINST, vol. 7, no. 02, p. C02051, 2012. doi:10.1088/1748-0221/7/02/C02051.

[35] *Efficiency and Hit Spatial Resolution of ATLAS IBL Sensors in LHC Run 2 Collision Events*, Tech. Rep. ATL-INDET-PUB-2016-001, CERN, Geneva, Aug 2016.

[36] *Optimisation of the ATLAS b-tagging performance for the 2016 LHC Run*, Tech. Rep. ATL-PHYS-PUB-2016-012, CERN, Geneva, Jun 2016.

[37] M. P. Giordani, *The Upgraded Pixel Detector of the ATLAS Experiment for Run-2 at the LHC*, Tech. Rep. ATL-INDET-PROC-2016-009, CERN, Geneva, Nov 2016.

[38] ATLAS Collaboration, *Impact Parameter Resolution* . `https://atlas.web.cern.ch/Atlas/GROUPS/PHYSICS/PLOTS/IDTR-2015-007/`. Accessed: 2017-12-30.

[39] ATLAS Collaboration, *Luminosity Results for Run-2*. `https://twiki.cern.ch/twiki/bin/view/AtlasPublic/LuminosityPublicResultsRun2`. Accessed: 2018-06-11.

[40] ATLAS Collaboration, *Technical Design Report for the ATLAS Inner Tracker Strip Detector*, Tech. Rep. CERN-LHCC-2017-005. ATLAS-TDR-025, CERN, Geneva, Apr 2017.

[41] ATLAS Collaboration, *Technical Design Report for the ATLAS Inner Tracker Pixel Detector*, Tech. Rep. CERN-LHCC-2017-021. ATLAS-TDR-030, CERN, Geneva, Sep 2017.

[42] RD53 Collaboration, *RD53A Integrated Circuit Specifications*, Tech. Rep. CERN-RD53-PUB-15-001, CERN, Geneva, Dec 2015.

[43] ams AG, *0.18 µm High-Voltage CMOS process*. `http://ams.com/eng/Products/Full-Service-Foundry/Process-Technology/High-Voltage-CMOS/0.18-m-HV-CMOS-process`. Accessed: 2018-03-06.

[44] M. Backhaus, *High bandwidth pixel detector modules for the ATLAS Insertable B-Layer*. PhD thesis, Universität Bonn, Feb 2014. CERN-THESIS-2013-303, BONN-IR-2014-02.

[45] M. F. Garcia et al., *Radiation hardness studies of neutron irradiated CMOS sensors fabricated in the ams H18 high voltage process*, JINST, vol. 11, no. 02, p. P02016, 2016. doi:10.1088/1748-0221/11/02/P02016.

[46] I. Perić and C. Takacs, *Large monolithic particle pixel-detector in high-voltage CMOS technology*, NIMA, vol. 624, no. 2, pp. 504 – 508, 2010. New Developments in Radiation Detectors. doi:10.1016/j.nima.2010.03.161.

[47] D. Hynds et al., *Capacitively coupled hybrid pixel assemblies for the CLIC vertex detector*, NIMA, vol. 823, pp. 1 – 8, 2016. doi:10.1016/j.nima.2016.03.072.

[48] S. Terzo et al., *Characterisation of novel prototypes of monolithic HV-CMOS pixel detectors for high energy physics experiments*, JINST, vol. 12, no. 06, p. C06009, 2017. doi:10.1088/1748-0221/12/06/C06009.

[49] B. Ristic et al., *The FE-I4 telescope for particle tracking in testbeam experiments*, JINST, vol. 11, no. 07, p. P07003, 2016. arXiv:1603.07776, doi:10.1088/1748-0221/11/07/P07003.

[50] J. Bilbao De Mendizabal, *Production, integration and commissioning of the ATLAS Insertable B-Layer and test beam studies of new pixel technologies for the HL-LHC*. PhD thesis, Université de Genève, Feb 2016. ID: unige:90515. doi:10.13097/archive-ouverte/unige:90515.

[51] ATLAS Collaboration, *ATLAS high-level trigger, data-acquisition and controls: Technical Design Report*. Technical Design Report ATLAS, Geneva: CERN, 2003. CERN-LHCC-2003-022.

[52] N. Terrasson, *Upgrade and improvements on the FEI4 Geneva Telescope*, Master's thesis, Université de Genève, Aug 2017.

[53] D. Muenstermann et al., *Testbeam results of irradiated ams H18 HV-CMOS pixel sensor prototypes*, JINST, vol. 13, pp. P02011–P02011, Feb 2018. doi:10.1088/1748-0221/13/02/p02011.

[54] G. McGoldrick, M. Červ, and A. Gorišek, *Synchronized analysis of test-beam data with the judith software*, NIMA, vol. 765, pp. 140 – 145, 2014. doi:10.1016/j.nima.2014.05.033.

[55] C. Hu-Guo et al., *First reticule size MAPS with digital output and integrated zero suppression for the EUDET-JRA1 beam telescope*, NIMA, vol. 623, no. 1, pp. 480 – 482, 2010. 1st International Conference on Technology and Instrumentation in Particle Physics. doi:10.1016/j.nima.2010.03.043.

[56] Proteus developers, *Proteus - Pixel telescope reconstruction*. `https://gitlab.cern.ch/unige-fei4tel/proteus`. Accessed: 2018-03-06.

[57] R. Turchetta, *Spatial resolution of silicon microstrip detectors*, NIMA, vol. 335, pp. 44–58, Oct. 1993. doi:10.1016/0168-9002(93)90255-G.

[58] N. P. Zarnecki A.F., *EUDET Telescope Geometry and Resolution Studies*, Tech. Rep. 2007-01, Feb 2007. EUDET-Report.

[59] J. Idarraga and M. Benoit, *The AllPix Simulation Framework*. `https://twiki.cern.ch/twiki/bin/view/Main/AllPix`. Accessed: 2018-03-06.

[60] C. Kleinwort, *General broken lines as advanced track fitting method*, NIMA, vol. 673, pp. 107 – 110, 2012. doi:10.1016/j.nima.2012.01.024.

[61] C. Riegel, *Performance test of depleted CMOS sensors for application at HL-LHC*. PhD thesis, Bergische Universität Wuppertal, Apr 2018.

[62] S. Viel et al., *Performance of silicon pixel detectors at small track incidence angles for the ATLAS Inner Tracker Upgrade*, Nov 2015. ATL-INDET-PROC-2015-011.

[63] F. D. Bello et al., *Results of the 2015 beamtest of a 180 nm AMS High-Voltage CMOS sensor prototype*, JINST, vol. 11, no. 07, p. P07019, 2016. arXiv:1603.07798, doi:10.1088/1748-0221/11/07/P07019.

[64] L. Paolozzi et al., *100 ps time resolution with thin silicon pixel detectors and a SiGe HBT amplifier*, JINST, vol. 11, no. 03, p. P03011, 2016. doi:10.1088/1748-0221/11/03/P03011.

[65] *AMS AG, Premstaetten, Austria*. `http://ams.com`. Accessed: 2018-4-24.

[66] *LFoundry S.r.l, Avezzano, Italy*. `http://www.lfoundry.com`. Accessed: 2018-4-24.

[67] *Tower Semiconductor Ltd., Migdal Haemek, Israel*. `http://www.towerjazz.com`. Accessed: 2018-4-24.

[68] International Business Machines Corp., *austriamicrosystems and IBM Announce Process Development Agreement on Advanced High-Voltage CMOS Process*. `http://www-03.ibm.com/press/us/en/pressrelease/21395.wss`. Accessed: 2018-4-24.

[69] F. Meier Aeschbacher et al., *MuPix7 - A fast monolithic HV-CMOS pixel chip for Mu3e*, JINST, vol. 11, no. 11, p. C11029, 2016. doi:10.1088/1748-0221/11/11/C11029.

[70] I. Kremastiotis et al., *Design and standalone characterisation of a capacitively coupled HV-CMOS sensor chip for the CLIC vertex detector*, JINST, vol. 12, no. 09, p. P09012, 2017. doi:10.1088/1748-0221/12/09/P09012.

[71] I. Peric, *Personal correspondance*, 2014.

[72] J. Rieger, *Detector Development for the High Luminosity Large Hadron Collider*. PhD thesis, Universität Göttingen, Jul 2016. CERN-THESIS-2016-090, II.Physik-UniGö-Diss-2016/01.

[73] Finetech GmbH&Co.KG, *Die Bonder for research and development*. `https://www.finetech.de/products/rd-bonders/`. Accessed: 2018-04-19.

[74] SET Corporation SA, *Flip-Chip Bonder Line*. `http://www.set-sas.fr/en/lp421389-FLIP-CHIP-BONDER-LINE.html`. Accessed: 2018-04-19.

[75] K. Dette, *Commissioning of the ATLAS Insertable B-Layer and first operation experience*. PhD thesis, TU Dortmund, Mar 2017. doi:10.17877/DE290R-17951.

[76] M. Benoit et al., *Test beam measurement of ams H35 HV-CMOS capacitively coupled pixel sensor prototypes with high-resistivity substrate*, JINST, vol. 13, pp. P12009–P12009, dec 2018. arXiv:1712.08338, doi:10.1088/1748-0221/13/12/p12009.

[77] P. Valerio, R. Ballabriga, and M. Campbell, *Design of the 65 nm CLICpix demonstrator chip*, Nov 2012. LCD-Note-2012-018.

[78] Peric, I., *HV-CMOS Overview*. `https://indico.cern.ch/event/273880/contributions/1614892`, Feb 2014. Talk at the 9th Trento Workshop an Advanced Silicon Radiation Detectors.

[79] R. Schimassek et al., *HVCMOS pixel detectors - methods for enhancement of time resolution*, IEEE - Proceedings of 2016 IEEE NSS/MIC/RTSD, Oct 2016. doi:10.1109/NSSMIC.2016.8069903.

[80] SILab, Physikalisches Institut, University of Bonn, *USBpix - USB based readout system for ATLAS FE-I3 and FE-I4*. `http://icwiki.physik.uni-bonn.de/twiki/bin/view/Systems/UsbPix`. Accessed: 2018-04-01.

[81] Xilinx, Inc., *Xilinx Zynq-7000 All Programmable SoC ZC706 Evaluation Kit*. `https://www.xilinx.com/products/boards-and-kits/ek-z7-zc706-g.html`. Accessed: 2018-4-24.

[82] P. Moreira et al., *The GBT: A proposed architecure for multi-Gb/s data transmission in high energy physics*, 2007. doi:10.5170/CERN-2007-007.332.

[83] H. Liu et al., *Development of a modular test system for the silicon sensor R&D of the ATLAS Upgrade*, JINST, vol. 12, no. 01, p. P01008, 2017. doi:10.1088/1748-0221/12/01/P01008.

[84] M. Caloz, *Active Pixel Sensors based on High Voltage CMOS Technology*, Master's thesis, Université de Genève, 2015.

[85] B. Ristic, *Measurements on HV-CMOS active sensors after irradiation to HL-LHC fluences*, JINST, vol. 10, no. 04, p. C04007, 2015. doi:10.1088/1748-0221/10/04/C04007.

[86] F. Ravotti et al., *Upgrade scenarios for irradiation lines:: Upgrade of the Proton Irradiation Facility in the CERN PS EAST AREA*, Sep 2014. AIDA-D8.4.

[87] J. Liu et al., *Performance of radiation-hard HV/HR CMOS sensors for the ATLAS inner detector upgrades*, JINST, vol. 11, no. 03, p. C03044, 2016. doi:10.1088/1748-0221/11/03/C03044.

[88] B. Ristic, *Active pixel sensors in AMS H18/H35 HV-CMOS technology for the ATLAS HL-LHC upgrade*, NIMA, vol. 831, pp. 88 – 93, 2016. doi:10.1016/j.nima.2016.06.001.

[89] S. Feigl, *Performance of capacitively coupled active pixel sensors in 180 nm HV-CMOS technology after irradiation to HL-LHC fluences*, JINST, vol. 9, no. 03, p. C03020, 2014. doi:10.1088/1748-0221/9/03/C03020.

[90] M. Backhaus, *Parametrization of the radiation induced leakage current increase of NMOS transistors*, JINST, vol. 12, no. 01, p. P01011, 2017. doi:10.1088/1748-0221/12/01/P01011.

[91] L. Snoj, G. Zerovnik, and A. Trkov, *Computational analysis of irradiation facilities at the JSI TRIGA reactor*, Applied Radiation and Isotopes, vol. 70, no. 3, pp. 483 – 488, 2012. doi:10.1016/j.apradiso.2011.11.042.

[92] S. Braccini, *The new Bern PET cyclotron, its research beam line, and the development of an innovative beam monitor detector*, AIP Conference Proceedings, vol. 1525, no. 1, pp. 144–150, 2013. doi:10.1063/1.4802308.

[93] J. Anders et al., *A facility for radiation hardness studies based on the Bern medical cyclotron*, 2018. arXiv:1803.01939.

[94] S. Feigl, *Novel Pixel-Detector Developments for Upgrades of the ATLAS Central Tracking System at the LHC*. PhD thesis, Universitetet i Oslo Fysisk institutt, Oct 2017.

[95] A.-K. Perrevoort, *Characterisation of High Voltage Monolithic Active Pixel Sensors for the Mu3e Experiment*, Master's thesis, University of Heidelberg, 2012.

[96] J. P. Hammerich, *Studies of HV-MAPS Analog Performance*, Bachelor's thesis, University of Heidelberg, 2015.

[97] G. Casse, *Charge multiplication in highly irradiated planar silicon sensors*, PoS, vol. 113, 01 2010. Proceedings of the 19th VERTEX conference 2010. doi:10.22323/1.113.0020.

[98] F. Di Bello, *Test-beam analysis and TCAD simulation of the HV-CMOS pixel technology proposed for the ATLAS experiment at the HL-LHC*, Master's thesis, Université de Genève, 2015.

[99] V. Fadeyev et al., *Investigation of HV/HR-CMOS technology for the ATLAS Phase-II Strip Tracker Upgrade*, NIMA, vol. 831, pp. 189 – 196, 2016. Proceedings of the 10th International "Hiroshima" Symposium. doi:10.1016/j.nima.2016.05.092.

Glossary

ADC	Analogue to Digital Converter
BCID	Bunch Crossing ID
CaRIBOu	Control and Readout Itk BOard
CCPD	Capacitively Coupled Pixel Device
CLK	Clock
CMD	Command
CMOS	Complementary Metal-Oxide-Semiconductor
CORBA	Common Object Request Broker Architecture
CPV	Clock-Phase Veto
CSA	Charge Sensitive Amplifier
CSC	Cathode Strip Chamber
DAC	Digital to Analogue Converter
DAQ	Data Acquisition
DCS	Detector Control System
DMAPS	Depleted MAPS
DRIE	Deep Reactive Ion Etching
DUT	Device Under Test
ELT	Enclosed Layout Transistor
EOCL	End Of Column Logic
ETCT	Edge TCT
FDAC	Feedback Current Digital to Analogue Converter
FE	Front-End
FPGA	Field Programmable Gate Array
GPIO	General Purpose Input Output
HEP	High Energy Physics
HV-CMOS	High Voltage CMOS
HSIO	High-Speed Input Output
HV	High Voltage
IBL	Insertable B-Layer
IC	Integrated Circuit
ID	Inner Detector
ITk	Inner Tracker
L1A	Level-1 Accept
LDO	Low Drop-Out Regulator
LEP	Large Elecron-Positron Collider
LHC	Large Hadron Collider
LV	Low Voltage
MAPS	Monolithic Active Pixel Sensor
MDT	Monitored Drift Tube
MGT	Multi-Gigabit Transceiver
MIP	Minimum Ionizing Particle
MOSFET	Metal-Oxide-Semiconductor Field-Effect Transistor
MPV	Most Probable Value
NIEL	Non Ionizing Energy Loss
NI	National Instruments
NTC	Negative Temperature Coefficient
PPS	Planar Pixel Sensor
PSB	PS Booster
PS	Proton Synchrotron
RAM	Random Access Memory
RCE	Reconfigurable Cluster Element
ROC	Readout Chip
ROI	Region Of Interest
RPC	Resistive Plate Chamber
SCT	Semi-Conductor Tracker
SDA	Smart Diode Array
SiPM	Silicon Photo-Multiplier
SOC	System On Chip
SPS	Super Proton Synchrotron
TCT	Transient Current Technique
TDAC	Threshold Digital to Analogue Converter
TDAQ	Trigger and Data Acquisition
TGC	Thin Gap Chamber
TID	Total Ionising Dose
ToA	Time of Arrival
ToT	Time over Threshold
TRT	Transition Radiation Tracker
UXIBO	USB Xilinx Board

Acknowledgements

This thesis would have not been possible without lots of support of colleagues, friends and supervisors. Here comes a shout-out and big thanks to all of you that I will name below and of course those I will miss and eventually remember the very moment I publish this thesis.

I would like to thank my professors Giuseppe Iacobucci and Marzio Nessi for giving me the opportunity for working on a highly interesting topic and being part of a cutting-edge development while experiencing the great environment that is CERN.

Furthermore, I would like to thank Christoph Rembser and Markus Joos, who made many a thing possible and have been a great source of support and advice.

Doing my research, I could always count on my fellow colleagues and supervisors at the University of Geneva for which I am grateful. This especially means Mathieu Benoit, Javier Bilbao De Mendizabal, Francesco Di Bello, Didier Ferrere, Moritz Kiehn, Sergio Gonzales-Sevilla, Sebastien Michal and Augusto Sciuccati.

I'd like to express my deep gratitude to Daniel Münstermann, a friend and mentor who did not only guide me through my PhD and share his vast knowledge about detectors, but was always there when help was needed... and when he had something new and usually urgent to be done in mind ;)

In addition to my supervisors, this thesis was shaped considerably by the inspiring and helpful comments of Didier, Jens, Mathieu, Sergio and Prof. Michele Weber. Thank you very much for all your time and efforts.

A good part of my time as a PhD student I have spent dwelling in CERN's test beam halls and beam areas. All my efforts would have not been fruitful without the kind and always fast support on short notice of Johannes Bernhard, Lau Gatignon, Michael Jeckel and all the PS and SPS operators, technicians and crane operators. Speaking of short notice, I would like to thank Raphael Berberat, Sylvain Kaufmann, the SMD workshop team, Ian McGill and Florentina Manolescu for their patience with my last-minute requests and their always top-notch assembly and repair of our detectors. I must not miss to thank Martin Kocian for countless hours of explaining me the working of a full-size readout system and making many a feature, I came up with, possible.

Working is half the fun without companions and I consider myself lucky that I had always very nice and friendly people around me. Yes, I am talking to you, inhabitants of the various labs and the infamous James Bond office and surrounding corridors, especially Abhi, Florian, Matevz, Sascha and Simon. Thank you very much for the long discussions, the Nerv gun fights, the crazy and late-night actions and in general a great time.

This one goes to certain people that I met during my time at universities and CERN as colleagues but who soon became much more. Alex, Jenny, Jens, Lingxin, Malte, Sonia and Timon, I am so grateful for knowing you and having the privilege to call you my friends.

Rushing through months to get this thesis written, I got very lucky by meeting you, my dear Elena. Your constant encouragement and patience, your understanding, all the kind words and deeds, and countless, very much needed coffee breaks carried me through that time.

I cannot adequately express my gratitude to a few people that are very dear to me. Without exaggeration I can say that your unconditional friendship has saved me on numerous occasions and made me forging ahead even in the hardest of times. André, Christian, Daniel, Fabian, Karo, Sarah, Silke and Steffi, thank you beyond measure.

Although far away, it never felt that way. My old friends from Essen and Dortmund - nowadays rather all over the world - our friendship and gatherings were always a source of strength for me.

Овај рад неби постојао без подршке и љубави моје фамилије, поготово мојих родитеља, мог малог брата и моје бабе и деде. Ви сте ми светло, нада и снага. Хвала вам много за вашу топлоту, ваше разумевање, ваше стрпљење сваки пут када ме ухватите у гужви и што сте ми увек близу где год да сам на свету.